Numerical simulations and uncertainty quantification for cloud simulation

Dissertation

zur Erlangung des Grades
Doktor der Naturwissenschaften (Dr. rer. nat.)

am Fachbereich Physik, Mathematik und Informatik
der Johannes Gutenberg-Universität
in Mainz

Bettina Wiebe

Mainz, September 2021

Datum der mündlichen Prüfung: 10.12.2021

Publications

Parts of this thesis, which will be indicated, have already been published. In the following, the list of publications, which all have undergone a peer-review process, and a short description of my contributions are stated.

[21] A. Chertock, A. Kurganov, M. Lukáčová–Medviďová, P. Spichtinger, and B. Wiebe, *Stochastic Galerkin method for cloud simulation*, Math. Clim. Weather Forecast., 5 (2019), pp. 65–106.

My contribution to this publication was the development, implementation and presentation of the numerical method as well as the simulation and visualization of the experimental results. The results presented in this thesis differ slightly to the ones presented in the publication due to a now more precise consideration of a cloud parameter as also mentioned in Remark 2.1.

[79] M. Lukáčová–Medviďová, J. Rosemeier, P. Spichtinger, and B. Wiebe, *IMEX finite volume methods for cloud simulation*, in Finite volumes for complex applications VIII—hyperbolic, elliptic and parabolic problems, vol. 200 of Springer Proc. Math. Stat., Springer, Cham, 2017, pp. 179–187.

This publication is a conference proceeding based on the talk I gave at the conference "Finite Volumes of Complex Applications" in June 2017 in Lille. My contribution to the published work was the development, implementation and presentation of the numerical method as well as the simulation of the numerical test and the presentation of the result.

Abstract

Clouds are one of the most important and at the same time one of the most uncertain components in the Earth-atmosphere system. In this thesis, we first consider a deterministic model for warm clouds derived from physical principles. This cloud model consists of the Navier-Stokes equations describing weakly compressible flows coupled to evolution equations for liquid water phases. In addition, we investigate two stochastic models which are derived from the deterministic one. The first stochastic model exhibits uncertainties in the cloud representations which do not propagate to the flow variables, whereas the second model is fully stochastic. Since cloud models are associated with very rich dynamics, especially due to their multi-scale behavior, and since a quantification of their uncertainties is computationally expensive, their numerical simulation requires sophisticated methods. In this work, we develop and study finite volume schemes with implicit-explicit time discretization combined with a spectral expansion in the stochastic space. We conduct extensive numerical benchmarking for both the deterministic and the stochastic models and compare the accuracy of the developed stochastic method for the fully stochastic model against a standard sampling method. In numerical experiments of two and three-dimensional Rayleigh-Bénard convection we further demonstrate the applicability of our stochastic methods for uncertainty quantification in complex atmospheric models.

Zusammenfassung

Wolken sind nicht nur eine der wichtigsten, sondern auch eine der unsichersten Komponenten in dem System von Erden und Atmosphäre. In dieser Arbeit betrachten wir erst ein deterministisches Modell für warme Wolken, das aus den Navier-Stokes-Gleichungen für schwach-kompressible Strömungen sowie aus Evolutionsgleichungen für Flüssigwasserphasen besteht. Des Weiteren untersuchen wir zwei stochastische Modelle, die aus dem deterministischen Modell abgeleitet sind. Das erste stochastische Modell enthält Unsicherheiten in den Wolkenrepräsentationsgleichungen, die sich nicht auf die Flussvariablen ausbreiten, wohingegen das zweite Modell vollständig stochastisch ist. Da Wolkenmodelle mit einer komplexen Dynamik, vorwiegend resultierend aus Multiskaleneffekten, einhergehen und da eine Quantifizierung ihrer Unsicherheiten rechenintensiv ist, bedarf es geeigneter Verfahren für ihre numerische Approximation. Wir entwickeln und untersuchen hier Finite-Volumen-Verfahren mit implizit-expliziter Zeitdiskretisierung kombiniert mit einer Spektralmethode im stochastischen Raum. Für das deterministische sowie die stochastischen Modelle führen wir numerische Benchmark-Teste durch und vergleichen die Genauigkeit des entwickelten stochastischen Verfahrens mit der eines üblichen Samplingverfahrens. Durch numerische Experimente von zwei- und dreidimensionaler Rayleigh-Bénard Konvektion demonstrieren wir zusätzlich die Anwendungsmöglichkeit unseres stochastischen Verfahren zur Unsicherheitenquantifizierung in komplexen atmosphärischen Modellen.

Contents

List of Figures

List of Tables

1 Introduction

Clouds constitute one of the most important components in the Earth-atmosphere system. They influence the hydrological cycle and by interacting with radiation they control the energy budget of the whole system. However, clouds are one of the most uncertain components and there exists no generally accepted cloud model derived from first principles, as for example for atmospheric flows.

Clouds are composed by myriads of water particles in different phases (liquid and solid), and thus they need to be described by a large ensemble in a statistical sense. A common way of obtaining such an ensemble is by using a mass or size distribution, which would lead to a Boltzmann-type evolution equation. Although there are some approaches available in the literature formulating cloud models in such a way [12, 61, 62], a complete and consistent description is missing. Since measurements of size distributions of cloud particles are difficult, we are often restricted to averaged quantities such as, for example, the mass of water per dry air (mass concentrations). Therefore, models are often formulated in terms of so-called bulk quantities, that is, mass and number concentrations of the respective water species. Many processes are necessary to describe the time evolution of the cloud as a statistical ensemble, that is, particle formation or annihilation, growth/evaporation of particles, collision processes, and sedimentation due to gravity. For each of the processes, we have to formulate a representative mathematical term in the sense of a rate equation. Although for some processes the physical mechanisms are quite understood, the formulation of the process rates usually contain uncertain parameters, thus cloud models come with inherent uncertainty. On the other hand, the initial conditions for atmospheric flows and the embedded clouds are also not perfectly constrained, leading to uncertainties in the environmental conditions. It is well-known from former studies that uncertainties in cloud processes and environmental conditions can lead to drastic changes in simulations, thus these uncertainties influence the predictability of moist atmospheric flows, clouds and precipitation crucially. The uncertainties can, for instance, affect the distribution of latent heat, which in turn can influence atmospheric dynamics, e.g., frontogenesis [53] or convection [45, 85].

For investigations of the impact of these uncertain cloud model parameters as well as the impact of variations in environmental conditions on atmospheric flows, sensitivity studies are usually carried out. Since one or more parameters are (randomly) varied, the Monte

Carlo approach can be used. This, however, requires a large ensemble of simulations to be conducted, which makes Monte Carlo methods computationally expensive and requires a very fine sampling of the parameter space and possible environmental conditions. In most practical studies, a much smaller set of ensembles (with about $10 - 100$ samples only) is used. In order to improve both the efficiency and accuracy of a numerical method, we choose a different way of representing random variations by using spectral expansions in the stochastic space. This approach enables us to investigate the impact of variations in cloud model parameters and initial conditions on the evolution of moist flows with embedded clouds.

In this thesis, we will consider three mathematical models of cloud physics. The first model (M1) is deterministic and consists of the Navier-Stokes equations coupled with the cloud evolution equations for the water vapor, cloud water and rain presented in [21, 79, 103]. In this model, the Navier-Stokes equations describe weakly compressible flows with viscous and heat conductivity effects, while microscale cloud physics is modeled by the system of advection-diffusion-reaction equations. Since meteorological applications typically inherit several sources of uncertainties, such as model parameters, initial and boundary conditions, purely deterministic models are insufficient in such situations and stochastic models need to be considered. Thus, the second model (M2) is a stochastic version of the deterministic model (M1) to account for uncertainties in input quantities and model parameters. In this model, which was investigated in [21], we restrict our consideration to the case in which the uncertainties are only in the cloud physics representation and do not propagate to the flow variables, that is, the Navier-Stokes equations. A more consistent approach, where the uncertainties affect also the flow, is realized by the third model (M3) in which the full cloud model is stochastic.

The main goal of this thesis is to develop suitable numerical methods for the three models, in particular, to design an efficient numerical method for quantifying uncertainties in solutions of the stochastic models (M2) and (M3).

In recent years, a wide variety of uncertainty quantification methods has been proposed and investigated in the context of physical and engineering applications. These methods include stochastic Galerkin methods based on generalized polynomial chaos (gPC) [25, 102, 125, 135, 146], stochastic collocation methods [82, 143, 145], and multilevel Monte Carlo methods [94, 95, 117]. Each of these groups of methods has its pros and cons. While results obtained by the Monte Carlo simulations are generally good, the approach is not very efficient due to the large number of realizations required. Stochastic collocation methods are typically more efficient than the Monte Carlo ones since they only require solving the underlying deterministic system at certain interpolation points in the stochastic space. These data are then used to reconstruct the gPC expansion using an appropriate set of orthogonal polynomials. The Monte Carlo as well as the stochastic collocation method fall into a class of the *non-intrusive methods*. Stochastic Galerkin methods offer an alternative approach for computing the gPC expansion. In general, they are more rigorous and efficient than the Monte Carlo and collocation ones; see, e.g., [27]. The stochastic Galerkin method is an *intrusive method* since it requires changes in the underlying code. One needs to solve a system of PDEs for the gPC expansion coefficients.

As a first step, we derive a second-order semi-discrete finite volume scheme for the purely deterministic version of the coupled Navier-Stokes-cloud system (M1) which we proposed in [79]. This method is based on the operator splitting approach, in which the system is split into the macroscopic Navier-Stokes equations and microscopic cloud equations. The Navier-Stokes equations are then solved by an implicit-explicit (IMEX) finite-volume method, while the cloud equations are numerically solved by a finite-volume method combined with an explicit Runge-Kutta method with an enlarged stability region [91]. Based on this time and space discretization we develop a stochastic Galerkin method for the stochastic cloud microphysics model (M2) and the fully stochastic Navier-Stokes-cloud model (M3). In the case of stochastic cloud physics (M2) we need to solve the deterministic Navier-Stokes equations coupled with the PDE system for the gPC expansion coefficients for the cloud variables which is then solved in time and space by the discretizations of the deterministic model. In the case of the fully stochastic model (M3) we extend the approach of the stochastic cloud physics model (M2) to the Navier-Stokes equations and then also end up with a PDE system for the gPC expansion coefficients of the Navier-Stokes variables. Finally, we carry out experimental convergence studies for our developed numerical methods, the deterministic and the stochastic ones, and present and discuss numerical experiments for two-dimensional (2D) and three-dimensional (3D) Rayleigh-Bénard convection.

The underlying work is organized as follows: In Chapter 2 we present mathematical modeling approaches for warm clouds. For the dynamics of fluids we introduce the compressible Navier-Stokes equations and for the cloud dynamics evolution equations for the liquid water phases. Based on that, we introduce in Chapter 3 the three different models which will be investigated in this work, that is, the deterministic cloud model (M1), the model with stochastic cloud dynamics (M2) and the fully stochastic cloud model (M3). We also state some existence and uniqueness results in the deterministic case for the ordinary differential equations (ODE) cloud model on which our cloud dynamics system is based, as well as for the compressible Navier-Stokes equations and a full moist atmospheric flow model similar to ours. The fourth chapter is devoted to a presentation of the numerical scheme for the deterministic cloud model (M1). We begin the chapter by introducing general finite volume methods for the space discretization and illustrate how a general Godunov-type scheme can achieve higher order of accuracy. We introduce Runge-Kutta methods for the time discretization and the Strang operator splitting approach which allow us to use different time integration methods for the Navier-Stokes and the cloud equations. This allows to take multiscale effects of cloud dynamics into account. Then we present implicit-explicit methods as well as an explicit Runge-Kutta method with an extended stability region which is third-order consistent in time, the DUMKA3 method. Afterward, in Chapter 5, we present the numerical methods for the stochastic models. We start by providing a general overview of uncertainty quantification and possible uncertainty quantification methods for cloud modeling and then focus on stochastic spectral methods, especially the stochastic Galerkin method which is the method of our choice. In Chapter 6 we exhibit experimental convergence studies and numerical experiments of dry and moist Rayleigh-Bénard convection in 2D and 3D with the deterministic cloud model (M1). In Chapter 7 we then present numerical result for the stochastic models (M2) and (M3). We begin by investigating the experimental

convergence and then state results for the stochastic Rayleigh-Bénard convection in 2D and 3D, where we compare the results obtained with all three different models in the case of uncertainty in the initial conditions. At the end of the chapter, we compare the stochastic Galerkin method with the Monte Carlo as well as the stochastic collocation method in one experimental scenario. We conclude our work in Chapter 8 and outline some possible future investigations. In Appendices A and B we state a closure for single moment schemes and an explicit formulation of the cloud equations which we used in our implementation.

2 Modeling

In this chapter, we introduce mathematical models for describing dynamics of clouds and fluids. We derive, in particular, a model for warm clouds that consists of evolution equations for the liquid water phases. The numerical study, especially the uncertainty quantification, of the coupled model (the dynamics of clouds combined with the dynamics of fluids) will be the chief subject of this thesis and will be addressed in the following chapters. For clarity, we build up the models separately.

To begin with we introduce in Section 2.1 the compressible Navier-Stokes equations which will be used to model fluid flows. Afterwards, we discuss in Section 2.2 the cloud equations that will be considered in this thesis and provide an overview of some aspects of cloud microphysics that play a role in modeling.

The modeling techniques we consider in Section 2.2 are a combination of different approaches that will be explained during the modeling process. The cloud model itself is based on [103], where the ODE form of the model was first introduced and where the involved processes are discussed in more detail. The description presented here is taken from [21]. The compressible Navier-Stokes equations in Section 2.1 are widely used for modeling air dynamics and our derivation is based on [78, 141]. For the prerequisites, we refer to [136] and for more details on continuum mechanics to [47, 112].

For alternative representations of cloud dynamics and their numerical investigations, we refer the reader to [11, 110] and references therein.

Remark 2.1*:* The considered cloud processes are as in [21] with the only difference that we have now considered the constant k_2 more precisely and set $k_2 = 4083$.

2.1 Dynamics of fluids

In this section, we will introduce the model that we use for describing dynamics of moist air, namely the nonhydrostatic compressible Navier-Stokes equations that model moist air as a compressible and viscous fluid. Additionally, we will make a few other assumptions on the fluid that will be explained during the modeling and derivation process.

Remark 2.2*:* A common modeling approach in meteorology is to model air as an incompressible fluid since air is weakly compressible. The corresponding equations are called the incompressible Navier-Stokes equations. Another commonly applied simplification is to assume that the fluid has zero viscosity because the viscosity of air is very low. The incompressible Navier-Stokes equations then reduce to the incompressible Euler equations. We decided against applying these assumptions, because we want to start with a general model and then investigate structure formation and identify the terms that are responsible for the formation of structures. For example, as already found out by Turing, see [126], diffusion plays a crucial role in the process of pattern formation. Consequently, it is not a priori clear if simulations based on the incompressible Euler equations will lead to the same patterns as such based on the compressible Navier-Stokes equations.

There exist many different ways to mathematically describe the motion of fluids. We will choose the way of continuum mechanics, where the evolution of the observed (macroscopic) variables is formulated in terms of partial differential equations (balance laws). These laws obey the fundamental physical principles, namely conservation of mass, momentum and energy.

There are two reference systems for describing fluid motion, the Lagrangian and the Eulerian reference system. In the Lagrangian setup, each fluid particle is followed along their trajectory through time and space, whereas in the Eulerian setup the change of the fluid flow is described at specific locations. In this thesis, we choose the Eulerian reference system and describe the state of the flow and its change over time. However, we will also use the terminology of trajectories (for a hypothetical particle) and control volumes.

We consider a bounded domain $\Omega \subseteq \mathbb{R}^d$ with $d \in \mathbb{N}_+$ (in our applications the space dimension is $d = 2$ or $d = 3$) and a time interval $[0, T]$, where $T > 0$ is the final time. Let $\boldsymbol{x} = (x_1, \dots, x_d)^T \in \Omega$ denote a point in the domain Ω and $t \in [0, T]$ a time instant. The change of the observed variables is then determined by the velocity $\boldsymbol{u}(\boldsymbol{x}, t) = (u_1(\boldsymbol{x}, t), \dots, u_d(\boldsymbol{x}, t))^T$ of the fluid passing through the point $\boldsymbol{x}$ at time t. For now, the function $F : \mathbb{R}^d \times \mathbb{R} \to \mathbb{R}$ will stand for a general observed variable. Later, it will be replaced by mass, momentum and energy.

We start by introducing the terminologies of *trajectories* and *control volumes*. Since we are not in the Lagrangian setup, we can think of hypothetical particles.

Definition 2.1 (Trajectory)
Let $\boldsymbol{X} : \mathbb{R}^d \times \mathbb{R} \to \mathbb{R}^d$ be a continuously differentiable function with $\boldsymbol{X}(\tilde{\boldsymbol{x}}, 0) = \tilde{\boldsymbol{x}} \in \Omega$ and $\frac{\partial}{\partial t}\boldsymbol{X}(\tilde{\boldsymbol{x}}, t) = \boldsymbol{u}(\boldsymbol{x}, t)$, where $\boldsymbol{x} = \boldsymbol{X}(\tilde{\boldsymbol{x}}, t)$. For every fixed $\tilde{\boldsymbol{x}} \in \Omega$ the function $\boldsymbol{X}(\tilde{\boldsymbol{x}}, \cdot)$ is called a *trajectory* of a particle that started at the point $\tilde{\boldsymbol{x}}$.

We note that the function $\boldsymbol{X}$ is a mapping between Lagrangian and Eulerian coordinates.

If we now set $\boldsymbol{x} = \boldsymbol{X}(\tilde{\boldsymbol{x}}, t)$, which describes the path of the fluid particle that at time 0

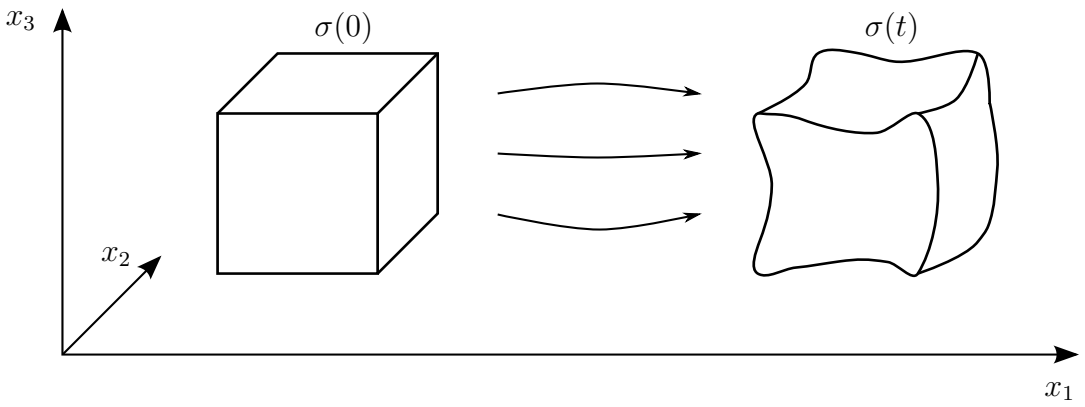

Figure 2.1: Control volume transported with the flow over time.

was at location $\tilde{\boldsymbol{x}} \in \Omega$, and apply the chain rule, we get

$$\begin{aligned} \frac{\mathrm{d}}{\mathrm{d}t} F(\boldsymbol{x}, t) = \frac{\mathrm{d}}{\mathrm{d}t} F(\boldsymbol{X}(\tilde{\boldsymbol{x}}, t), t) &= \frac{\partial F(\boldsymbol{X}(\tilde{\boldsymbol{x}}, t), t)}{\partial t} + \sum_{i=1}^{d} \frac{\partial F(\boldsymbol{X}(\tilde{\boldsymbol{x}}, t), t)}{\partial x_i} \frac{\partial X_i(\tilde{\boldsymbol{x}}, t)}{\partial t} \\ &= \frac{\partial F(\boldsymbol{x}, t)}{\partial t} + \boldsymbol{u}(\boldsymbol{x}, t) \cdot \nabla F(\boldsymbol{x}, t). \end{aligned} \tag{2.1}$$

Definition 2.2 (Material and convective derivative)
The derivative $\frac{\mathrm{d}}{\mathrm{d}t} F(\boldsymbol{x}, t)$ in equation (2.1) is called *material derivative* and the term $\boldsymbol{u}(\boldsymbol{x}, t) \cdot \nabla F(\boldsymbol{x}, t)$ is called *convective derivative*.

Definition 2.3 (Control volume)
We denote by $\sigma(0) \subset \Omega$ an open, connected and bounded subset of our domain Ω at start time 0 and call it *control volume*. Then

$$\sigma(t) = \{\boldsymbol{X}(\boldsymbol{x}, t) : \boldsymbol{x} \in \sigma(0)\}$$

is the control volume transported with the flow at time t.

The idea of a control volume and its time evolution is illustrated in Figure 2.1.

With these tools, we are now able to formulate the transport theorem of Reynolds, which describes the change of the amount of a quantity given by F in the control volume $\sigma(t)$ over time. We note that both the quantity F and the control volume $\sigma(t)$ depend on time.

Theorem 2.1 (Reynolds transport theorem, [47, 105])
Let the function $F : \mathbb{R}^d \times \mathbb{R} \to \mathbb{R}$ as well as the mapping $\boldsymbol{X}(t) : \mathbb{R}^d \to \mathbb{R}^d$ be continuously

differentiable. Then the equality

$$\begin{aligned}\frac{\mathrm{d}}{\mathrm{d}t}\int\limits_{\sigma(t)} F(\boldsymbol{x},t)\,\mathrm{d}\boldsymbol{x} &= \int\limits_{\sigma(t)} \frac{\partial F}{\partial t}(\boldsymbol{x},t) + \boldsymbol{u}(\boldsymbol{x},t)\cdot\nabla F(\boldsymbol{x},t) + F(\boldsymbol{x},t)\nabla\cdot\boldsymbol{u}(\boldsymbol{x},t)\,\mathrm{d}\boldsymbol{x} \\ &= \int\limits_{\sigma(t)} \frac{\partial F}{\partial t}(\boldsymbol{x},t) + \nabla\cdot(F(\boldsymbol{x},t)\boldsymbol{u}(\boldsymbol{x},t))\;\mathrm{d}\boldsymbol{x}\end{aligned} \tag{2.2}$$

holds for every control volume $\sigma(t)$.

Proof. For the proof of the first equality we refer to [136, pages 21-23], the second one is obtained by using the chain rule. □

An alternative form of the transport theorem can be obtained by using the divergence theorem which allows us to rewrite the volume integral of $\nabla\cdot(F(\boldsymbol{x},t)\boldsymbol{u}(\boldsymbol{x},t))$ into a surface/boundary integral, more precisely,

$$\frac{\mathrm{d}}{\mathrm{d}t}\int\limits_{\sigma(t)} F(\boldsymbol{x},t)\,\mathrm{d}\boldsymbol{x} = \int\limits_{\sigma(t)} \frac{\partial F}{\partial t}(\boldsymbol{x},t)\,\mathrm{d}\boldsymbol{x} + \int\limits_{\partial\sigma(t)} (F(\boldsymbol{x},t)\boldsymbol{u}(\boldsymbol{x},t))\cdot\boldsymbol{n}(\boldsymbol{x},t)\,dS, \tag{2.3}$$

where $\partial\sigma(t)$ is the boundary of $\sigma(t)$ and $\boldsymbol{n}(\boldsymbol{x},t)$ is the outward pointing unit normal vector at the point $\boldsymbol{x}\in\partial\sigma(t)$. Equation (2.3) and consequently the transport theorem of Reynolds state that the change of the amount of the quantity $(\frac{\mathrm{d}}{\mathrm{d}t}\int_{\sigma(t)} F(\boldsymbol{x},t)\,\mathrm{d}\boldsymbol{x})$ is determined by the amount of change inside the volume $(\int_{\sigma(t)} \frac{\partial F}{\partial t}(\boldsymbol{x},t)\,\mathrm{d}\boldsymbol{x})$ plus the flux of the quantity through the boundary of the volume $(\int_{\partial\sigma(t)} (F(\boldsymbol{x},t)\boldsymbol{u}(\boldsymbol{x},t))\cdot\boldsymbol{n}(\boldsymbol{x},t)\,dS)$. If we consider general balance laws, the change of the amount of the quantity will also be influenced by the change inside the volume due to sources and sinks, which we will denote by $s(\boldsymbol{x},t)$. Consequently, we obtain

$$\frac{\mathrm{d}}{\mathrm{d}t}\int\limits_{\sigma(t)} F(\boldsymbol{x},t) = \int\limits_{\sigma(t)} s(\boldsymbol{x},t)\,\mathrm{d}\boldsymbol{x}$$

and by applying the Reynolds transport theorem (2.2) and bringing all the terms to the left-hand side (LHS), we get

$$\int\limits_{\sigma(t)} \frac{\partial F}{\partial t}(\boldsymbol{x},t) + \nabla\cdot(F(\boldsymbol{x},t)\boldsymbol{u}(\boldsymbol{x},t)) - s(\boldsymbol{x},t)\,\mathrm{d}\boldsymbol{x} = 0. \tag{2.4}$$

Since (2.4) holds for every control volume, it follows from the fundamental lemma of calculus of variations that the integrand itself has to be zero, leading to the partial differential equation for general balance laws

$$\frac{\partial F}{\partial t}(\boldsymbol{x},t) + \nabla\cdot(F(\boldsymbol{x},t)\boldsymbol{u}(\boldsymbol{x},t)) - s(\boldsymbol{x},t) = 0. \tag{2.5}$$

With these prerequisites, we are now able to formulate the fundamental physical principles, the conservation of mass, the balance of momentum and the balance of energy. We follow the approach of [78, 141].

2.1.1 Conservation of mass

Here, we introduce the basic law of physics, the conservation of mass, which states that the amount of mass stays constant over time. Mass can neither be created nor destroyed.

The mass of a fluid is given by the integral of its density over the respective volume. Thus, denoting the density function by $\rho : \mathbb{R}^d \times \mathbb{R} \to \mathbb{R}$ (i.e., $\rho(\boldsymbol{x}, t)$ is the fluid density at point $\boldsymbol{x} \in \Omega$ at time $t \in [0, T]$) the mass in a control volume $\sigma(t)$ is given by

$$\int_{\sigma(t)} \rho(\boldsymbol{x}, t) \, \mathrm{d}\boldsymbol{x}.$$

Requiring that the mass stays constant over time means that the rate of change over time is zero. If ρ is sufficiently smooth, this can be expressed as

$$\frac{\mathrm{d}}{\mathrm{d}t} \int_{\sigma(t)} \rho(\boldsymbol{x}, t) \, \mathrm{d}\boldsymbol{x} = 0$$

and we may apply the transport theorem of Reynolds (2.2) to obtain

$$\int_{\sigma(t)} \frac{\partial \rho}{\partial t}(\boldsymbol{x}, t) + \nabla \cdot (\rho(\boldsymbol{x}, t)\boldsymbol{u}(\boldsymbol{x}, t)) \, \mathrm{d}\boldsymbol{x} = 0 \tag{2.6}$$

for every control volume $\sigma(t) \subset \Omega$ with $t \in [0, T]$. Since (2.6) holds for every control volume, the integrand itself has to be zero, leading to the partial differential equation for the conservation of mass

$$\frac{\partial \rho}{\partial t}(\boldsymbol{x}, t) + \nabla \cdot (\rho(\boldsymbol{x}, t)\boldsymbol{u}(\boldsymbol{x}, t)) = 0 \quad \text{for } \boldsymbol{x} \in \Omega \text{ and } t \in [0, T]. \tag{2.7}$$

For simplicity, we will write (2.7) as

$$\rho_t + \nabla \cdot (\rho \boldsymbol{u}) = 0. \tag{2.8}$$

Remark 2.3*:* One could also have derived the mass conservation by using equation (2.5) for the density ρ. Since it should be a conservation law, the sources and sinks would be equal to zero and we would end up with equation (2.8).

2.1.2 Balance of momentum

In this subsection, we will derive a balance law for the momentum, which is the product of the mass and the flow velocity, that means the momentum density $\rho\boldsymbol{u}$ integrated over a volume. Substituting the momentum density into the general balance law (2.4) results in the following system of equations for the momentum

$$\int_{\sigma(t)} \frac{\partial \rho \boldsymbol{u}}{\partial t}(\boldsymbol{x}, t) + \nabla \cdot (\rho \boldsymbol{u}(\boldsymbol{x}, t) \otimes \boldsymbol{u}(\boldsymbol{x}, t)) \, \mathrm{d}\boldsymbol{x} = \int_{\sigma(t)} \boldsymbol{s}(\boldsymbol{x}, t) \, \mathrm{d}\boldsymbol{x}, \tag{2.9}$$

where $\otimes$ is the outer vector product.

The forces on the right-hand side (RHS) of (2.9) are still to be determined. In fact, there are two types of forces acting in a flow, namely the body forces and the surface forces, also called contact forces. In the following, we will describe these forces.

In our case, only gravity is considered acting as a body force. In general, a body force is a force acting on material particles and thus obeys Newton's second law. This means that the total force acting on a control volume $\sigma(t)$ is given through

$$\int_{\sigma(t)} \rho(\boldsymbol{x},t)\boldsymbol{f}(\boldsymbol{x},t)\,\mathrm{d}\boldsymbol{x}, \tag{2.10}$$

where $\boldsymbol{f}(\boldsymbol{x},t)$ denotes the acceleration due to gravity. Denoting by $\boldsymbol{e_d}$ the unit vector in vertical direction (i.e., $\boldsymbol{e_d} = (0,1)$ if $d = 2$ and $\boldsymbol{e_d} = (0,0,1)$ if $d = 3$) we get $\boldsymbol{f}(\boldsymbol{x},t) = -g\boldsymbol{e_d}$, where g is the gravitational acceleration, and so (2.10) reads

$$\int_{\sigma(t)} \rho(\boldsymbol{x},t)\boldsymbol{f}(\boldsymbol{x},t)\,\mathrm{d}\boldsymbol{x} = \int_{\sigma(t)} \rho(\boldsymbol{x},t)(-g\boldsymbol{e_d})\,\mathrm{d}\boldsymbol{x}. \tag{2.11}$$

The surface forces can be described by a stress tensor $\boldsymbol{\tau}$ through the surface integral

$$\int_{\partial\sigma(t)} \boldsymbol{\tau}(\boldsymbol{x},t)\cdot\boldsymbol{n}(\boldsymbol{x},t)\,dS. \tag{2.12}$$

Using the divergence theorem we can rewrite (2.12) into a volume integral, i.e.,

$$\int_{\partial\sigma(t)} \boldsymbol{\tau}(\boldsymbol{x},t)\cdot\boldsymbol{n}(\boldsymbol{x},t)\,dS = \int_{\sigma(t)} \nabla\cdot\boldsymbol{\tau}(\boldsymbol{x},t)\,\mathrm{d}\boldsymbol{x}. \tag{2.13}$$

Inserting (2.11) and (2.13) for the force term on the RHS of (2.9) gives

$$\int_{\sigma(t)} \frac{\partial\rho\boldsymbol{u}}{\partial t}(\boldsymbol{x},t) + \nabla\cdot(\rho\boldsymbol{u}(\boldsymbol{x},t)\otimes\boldsymbol{u}(\boldsymbol{x},t))\,\mathrm{d}\boldsymbol{x} = \int_{\sigma(t)} \rho(\boldsymbol{x},t)(-g\boldsymbol{e_d})\,\mathrm{d}\boldsymbol{x} + \int_{\sigma(t)} \nabla\cdot\boldsymbol{\tau}(\boldsymbol{x},t)\,\mathrm{d}\boldsymbol{x}. \tag{2.14}$$

Since equations (2.14) again hold for every control volume $\sigma(t)$, it follows that

$$\frac{\partial\rho\boldsymbol{u}}{\partial t}(\boldsymbol{x},t) + \nabla\cdot(\rho\boldsymbol{u}(\boldsymbol{x},t)\otimes\boldsymbol{u}(\boldsymbol{x},t)) = \rho(\boldsymbol{x},t)(-g\boldsymbol{e_d}) + \nabla\cdot\boldsymbol{\tau}(\boldsymbol{x},t). \tag{2.15}$$

It remains to determine the stress tensor $\boldsymbol{\tau}$ which describes the normal and shear forces that act on the surface of a body. Cauchy's theorem ensures that there exists a tensor that fulfills equation (2.15) and it says that the tensor is symmetric, which means that the angular momentum is balanced. For the proof of the theorem we refer to [47, pages 101ff.]. The so called *constitutive relation* determines now the stress tensor by relating it to the motion of the fluid. Looking at inviscid fluids that exhibit no shear stresses,

it can be shown that the normal forces are given by $-p(\boldsymbol{x},t)\mathrm{Id}$, where p is the pressure and Id is the identity matrix, see, e.g., [112]. Thus, we can write the stress tensor as

$$\boldsymbol{\tau}(\boldsymbol{x},t) = -p(\boldsymbol{x},t)\mathrm{Id} + \boldsymbol{\tau}^{\boldsymbol{V}}(\boldsymbol{x},t), \tag{2.16}$$

where $\boldsymbol{\tau}^{\boldsymbol{V}}$ denotes the viscous part of the stress tensor. The first assumption that we will make is that $\boldsymbol{\tau}^{\boldsymbol{V}}$ depends linearly on the strain rate tensor $\nabla\boldsymbol{u} + (\nabla\boldsymbol{u})^\top$ that models the deformation of the fluid. This is equivalent to saying that the fluid is a *Newtonian fluid*, which is a proper assumption for air and water. Additionally, we assume that the volume viscosity is negligible, which means that the mechanical pressure is equal to the thermodynamic pressure (i.e. the relaxation time is so small that it is assumed to be zero). All in all, this leads to

$$\boldsymbol{\tau}^{\boldsymbol{V}}(\boldsymbol{x},t) = \mu(\boldsymbol{x},t)\left(\nabla\boldsymbol{u}(\boldsymbol{x},t) + (\nabla\boldsymbol{u}(\boldsymbol{x},t))^\top\right), \tag{2.17}$$

where μ is the dynamic viscosity. The dynamic viscosity can be expressed through the kinematic viscosity μ_m through the relation $\mu_m(\boldsymbol{x},t)\rho(\boldsymbol{x},t) = \mu(\boldsymbol{x},t)$, which for (2.17) yields

$$\boldsymbol{\tau}^{\boldsymbol{V}}(\boldsymbol{x},t) = \mu_m(\boldsymbol{x},t)\rho(\boldsymbol{x},t)\left(\nabla\boldsymbol{u}(\boldsymbol{x},t) + (\nabla\boldsymbol{u}(\boldsymbol{x},t))^\top\right). \tag{2.18}$$

Inserting (2.16) and (2.18) in equation (2.15) gives the following balance equation for the momentum

$$\begin{aligned}\frac{\partial\rho\boldsymbol{u}}{\partial t}(\boldsymbol{x},t) + \nabla\cdot(\rho\boldsymbol{u}(\boldsymbol{x},t)\otimes\boldsymbol{u}(\boldsymbol{x},t)) &= \rho(\boldsymbol{x},t)(-g\boldsymbol{e_d}) \\ &+ \nabla\cdot\left(-p(\boldsymbol{x},t)\mathrm{Id} + \mu_m(\boldsymbol{x},t)\rho(\boldsymbol{x},t)\left(\nabla\boldsymbol{u}(\boldsymbol{x},t) + (\nabla\boldsymbol{u}(\boldsymbol{x},t))^\top\right)\right).\end{aligned} \tag{2.19}$$

For simplicity, we will write (2.19) as

$$(\rho\boldsymbol{u})_t + \nabla\cdot\left(\rho\boldsymbol{u}\otimes\boldsymbol{u} + p\,\mathrm{Id} - \mu_m\rho\left(\nabla\boldsymbol{u} + (\nabla\boldsymbol{u})^\top\right)\right) = -\rho g\boldsymbol{e_d}. \tag{2.20}$$

Here, μ_m depends on space and time. In what follows, we will take a simplified approach and assume it to be constant.

2.1.3 Balance of energy

The last balance law that we will consider for the fluid motion is the balance of energy. Let E denote the total energy per unit mass given by

$$E = e + \frac{1}{2}\boldsymbol{u}\cdot\boldsymbol{u}, \tag{2.21}$$

where e is the internal energy and $\frac{1}{2}\boldsymbol{u}\cdot\boldsymbol{u}$ the kinetic energy. Here, $\cdot$ denotes the scalar product. Then the total energy in a volume is given by the integral of the energy density ρE over this volume. By substituting the energy density into the general balance law (2.4), we end up with

$$\int_{\sigma(t)} \frac{\partial\rho E}{\partial t}(\boldsymbol{x},t) + \nabla\cdot(\rho E(\boldsymbol{x},t)\boldsymbol{u}(\boldsymbol{x},t))\,\mathrm{d}\boldsymbol{x} = \int_{\sigma(t)} s(\boldsymbol{x},t)\,\mathrm{d}\boldsymbol{x}. \tag{2.22}$$

The first law of thermodynamics states that the change of energy is given by the rate of work $-W$ of the system on its surroundings, meaning the rate of body and surface forces, as well as the rate of heat Q added to the system. By adapting the RHS in (2.22) according to this, we get

$$\int_{\sigma(t)} \frac{\partial \rho E}{\partial t}(\boldsymbol{x},t) + \nabla \cdot (\rho E(\boldsymbol{x},t)\boldsymbol{u}(\boldsymbol{x},t))\ \mathrm{d}\boldsymbol{x} = W(\sigma(t)) + Q(\sigma(t)). \tag{2.23}$$

Following the approach used for the balance laws, see (2.11) and (2.12), the rate of work is given by

$$\begin{aligned} W(\sigma(t)) &= \int_{\sigma(t)} \rho(\boldsymbol{x},t)\boldsymbol{f}(\boldsymbol{x},t)\cdot\boldsymbol{u}(\boldsymbol{x},t)\,\mathrm{d}\boldsymbol{x} + \int_{\partial\sigma(t)} (\boldsymbol{\tau}(\boldsymbol{x},t)\cdot\boldsymbol{u}(\boldsymbol{x},t))\cdot\boldsymbol{n}(\boldsymbol{x},t)\,dS \\ &= \int_{\sigma(t)} \rho(\boldsymbol{x},t)(-g\boldsymbol{e_d})\cdot\boldsymbol{u}(\boldsymbol{x},t)\,\mathrm{d}\boldsymbol{x} + \int_{\sigma(t)} \nabla\cdot(\boldsymbol{\tau}(\boldsymbol{x},t)\cdot\boldsymbol{u}(\boldsymbol{x},t))\,\mathrm{d}\boldsymbol{x}. \end{aligned} \tag{2.24}$$

We now denote by q the rate of added heat per unit mass and by $\boldsymbol{h}$ the heat flux density, meaning the heat flux per unit area, through $\partial\sigma(t)$. Thus we can write the rate of added heat in the volume $\sigma(t)$ as

$$\begin{aligned} Q(\sigma(t)) &= \int_{\sigma(t)} \rho(\boldsymbol{x},t)q\,\mathrm{d}\boldsymbol{x} - \int_{\partial\sigma(t)} \boldsymbol{h}(\boldsymbol{x},t)\cdot\boldsymbol{n}(\boldsymbol{x},t)\,dS \\ &= \int_{\sigma(t)} \rho(\boldsymbol{x},t)q\,\mathrm{d}\boldsymbol{x} - \int_{\sigma(t)} \nabla\cdot\boldsymbol{h}(\boldsymbol{x},t)\,\mathrm{d}\boldsymbol{x}. \end{aligned} \tag{2.25}$$

Inserting (2.24) and (2.25) into equation (2.23) gives

$$\begin{aligned} \int_{\sigma(t)} \frac{\partial \rho E}{\partial t}(\boldsymbol{x},t) + \nabla\cdot(\rho E(\boldsymbol{x},t)\boldsymbol{u}(\boldsymbol{x},t))\ \mathrm{d}\boldsymbol{x} &= \int_{\sigma(t)} \rho(\boldsymbol{x},t)(-g\boldsymbol{e_d})\cdot\boldsymbol{u}(\boldsymbol{x},t) \\ &\quad + \nabla\cdot(\boldsymbol{\tau}(\boldsymbol{x},t)\cdot\boldsymbol{u}(\boldsymbol{x},t)) + \rho(\boldsymbol{x},t)q - \nabla\cdot\boldsymbol{h}(\boldsymbol{x},t)\,\mathrm{d}\boldsymbol{x}. \end{aligned} \tag{2.26}$$

Since equation (2.26) holds for every control volume $\sigma(t)$, it follows that

$$\begin{aligned} \frac{\partial \rho E}{\partial t}(\boldsymbol{x},t) + \nabla\cdot(\rho E(\boldsymbol{x},t)\boldsymbol{u}(\boldsymbol{x},t)) &= \rho(\boldsymbol{x},t)(-g\boldsymbol{e_d})\cdot\boldsymbol{u}(\boldsymbol{x},t) \\ &\quad + \nabla\cdot(\boldsymbol{\tau}(\boldsymbol{x},t)\cdot\boldsymbol{u}(\boldsymbol{x},t)) + \rho(\boldsymbol{x},t)q - \nabla\cdot\boldsymbol{h}(\boldsymbol{x},t). \end{aligned} \tag{2.27}$$

To determine the heat flux density $\boldsymbol{h}$, we use a constitutive relation that is obtained from Fourier's law. It relates the heat flux density to the temperature gradient in the following way

$$\boldsymbol{h}(\boldsymbol{x},t) = -\kappa\nabla T(\boldsymbol{x},t), \tag{2.28}$$

where κ is the thermal conductivity and T the temperature. Inserting (2.28) into the energy balance equation (2.27) and bringing the heat term to the LHS results in

$$\begin{aligned} \frac{\partial \rho E}{\partial t}(\boldsymbol{x},t) + \nabla\cdot(\rho E(\boldsymbol{x},t)\boldsymbol{u}(\boldsymbol{x},t) - \kappa\nabla T(\boldsymbol{x},t)) \\ = \rho(\boldsymbol{x},t)(-g\boldsymbol{e_d})\cdot\boldsymbol{u}(\boldsymbol{x},t) + \nabla\cdot(\boldsymbol{\tau}(\boldsymbol{x},t)\cdot\boldsymbol{u}(\boldsymbol{x},t)) + \rho(\boldsymbol{x},t)q. \end{aligned} \tag{2.29}$$

For simplicity, we will now omit the dependence on time and space and thus write (2.29) as

$$\frac{\partial \rho E}{\partial t} + \nabla \cdot (\rho E \boldsymbol{u} - \kappa \nabla T) = -\rho g \boldsymbol{e_d} \cdot \boldsymbol{u} + \nabla \cdot (\boldsymbol{\tau} \cdot \boldsymbol{u}) + \rho q. \tag{2.30}$$

We want to express (2.30) in terms of the internal energy e. Therefore, we substitute (2.21) into equation (2.30), which leads to

$$\begin{aligned}\frac{\partial \rho e}{\partial t} + \frac{\partial \rho}{\partial t}\frac{1}{2}\boldsymbol{u} \cdot \boldsymbol{u} + \frac{\partial \boldsymbol{u}}{\partial t} \cdot \rho \boldsymbol{u} + \nabla \cdot (\rho \boldsymbol{u})\frac{1}{2}\boldsymbol{u} \cdot \boldsymbol{u} + (\nabla \boldsymbol{u}) \cdot \rho \boldsymbol{u} \cdot \boldsymbol{u} \\ + \nabla \cdot (\rho e \boldsymbol{u} - \kappa \nabla T) = -\rho g \boldsymbol{e_d} \cdot \boldsymbol{u} + \nabla \cdot (\boldsymbol{\tau} \cdot \boldsymbol{u}) + \rho q.\end{aligned}$$

Using the conservation of mass gives $\frac{\partial \rho}{\partial t}\frac{1}{2}\boldsymbol{u} \cdot \boldsymbol{u} + \nabla \cdot (\rho \boldsymbol{u})\frac{1}{2}\boldsymbol{u} \cdot \boldsymbol{u} = 0$ and thus

$$\frac{\partial \rho e}{\partial t} + \frac{\partial \boldsymbol{u}}{\partial t} \cdot (\rho \boldsymbol{u}) + (\nabla \boldsymbol{u}) \cdot (\rho \boldsymbol{u}) \cdot \boldsymbol{u} + \nabla \cdot (\rho e \boldsymbol{u} - \kappa \nabla T) = -\rho g \boldsymbol{e_d} \cdot \boldsymbol{u} + \nabla \cdot (\boldsymbol{\tau} \cdot \boldsymbol{u}) + \rho q. \tag{2.31}$$

Next, we will rewrite the balance of momentum (2.15) in a suitable way and subtract the result from (2.31). Using the chain rule, (2.15) can be written as

$$\frac{\partial \rho}{\partial t}\boldsymbol{u} + \frac{\partial \boldsymbol{u}}{\partial t}\rho + \nabla \cdot (\rho \boldsymbol{u})\boldsymbol{u} + (\nabla \boldsymbol{u}) \cdot (\rho \boldsymbol{u}) = -\rho g \boldsymbol{e_d} + \nabla \cdot \boldsymbol{\tau}$$

and due to the conservation of mass we have $\frac{\partial \rho}{\partial t}\boldsymbol{u} + \nabla \cdot (\rho \boldsymbol{u})\boldsymbol{u} = 0$ and thus

$$\frac{\partial \boldsymbol{u}}{\partial t}\rho + (\nabla \boldsymbol{u}) \cdot (\rho \boldsymbol{u}) = -\rho g \boldsymbol{e_d} + \nabla \cdot \boldsymbol{\tau}. \tag{2.32}$$

Multiplying (2.32) with the vector $\boldsymbol{u}$ from the right leads to

$$\frac{\partial \boldsymbol{u}}{\partial t} \cdot (\rho \boldsymbol{u}) + (\nabla \boldsymbol{u}) \cdot (\rho \boldsymbol{u}) \cdot \boldsymbol{u} = -\rho g \boldsymbol{e_d} \cdot \boldsymbol{u} + (\nabla \cdot \boldsymbol{\tau}) \cdot \boldsymbol{u}. \tag{2.33}$$

Subtracting (2.33) from (2.31) gives the following balance law for the internal energy

$$\frac{\partial \rho e}{\partial t} + \nabla \cdot (\rho e \boldsymbol{u} - \kappa \nabla T) = \rho q + \nabla \cdot (\boldsymbol{\tau} \cdot \boldsymbol{u}) - (\nabla \cdot \boldsymbol{\tau}) \cdot \boldsymbol{u}. \tag{2.34}$$

We will now make the assumption that we model an ideal gas, meaning that we assume that particles are points and that the kinetic energy of the particles stays the same during collisions and is not transformed. The advantage of this assumption is that an ideal gas obeys the *ideal gas law*

$$p = R\rho T, \tag{2.35}$$

a simplified *equation of state* that relates the pressure p to the temperature T. Here, $R = c_p - c_v$ is the ideal gas constant of dry air, c_p is the specific heat capacity of dry air for constant pressure and c_v the one for constant volume.

Remark 2.4*:* For the moment, we just consider the equation of state for dry air. When we later couple the balance laws for a fluid derived in this section to the balance laws for liquid water phase concentrations, we will modify (2.35) and (2.43) so that they hold for moist air, see Section 3.1.

It is also known that in an ideal gas the internal energy e only depends on the temperature T and is given through

$$e(T) = c_v T. \tag{2.36}$$

Inserting (2.36) into (2.34) leads to

$$c_v \frac{\partial \rho T}{\partial t} + \nabla \cdot (c_v \rho T \boldsymbol{u} - \kappa \nabla T) = \rho q + \nabla \cdot (\boldsymbol{\tau} \cdot \boldsymbol{u}) - (\nabla \cdot \boldsymbol{\tau}) \cdot \boldsymbol{u}. \tag{2.37}$$

When considering adiabatic processes, one can express the temperature in terms of a new conserved quantity, the potential temperature θ. We will briefly demonstrate how to obtain this relation. The first law of thermodynamics for an infinitesimal process states

$$de = \delta Q + \delta W, \tag{2.38}$$

where de is the change of internal energy, δQ is a small amount of added heat added and $-\delta W$ is a small amount of work performed by the system on its surroundings. The second law of thermodynamics states that δQ is proportional to the change of entropy. In adiabatic processes, energy is transferred to the surroundings only as work, thus, the change of entropy is zero. Furthermore, the work is only pressure-volume work, which means $-\delta W = pdV$, where V is the specific volume. Hence, the first law reduces to

$$de = -pdV. \tag{2.39}$$

Adding $d(pV)$ on both sides of equation (2.39) leads to

$$\begin{aligned} de + d(pV) &= -pdV + d(pV) \\ \Leftrightarrow d(e + pV) &= V dp. \end{aligned} \tag{2.40}$$

By noting that the specific volume is given through $\frac{1}{\rho}$ and that the expression on the LHS of the last equation in (2.40) is the change of enthalpy, which for an ideal gas is $c_p dT$, we obtain

$$c_p dT = \frac{1}{\rho} dp. \tag{2.41}$$

Multiplying (2.41) by ρ/p, using the ideal gas law (2.35) and rearranging gives

$$\frac{dT}{T} = \frac{R}{c_p} \frac{dp}{p}. \tag{2.42}$$

Integrating (2.42) from p_0, the reference pressure at sea level, to a pressure p_1 leads to

$$\int_{T(p_0)}^{T(p_1)} \frac{dT}{T} = \int_{p_0}^{p_1} \frac{R}{c_p} \frac{dp}{p} \Leftrightarrow \ln(T(p_1)) - \ln(T(p_0)) = \frac{R}{c_p} (\ln(p_1) - \ln(p_0))$$

$$\Leftrightarrow \frac{T(p_1)}{T(p_0)} = \left(\frac{p_1}{p_0} \right)^{\frac{R}{c_p}}.$$

Solving for $T(p_0) =: \theta$ and substituting $p := p_1$, one obtains the following equation for the temperature needed to move a parcel adiabatically to the pressure level p_0

$$\theta = T\left(\frac{p_0}{p}\right)^{\frac{R}{c_p}}.$$

Solving, on the other hand, for the temperature T, gives the following relation

$$T = \theta\left(\frac{p}{p_0}\right)^{\frac{R}{c_p}}. \tag{2.43}$$

In atmospheric applications, it is common to use as conservative variable the potential temperature θ instead of the temperature T. Consequently, our next goal is to rewrite (2.37) in terms of the potential temperature θ. We start by inserting (2.35) into (2.43) which gives the following equation for the temperature

$$T = \theta^{\frac{c_p}{c_v}}\left(\frac{R\rho}{p_0}\right)^{\frac{R}{c_v}} \tag{2.44}$$

which just depends on the density ρ and the potential temperature θ. If we would insert (2.44) into equation (2.37) we would get a balance for the potential temperature that would be very complicated. Here, we choose an approach that is partly heuristic, but will lead to a much simpler equation for the potential temperature. First we discard the source term ρq in (2.37) as well as the viscous effects that are modeled through $-\nabla(\kappa\nabla T)$ and the viscous stress tensor $\boldsymbol{\tau}^{\boldsymbol{V}}$. That is, we consider an inviscid fluid for which there is an energy conservation without sources or sinks. Under these assumptions the following equation for the stress tensor holds

$$\nabla\cdot(\boldsymbol{\tau}\cdot\boldsymbol{u}) - (\nabla\cdot\boldsymbol{\tau})\boldsymbol{u} = -\nabla\cdot(p\,\mathrm{Id}\cdot\boldsymbol{u}) + (\nabla\cdot p\,\mathrm{Id})\boldsymbol{u} = -p\nabla\cdot\boldsymbol{u}.$$

In particular, (2.37) reduces to

$$c_v\frac{\partial\rho T}{\partial t} + c_v\nabla\cdot(\rho T\boldsymbol{u}) + p\nabla\cdot\boldsymbol{u} = 0. \tag{2.45}$$

Dividing by c_v and inserting (2.35) in (2.45) gives

$$\frac{\partial\rho T}{\partial t} + \nabla\cdot(\rho T\boldsymbol{u}) + \frac{R}{c_v}\rho T\nabla\cdot\boldsymbol{u} = 0.$$

Next, we insert the representation for the temperature (2.44) which –after careful computation of the derivatives using the chain rule– leads to

$$\left(\frac{R\rho\theta}{p_0}\right)^{\frac{R}{c_v}}\left(\frac{c_p}{c_v}\frac{\partial\rho\theta}{\partial t} + \nabla\cdot(\rho\theta\boldsymbol{u}) + \frac{R}{c_v}\boldsymbol{u}\cdot\nabla(\rho\theta) + \frac{R}{c_v}\rho\theta\nabla\cdot\boldsymbol{u}\right) = 0.$$

Observing that $1 + \frac{R}{c_v} = \frac{c_p}{c_v}$, we obtain

$$\left(\frac{R\rho\theta}{p_0}\right)^{\frac{R}{c_v}}\left(\frac{c_p}{c_v}\frac{\partial\rho\theta}{\partial t} + \frac{c_p}{c_v}\nabla\cdot(\rho\theta\boldsymbol{u})\right) = 0$$

and dividing by $\frac{c_p}{c_v}\left(\frac{R\rho\theta}{p_0}\right)^{\frac{R}{c_v}}$ we get

$$\frac{\partial \rho\theta}{\partial t} + \nabla \cdot (\rho\theta \boldsymbol{u}) = 0. \tag{2.46}$$

This means that the balance of energy (2.37) in terms of temperature is equivalent to the conservation of potential temperature (2.46). We note that we have assumed that there is no viscosity and that there are no heat sources or sinks, e.g., phase changes. Since they are effectively present, we follow the modeling approach in [110] and add a source term for the potential temperature denoted by S_θ and we choose to model viscous effects through the term $-\mu_h \nabla \cdot (\rho \nabla \theta)$, where μ_h can be seen as thermal conductivity. By adding both of these terms to (2.46), we obtain

$$(\rho\theta)_t + \nabla \cdot (\rho\theta \boldsymbol{u} - \mu_h \rho \nabla \theta) = S_\theta, \tag{2.47}$$

which will be our equation to model the balance of energy.

Remark 2.5*:* The term S_θ will be specified in Chapter 3, see equation (3.2).

2.1.4 Compressible Navier-Stokes equations

Combining the conservation of mass (2.8), the balance of momentum (2.20) and the balance of energy (2.47), we end up with the following system of equations

$$\begin{aligned} \rho_t + \nabla \cdot (\rho \boldsymbol{u}) &= 0, \\ (\rho \boldsymbol{u})_t + \nabla \cdot \left(\rho \boldsymbol{u} \otimes \boldsymbol{u} + p\,\mathrm{Id} - \mu_m \rho \left(\nabla \boldsymbol{u} + (\nabla \boldsymbol{u})^\top\right)\right) &= -\rho g \boldsymbol{e_d}, \\ (\rho\theta)_t + \nabla \cdot (\rho\theta \boldsymbol{u} - \mu_h \rho \nabla \theta) &= S_\theta. \end{aligned} \tag{2.48}$$

The momentum equations are called the *Navier-Stokes equations* after Claude Louis Marie Henri Navier (1785–1836) and George Gabriel Stokes (1819–1903), who derived the momentum balance in a differential form for Newtonian fluids. Also, Siméon Denis Poisson and Barré de Saint-Venant derived the balance of momentum, Saint-Venant even before Stokes, but still the name Navier-Stokes equations became established.

System (2.48) is not yet closed since we have more unknowns than equations. This issue will be solved in the next chapter in Section 3.1, where we will introduce the equation of state for moist air that will relate the pressure p to the density ρ and the potential temperature θ. There, we will also introduce the energy source term S_θ in the energy equation, which can be determined when system (2.48) is coupled to the cloud equations.

2.2 Dynamics of clouds

In this section, we describe the different microscopic physical cloud processes and introduce evolution equations, more precisely, advection-diffusion-reaction equations, for the liquid phases of cloud water. We note that in this thesis we restrict our investigations to clouds in the lower part of the troposphere, that is, to clouds consisting of liquid droplets exclusively, such as warm clouds occurring at temperatures $T > 273\,\mathrm{K}$, where liquid

water is the stable phase. All of the processes involving ice particles are left for future research and future works. For the representation of liquid clouds, we use the so-called single moment scheme, that is, equations for the bulk quantities of mass concentrations of different water phases. For the representation of the relevant cloud processes, we adapt a recently developed cloud model [103]. Note that for bulk models, the process rates cannot be derived completely from first principles. Consequently, some uncertain parameters show up naturally. This underlines the need for a rigorous sensitivity study which is the goal of the present work.

Generally, we follow the standard approach in cloud physics modeling for separating hydrometeors of different sizes as first introduced in [60]. This relies on the observation that small droplets have a negligible falling velocity. In addition, measurements indicate two different modes of droplets in the size distribution: small cloud droplets and large rain drops [137]. Thus, we use the cloud variables q_c and q_r indicating the mass concentrations of (spatially stationary) cloud droplets and (falling) rain drops, respectively, and the water vapor concentration q_v, that is,

$$q_\ell = \frac{\text{mass of the respective phase}}{\text{mass of dry air}} \quad \text{for} \quad \ell \in \{v, c, r\}. \tag{2.49}$$

We then consider balance laws in the form of (2.3) derived in Section 2.1 for the mass densities ρq_ℓ and, following [110], we add diffusive terms of the form $-\mu_q \nabla \cdot (\rho \nabla q_\ell)$ for $\ell \in \{v, c, r\}$, where μ_q is the cloud diffusivity. A priori, it is not clear that all the liquid water pahses have the same diffusivity μ_q. We assume it here for simplicity, but in general, a parameter study would be useful and neccessary to determine the diffusivities. With this assumption the balance equations for the cloud variables read

$$\begin{aligned} (\rho q_v)_t + \nabla \cdot (\rho q_v \boldsymbol{u} - \mu_q \rho \nabla q_v) &= \rho(-C + E), \\ (\rho q_c)_t + \nabla \cdot (\rho q_c \boldsymbol{u} - \mu_q \rho \nabla q_c) &= \rho(C - A_1 - A_2), \\ (\rho q_r)_t + \nabla \cdot (-v_q \rho q_r \boldsymbol{e_d} + \rho q_r \boldsymbol{u} - \mu_q \rho \nabla q_r) &= \rho(A_1 + A_2 - E). \end{aligned} \tag{2.50}$$

The rest of this section is devoted to a description of the different terms on the RHS of (2.50), which represent the following relevant cloud processes, see [103].

2.2.1 Single particle properties

- *General properties of a single water particle*

  As we exclusively investigate warm clouds, we can assume a spherical shape of water particles. For small cloud droplets, this is a very good approximation. In contrast to that, the shape of large rain drops is changed by drag effects [119, 120]. However, for our investigations of ensembles of rain drops, the spherical shape approximation is still appropriate. Thus, mass and radius of droplets are related by the usual equation

$$m = \frac{4}{3}\pi \rho_\ell r^3 \quad \Longleftrightarrow \quad r = \left(\frac{3}{4\pi\rho_\ell}\right)^{\frac{1}{3}} m^{\frac{1}{3}}$$

with the liquid water density $\rho_\ell = 10^3\,\mathrm{kg\,m^{-3}}$. We make the general assumption that small cloud droplets are stationary, while large rain drops are accelerated by gravity. After balancing gravity by frictional forces, spherical rain drops fall with a terminal velocity, depending only on the drop mass and the density of air. According to [103], the terminal velocity for a droplet of mass m is given by

$$v_\tau(m) = \alpha\, m^\beta \left(\frac{m_\tau}{m_\tau + m}\right)^\beta \left(\frac{\rho_*}{\rho}\right)^{\frac{1}{2}}$$

with

$$\alpha = 190.3\,\mathrm{m\,s^{-1}\,kg^{-\beta}}, \quad \beta = \frac{4}{15}, \quad m_\tau = 1.21 \cdot 10^{-5}\mathrm{kg},$$

and the reference density $\rho_* = 1.255\,\mathrm{kg\,m^{-3}}$ at $T_* = 288\,\mathrm{K}$ and $p_* = 101\,325\,\mathrm{Pa}$. For masses $m \ll m_\tau$, we can approximate the terminal velocity by

$$v_\tau = \alpha\, m^\beta \sqrt{\frac{\rho_*}{\rho}}.$$

This approximation will be used in the description of the process *accretion* (collection of cloud droplets by rain drops).

- *Diffusion processes: Growth and evaporation*

  Diffusion processes (transfer of water molecules to and from the liquid particle) can be described by the following growth equation

$$\frac{dm}{dt} = -4\pi r D_v G \rho (q_* - q_v)\, f_v = -\underbrace{4\pi D_v G \left(\frac{3}{4\pi\rho_\ell}\right)^{\frac{1}{3}}}_{=:d} \rho (q_* - q_v) m^{\frac{1}{3}} f_v,$$

  where D_v denotes the diffusion constant, G determines corrections due to the latent heat release for phase changes, and f_v is the ventilation correction for large particles taking into account the effect of flows around the falling spheres. A thermodynamics equilibrium is determined by the saturation mixing ratio

$$q_* = q_*(p, T) = \frac{\varepsilon p_s(T)}{p}$$

  with the ratio of molar masses of water and dry air ε and the saturation water vapor pressure over a liquid surface $p_s(T)$ given in [97]. By neglecting curvature effects, water particles grow for $q_v > q_*$ and evaporate for $q_v < q_*$. According to [104], the diffusion constant is given by

$$D_v = D_{v0} \left(\frac{T}{T_0}\right)^{1.94} \frac{p_0}{p}$$

  with

$$D_{v0} = 2.11 \cdot 10^{-5}\mathrm{m^2\,s^{-1}}, \quad T_0 = 273.15\,\mathrm{K}, \quad p_0 = p_* = 101\,325\,\mathrm{Pa}.$$

The impact of latent heat release is described by

$$G = \left[\left(\frac{L}{R_v T} - 1 \right) \frac{L p_s(T)}{R_v T^2} \frac{D_v}{K_T} + 1 \right]^{-1},$$

where the latent heat of vaporization is $L = 2.53 \cdot 10^6 \,\mathrm{J\,kg^{-1}}$ and the heat conduction of dry air, see [26], is

$$K_T = \frac{a_K T^{\frac{3}{2}}}{T + b_K 10^{\frac{c_K}{T}}}$$

with

$$a_K = 0.002646 \,\mathrm{W\,m^{-1}\,K^{-\frac{5}{2}}}, \quad b_K = 245.4 \,\mathrm{K}, \quad c_K = -12 \,\mathrm{K}.$$

Ventilation of large spherical particles of radius r – that is, additional uptake of water vapor by (turbulent) airflow around the particles – can be taken into account using an empirical ventilation coefficient

$$f_v = a_v + b_v N_{\mathrm{Sc}}^{\frac{1}{3}} N_{\mathrm{Re}}^{\frac{1}{2}} \quad \text{with} \quad a_v = 0.78, \quad b_v = 0.308,$$

where the Schmidt and Reynolds numbers are defined as

$$N_{\mathrm{Sc}} = \frac{\mu}{\rho D_v} \quad \text{and} \quad N_{\mathrm{Re}} = \frac{\rho}{\mu} v_\tau(2r), \tag{2.51}$$

respectively. In (2.51), μ is the dynamic viscosity of air. According to [26], it is given by

$$\mu = \frac{\mu_0 T^{\frac{3}{2}}}{T + T_\mu}, \quad \text{where} \quad \mu_0 = 1.458 \cdot 10^{-6} \mathrm{s\,Pa\,K^{-\frac{1}{2}}}, \quad T_\mu = 110.4 \,\mathrm{K}.$$

For cloud droplets, we neglect the ventilation correction. Thus, the mass rate of diffusion for a cloud droplet of mass m_c can be expressed as

$$\frac{dm_c}{dt} = d\rho(q_v - q_*) m_c^{\frac{1}{3}}.$$

For rain drops, growth due to diffusion is negligible, and thus the mass rate for rain drops of mass m_r satisfies

$$\frac{dm_r}{dt} = -d\rho(q_* - q_v)_+ \left[a_E m_r^{\frac{1}{3}} + b_E v_\tau(m_r)^{\frac{1}{2}} m_r^{\frac{1}{2}} \right]$$

with

$$a_E = a_v, \quad b_E = b_v \left(\frac{\mu}{\rho D_v} \right)^{\frac{1}{3}} \sqrt{\frac{2\rho}{\mu}} \left(\frac{3}{4\pi\rho_\ell} \right)^{\frac{1}{6}}.$$

Here, $(\cdot)_+ := \max(\cdot, 0)$ denotes the positive part.

- *Collision of rain drops with cloud droplets: Accretion*

  A spherical rain drop of mass m_r (radius r) falls with terminal velocity $v_\tau(m_r)$ through a volume $V = \pi r^2 v_\tau(m_r) \Delta t$ during a time interval Δt and collects cloud droplets of total mass $M_c = V \rho q_c$. Thus, the corresponding growth rate of the rain drop is given by

$$\frac{dm_r}{dt} = k_2' \rho \pi q_c v_\tau(m_r) \left(\frac{3}{4\pi\rho_\ell} \right)^{\frac{2}{3}} m_r^{\frac{2}{3}}$$

  with an efficiency $k_2' > 0$.

2.2.2 Ensemble/collective properties

For the description of clouds as an ensemble of water particles, we would have to introduce averaged quantities such as mass concentrations (as described above, that is, q_c and q_r) as well as number concentrations of cloud droplets n_c and rain drops n_r. Since we do not extend the systems of equations for these two quantities, we introduce relations between mass and number concentrations in order to keep the main effects in a simplified way.

- *Formation of cloud droplets: Activation*

  Cloud droplets can be formed by the activation of so-called cloud condensation nuclei. Liquid aerosol particles can grow by water vapor uptake to larger sizes. This effect can be described by the Köhler theory, see, e.g., [64, 101]. As described in detail in [103], we represent the cloud droplet number concentration n_c by a nonlinear relation

  $$n_c = q_c \frac{N_\infty}{q_c + N_\infty m_0} \coth\left(\frac{q_c}{N_0 m_0}\right).$$

  Here, N_∞ denotes the maximum number of cloud condensation nuclei that depends on environmental conditions such as the cleanness of air, m_0 can be interpreted as the activation mass of cloud droplets, and N_0 is the approximated number of activated droplets at $q_v = q_*$. In our investigations, we set these three parameters to the following values

  $$N_\infty = 8 \cdot 10^8\,\mathrm{kg}^{-1}, \quad m_0 = 5.236 \cdot 10^{-16}\mathrm{kg}, \quad N_0 = 10^3\,\mathrm{kg}^{-1}.$$

  For the initialization of the cloud droplet production, we introduce an additional factor in case of supersaturation

  $$C_{\mathrm{act}} = N_0\, d\rho (q_v - q_*)_+\, m_0{}^{\frac{1}{3}}. \tag{2.52}$$

  Remark 2.6*:* The activation term for the cloud droplet production C_{act} is necessary for our model when starting with no cloud drops since we solve it explicitly in time. In [103] it is not needed, because there an implicit time integration method is used.

- *Relation between number and mass concentration for rain drops*

  In contrast to the formulation in [103], we do not include another equation for the number concentration of rain drops. In a similar way as for cloud activation, we use a relation between n_r and q_r, that is, a closure of the form $n_r = f(q_r, c_r)$. Since we implicitly assume that the rain drops are distributed according to their size, this approach should be used for mimicking the shape of the distribution properly. We propose the (non)linear relation

  $$n_r = c_r q_r^\gamma, \quad 0 < \gamma \leq 1.$$

  Assuming a constant mean mass of rain drops $\overline{m_r}$, we can determine the constants as $c_r = \overline{m_r}^{-1}$ and $\gamma = 1$. This approach would be meaningful for the case of a symmetric size distribution of rain droplets centered around the mean mass. However, it is well-known that size distributions of rain drops are usually skew to

larger sizes. Thus, a linear relation is not appropriate. For sizes of rain drops, often an exponential distribution is assumed. This leads to an exponent $\gamma = \frac{1}{4}$ and a coefficient $c_r = c_{r0}\rho^{-\frac{3}{4}}$ ($c_{r0} = 23752.6753\,\mathrm{kg}^{-\frac{1}{4}}\mathrm{m}^{\frac{3}{4}}$, $[c_r] = \mathrm{kg}^{-1}$) as derived in Appendix A.

- *Rates for diffusion processes*

  For the mass mixing ratios q_c and q_r, the rates for the diffusion processes are given by multiplication of the single particle rates by the number concentration of the respective particles, namely

  $$\frac{dq_c}{dt} = n_c\frac{dm_c}{dt}, \quad \text{and} \quad \frac{dq_r}{dt} = n_r\frac{dm_r}{dt}.$$

  Applying the relations between the mass and number concentrations as stated above, we obtain

  $$C_1 = \frac{dq_c}{dt} = n_c d\rho(q_v - q_*)m_c^{\frac{1}{3}} \overset{m_c=\frac{q_c}{n_c}}{=} d\rho(q_v - q_*)\left(\frac{N_\infty}{q_c + N_\infty m_0}\coth\left(\frac{q_c}{N_0 m_0}\right)\right)^{\frac{2}{3}} q_c$$

  and

  $$\begin{aligned} E = -\frac{dq_r}{dt} &= n_r d\rho(q_* - q_v)_+\left[a_E m_r^{\frac{1}{3}} + b_E v_\tau(m_r)m_r^{\frac{1}{2}}\right] \\ &\overset{m_r=\frac{q_r}{n_r}}{=} d\rho(q_* - q_v)_+\left[a_E c_r{}^{\frac{2}{3}} q_r^{\frac{1}{3}+\gamma\frac{2}{3}} + b_E c_r{}^{\frac{1}{2}} v_\tau(q_r)^{\frac{1}{2}} q_r^{\frac{1}{2}+\gamma\frac{1}{2}}\right] \end{aligned}$$

  using a reformulated terminal velocity

  $$v_\tau(m_r) = v_\tau(q_r) = \alpha q_r^\beta\left(\frac{m_\tau}{q_r + m_\tau c_r q_r^\gamma}\right)^\beta\left(\frac{\rho_*}{\rho}\right)^{\frac{1}{2}}.$$

  Note that the rates for activation and diffusion growth of cloud droplets are combined in the model formulation, that is, $C = C_1 + C_{\mathrm{act}}$.

- *Rate for accretion*

  For the rate of accretion of rain water, we obtain

  $$A_2 = \frac{dq_r}{dt} = n_r\frac{dm_r}{dt} = k_2\rho\pi c_r{}^{\frac{1}{3}}\left(\frac{3}{4\pi\rho_\ell}\right)^{\frac{2}{3}} q_c v_\tau(q_r) q_r^{\frac{2+\gamma}{3}}.$$

  Note that for compensating effects of the averaging, the parameter k_2 can be adjusted (such that $k_2 = 0.8\,\mathrm{kg} \neq k_2'$). The impact of the uncertainty of this parameter is of high interest since it cannot be measured or derived from the first principles.

- *Collisions of cloud droplets forming a rain drop: Autoconversion*

  Besides the growth of an existing rain drop by collecting cloud droplets, a rain drop can be formed by the collision of two cloud droplets. According to [103], we formulate the growth rate similarly to population models, namely

  $$A_1 = \frac{dq_c}{dt} = k_1\frac{\rho q_c^2}{\rho_\ell}.$$

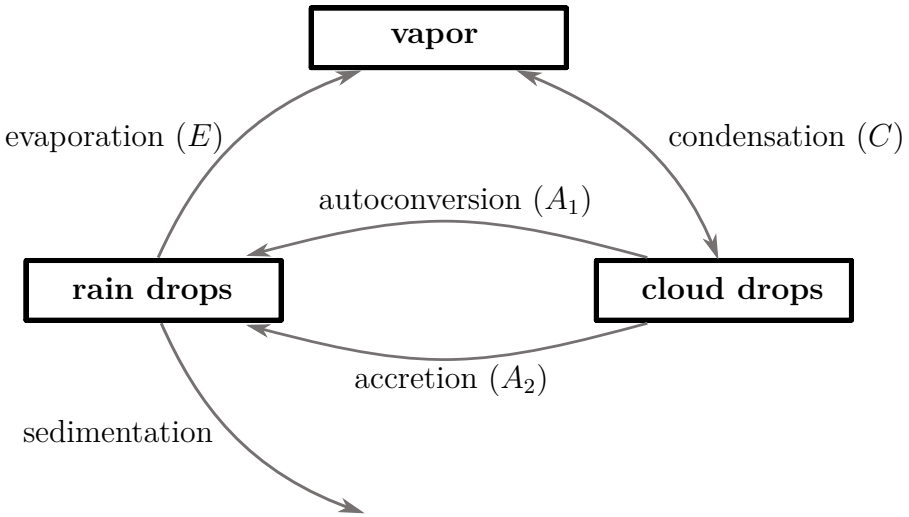

Figure 2.2: Processes and interactions between the liquid water phases vapor, cloud drops and rain drops in the cloud equations.

Note that the coefficient k_1 cannot be measured or derived from the first principles. It is a free parameter that must be fixed using parameter estimations. Thus, the impact of the uncertainty of this parameter is of high interest. In our deterministic experiments, we choose $k_1 = 4083\,\mathrm{kg\,s^{-1}}$, as indicated in [103].

- *Sedimentation of rain mass mixing ratio*

  We have added the convection term $\nabla\cdot(-v_q\rho q_r \boldsymbol{e_3})$ to the equation for the evolution of q_r in (2.50), where

$$v_q = v_q(q_r) = \alpha q_r^{\beta}\left(\frac{m_\tau}{q_r + m_\tau c_r q_r^{\gamma}}\right)^{\beta}\left(\frac{\rho_*}{\rho}\right)^{\frac{1}{2}}. \tag{2.53}$$

  The parameter α can be derived empirically, but the influence of uncertainty in α is of high interest.

Figure 2.2 summarizes the connections of the different liquid water phases and the interactions between them.

Note that activation and diffusion processes are formulated explicitly, in contrast to the usual approach of saturation adjustment (see, e.g., [67]). The latter is less accurate, but commonly used in operational weather forecast models. This explicit formulation introduces stiffness caused by modeling cloud processes on the RHS of the cloud equations with fractional exponents between -1 and 1. In order to avoid the root evaluation for an argument that is close to zero, we introduce a cut-off function and replace ζ^ξ, $\xi \in (-1, 1)$, with

$$\begin{cases} \zeta^\xi, & \text{if } \zeta > 10^{-16}, \\ 0, & \text{otherwise.} \end{cases}$$

3 Cloud models

We introduce the different models that will be investigated in this work. The modeling assumptions for the dynamics of clouds and fluids were explained in Chapter 2 and will be combined to a coupled deterministic model in Section 3.1. Since meteorological applications typically inherit several sources of uncertainties, such as model parameters, initial and boundary conditions, we want to investigate uncertainty propagation and therefore present in Section 3.2 random models, first just for the cloud dynamics in Subsection 3.2.1 and then for the fully coupled model in Subsection 3.2.2.

3.1 Deterministic mathematical model

We study a mathematical model of cloud dynamics, which is based on the compressible nonhydrostatic Navier-Stokes equations for moist atmosphere (that is, a mixture of the ideal gases dry air and water vapor). The model is a combination of the balance equations (2.48), which express basic physical principles, and balance equations for liquid water phases (2.50) modeling cloud dynamics,

$$\begin{aligned}
\rho_t + \nabla \cdot (\rho \boldsymbol{u}) &= 0, \\
(\rho \boldsymbol{u})_t + \nabla \cdot \left(\rho \boldsymbol{u} \otimes \boldsymbol{u} + p\,\mathrm{Id} - \mu_m \rho \left(\nabla \boldsymbol{u} + (\nabla \boldsymbol{u})^\top\right)\right) &= -\rho g \boldsymbol{e_d}, \\
(\rho\theta)_t + \nabla \cdot (\rho\theta \boldsymbol{u} - \mu_h \rho \nabla\theta) &= S_\theta,
\end{aligned} \tag{M1.a$*$}$$

$$\begin{aligned}
(\rho q_v)_t + \nabla \cdot (\rho q_v \boldsymbol{u} - \mu_q \rho \nabla q_v) &= \rho(-C + E), \\
(\rho q_c)_t + \nabla \cdot (\rho q_c \boldsymbol{u} - \mu_q \rho \nabla q_c) &= \rho(C - A_1 - A_2), \\
(\rho q_r)_t + \nabla \cdot (-v_q \rho q_r \boldsymbol{e_d} + \rho q_r \boldsymbol{u} - \mu_q \rho \nabla q_r) &= \rho(A_1 + A_2 - E).
\end{aligned} \tag{M1.b$*$}$$

All the quantities and variables were already introduced in Sections 2.1 and 2.2, but for convenience we repeat briefly the notations here to obtain a compact model description: ρ is the density, $\boldsymbol{u} = (u_1, \ldots, u_d)^\top$ is the velocity vector, where d is the space dimension, θ is the moist potential temperature, p is the pressure, g is the acceleration due to gravity, μ_m is the dynamic viscosity, μ_h is the thermal conductivity, and μ_q is the cloud diffusivity. Furthermore, $\boldsymbol{e_d} = \boldsymbol{e_3} = (0, 0, 1)^\top$ and $\boldsymbol{e_d} = \boldsymbol{e_2} = (0, 1)^\top$ in the 3D and 2D cases, respectively. We set $\mu_m = 10^{-3}$ and $\mu_h = 10^{-2} = \mu_q$ for consistency as it is

done in [110]. In general, a parameter study is necessary to determine μ_h. Note that the systems (M1.a∗) and (M1.b∗) are coupled through the source term S_θ in the energy equation. Due to phase changes (activation and growth/evaporation of water particles), latent heat is released or absorbed. These processes are modeled by

$$S_\theta = \rho \frac{L\theta}{c_p T} (C - E), \tag{3.2}$$

where the terms $C = C_1 + C_{\text{act}}$ (condensation) and E (evaporation) are explained in details in Section 2.2.2, *Rates for diffusion processes*.

We will follow the approach of [110] and close the system by using the ideal gas law for moist air instead of using the one for dry air as in Section 2.1. Thus, the temperature T can be obtained from the moist adiabatic ideal gas equation

$$T = \frac{R}{R_m} \theta \left(\frac{p}{p_0} \right)^{R_m/c_p},$$

where $p_0 = 10^5$ Pa is the reference pressure at sea level. In addition to the usual definition of a potential temperature, we use $R_m = (1 - q_v - q_c - q_r)R + q_v R_v$ with the ideal gas constant of dry air $R = 287.05\,{}^{J}/_{(\text{kg·K})}$, the gas constant of water vapor $R_v = 461.51\,{}^{J}/_{(\text{kg·K})}$ and the specific heat capacity of dry air for constant pressure $c_p = 1005\,{}^{J}/_{(\text{kg·K})}$, cf. [110]. In order to close the system, we determine the pressure from the equation of state including moisture

$$p = p_0 \left(\frac{R\rho\theta}{p_0} \right)^{\gamma_m} \quad \text{with} \quad \gamma_m = \frac{c_p}{c_p - R_m}. \tag{3.3}$$

We note that in the dry case R_m reduces to R, $S_\theta = 0$ and the moist ideal gas equation as well as the moist equation of state become their dry analogon, see (2.48) with (2.35) and (2.43).

Solving the Navier-Stokes equations (M1.b∗) in a weakly compressible regime is known to cause numerical instabilities due to the multiscale effects. We follow the approach typically used in meteorological models, in which the dynamics of interest is described by a perturbation of a background state, which is the hydrostatic equilibrium. The latter expresses a balance between the gravity and pressure forces. Denoting by $\bar{p}$, $\bar{\rho}$, $\bar{\boldsymbol{u}} = 0$, $\bar{\theta}$ and $\overline{\rho\theta}$ the respective background state, the hydrostatic equilibrium satisfies

$$\frac{\partial \bar{p}}{\partial x_d} = -\bar{\rho} g, \quad S_\theta = 0, \tag{3.4}$$

where $\bar{p}$ is obtained from the equation of state (3.3)

$$\bar{p} = p(\overline{\rho\theta}) = p_0 \left(\frac{R\overline{\rho\theta}}{p_0} \right)^{\gamma_m}. \tag{3.5}$$

Let p', ρ', $\boldsymbol{u}'$, θ' and $(\rho\theta)'$ stand for the corresponding perturbations of the equilibrium state, then

$$p = \bar{p} + p', \quad \rho = \bar{\rho} + \rho', \quad \theta = \bar{\theta} + \theta', \quad \boldsymbol{u} = \boldsymbol{u}', \quad \rho\theta = \bar{\rho}\bar{\theta} + \bar{\rho}\theta' + \rho'\bar{\theta} + \rho'\theta' = \overline{\rho\theta} + (\rho\theta)'. \tag{3.6}$$

The pressure perturbation p' is derived from (3.3) and (3.5) using the following Taylor expansion

$$p(\rho\theta) \approx p(\overline{\rho\theta}) + \frac{\partial p}{\partial(\rho\theta)}\left(\rho\theta - \overline{\rho\theta}\right) = \bar{p} + \gamma_m p_0 \left(\frac{R\overline{\rho\theta}}{p_0}\right)^{\gamma_m} \frac{(\rho\theta)'}{\overline{\rho\theta}},$$

which results in

$$p' \approx \gamma_m p_0 \left(\frac{R\overline{\rho\theta}}{p_0}\right)^{\gamma_m} \frac{(\rho\theta)'}{\overline{\rho\theta}}.$$

Inserting the expansions (3.6) into the Navier-Stokes equations (M1.b$*$) and using the hydrostatic balance (3.4) directly leads to

$$\begin{aligned} \rho'_t + \nabla\cdot(\rho\boldsymbol{u}) &= 0,\\ (\rho\boldsymbol{u})_t + \nabla\cdot\left(\rho\boldsymbol{u}\otimes\boldsymbol{u} + p'\,\mathrm{Id} - \mu_m\rho\left(\nabla\boldsymbol{u} + (\nabla\boldsymbol{u})^\top\right)\right) &= -\rho' g\boldsymbol{e_d},\\ (\rho\theta)'_t + \nabla\cdot(\rho\theta\boldsymbol{u} - \mu_h\rho\nabla\theta) &= S_\theta. \end{aligned} \tag{3.7}$$

Consequently, a physical motivation from the hydrostatic balance state leads to a numerically preferable scaling and the perturbation formulation of the deterministic cloud model (M1$*$) then reads as

$$\begin{aligned} \rho'_t + \nabla\cdot(\rho\boldsymbol{u}) &= 0,\\ (\rho\boldsymbol{u})_t + \nabla\cdot\left(\rho\boldsymbol{u}\otimes\boldsymbol{u} + p'\,\mathrm{Id} - \mu_m\rho\left(\nabla\boldsymbol{u} + (\nabla\boldsymbol{u})^\top\right)\right) &= -\rho' g\boldsymbol{e_d},\\ (\rho\theta)'_t + \nabla\cdot(\rho\theta\boldsymbol{u} - \mu_h\rho\nabla\theta) &= S_\theta, \end{aligned} \tag{M1.a}$$

$$\begin{aligned} (\rho q_v)_t + \nabla\cdot(\rho q_v\boldsymbol{u} - \mu_q\rho\nabla q_v) &= \rho(-C+E),\\ (\rho q_c)_t + \nabla\cdot(\rho q_c\boldsymbol{u} - \mu_q\rho\nabla q_c) &= \rho(C-A_1-A_2),\\ (\rho q_r)_t + \nabla\cdot(-v_q\rho q_r\boldsymbol{e_d} + \rho q_r\boldsymbol{u} - \mu_q\rho\nabla q_r) &= \rho(A_1+A_2-E). \end{aligned} \tag{M1.b}$$

From now on (M1) will always stand for the above deterministic cloud model and (M1.a) will refer to the Navier-Stokes and (M1.b) to the cloud dynamics part.

3.2 Stochastic mathematical model

Meteorological applications typically inherit several sources of uncertainties, such as model parameters as pointed out in Section 2.2, initial and boundary conditions. Consequently, purely deterministic models are insufficient in such situations and more sophisticated methods need to be applied to analyze the influence of uncertainties on numerical solutions.

In general, there are different ways to represent and take into account model uncertainty. A common way is to model the uncertainty through a *Wiener process*, for example, a *Brownian motion*, and then obtain a stochastic differential equation which has to be solved with proper numerical methods. In this thesis, we choose another widely used approach, namely to describe the uncertainty by a random variable. To this end, we first need to introduce some concepts. We start with the definition of abstract probability spaces.

Definition 3.1
A *probability space* is a triple (Γ, Σ, P), where Γ is a nonempty set which is called *sample space*, Σ is a σ-algebra over Γ which is called *event space* and $P : \Sigma \to [0, 1]$ is a *probability measure*. The sample space Γ is the set of all possible outcomes of an experiment, the event space Σ contains all events of interest and the probability measure P satisfies the postulates

1. $P(\emptyset) = 0$,
2. $P(\Gamma) = 1$,
3. if $\{A_i\}_{i\in\mathbb{N}} \subset \Sigma$ and $A_i \cap A_j = \emptyset$ for all $i, j \in \mathbb{N}$, then $P\left(\bigcup_{i=1}^{\infty} A_i\right) = \sum_{i=1}^{\infty} P(A_i)$.

One can think of a probability space as a measure space where the measure of the whole space is equal to 1, because $P(\Gamma) = 1$ holds.

Definition 3.2
A *random variable* is a measurable function $X : \Gamma \to \mathbb{R}$. Here, measurable means that $\{\omega \in \Gamma \,|\, X(\omega) \leq x\} \in \Sigma$ for each $x \in \mathbb{R}$. The probability that X takes the value y is then given by

$$P(X = y) = P(\{\omega \in \Gamma \,|\, X(\omega) = y\}).$$

Definition 3.3
The value $X(\omega)$ of a random variable X for an outcome $\omega \in \Gamma$ is termed a realization of X.

In the following, we will denote by ω always an outcome $\omega \in \Gamma$.

Definition 3.4
Associated with every random variable X is a *distribution function* $\mathcal{F}_X : \mathbb{R} \to [0, 1]$ with

$$\mathcal{F}_X(x) := P(\omega \in \Gamma | X(\omega) \leq x).$$

Definition 3.5
If the distribution function is absolutely continuous, it can be expressed as

$$\mathcal{F}_X(x) = \int_{-\infty}^{x} f_X(s)\,\mathrm{d}s,$$

where the derivative $\frac{d\mathcal{F}_X(x)}{dx} =: f_X(s) : \mathbb{R} \to [0, \infty)$ is called the *probability density function* of X.

With these brief prerequisites, we will now introduce uncertainty first just for the cloud dynamics in Section 3.2.1 and then for the whole coupled dynamics in Section 3.2.2. In

this thesis, we consider the cases where the uncertainty arises from the initial data or some coefficients in the microphysical cloud parametrizations.

3.2.1 Stochastic cloud dynamics

We assume that either the initial data or some well-chosen model parameters, see Section 2.2, depend on $\omega(= X(\omega))$, that is,

$$(\rho q_\ell)\big|_{t=0} = (\rho q_\ell)(\boldsymbol{x}, t = 0, \omega) \quad \text{with} \quad \ell \in \{v, c, r\} \tag{3.9}$$

or

$$k_1 = k_1(\omega), \quad k_2 = k_2(\omega), \quad \alpha = \alpha(\omega). \tag{3.10}$$

Consequently, the solution at later times will also depend on ω, that is, $(\rho q_\ell)(\boldsymbol{x}, t, \omega)$ for $\ell \in \{v, c, r\}$, and then

$$\begin{aligned}
((\rho q_v)(\omega))_t + \nabla \cdot ((\rho q_v)(\omega)\boldsymbol{u} - \mu_q \rho \nabla q_v(\omega)) &= \rho(-C + E)(\omega), \\
((\rho q_c)(\omega))_t + \nabla \cdot ((\rho q_c)(\omega)\boldsymbol{u} - \mu_q \rho \nabla q_c(\omega)) &= \rho(C - A_1 - A_2)(\omega), \\
((\rho q_r)(\omega))_t + \nabla \cdot ((\rho q_r)(\omega)(-v_q(\omega)\boldsymbol{e_d} + \boldsymbol{u}) - \mu_q \rho \nabla q_r(\omega)) &= \rho(A_1 + A_2 - E)(\omega).
\end{aligned} \tag{3.11}$$

From now on, we will stress the dependence on ω, but we will omit the dependence on $\boldsymbol{x}$ and t to simplify the notation.

We would like to point out that the solution of the Navier-Stokes equations (M1.a) should also depend on ω because of the source term S_θ which depends on quantities that depend on ω. This case will be considered in Section 3.2.2. Here, we will consider a simplified situation by replacing

$$S_\theta(\omega) = \rho \frac{L\theta}{c_p T} \left[C((\rho q_v)(\omega), (\rho q_c)(\omega)) - E((\rho q_v)(\omega), (\rho q_r)(\omega)) \right]$$

in (M1.a) by $\bar{S}_\theta$ which only depends on the expected values of the cloud variables

$$\bar{S}_\theta := \rho \frac{L\theta}{c_p T} \left[C(\mathbb{E}[\rho q_v], \mathbb{E}[\rho q_c]) - E(\mathbb{E}[\rho q_v], \mathbb{E}[\rho q_r]) \right]. \tag{3.12}$$

Thus, (M2.a) is deterministic, but depends on the expected values of the stochastic system (M2.b). This ensures that all of the fluid variables ρ', $\rho\boldsymbol{u}$ and $(\rho\theta)'$ remain deterministic. Thus, we obtain the following semi-stochastic cloud model

$$\begin{aligned}
\rho'_t + \nabla \cdot (\rho \boldsymbol{u}) &= 0, \\
(\rho \boldsymbol{u})_t + \nabla \cdot \left(\rho \boldsymbol{u} \otimes \boldsymbol{u} + p' \,\mathrm{Id} - \mu_m \rho \left(\nabla \boldsymbol{u} + (\nabla \boldsymbol{u})^\top \right) \right) &= -\rho' g \boldsymbol{e_d}, \\
(\rho\theta)'_t + \nabla \cdot (\rho\theta \boldsymbol{u} - \mu_h \rho \nabla \theta) &= \bar{S}_\theta,
\end{aligned} \tag{M2.a}$$

$$\begin{aligned}
((\rho q_v)(\omega))_t + \nabla \cdot ((\rho q_v)(\omega)\boldsymbol{u} - \mu_q \rho \nabla q_v(\omega)) &= \rho(-C + E)(\omega), \\
((\rho q_c)(\omega))_t + \nabla \cdot ((\rho q_c)(\omega)\boldsymbol{u} - \mu_q \rho \nabla q_c(\omega)) &= \rho(C - A_1 - A_2)(\omega), \\
((\rho q_r)(\omega))_t + \nabla \cdot ((\rho q_r)(\omega)(-v_q(\omega)\boldsymbol{e_d} + \boldsymbol{u}) - \mu_q \rho \nabla q_r(\omega)) &= \rho(A_1 + A_2 - E)(\omega).
\end{aligned} \tag{M2.b}$$

Remark 3.1*:* This model uses a simplified approach by only considering the expected values for the latent heat release and absorption in (3.12). Consequently, the condensate of a given realization $X(\omega)$ does not necessarily correspond to the latent heat. Thus, the model is not consistent since the energy is not conserved.

Additionally to the time and space dependence, the variables $(\rho q_\ell)(\boldsymbol{x}, t, \omega)$, $\ell \in \{v, c, r\}$, exhibit randomness. To interpret this concept of solutions, the introduction of random fields is necessary.

Definition 3.6
A *random field* is a collection

$$X = \{X_z,\ z \in Z\} = \{X(z),\ z \in Z\}$$

of random variables defined on the same probability space (Γ, Σ, P) and indexed by elements z of a topological space Z. In our case, the elements are $z := (\boldsymbol{x}, t)$ in the space $Z := \Omega \times [0, T]$.

The random solutions $(\rho q_\ell)(\boldsymbol{x}, t, \omega)$, $\ell \in \{v, c, r\}$, are random fields. They can be interpreted in the following ways:

- $(\rho q_\ell)(\boldsymbol{x}, t, \cdot)$ is a random variable for fixed $(\boldsymbol{x}, t) \in \Omega \times [0, T]$.
- ρq_ℓ is a function on the space $\Omega \times [0, T] \times \Gamma$ with the realization $(\rho q_\ell)(\boldsymbol{x}, t, \omega)$ for $(\boldsymbol{x}, t) \in \Omega \times [0, T]$ and $\omega \in \Gamma$.
- For an outcome $\omega \in \Gamma$, the realization $(\rho q_\ell)(\boldsymbol{x}, t, \omega)$ is a function of $(\boldsymbol{x}, t)$.

The concepts of deterministic solutions will be briefly discussed in Subsection 3.3.2 and for more details on that topic we refer, e.g., to [28, 74]. Here, we want to state a concept of *random weak solutions* $(\rho q_\ell)(\boldsymbol{x}, t, \omega)$, $\ell \in \{v, c, r\}$. Let $(\rho q_\ell)(\boldsymbol{x}, t, \omega) \in \mathcal{V} \otimes \mathcal{S}$, $\ell \in \{v, c, r\}$, where $\mathcal{V}$ is a suitable space for the deterministic solution $(\rho q_\ell)(\cdot, \cdot, \omega)$ for fixed ω and $\mathcal{S}$ is a suitable stochastic space for the random variable $(\rho q_\ell)(\boldsymbol{x}, t, \cdot)$ for fixed $(\boldsymbol{x}, t)$. If all random quantities are of second order, i.e. $\mathbb{E}[|(\rho q_\ell)(\boldsymbol{x}, t, \cdot)|^2] < \infty$, $\ell \in \{v, c, r\}$, one can take $\mathcal{S} = L^2(\Gamma, P)$. Here, $\mathbb{E}$ denotes the mathematical expectation which is given for a function $f \in \mathcal{S}$ through

$$\mathbb{E}[f] = \int_\Gamma f(\omega)\, \mathrm{d}P(\omega).$$

We seek solutions $(\rho q_\ell)(\boldsymbol{x}, t, \omega) \in \mathcal{V} \otimes \mathcal{S}$, $\ell \in \{v, c, r\}$, that satisfy (M2.b) in a weak and probabilistic sense. Here, in a probabilistic sense means that the stochastic problem (M2.b) is interpreted in the mean. Thus, a random weak solution is a function

$(\rho q_\ell)(\boldsymbol{x},t,\omega) \in \mathcal{V}\otimes\mathcal{S}$, $\ell \in \{v,c,r\}$, such that

$$\mathbb{E}\left[\left(\int_0^T\int_\Omega (\rho q_v)(\boldsymbol{x},t,\omega)\varphi_t(\boldsymbol{x},t) + \nabla\varphi(\boldsymbol{x},t)\cdot((\rho q_v)(\boldsymbol{x},t,\omega)\boldsymbol{u}(\boldsymbol{x},t) - \mu_q\rho(\boldsymbol{x},t)\nabla q_v(\boldsymbol{x},t,\omega))\right.\right.$$
$$\left.\left. - \rho(\boldsymbol{x},t)(-C+E)(\boldsymbol{x},t,\omega)\varphi(\boldsymbol{x},t)\,\mathrm{d}\boldsymbol{x}\,\mathrm{d}t\right)\beta(\omega)\right] = 0,$$

$$\mathbb{E}\left[\left(\int_0^T\int_\Omega (\rho q_c)(\boldsymbol{x},t,\omega)\varphi_t(\boldsymbol{x},t) + \nabla\varphi(\boldsymbol{x},t)\cdot((\rho q_c)(\boldsymbol{x},t,\omega)\boldsymbol{u}(\boldsymbol{x},t) - \mu_q\rho(\boldsymbol{x},t)\nabla q_c(\boldsymbol{x},t,\omega))\right.\right.$$
$$\left.\left. - \rho(\boldsymbol{x},t)(C-A_1-A_2)(\boldsymbol{x},t,\omega)\varphi(\boldsymbol{x},t)\,\mathrm{d}\boldsymbol{x}\,\mathrm{d}t\right)\beta(\omega)\right] = 0,$$

$$\mathbb{E}\left[\left(\int_0^T\int_\Omega (\rho q_r)(\boldsymbol{x},t,\omega)\varphi_t(\boldsymbol{x},t) + \nabla\varphi(\boldsymbol{x},t)\cdot((\rho q_r)(\boldsymbol{x},t,\omega)\boldsymbol{u}(\boldsymbol{x},t) - \mu_q\rho(\boldsymbol{x},t)\nabla q_r(\boldsymbol{x},t,\omega))\right.\right.$$
$$- \nabla\varphi(\boldsymbol{x},t)\cdot(v_q(\boldsymbol{x},t,\omega)(\rho q_r)(\boldsymbol{x},t,\omega)\boldsymbol{e_d})$$
$$\left.\left. - \rho(\boldsymbol{x},t)(A_1+A_2-E)(\boldsymbol{x},t,\omega)\varphi(\boldsymbol{x},t)\,\mathrm{d}\boldsymbol{x}\,\mathrm{d}t\right)\beta(\omega)\right] = 0,$$

for all $\beta\in\mathcal{S}$ and $\varphi \in C_0^2([0,T)\times\Omega)$, where C_0^2 denotes the class of functions which are two time continously differentiable with compact support.

3.2.2 Fully stochastic model

As in the previous section, we assume that either the initial data or some well-chosen model parameters in the cloud dynamics depend on ω, see (3.9) and (3.10), and consequently we end up again with equations (3.11). Due to the coupling of the source term S_θ in the energy equation, also the Navier-Stokes variables will depend on ω, that is,

$$\rho'(\boldsymbol{x},t,\omega),\ (\rho\boldsymbol{u})(\boldsymbol{x},t,\omega) \quad\text{and}\quad (\rho\theta)'(\boldsymbol{x},t,\omega)$$

and then the Navier-Stokes system (M1.a) reads as

$$\begin{aligned}
(\rho'(\omega))_t + \nabla\cdot((\rho\boldsymbol{u})(\omega)) &= 0,\\
((\rho\boldsymbol{u})(\omega))_t + \nabla\cdot\big((\rho\boldsymbol{u})(\omega)\otimes\boldsymbol{u}(\omega) + p'(\omega)\,\mathrm{Id}&\\
-\mu_m\rho(\omega)\left(\nabla\boldsymbol{u}(\omega) + (\nabla\boldsymbol{u}(\omega))^\top\right)\big) &= -\rho'(\omega)g\boldsymbol{e_d},\\
((\rho\theta)'(\omega))_t + \nabla\cdot((\rho\theta)(\omega)\boldsymbol{u}(\omega) - \mu_h\rho(\omega)\nabla\theta(\omega)) &= S_\theta(\omega).
\end{aligned}$$

Remark 3.2*:* We note that it is also (additionally) possible to start with uncertain initial fluid variables, that is,

$$\rho'\big|_{t=0} = \rho'(\boldsymbol{x},t=0,\omega),\ (\rho\boldsymbol{u})\big|_{t=0} = (\rho\boldsymbol{u})(\boldsymbol{x},t=0,\omega) \quad\text{and}\quad (\rho\theta)'\big|_{t=0} = (\rho\theta)'(\boldsymbol{x},t=0,\omega),$$

which would lead to the stochastic system (M3) too.

The fully stochastic cloud model is then given through

$$\begin{aligned}
(\rho'(\omega))_t + \nabla \cdot ((\rho \boldsymbol{u})(\omega)) &= 0, \\
((\rho \boldsymbol{u})(\omega))_t + \nabla \cdot \big((\rho \boldsymbol{u})(\omega) \otimes \boldsymbol{u}(\omega) + p'(\omega)\,\mathrm{Id} \\
-\mu_m \rho(\omega) \left(\nabla \boldsymbol{u}(\omega) + (\nabla \boldsymbol{u}(\omega))^\top\right)\big) &= -\rho'(\omega) g \boldsymbol{e_d}, \\
((\rho\theta)'(\omega))_t + \nabla \cdot ((\rho\theta)(\omega)\boldsymbol{u}(\omega) - \mu_h \rho(\omega) \nabla \theta(\omega)) &= S_\theta(\omega),
\end{aligned} \tag{M3.a}$$

$$\begin{aligned}
((\rho q_v)(\omega))_t + \nabla \cdot ((\rho q_v)(\omega)\boldsymbol{u}(\omega) - \mu_q \rho(\omega) \nabla q_v(\omega)) &= \rho(\omega) \\
&\cdot (-C + E)(\omega), \\
((\rho q_c)(\omega))_t + \nabla \cdot ((\rho q_c)(\omega)\boldsymbol{u}(\omega) - \mu_q \rho(\omega) \nabla q_c(\omega)) &= \rho(\omega) \\
&\cdot (C - A_1 - A_2)(\omega), \\
((\rho q_r)(\omega))_t + \nabla \cdot ((\rho q_r)(\omega)(-v_q(\omega)\boldsymbol{e_d} + \boldsymbol{u}(\omega)) - \mu_q \rho(\omega) \nabla q_r(\omega)) &= \rho(\omega) \\
&\cdot (A_1 + A_2 - E)(\omega).
\end{aligned} \tag{M3.b}$$

Here, the random solutions $\rho'(\boldsymbol{x}, t, \omega)$, $(\rho \boldsymbol{u})(\boldsymbol{x}, t, \omega)$, $(\rho\theta)'(\boldsymbol{x}, t, \omega)$ and $(\rho q_\ell)(\boldsymbol{x}, t, \omega)$, $\ell \in \{v, c, r\}$, are random fields, cf. Definition 3.6. This fully stochastic approach is numerically more complex, but it is also consistent and conserves the energy. The concept of stochastic solutions was explained in Subsection 3.2.1.

3.3 Existence and uniqueness results

In this section, we state some existence and uniqueness results of systems similar to our deterministic model (M1). It is outside the scope of this thesis to look at the existence and uniqueness of solutions of our coupled model (M1), but for completeness we summarize some known existing results related to model (M1). In Subsection 3.3.1, we formulate a recent result for the ODE cloud model on which our cloud dynamics system (M1.b) is based, see [103]. In Subsection 3.3.2, we refer to some results for compressible Navier-Stokes equations and in Subsection 3.3.3, we state a recent result from [51], which shows global solvability of a full moist atmospheric flow model very similar to our model (M1).

3.3.1 ODE cloud model

Here, we will introduce the ODE cloud model our cloud equations (M1.b) are based on and present some results from [103].

The equations of the ODE model are written in the Lagrangian reference system, where each fluid particle is followed along its trajectory through time and space in contrast to a formulation in the Eulerian coordinates, see Definition 2.1 and the short introduction to the different reference systems therein. Because of that, the ODE model is used as a box model for a single volume parcel or as a model of a vertical column of air, which is transported along a given trajectory. The cloud quantities are given through the

following equations

$$\begin{aligned}(q_v)_t &= -C + E,\\ (q_c)_t &= C - A_1 - A_2,\\ (q_r)_t &= A_1 + A_2 - E - S,\\ (n_r)_t &= A_1' - E' - S',\end{aligned} \tag{3.15}$$

where q_ℓ, $\ell \in \{v, c, r\}$, are defined as in (2.49). In contrast to our single moment scheme which just considers the evolution of the water phase concentrations q_ℓ, $\ell \in \{v, c, r\}$, (3.15) is a one-and-a-half moment scheme. This means that its complexity is somewhere between a single moment scheme and a double moment scheme which in addition also considers the evolution of the number concentrations of the considered particles. In practice, the difference is that instead of using the closure for single moment schemes, see Appendix A, here, the number concentration of rain drops is determined by an ODE in (3.15). The respective autoconversion and evaporation terms are given through

$$A_1' = k_1 \frac{\rho n_c q_c}{2\rho_\ell}, \quad E' = \frac{E}{\overline{m_r}},$$

where $\overline{m_r} = \frac{q_r}{n_r}$ denotes the mean mass of rain drops. Another difference is that due to the ODE formulation the sedimentation terms are realized by reaction instead of advection terms, i.e.,

$$S = \frac{1}{\rho}\frac{\partial J}{\partial z}, \quad S' = \frac{1}{\rho}\frac{\partial J'}{\partial z}.$$

Here, J and J' denote fluxes and are determined by

$$J = v_r \rho q_r, \quad J' = v_n \rho n_r$$

with $v_r = c_r v_q$ and $v_n = c_n v_q$, where $c_r = 1.84$, $c_n = 0.58$ and v_q as in (2.53). In [103], the cloud equations (3.15) are solved semi-implicitly in time. In our approach, we prefer a fully explicit time discretization. Consequently, we need to take care of the case where we start with no cloud droplet concentration, but still want to allow condensation to take place. To avoid a nonphysical zero solution of an explicit time integration, we add an activation term for the condensation in our cloud model, see (2.52).

All in all, the two models (M1.b) and (3.15) are still very similar since they are based on the same microphysical cloud parametrizations.

In general, system (3.15) has no unique solution since the RHS is not Lipschitz continuous. However, the existence of a solution is guaranteed by Peano's theory, see, for example, [134]. In [103], a consistent numerical scheme was proposed which is positivity preserving and also preserves the air and water mass balance.

3.3.2 Compressible Navier-Stokes equations

The mathematical theory of the Navier-Stokes equations has a long history and is still a very active research field. In fact, the fundamental problems on well-posedness of these fundamental and widely-used governing equations describing dynamics of fluids remain

open. In this subsection, we will briefly summarize some existing results for the Navier-Stokes equations for the 3D case. For a more detailed insight into the numerical analysis of compressible fluid flows we refer, for example, to [28].

The results which we will present are mostly for the following formulation of the Navier-Stokes equations

$$\rho_t + \nabla \cdot (\rho \boldsymbol{u}) = 0, \tag{3.16}$$

$$(\rho \boldsymbol{u})_t + \nabla \cdot (\rho \boldsymbol{u} \otimes \boldsymbol{u} + p\,\mathrm{Id}) = \nabla \cdot \boldsymbol{\tau}^V + \rho \boldsymbol{f}, \tag{3.17}$$

$$c_v \frac{\partial \rho T}{\partial t} + \nabla \cdot (c_v \rho T \boldsymbol{u} - \kappa \nabla T) = \rho q + \nabla \cdot (\boldsymbol{\tau} \cdot \boldsymbol{u}) - (\nabla \cdot \boldsymbol{\tau})\boldsymbol{u}, \tag{3.18}$$

where $p = p(\rho, T)$. The difference to our formulation (M1.a) is that in (3.17) and (3.18) also the bulk viscosity is considered in the viscous stress tensor, see (2.17), i.e.,

$$\boldsymbol{\tau}^V = \mu \left(\nabla \boldsymbol{u} + (\nabla \boldsymbol{u})^\top \right) + \lambda \left(\nabla \cdot \boldsymbol{u} \right) \mathrm{Id},$$

where $\lambda \geq -\frac{2}{3}\mu$ is the bulk viscosity coefficient, and $\boldsymbol{f}$ is a general body force as in (2.10). The energy equation (3.18) is the one from (2.37) and $\boldsymbol{\tau}$ is defined as in (2.16).

We start by a brief explanation of the different concepts of solutions, without noting their mathematical definitions (for more details see, for example, [28]):

- *Classical solution*: The solutions are smooth enough to fulfill equations (3.16)–(3.18) at each space-time point $(\boldsymbol{x}, t)$.
- *Weak solution*: In this case, the equations (3.16)–(3.18) are written in terms of integral averages. Consequently, the solutions do not have to be differentiable.

  If there exist a classical and a weak solution of the Navier-Stokes equations (3.16)–(3.18) with the same initial data, then the *weak-strong uniqueness principle* states that these solutions coincide, see [29, 31].
- *Measure-valued solution*: The solutions satisfy (3.16)–(3.18) modulo defect measures related to possible oscillations and concentrations. They may be seen as an expected value of the associated Young measure. The latter is a space-time parametrized probability measure.

  If there exist a measure-valued and a classical solution of the Navier-Stokes equations (3.16)–(3.18) with the same initial data, then the *weak-strong uniqueness principle* for measured-valued solutions states that these solutions coincide, see [30].

When considering classical solutions, the most prominent result for (3.16)–(3.18) is the one from Matsumura and Nishida which ensures global-in-time existence for initial data close to an equilibrium state, see [88, 89]. Without this assumption on the initial data one still can guarantee the existence of solutions, but just up to some time $t \in (0, T]$, which can be arbitrarily small, see Valli [127, 128] and Tani [121].

Since the world is discontinuous and real-world phenomena which are modeled by the Navier-Stokes equations may exhibit nonsmooth behaviors (i.e., not all of the required

derivatives of the solution exist), it is actually reasonable to consider also weak solutions. For the weak formulation, there exist results for the case when the pressure p is given through the isentropic state equation

$$p = p(\rho) = a\rho^\gamma \quad \text{with} \quad a > 0, \gamma > 1, \tag{3.19}$$

whereas the physically relevant values of γ are $\gamma \in (1, 5/3]$. Thereby isentropic means that the entropy does not change for a process that is internally reversible and adiabatic (no heat or mass transfer with the surroundings).

In 1998, Lions proved the existence of a global-in-time weak solution of (3.16), (3.17) with (3.19) and $\gamma \geq 9/5$ without the assumption that the initial data is close to an equilibrium state, see [76]. A few years later, Feireisl, Novotný and Petzeltová improved the result to the case where $\gamma > 3/2$, see [39].

For the measure-valued case, Feireisl, Gwiazda, Świerczewska-Gwiazda, and Wiedemann showed that there exists a global-in-time measure-valued solution of (3.16), (3.17) for a class of pressure state equations including (3.19) with $\gamma \geq 1$.

Feireisl and Lukáčová-Medvid'ová proved in [33] the existence of a measure-valued solution by a convergence analysis of a numerical scheme from [32] which was developed by Karlsen and Karper, cf. [56, 57, 58, 59], for (3.16), (3.17) with (3.19) and $\gamma \in (6/5, 2)$ (which is a correction to $\gamma \in (1, 2)$ as stated in their paper). In [36], the existence of dissipative measure-valued solutions for the barotropic Navier-Stokes equations with $\gamma \geq 1$ was obtained by the finite volume method. This result was recently generalized in [37] to the full Navier-Stokes-Fourier system including the energy equation. Note that the authors were able to work with the state equation of a perfect gas. In the case of the Navier-Stokes-Fourier system, the global-in-time existence of weak solutions is available only for a specific pressure law, see [38].

We also refer to [109], where the existence of a measure-valued solution to (M1.a) with $\mu_h = 0 = S_\theta$ and no gravity force has been proven for $\gamma > 1$.

In [83], the global existence of a weak solution of a Navier-Stokes system comparable to our system (2.48) was proven for $\gamma > \frac{3}{2}$. Differences to our system are the formulation in terms of pressure instead as in our case in potential temperature and also that heat conductivity effects (the viscous term in our potential temperature equation) are neglected.

3.3.3 Full PDE cloud model coupled to primitive equations for the atmosphere

In [51], the authors show the global well-posedness of strong solutions for the primitive equations for the atmosphere

$$\begin{aligned} (\boldsymbol{u}_{1,2})_t + (\boldsymbol{u}_{1,2} \cdot \nabla_{x_1,x_2})\, \boldsymbol{u}_{1,2} + u_3\, (\boldsymbol{u}_{1,2})_p + \nabla_{x_1,x_2}\Phi + f(\boldsymbol{e_3} \times \boldsymbol{u})_{1,2} &= \mathcal{D}^{\boldsymbol{u}_{1,2}}\boldsymbol{u}_{1,2}, \\ \Phi_p + \frac{RT}{p} &= 0, \\ \nabla_{x_1,x_2} \cdot \boldsymbol{u}_{1,2} + (u_3)_p &= 0, \end{aligned} \tag{3.20}$$

written in pressure coordinates (x_1, x_2, p), coupled to a PDE model for warm clouds

$$\begin{aligned}
(q_v)_t + \boldsymbol{u}_{1,2} \cdot \nabla_{x_1,x_2} q_v + u_3 (q_v)_p &= S_E - S_C + \mathcal{D}^{q_v} q_v, \\
(q_c)_t + \boldsymbol{u}_{1,2} \cdot \nabla_{x_1,x_2} q_c + u_3 (q_c)_p &= S_C - S_{A_1} - S_{A_2} + \mathcal{D}^{q_c} q_c, \\
(q_r)_t + \boldsymbol{u}_{1,2} \cdot \nabla_{x_1,x_2} q_r + u_3 (q_r)_p + V \left(\frac{p}{R\bar{T}} q_r \right)_p &= S_{A_1} + S_{A_2} - S_E + \mathcal{D}^{q_r} q_r.
\end{aligned} \tag{3.21}$$

Here, the operator

$$\mathcal{D}^* = \mu_* \Delta_{x_1,x_2} + \nu_* \partial_p \left(\left(\frac{gp}{R\bar{T}} \right)^2 \partial_p \right)$$

is a close approximation to the full Laplacian in Cartesian coordinates and is used for the eddy viscosity closure of turbulence and molecular transport, see [122]. Moreover, the subscript $*_{1,2}$ denotes the two first components of a vector, Φ with $\Phi_{x_3} = g$ is the geopotential, f corresponds to the Coriolis force, V is the terminal velocity of falling rain and is assumed to be constant. The terms S_E, S_C, S_{A_1}, S_{A_2} are, respectively, the rates of evaporation, condensation, autoconversion and the accretion from the setting of Klein and Majda in [63]. The considered equation for changes in temperature takes into account the effect of latent heat in association with phase changes, cf. [51].

The considered system for warm cloud dynamics (3.21) is very similar to our system (M1.b) and also the primitive equation (3.20) model compressible dynamics of the atmosphere as our considered Navier-Stokes equations (M1.a). A major difference to our model is the neglect of the difference of the gas constants for dry air and water vapor as well as the dependence of the internal energy on the moisture components via different heat capacities. Our moisture model has a stronger coupling of the thermodynamic equation to the moisture components and provides a refined thermodynamical setting which can be essential in some cases, for example, the deep convection of clouds, see [50]. The authors mention this in Remark 1 of [51] and plan to investigate also the resulting moist model in a forthcoming paper.

4 Implicit-explicit finite volume method for the deterministic model

In this chapter, we will introduce the numerical scheme we chose for the deterministic model (M1). The complete scheme will be formulated in Section 4.3, where we will begin by writing the system into an operator form in Subsection 4.3.1, because the operators will be approximated differently in space as well as in time. For the spatial discretization we apply finite volume methods for both the Navier-Stokes equations (M1.a) and the cloud equations (M1.b), see Subsection 4.3.2. For the time discretization an implicit-explicit Runge-Kutta method is used for the Navier-Stokes equations (M1.a) and an explicit Runge-Kutta method with enlarged stability domain, the DUMKA3 method, for the cloud equations (M1.b), see Subsection 4.3.3. The prerequisites for the methods above are covered in the sections at the beginning of this chapter.

We start with Section 4.1, where we introduce general finite volume methods giving detailed descriptions of both the upwind, see Subsection 4.1.1, and the central scheme approach, see Subsection 4.1.2. In Subsection 4.1.3, we present how a general Godunov type scheme can be summarized by reconstruction-evolution-averaging steps and how the scheme can achieve a higher order of accuracy. To obtain a high-resolution method for nonlinear equations, typically a semi-discrete formulation is used which can be written as an ODE and is introduced in Subsection 4.1.4. Thus, in Section 4.2 we will briefly summarize some fundamentals of time discretization for ODEs. We introduce the Runge-Kutta methods in Subsection 4.2.1 and the Strang operator splitting approach in Subsection 4.2.2 which will allow us to use different time integration methods for the Navier-Stokes equations (M1.a) and the cloud equations (M1.b). We then explain the idea behind implicit-explicit methods in Subsection 4.2.3 which couple a diagonally implicit Runge-Kutta scheme to an explicit Runge-Kutta scheme. In Subsection 4.2.4, we introduce an explicit Runge-Kutta method with an extended stability region which is third-order consistent in time, the DUMKA3 method. Since our choice for the time integration method requires solving linear systems in each time step, we present in Subsection 4.2.5 our choice for the linear solver. In Subsection 4.2.6, we briefly make some comments on restrictions for choosing the length of the time steps.

4.1 Finite volume methods

The numerical scheme we propose for (M1) employs a finite volume approach for both the Navier-Stokes equations (M1.a) and the microphysical cloud equations (M1.b). Here, we will briefly introduce the finite volume framework for nonlinear hyperbolic equations. For simplicity, we will restrict ourselves to the scalar case. The content of this section is based on lecture notes of Mishra, see [93], and Chertock, see [20]. For further details we refer to some classical books, such as [40, 75, 124].

We consider the following nonlinear conservation law in 1D

$$w_t + F(w)_x = 0 \tag{4.1}$$

subject to prescribed initial data

$$w(x,0) = w_0(x). \tag{4.2}$$

Here x is a space variable, $t > 0$ is time, $w = w(x,t)$ is an unknown quantity in $\mathbb{R}$ and $F(w)$ is a flux function.

Example 4.1
If $F(w) = aw$ for a constant a, then (4.1) becomes the linear transport equation

$$w_t + aw_x = 0. \tag{4.3}$$

Example 4.2
For $F(w) = \frac{1}{2}w^2$ one ends up with the inviscid Burgers' equation

$$w_t + \frac{1}{2}(w^2)_x = 0.$$

Solutions of (4.1) with (4.2) may develop nonsmooth structures such as shock waves, contact discontinuities, rarefaction waves or singular δ-shocks – even when one starts with infinitely differentiable initial data (4.2). Therefore, the numerical approximation is somewhat delicate. Nevertheless, the scalar case (4.1) is nowadays analytically and numerically well understood. For more general situations, for example, systems of hyperbolic conservations laws, there are still many open problems in particular concerning the well-posedness of weak solutions, see [75].

In general, a finite volume method is based on dividing the spatial domain into subintervals and approximating the integral of the exact solution w of (4.1) with (4.2) over these finite volumes. In each step, these integrals are updated using approximations for the flux through the interfaces of the intervals.

We first introduce a finite volume mesh for a one-dimensional domain $\Omega = (a,b) \subset \mathbb{R}$ by dividing it into $N \in \mathbb{N}$ uniform Cartesian cells

$$C_i = (x_{i-\frac{1}{2}}, x_{i+\frac{1}{2}}), \quad i = 1, \dots, N, \tag{4.4}$$

for which $\bigcup_{i=1}^{N} \overline{C_i} = \overline{\Omega}$ holds. Thereby, the corresponding cell midpoints and interfaces are defined as

$$x_i = a + \sum_{j=1}^{i-1} h + \frac{h}{2}, \quad x_{i\pm\frac{1}{2}} = x_i \pm \frac{h}{2}, \quad i = 1, \dots, N,$$

where $h = 2|x_1 - a|$ is the grid size which is constant for uniform cells.

In the finite volume setup, we integrate the conservation law (4.1) over the space-time control volume $C_i \times (t^n, t^{n+1})$, where t^n is a discrete time level and $t^{n+1} = t^n + \Delta t^n$, for some time step Δt^n. This leads to

$$\int_{t^n}^{t^{n+1}} \int_{C_i} w_t(x,t)\,\mathrm{d}x\mathrm{d}t + \int_{t^n}^{t^{n+1}} \int_{C_i} F(w(x,t))_x\,\mathrm{d}x\mathrm{d}t = 0$$

$$\Leftrightarrow \quad \int_{C_i} \left[w(x,t^{n+1}) - w(x,t^n)\right]\,\mathrm{d}x + \int_{t^n}^{t^{n+1}} \left[F\left(w(x_{i+\frac{1}{2}},t)\right) - F\left(w(x_{i-\frac{1}{2}},t)\right)\right]\,\mathrm{d}t = 0.$$

Rearranging and dividing the above equation by h gives

$$\frac{1}{h}\int_{C_i} w(x,t^{n+1})\,\mathrm{d}x = \frac{1}{h}\int_{C_i} w(x,t^n)\,\mathrm{d}x - \frac{1}{h}\int_{t^n}^{t^{n+1}} \left[F\left(w(x_{i+\frac{1}{2}},t)\right) - F\left(w(x_{i-\frac{1}{2}},t)\right)\right]\,\mathrm{d}t.$$

The space integrals can now be rewritten by introducing the sliding averages of w which are given by

$$w_i(t^n) := \frac{1}{h}\int_{C_i} w(x,t^n)\,\mathrm{d}x \tag{4.5}$$

leading to

$$w_i(t^{n+1}) = w_i(t^n) - \frac{1}{h}\int_{t^n}^{t^{n+1}} \left[F\left(w(x_{i+\frac{1}{2}},t)\right) - F\left(w(x_{i-\frac{1}{2}},t)\right)\right]\,\mathrm{d}t. \tag{4.6}$$

Defining the averaged fluxes

$$H^n(x_{i+\frac{1}{2}}) := \frac{1}{\Delta t^n}\int_{t^n}^{t^{n+1}} F(w(x_{i+\frac{1}{2}},t))\,\mathrm{d}t$$

and inserting them in (4.6) results in the following formulation

$$w_i(t^{n+1}) = w_i(t^n) - \frac{\Delta t^n}{h}\left[H^n(x_{i+\frac{1}{2}}) - H^n(x_{i-\frac{1}{2}})\right]. \tag{4.7}$$

The question that remains is how to compute the averaged fluxes in the above equation. There are two main possibilities, either one chooses an upwind or a central scheme. In the following subsections, we will present both of the approaches. To begin with, we consider first-order approximations and afterward we explain how to obtain higher-order approximations.

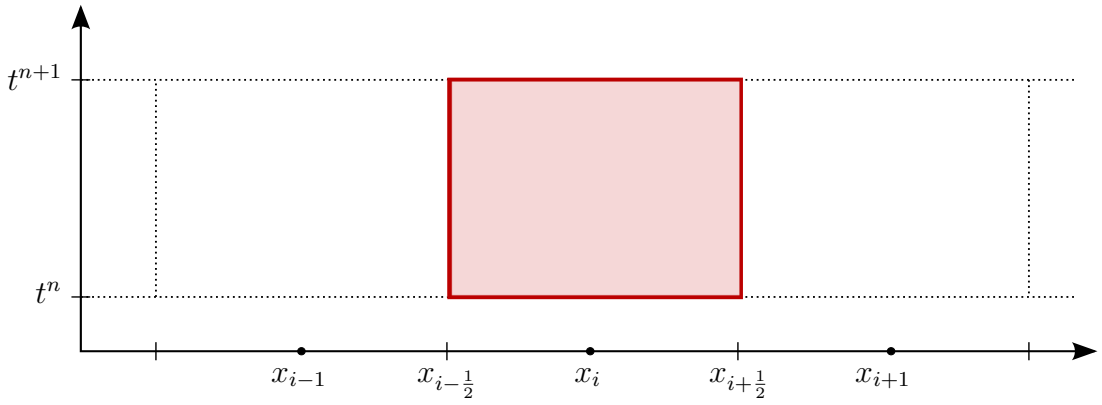

Figure 4.1: The space-time control volume in an upwind scheme.

4.1.1 First-order upwind schemes

To determine the averaged fluxes in (4.7), the space-time control volume $C_i \times [t^n, t^{n+1}]$, cf. Figure 4.1, is used. By denoting

$$w_i^n \approx w_i(t^n) \quad \text{and} \quad H_{i+\frac{1}{2}}^n \approx H^n(x_{i+\frac{1}{2}}) = \frac{1}{\Delta t^n} \int_{t^n}^{t^{n+1}} F(w(x_{i+\frac{1}{2}}, t))\,\mathrm{d}t,$$

we obtain for (4.7) the following approximation

$$w_i^{n+1} = w_i^n - \frac{\Delta t^n}{h}\left[H_{i+\frac{1}{2}}^n - H_{i-\frac{1}{2}}^n\right].$$

The first finite volume upwind scheme was proposed by Godunov in 1959, see [44], and is called the Godunov method today. The idea is the following: Since the cell averages w_i^n are constant in each cell C_i at each time level t^n, cf. Figure 4.2, they define at each cell interface $x_{i+1/2}$ the following Riemann problem

$$\begin{cases} w_t + F(w)_x = 0, \\ \qquad w(x, t^n) = \widetilde{w}^n(x) := \begin{cases} w_i^n, & x < x_{i+\frac{1}{2}}, \\ w_{i+1}^n, & x > x_{i+\frac{1}{2}}, \end{cases} \end{cases}$$

for $i = 1, \ldots, N$. In our scalar case, this Riemann problem can be solved analytically in terms of waves (shocks, rarefaction waves and contact discontinuities) by using the method of characteristics. Characteristics are lines along which the solution remains constant in the space-time plane. When these characteristic lines intersect, shocks are formed and when they separate forming a fan, one ends up with a rarefaction wave. Thus, at each cell interface we approximate the point value $w(x_{i+1/2}, t^n)$ by the self-similar solution w^{RP} of the respective Riemann problem,

$$w(x_{i+\frac{1}{2}}, t^n) \approx w^{RP}(x_{i+\frac{1}{2}}),$$

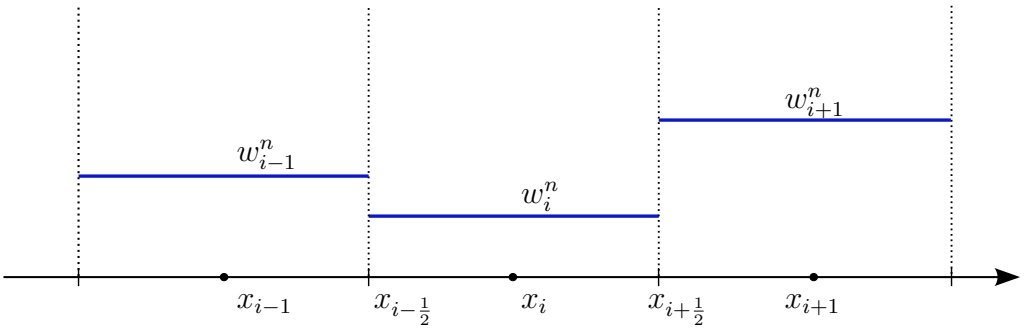

Figure 4.2: Constant cell averages of the solution at time t^n.

and compute the fluxes through

$$H^n_{i+\frac{1}{2}} \approx \frac{1}{\Delta t^n} \int_{t^n}^{t^{n+1}} F\left(w^{RP}(x_{i+\frac{1}{2}})\right) \mathrm{d}t = F\left(w^{RP}(x_{i+\frac{1}{2}})\right).$$

Example 4.3
For the linear transport equation (4.3) with $a > 0$ we can easily see that the Godunov flux reduces to the so-called upwind flux given by

$$H^n_{i+\frac{1}{2}} = F(w^n_i).$$

Remark 4.1*:* Waves from neighboring Riemann problems might intersect after some time, see Figure 4.3. To avoid this, one has to choose the time step Δt^n in such a way that waves from neighboring Riemann problems do not interact before reaching the next time level. This is done by imposing the following Courant-Friedrichs-Lewy (CFL) condition

$$\max_i \left|F'\left(w^n_i\right)\right| \frac{\Delta t^n}{h} \leq \frac{1}{2},$$

which will be discussed in more detail in Subsection 4.2.6. Here $\max_i \left|F'\left(w^n_i\right)\right|$ is the upper bound for the wave speed of any Riemann problem since each wave has a finite speed of propagation.

The Godunov scheme has many desirable properties and is a clever idea to approximate fluxes. However, it has some drawbacks. First of all, it relies on the availability of an explicit formula for the solution of the Riemann problem at the cell interfaces. For scalar conservation laws such formulas are known, but for systems of general conservation laws this is not necessarily the case. Another point is that one only needs the value of the flux at the cell interfaces to compute the numerical fluxes. It is quite an effort to solve an entire Riemann problem at each cell interface to achieve this.

4.1.2 First-order central schemes

A first-order central scheme is a Godunov-type scheme that is obtained using (4.7), but sampled at the points $(x_{i+1/2}, t^n)$ instead of (x_i, t^n). The difference to the upwind setting

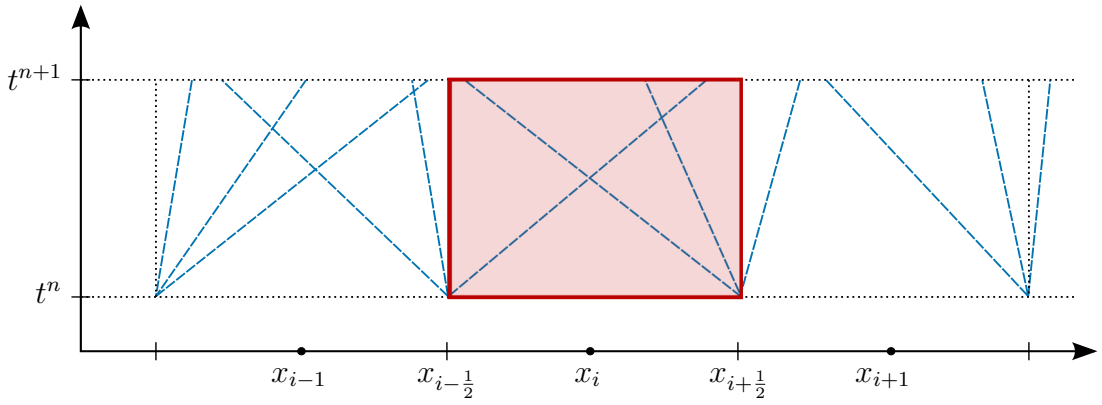

Figure 4.3: Intersecting characteristics of the Riemann problems in an upwind scheme.

is that here the space-time control volume is shifted by $h/2$, i.e. $[x_i, x_{i+1}] \times [t^n, t^{n+1}]$ as can be seen in Figure 4.4. The data at the discrete time t^n are still given over the original grid cells C_i as in (4.4), but the newly computed solution will be realized over the staggered grid.

We do the same computation as for the upwind scheme just with the shifted control volume and end up with

$$w_{i+\frac{1}{2}}^{n+1} = \frac{1}{h} \int_{x_i}^{x_{i+1}} \widetilde{w}^n(x)\,\mathrm{d}x - \frac{1}{h} \int_{t^n}^{t^{n+1}} \left[F\left(w(x_{i+1}, t)\right) - F\left(w(x_i, t)\right)\right] \mathrm{d}t, \tag{4.8}$$

where

$$w_{i+\frac{1}{2}}^{n+1} \approx w_{i+\frac{1}{2}}(t^{n+1}) := \frac{1}{h} \int_{x_i}^{x_{i+1}} w(x, t^{n+1})\,\mathrm{d}x$$

and $\widetilde{w}^n(x)$ is a piecewise constant function built from the cell averages through

$$\widetilde{w}^n(x) = \begin{cases} w_i^n, & x < x_{i+\frac{1}{2}}, \\ w_{i+1}^n, & x > x_{i+\frac{1}{2}}. \end{cases} \tag{4.9}$$

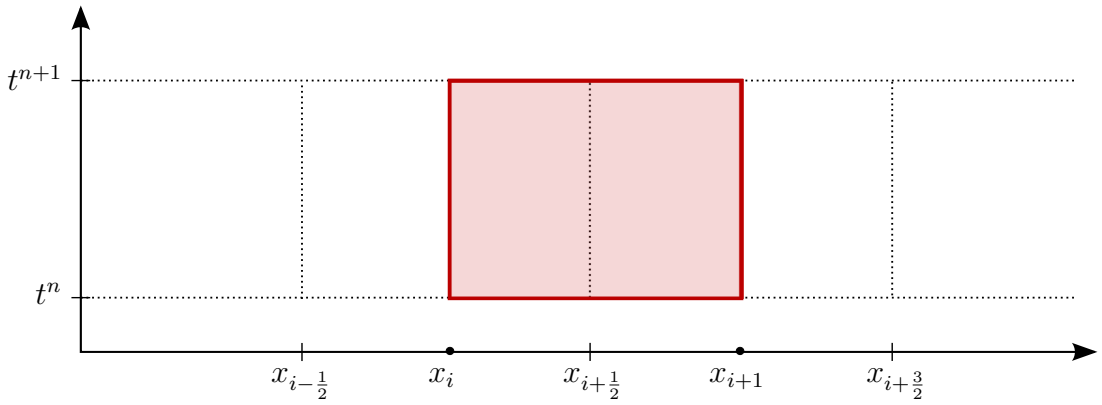

Figure 4.4: The space-time control volume in a central scheme.

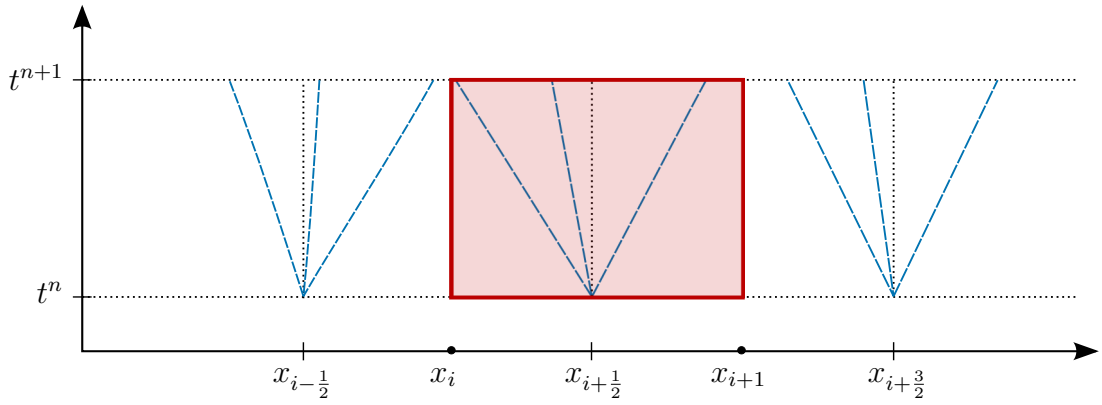

Figure 4.5: The characteristics in a central scheme.

The space integral can be exactly evaluated in a straightforward manner and is given through

$$\frac{1}{h}\int_{x_i}^{x_{i+1}} \widetilde{w}^n(x)\,\mathrm{d}x = \frac{w_{i+1}^n + w_i^n}{2}.$$

As long as a proper time step restriction is chosen and no waves generated at the cell interfaces intersect, see Figure 4.5, the solution remains constant at the space points x_i. From the latter, it follows that

$$\frac{1}{h}\int_{t^n}^{t^{n+1}} \left[F\left(w(x_{i+1},t)\right) - F\left(w(x_i,t)\right)\right]\,\mathrm{d}t = \frac{\Delta t^n}{h}\left[F\left(w_{i+1}^n\right) - F\left(w_i^n\right)\right].$$

Using (4.8), the above equation can be written as

$$w_{i+\frac{1}{2}}^{n+1} = \frac{w_{i+1}^n + w_i^n}{2} - \frac{\Delta t^n}{h}\left[F\left(w_{i+1}^n\right) - F\left(w_i^n\right)\right] \tag{4.10}$$

which is the *staggered Lax-Friedrichs* scheme. By averaging the solution at the next time level t^{n+1} over each cell C_i and using (4.10), we get

$$\begin{aligned} w_i^{n+1} &= \frac{w_{i+\frac{1}{2}}^{n+1} + w_{i-\frac{1}{2}}^{n+1}}{2} \\ &= \frac{w_{i+1}^n + w_i^n + w_i^n + w_{i-1}^n}{4} - \frac{\Delta t^n}{2h}\left[F\left(w_{i+1}^n\right) - F\left(w_i^n\right) + F\left(w_i^n\right) - F\left(w_{i-1}^n\right)\right] \\ &\approx \frac{w_{i+1}^n + w_{i-1}^n}{2} - \frac{\Delta t^n}{2h}\left[F\left(w_{i+1}^n\right) - F\left(w_{i-1}^n\right)\right], \end{aligned}$$

where in the last step w_i^n is replaced and thus approximated by the average $\frac{w_{i+1}^n + w_{i-1}^n}{2}$ due to stability reasons. The scheme can be written equivalently in the following conservative form

$$w_i^{n+1} = w_i^n - \frac{\Delta t^n}{h}\left[H^n(x_{i+\frac{1}{2}}) - H^n(x_{i-\frac{1}{2}})\right],$$

where

$$H^n(x_{i+\frac{1}{2}}) = H^{\mathrm{LxF}}(w^n_{i+1}, w^n_i) = \frac{F\left(w^n_{i+1}\right) + F\left(w^n_i\right)}{2} - \frac{h}{2\Delta t^n}\left(w^n_{i+1} - w^n_i\right)$$

is the well-known Lax-Friedrichs numerical flux, see [75]. For our cloud model we will use the *Rusanov* (or *local Lax-Friedrichs*) numerical flux

$$\begin{aligned} H^n(x_{i+\frac{1}{2}}) &= H^{\mathrm{Rus}}(w^n_{i+1}, w^n_i) \\ &= \frac{F\left(w^n_{i+1}\right) + F\left(w^n_i\right)}{2} - \frac{\max(|F'(w^n_{i+1})|, |F'(w^n_i)|)}{2}\left(w^n_{i+1} - w^n_i\right) \end{aligned} \tag{4.11}$$

which considers local wave speeds and thus is less diffusive than the original Lax-Friedrichs flux, see [16, 93] and references therein.

A big advantage of the central schemes is that they do not depend on the structure of the eigenvalues of the problem. In particular, one does not have to solve any Riemann problems. Thus, they can be easily applied to systems of conservation laws which is the reason why we chose them for the approximation of (M1) in Section 4.3.

4.1.3 REA algorithm and higher order schemes

A general Godunov-type scheme, which includes the ones presented in the previous Sections 4.1.1 and 4.1.2, can be summarized by the following reconstruction-evolution-averaging (REA) steps.

We start at time level t^n, where on each cell $C_i = (x_{i-1/2}, x_{i+1/2})$, $i = 1, \dots, N$, we have the approximated cell average

$$w^n_i \approx \frac{1}{h}\int_{C_i} w(x, t^n)\,\mathrm{d}x.$$

- **Reconstruction**: The global solution $\widetilde{w}^n(x)$, cf. (4.9), is reconstructed from the cell averages.
- **Evolution**: The reconstructed solution is evolved in time using either an exact or an approximate solution of the conservation law.
  - *Upwind schemes*: Solve the Riemann problems at the cell interfaces

    $$w_t + F(w)_x = 0, \quad w(x, t^n) = \widetilde{w}^n(x).$$

  - *Central schemes*: Compute the shifted averages

    $$w^{n+1}_{i+\frac{1}{2}} = \frac{1}{h}\int_{x_i}^{x_{i+1}} \widetilde{w}^n(x)\,\mathrm{d}x - \frac{1}{h}\int_{t^n}^{t^{n+1}} \left[F\left(w(x_{i+1}, t)\right) - F\left(w(x_i, t)\right)\right]\mathrm{d}t.$$

- **Averaging**: Average the solution at the next time level t^{n+1} over each cell C_i, $i = 1, \dots, N$.

Most of the finite volume schemes can be obtained from the REA algorithm by a suitable approximation and adaption of the evolution step.

So far, $\widetilde{w}^n(x)$ was a piecewise constant function, cf. Figure 4.2, which was built from the cell averages w_i^n. It is a piecewise constant interpolation and thus results in a first-order scheme in space. To achieve a higher-order accuracy, one can employ higher-order reconstructions. We will use a second-order accurate scheme which means that we change the reconstruction step by replacing the piecewise constant function $\widetilde{w}^n(x)$ with a piecewise linear function, see Figure 4.6. This approach is called Monotonic Upstream-Centered Scheme for Conservation Laws (MUSCL). It was introduced by van Leer in [131].

Now, the piecewise linear solution $\widetilde{w}^n(x)$ is given as

$$\widetilde{w}^n(x) = \sum_{i=1}^{N} \chi_{C_i}(w_i^n + s_i^n(x - x_i)), \tag{4.12}$$

where s_i^n is the slope and χ_{C_i} is the characteristic function on cell C_i. This ensures that the reconstruction step is conservative, meaning

$$\frac{1}{h}\int_{C_i} \widetilde{w}^n(x)\,\mathrm{d}x = w_i^n, \quad i = 1, \dots, N.$$

For the slopes s_i^n in the linear reconstruction (4.12) one has a variety of choices, for example the following straightforward ones

- central: $s_i^n = \frac{w_{i+1}^n - w_{i-1}^n}{2h}$,
- backward: $s_i^n = \frac{w_i^n - w_{i-1}^n}{h}$,
- forward: $s_i^n = \frac{w_{i+1}^n - w_i^n}{h}$.

Near extrema and discontinuities of the solution in high resolutions, these choices for the slopes exhibit oscillations due to over- and undershooting of the interface reconstruction

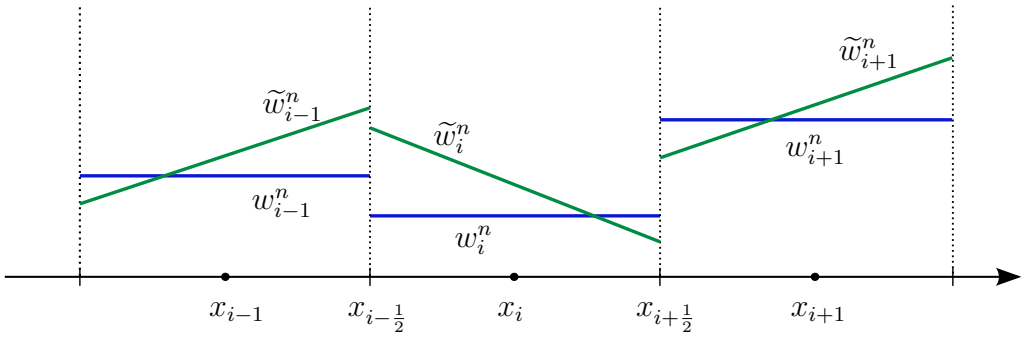

Figure 4.6: Piecewise constant w^n (in blue) and piecewise linear reconstructions $\widetilde{w}^n$ (in green) of the solution at time t^n.

and ultimately lead to numerical instabilities. Thus, slope limiters were proposed to ensure a nonoscillatory scheme. We will consider the following minmod limiter

$$s_i^n = \frac{1}{h}\text{minmod}\left(w_{i+1}^n - w_i^n, w_i^n - w_{i-1}^n\right), \tag{4.13}$$

where the minmod function is defined as

$$\text{minmod}(a,b) = \begin{cases} a, & \text{if } |a| < |b| \text{ and } ab > 0, \\ b, & \text{if } |b| < |a| \text{ and } ab > 0, \\ 0, & \text{if } ab \leq 0. \end{cases} \tag{4.14}$$

The minmod limiter (4.14) compares the backward and the forward slope and selects the smallest one if they are of the same sign. If they have different signs, it sets the slope to zero. Thus, the limiter avoids oscillations and the linear reconstructions are limited by the local gradients.

4.1.4 Semi-discrete formulation

To obtain a high-resolution method for nonlinear equations, one typically uses a semi-discrete formulation of the conservation law (4.1). For that, the previously described reconstructions (4.12) are still used, but the REA algorithm is not fully applied. We integrate the conservation law (4.1) again, but this time just over space, to obtain

$$0 = \frac{1}{h}\int_{C_i} (w_t + F(w)_x)\,\mathrm{d}x \approx \frac{\mathrm{d}}{\mathrm{d}t}w_i(t) + \frac{F\left(w_{i+\frac{1}{2}}^-(t)\right) - F\left(w_{i-\frac{1}{2}}^+(t)\right)}{h}, \tag{4.15}$$

where $w_i(t)$ are the sliding averages as defined in (4.5) and $w_{i+\frac{1}{2}}^-$, $w_{i+\frac{1}{2}}^+$ are the interface reconstructions of the solution from the left and the right

$$w_{i+\frac{1}{2}}^-(t) = w_i(t) + s_i\frac{h}{2}, \quad w_{i+\frac{1}{2}}^+(t) = w_{i+1}(t) - s_{i+1}\frac{h}{2}.$$

The fluxes are then approximated by numerical fluxes $H_{i+\frac{1}{2}}^\pm(t) \approx F(w_{i+\frac{1}{2}}^\pm(t))$, which in our case will be the Rusanov flux (4.11). To achieve a higher accuracy of the scheme, the numerical flux function is evaluated at the interface reconstructions instead of the cell averages, i.e.

$$H_{i+\frac{1}{2}}^+(t) = H_{i+\frac{1}{2}}^-(t) = H_{i+\frac{1}{2}}^{\text{Rus}}\left(w_{i+\frac{1}{2}}^-(t), w_{i+\frac{1}{2}}^+(t)\right).$$

The semi-discrete formulation (4.15) then reads

$$\frac{\mathrm{d}}{\mathrm{d}t}w_i(t) + \frac{H_{i+\frac{1}{2}}(t) - H_{i-\frac{1}{2}}(t)}{h} = 0. \tag{4.16}$$

Introducing the vector

$$\boldsymbol{w}_h(t) := [w_1(t), \ldots, w_N(t)]^\top,$$

the semi-discrete finite volume scheme (4.16) can be written as the following ODE

$$\frac{\mathrm{d}}{\mathrm{d}t}\boldsymbol{w}_h(t) = \mathcal{A}\left(\boldsymbol{w}_h(t)\right), \tag{4.17}$$

where $\mathcal{A}$ acts pointwise on $\boldsymbol{w}_h(t)$ and is given through

$$\mathcal{A}\left(\boldsymbol{w}_h(t)\right)_i := -\frac{H_{i+\frac{1}{2}}(t) - H_{i-\frac{1}{2}}(t)}{h}.$$

The spatial accuracy of the scheme (4.17) is then given by the following definition.

Definition 4.1
Let $w(x,t)$ be the solution of PDE (4.1). The method (4.17) is *consistent of order p in space*, if

$$\frac{\mathrm{d}}{\mathrm{d}t}w(t) = \mathcal{A}\left(w(t)\right) + \mathcal{O}(h^p), \quad t \in [0,T].$$

Here the operator $\mathcal{A}$ is evaluated at $w(x_i,t)$, $i = 1,\dots,N$.

Since we mostly have a local truncation error of second-order due to the linear reconstruction (4.12) (except in regions near extrema and discontinuities where the numerical fluxes reduce due to the flux limiter, see (4.13), to a first-order approximation), we expect the above spatial error to be of second order. This will be confirmed in our experimental convergence study in Section 6.1. Theoretical investigations concerning the error estimates for hyperbolic conservation laws can be found, e.g., in [133] for scalar hyperbolic conservation laws and in [28] for the Euler equations.

The advantage of the semi-discrete formulation (4.16) is that we can separately increase the order of spatial and temporal accuracy, cf. Definition 4.22. With our piecewise linear reconstruction we achieve a second-order spatial accuracy. The temporal evolution of (4.16) will be discussed in Section 4.2.

Remark 4.2*:* Up to now, we have not yet discussed the boundary conditions. Since $\Omega = (a,b) \subset \mathbb{R}$ is bounded, suitable boundary conditions need to be imposed. For that we define the following *ghost cells*

$$C_0 = (a-h, a), \quad C_{N+1} = (b, b+h)$$

and denote by w_0^n and w_{N+1}^n the cell averages at time level t^n, cf. (4.5), of the unknown quantity over the cells C_0 and C_{N+1}, respectively.

In this thesis, we consider the following boundary conditions:

- Periodic: Objects passing through one end of the domain re-appear on the opposite end with the same velocity. This is implemented through

$$w_0^n = w_N^n \quad \text{and} \quad w_{N+1}^n = w_1^n. \tag{4.18}$$

- Dirichlet: Here, fixed values of the unknown quantity are prescribed at the boundary which in our case will stay constant in time. This is realized through

$$w_1^n = w(a,0) \quad \text{and} \quad w_N^n = w(b,0). \tag{4.19}$$

  In this case, we do not use the ghost cells.

- Zero Neumann: In this case, one prescribes the derivatives in the direction of the outer normal vector to be zero, i.e., there is no flux exiting the domain. Denoting the velocity by $\boldsymbol{w} = (u_1, \dots, u_d)$, we implement this through

$$\boldsymbol{w}_0^n \cdot \boldsymbol{n} = \boldsymbol{w}_1^n \cdot \boldsymbol{n} \quad \text{and} \quad \boldsymbol{w}_{N+1}^n \cdot \boldsymbol{n} = \boldsymbol{w}_N^n \cdot \boldsymbol{n}. \tag{4.20}$$

- No-slip: In this case, one assumes a solid boundary at which the fluid velocity is zero. Denoting the velocity by $\boldsymbol{w} = (u_1, \dots, u_d)$, this condition is realized by setting

$$\boldsymbol{w}_0^n \cdot \boldsymbol{n} = -\boldsymbol{w}_1^n \cdot \boldsymbol{n} \quad \text{and} \quad \boldsymbol{w}_{N+1}^n \cdot \boldsymbol{n} = -\boldsymbol{w}_N^n \cdot \boldsymbol{n} \tag{4.21}$$

  which means that the mean velocity at the boundary is zero.

For a piecewise linear solution, see (4.12), one needs two ghost cells on each side because the slopes for the linear reconstructions on the ghost cells adjacent to the boundary need to be computed. The implementation of the respective boundary condition can easily be extended from the above implementation with only one ghost cell.

Remark 4.3*:* The central scheme (4.16) can be extended straightforwardly to higher dimensions and to advection-diffusion-reaction equations of the form

$$w_t + F(w)_x = Dw_{xx} + S(w),$$

where S is a source term and D a diffusion coefficient. This extension will be presented in Section 4.3 for the deterministic cloud model (M1). The linear advection is then approximated as introduced here with the Rusanov numerical flux, the nonlinear advection by a central difference evaluation of the fluxes, the second derivatives by central finite differences and the source terms by evaluating at the cell averages.

4.2 Fundamentals of time discretization

In this section, we summarize some basics of numerical methods for ODEs, which we will use to solve (4.17) in a stable way and with an appropriate order. The content of this section is based on the lecture notes [93] and [20], as well as on [65].

Before we present some time integration schemes, we define similarly as for the semi-discrete scheme, cf. Definition 4.1, the order of accuracy. The time axis is discretized by choosing time instances t^n, $n = 0, 1, 2, \dots$, and introducing the corresponding time step sizes $\Delta t^n = t^{n+1} - t^n$. Then the numerical solution at t^n will be denoted as $\boldsymbol{w}_h^n \approx \boldsymbol{w}_h(t^n)$.

Definition 4.2
Let $\boldsymbol{w}_h(t)$ denote the exact solution of the semi-discrete equation (4.17) and $\boldsymbol{w}_h^1$ the numerical solution of (4.17) after one time step of length $\Delta t = \Delta t^n$. Assuming that both start with the same arbitrary initial data $\boldsymbol{w}_h(t^0) = \boldsymbol{w}_h^0$, the method is *consistent of order q in time* if the following holds

$$|w_i(\Delta t) - w_i^1| = \mathcal{O}((\Delta t)^{q+1}). \tag{4.22}$$

Assuming a linear problem with a linear semi-discrete scheme (4.17) which is consistent of order p in space, see Definition 4.1, and consistent of order q in time, the error in time and space behaves as

$$|w(x_i, t^n) - w_i^n| \leq C_1 h^p + C_2 \tau^q, \quad i = 1, \dots, N, \ n = 0, 1, \dots, \tag{4.23}$$

where $\tau = \max_n \Delta t^n$, see for example [74]. If the numerical method is stable, it follows with the Lax equivalence theorem, see [74], that also the global error – and thus the convergence – is of order p in space and q in time. Here, stability of the numerical methods means that if the initial data $\boldsymbol{w}_h^0$ are bounded, then also $\boldsymbol{w}_h^n$ is bounded for all $n \in \mathbb{N}$. For nonlinear systems there exist also some recent results. The convergence against a measure-valued solution is shown for the full and isentropic Euler system of a finite volume scheme in [34, 35], for the isentropic Navier-Stokes system of mixed finite element-finite volume scheme in [33], for the Navier–Stokes–Fourier system of a finite volume scheme in [37] and for the compressible Navier-Stokes system of a finite volume scheme in [36]. We also refer to [81], where the convergence against a measure-valued solution for (M1.a) with $\mu_h = 0 = S_\theta$ and no gravity force is shown for $\gamma > 1$. In these works, the consistency and stability is shown yielding the weak convergence to the dissipative measure-valued solutions. On the other hand, the dissipative measure-valued solutions are strong solutions, if the latter exists and then the convergence is strong.

The simplest time integration method to solve (4.17) is the *forward* or *explicit Euler* scheme

$$\boldsymbol{w}_h^{n+1} = \boldsymbol{w}_h^n + \Delta t^n \mathcal{A}(\boldsymbol{w}_h^n)$$

for which the time step Δt^n has to be chosen appropriately, see Subsection 4.2.6. However, the explicit Euler method is first-order accurate in time and thus leads to an overall first-order accuracy of the fully discrete scheme which negates the advantage of a piecewise linear reconstruction (4.12) in space, see (4.23). Therefore, we will employ a higher-order time integration method. Here, the standard schemes are the Runge-Kutta methods which will be introduced in the next subsection.

4.2.1 Runge-Kutta methods

Runge-Kutta methods are the most commonly used single-step integration methods to solve an ODE of the form (4.17). In this subsection, we will briefly introduce the scheme and give some comments on consistency and stability based on [49].

$$\begin{array}{c|c} \boldsymbol{c} & A \\ \hline & \boldsymbol{b}^\top \end{array} \quad = \quad \begin{array}{c|ccc} c_1 & a_{11} & \dots & a_{1s} \\ \vdots & \vdots & & \vdots \\ c_s & a_{s1} & \dots & a_{ss} \\ \hline & b_1 & \dots & b_s \end{array}$$

Table 4.1: Butcher tableau of a Runge-Kutta scheme with $A := (a_{ij})_{i,j=1}^s \in \mathbb{R}^{s\times s}$ and $\boldsymbol{b}, \boldsymbol{c} \in \mathbb{R}^s$.

A general s-stage Runge-Kutta scheme is given through

$$\begin{cases} \boldsymbol{w}_h^{n+1} = \boldsymbol{w}_h^n + \Delta t^n \sum_{j=1}^s b_j \boldsymbol{k}_j^n, \\ \quad \boldsymbol{k}_j^n = \mathcal{A}\left(t^n + c_j \Delta t^n,\ \boldsymbol{w}_h^n + \Delta t^n \sum_{\nu=1}^s a_{j\nu} \boldsymbol{k}_\nu^n \right), \quad j = 1, \dots, s, \end{cases}$$

for a given coefficient matrix $A := (a_{ij})_{i,j=1}^s \in \mathbb{R}^{s\times s}$, weights $\boldsymbol{b} \in \mathbb{R}^s$ and nodes $\boldsymbol{c} \in \mathbb{R}^s$. This method is often noted in a so-called Butcher tableau, see Table 4.1. The scheme is explicit if A is a strictly lower triangular matrix and it is consistent if certain algebraic equations hold for the coefficient matrix and the vectors $\boldsymbol{b}$ and $\boldsymbol{c}$. In particular, we briefly recall the following:

1) A Runge-Kutta scheme $(A, \boldsymbol{b}, \boldsymbol{c})$ is consistent of at least order 1 if

$$\sum_{j=1}^s b_j = 1. \tag{4.24}$$

2) It is consistent of at least order 2 if both (4.24) and

$$\sum_{j=1}^s b_j c_j = \frac{1}{2} \tag{4.25}$$

are satisfied.

In terms of stability one has the following terms to classify the schemes:

- **A-stability:** Let $\{y_i\}$ be approximations obtained with a numerical method for the test equation $y_t = \lambda y$, $y(0) = 1$ and $\lambda \in \mathbb{C}$. The method is called *A-stable* if for every $\lambda \in \mathbb{C}^- = \{\lambda : \mathrm{Re}\lambda \le 0\}$ the approximations with arbitrary but fixed step size $h > 0$ fulfill the inequality
$$|y_{i+1}| \le |y_i|$$
for all i.
- **L-stability:** Let now $\mathbb{1} = [1, \dots, 1]^\top \in \mathbb{R}^s$ and $\hat{\mathbb{C}} = \mathbb{C} \cup \{\infty\}$. The function
$$R : \hat{\mathbb{C}} \to \hat{\mathbb{C}}, \quad R(\zeta) = 1 + \zeta \boldsymbol{b}^\top (\mathrm{Id} - \zeta A)^{-1} \mathbb{1} \tag{4.26}$$

which is associated to a Runge-Kutta method $(A, \boldsymbol{b}, \boldsymbol{c})$ is called the *stability function*.

An A-stable Runge-Kutta method with stability function R is called *L-stable*, if R satisfies $\lim_{\zeta\to\infty} R(\zeta) = 0$.

It can be shown that A-stability is equivalent to

$$|R(\zeta)| \leq 1 \quad \text{for all } \zeta \in \mathbb{C}^-, \tag{4.27}$$

see [49]. The region $U = \{\zeta \in \mathbb{C} : |R(\zeta)| \leq 1\}$ is called *stability region* of the Runge-Kutta method.

4.2.2 The Strang splitting method

In this subsection, we will introduce the Strang operator splitting approach which was introduced by Strang in 1968, see [115]. The description will be based on [65].

In general, an operator splitting allows the use of different time integration methods for a system of ODEs. Thus, we assume that we have, analogous to (4.17) in the scalar case, the following semi-discrete scheme

$$\frac{\mathrm{d}}{\mathrm{d}t}\boldsymbol{w}_h(t) = \mathcal{A}_1(\boldsymbol{w}_h(t)) + \mathcal{A}_2(\boldsymbol{w}_h(t)) \tag{4.28}$$

derived for a system of PDEs. Let $\Xi_{\mathcal{F}}(\Delta t^n)$ be an approximation operator of the initial value problem

$$\frac{\mathrm{d}}{\mathrm{d}t}\boldsymbol{w}_h(t) = \mathcal{F}(\boldsymbol{w}_h(t)), \quad \boldsymbol{w}_h(0) = \boldsymbol{y}$$

at time $t = \Delta t^n$. Then the following splitting of (4.28)

$$\boldsymbol{w}_h^{n+1} = \Xi_{\mathcal{A}_2}(\Delta t^n)\Xi_{\mathcal{A}_1}(\Delta t^n)\boldsymbol{w}_h^n$$

is first-order consistent in time if the approximations $\Xi_{\mathcal{A}_1}$ and $\Xi_{\mathcal{A}_2}$ are consistent of at least first order in time, see [75]. The Strang splitting is the following modification of the above approach:

$$\boldsymbol{w}_h^{n+1} = \Xi_{\mathcal{A}_1}\left(\frac{\Delta t^n}{2}\right)\Xi_{\mathcal{A}_2}(\Delta t^n)\Xi_{\mathcal{A}_1}\left(\frac{\Delta t^n}{2}\right)\boldsymbol{w}_h^n.$$

It is second-order accurate, provided $\Xi_{\mathcal{A}_1}$ and $\Xi_{\mathcal{A}_2}$ are at least second-order consistent in time.

In our case of model (M1), the first operator will be the Navier-Stokes part (M1.a) and the second operator the microphysical cloud equations (M1.b). Thus, for the computation of a time step of length Δt^n the Navier-Stokes equations (M1.a) will be solved two times with time step $\Delta t^n/2$ and the cloud dynamics equations (M1.b) once with time step Δt^n. This particular choice and order of operators were chosen for flexibility in choosing time integration methods as well as efficiency. Since the cloud dynamics take place on smaller scales than the dynamics of fluids, it is computationally faster to solve the cloud dynamics equations (M1.b) just once applying smaller time steps which resolve fast dynamics.

4.2.3 Implicit-explicit Runge-Kutta methods

To solve the Navier-Stokes equations (M1.a) of the deterministic cloud system (M1), we apply an *implicit-explicit (IMEX) Runge-Kutta method*. It is basically a splitting method for the time discretization of (4.17) which couples a diagonally implicit Runge-Kutta scheme for the linear stiff advection and reaction terms to an explicit Runge-Kutta scheme for the remaining terms. The content of this subsection will be based on [65] as well as [13].

We start by writing (4.17) as

$$\frac{\mathrm{d}}{\mathrm{d}t}\boldsymbol{w}_h(t) = \mathcal{L}\left(\boldsymbol{w}_h(t)\right) + \mathcal{N}\left(\boldsymbol{w}_h(t)\right), \tag{4.29}$$

where $\mathcal{L}\left(\boldsymbol{w}_h(t)\right) + \mathcal{N}\left(\boldsymbol{w}_h(t)\right) = \mathcal{A}\left(\boldsymbol{w}_h(t)\right)$ and the operator $\mathcal{L}$ consists of the implicitly treated terms and the operator $\mathcal{N}$ of the remaining ones. For the Navier-Stokes equations (M1.a) this splitting will be explained and defined in (4.42).

A general s-stage IMEX Runge-Kutta method is given through

$$\begin{aligned}
\boldsymbol{w}_h^{n+1} &= \boldsymbol{w}_h^n + \Delta t^n \sum_{i=1}^{s} \bar{b}_i \mathcal{N}\left(t^n + \bar{c}_i \Delta t_n, \boldsymbol{W}_i\right) + \Delta t^n \sum_{i=1}^{s} b_i \mathcal{L}\left(t^n + c_i \Delta t^n, \boldsymbol{W}_i\right), \\
\boldsymbol{W}_i &= \boldsymbol{w}_h^n + \Delta t^n \sum_{j=1}^{i-1} \bar{a}_{ij} \mathcal{N}\left(t^n + \bar{c}_j \Delta t^n, \boldsymbol{W}_j\right) \\
&\quad + \Delta t^n \sum_{j=1}^{i} a_{ij} \mathcal{L}\left(t^n + c_j \Delta t^n, \boldsymbol{W}_j\right), \quad i = 1, \ldots, s,
\end{aligned}$$

where $\bar{\boldsymbol{b}}$, $\bar{\boldsymbol{c}} \in \mathbb{R}^s$ and $\bar{A} \in \mathbb{R}^{s \times s}$ denote the coefficients of the explicit and $\boldsymbol{b}$, $\boldsymbol{c} \in \mathbb{R}^s$ and $A \in \mathbb{R}^{s \times s}$ the coefficients of the implicit scheme. The method can also be noted with two Butcher tableaux as can be seen in Table 4.2

To compute one time step with an s-stage IMEX Runge-Kutta method, one needs to solve s linear systems which will be discussed in Subsection 4.2.5. To obtain an IMEX Runge-Kutta scheme of a particular order, the respective order conditions for the individual schemes have to be fulfilled as well as additional coupling conditions for the two schemes. For a method of order 2, which we are aiming for, conditions (4.24) and (4.25) have to be satisfied for $(\bar{A}, \bar{\boldsymbol{b}}, \bar{\boldsymbol{c}})$ and $(A, \boldsymbol{b}, \boldsymbol{c})$ and the following coupling conditions have to hold

$$\boldsymbol{b} \cdot \bar{\boldsymbol{c}} = \bar{\boldsymbol{b}} \cdot \boldsymbol{c} = \frac{1}{2}. \tag{4.30}$$

In what follows, we will present the second-order method of our choice.

ARS(2,2,2) scheme: The ARS(2,2,2) scheme was introduced by Asher, Ruuth and Spiteri, see [6], and is given by the tableaux in Table 4.3. It is an IMEX Runge-Kutta scheme of second order, meaning that the respective explicit and implicit Runge-Kutta schemes are of second order and (4.30) is satisfied. Applied to equation (4.29), we get

$\bar{\boldsymbol{c}}$	$\bar{A}$
	$\bar{\boldsymbol{b}}^T$

$\boldsymbol{c}$	A
	$\boldsymbol{b}^T$

Table 4.2: Butcher tableaux of an IMEX Runge-Kutta scheme, where $(\bar{A}, \bar{\boldsymbol{b}}, \bar{\boldsymbol{c}})$ represents the explicit and $(A, \boldsymbol{b}, \boldsymbol{c})$ the implicit scheme.

0	0	0	0
γ	γ	0	0
1	δ	$1-\delta$	0
	δ	$1-\delta$	0

0	0	0	0
γ	0	γ	0
1	0	$1-\gamma$	γ
	0	$1-\gamma$	γ

Table 4.3: Butcher tableaux of the ARS(2,2,2) scheme with $\gamma = 1 - \frac{1}{\sqrt{2}}$ and $\delta = 1 - \frac{1}{2\gamma}$.

the following stages

$$\begin{aligned}
\boldsymbol{W}_1 &= \boldsymbol{w}_h^n, \\
\boldsymbol{W}_2 &= \boldsymbol{w}_h^n + \Delta t^n \gamma \left[\mathcal{N}(t^n, \boldsymbol{W}_1) + \mathcal{L}(t^n + \gamma \Delta t^n, \boldsymbol{W}_2)\right], \\
\boldsymbol{W}_3 &= \boldsymbol{w}_h^n + \Delta t^n \left[\delta \mathcal{N}(t^n, \boldsymbol{W}_1) + (1-\delta)\mathcal{N}(t^n + \gamma \Delta t^n, \boldsymbol{W}_2)\right] \\
&\quad + \Delta t^n \left[(1-\gamma)\mathcal{L}(t^n + \gamma \Delta t^n, \boldsymbol{W}_2) + \gamma \mathcal{L}(t^n + \Delta t^n, \boldsymbol{W}_3)\right],
\end{aligned}$$

where one effectively has just two stages since $\boldsymbol{W}_1 = \boldsymbol{w}_h^n$. Thus, we first solve the following linear system

$$\boldsymbol{W}_2 - \Delta t^n \gamma \mathcal{L}(t^n + \gamma \Delta t^n, \boldsymbol{W}_2) = \boldsymbol{w}_h^n + \Delta t^n \gamma \mathcal{N}(t^n, \boldsymbol{w}_h^n) \tag{4.31}$$

and then

$$\begin{aligned}
\boldsymbol{w}_h^{n+1} - \Delta t^n \gamma \mathcal{L}(t^n + \Delta t^n, \boldsymbol{w}_h^{n+1}) = \boldsymbol{w}_h^n &+ \Delta t^n \left[\delta \mathcal{N}(t^n, \boldsymbol{w}_h^n) + (1-\delta)\mathcal{N}(t^n + \gamma \Delta t^n, \boldsymbol{W}_2)\right] \\
&+ \Delta t^n (1-\gamma)\mathcal{L}(t^n + \gamma \Delta t^n, \boldsymbol{W}_2).
\end{aligned} \tag{4.32}$$

Consequently, the computation of one time step requires the solution of two linear systems. Our choice of linear solver will be introduced in Subsection 4.2.5.

We followed the approach in [14] and [13] in choosing this particular second-order IMEX Runge-Kutta scheme for the time integration of the compressible Navier-Stokes equations (M1.a) because of its asymptotic preserving property. The terminology was introduced by Jin, see [55], and means that the scheme is stable and approximates the solution in all regimes accurately. In our case, we are in a low Mach number regime. The method thus yields a consistent approximation of the limit equations as the Mach number goes to zero, i.e. the incompressible Navier-Stokes equations, with stability constraints independent of the small Mach number itself.

4.2.4 DUMKA3 method

In this subsection, we will introduce the DUMKA3 time integration method which will be used to discretize (M1.b) in time. The content will be based on the lecture notes of

Massot [87], the original paper of Medovikov [91] and [48, 52, 132].

The DUMKA3 method is an explicit Runge-Kutta method with an extended stability region which is third-order consistent in time. It belongs to the class of *stabilized explicit Runge-Kutta methods*. Typical applications of such kinds of methods are stiff ODEs, i.e. the Jacobian matrix of $\mathcal{A}$, see (4.17), has (large) eigenvalues close to the real negative axis, arising from a semi-discretized parabolic PDE. An example for this is the discretized heat equation, for which the real negative eigenvalues even increase with finer spatial discretizations, see [87]. Instead of using an A-stable but time-consuming implicit scheme, one can use stabilized explicit Runge-Kutta methods. Since these methods are explicit, they avoid the solution of an implicit system which is in particular efficient for problems in multiple space dimensions. Additionally, they feature a low memory demand and an enlarged stability domain along the negative real axis which is still a finite real interval for absolute stability. Thus, stabilized explicit Runge-Kutta methods are advocated to be used for parabolic PDEs with multiple space dimensions which give rise to moderate stiffness. This is often the case for problems whose solutions are of a traveling wave front type, as these normally require small time step sizes for resolving the front. In general, advection-reaction-diffusion systems, where the reaction term is moderately stiff and the diffusion constant is much smaller than 1, can be efficiently solved with stabilized methods. Since our microphysical cloud dynamics equations (M1.b) belong to this class of equations we chose this kind of method. A more detailed description of stabilized explicit Runge-Kutta methods can be found in [132] and [52].

Since explicit Runge-Kutta methods are not A-stable, cf. (4.27), the main idea is to construct s-stage explicit Runge-Kutta methods of order p with a family of stability polynomials R_s, cf. (4.26), of order s such that R_s remains bounded as much as possible along the the negative real axis. This means that

$$|R_s(\zeta)| \leq 1, \quad \zeta \in [-l_s, 0], \tag{4.33}$$

holds with l_s as large as possible. We are looking for stability polynomials of the form

$$R_s(\zeta) = 1 + \zeta + \cdots + \frac{\zeta^p}{p!} + \sum_{i=p+1}^{s} \alpha_{i,s} \zeta^i, \tag{4.34}$$

where $\alpha_{i,s} \in \mathbb{C}$. Riha proved the existence of such polynomials for $p \geq 1$ and $s \geq p$ in [106]. For $p = 1$ the optimal polynomials which are of the form (4.34) and satisfy (4.33) are the shifted Chebyshev polynomials

$$R_s(\zeta) = T_s\left(1 + \frac{\zeta}{s^2}\right), \tag{4.35}$$

where T_s can be defined recursively through

$$T_0(\zeta) = 1, \quad T_1(\zeta) = \zeta, \quad T_j(\zeta) = 2\zeta T_{j-1}(\zeta) - T_{j-2}(\zeta), \quad 2 \leq j \leq s.$$

They lead to the optimal $l_s = 2s^2$. This quadratic dependence is very favorable. Indeed, taking into account the workload per step, the length of the stability region increases

linearly with the number of stages. One undesirable property of the polynomials (4.35) is that the stability region contains interior points $\zeta \in [-l_s, 0]$ with $|R_s(\zeta)| = 1$. This means that the stability domain has zero width and therefore a small imaginary perturbation on ζ might lead to instabilities. A more desirable property would be a narrow stripe along the negative half-line. This can be achieved by modifying (4.35) through a little damping. The approach of Guillou and Lago, see [46], is to consider the following damped versions of the shifted Chebyshev polynomials (4.35)

$$R_s(\zeta) = \frac{1}{T_s(w_0)} T_s(w_0 - w_1\zeta), \quad w_0 = 1 + \frac{\varepsilon}{s^2}, \quad w_1 = \frac{T_s(w_0)}{T_s'(w_0)}.$$

As a consequence, the stability domain reduces by approximately ε since now $|R_s(\zeta)| \leq 1 - \varepsilon$, and the length of the stability interval $[-l_s, 0]$ is by approximately $(4\varepsilon/3)^2$ shorter, which can be seen by a simple calculation, cf. [52, 132]. Still, the order of the scheme is preserved, see [48].

For $p > 1$ no explicit analytical expressions for (4.34) are known. However, various authors were able to construct approximations to the optimal polynomials. In what follows, we will briefly explain the idea behind the family of DUMKA methods developed by Lebedev and Medovikov, see [69, 71, 91] and references therein, which cover nearly 100% of the optimal stability interval. There exist DUMKA methods of order $2, 3$ and 4. We also want to note that there are the families of second-order Runge-Kutta-Chebyshev (RKC) methods proposed by van der Houwen and Sommeijer, cf. [130], and the family of second and fourth-order Orthogonal-Runge-Kutta-Chebyshev (ROCK) methods proposed by Abdulle and Medovikov, cf. [3, 4]. The RKC methods cover nearly 80% and the ROCK methods nearly 100% of the optimal real stability interval.

Lebedev's realization is based on the idea proposed by Saul'ev, cf. [108], and Guillou and Lago [46] who write the optimal stability polynomials as

$$R_s(\zeta) = \prod_{i=1}^{s} (1 + \delta_i \zeta), \quad \delta_i = -\frac{1}{z_i},$$

where z_i are the roots of $R_s(\zeta)$. To realize these stability polynomials, the Runge-Kutta method is written as a composition of explicit Euler steps

$$\begin{cases} \boldsymbol{k}_0^n := \boldsymbol{w}_h^n, \\ \boldsymbol{k}_i^n := \boldsymbol{k}_{i-1}^n + \Delta t^n \delta_i \mathcal{A}(\boldsymbol{k}_{i-1}^n), \quad i = 1, \ldots, s, \\ \boldsymbol{w}_h^{n+1} := \boldsymbol{k}_s^n. \end{cases}$$

The absolute value of the first root is much smaller than the one of the others which leads to a very large Euler step. Lebedev overcame this problem by grouping the roots together symmetrically two-by-two and representing the corresponding quadratic factor by a two-stage scheme. To assure stability properties of the scheme, some attention has to be paid to the order in which the roots are used, i.e., in which sequence the Euler steps are performed, cf. [72]. For more details see also [48].

Lebedev constructed approximations to the optimal stability polynomials in [70, 73] and computed them numerically for order 2 (DUMKA). Medovikov has extended this

approach to the orders 3 and 4 (DUMKA3 and DUMKA4) up to the degree 243 of the polynomials. He observed that the length of the stability domain behaves approximately as $l_s \approx \beta_p s^2$, where p is the order of the method and $\beta_2 \approx 0.81$, $\beta_3 \approx 0.49$ and $\beta_4 \approx 0.35$. This corresponds nicely to the values found in the literature, see, for example, [129]. In comparison to the explicit Euler method, whose stability domain has length 2 per time step the DUMKA method is $\frac{\beta_p s^2}{2s} = \frac{\beta_p}{2} s$ times faster. This becomes very favorable especially for a large number of stages s. For more details on the derivation of the DUMKA3 and DUMKA4 methods, we refer the reader to [91]. For the time integration of (M1.b) we chose the DUMKA3 method for which a free implementation is available online at [90].

4.2.5 GMRES

In this subsection, we briefly describe the *generalized minimal residual* (GMRES) method which iteratively solves a linear system. We use it to solve (4.31) and (4.32) within the time integration of the Navier-Stokes equations (M1.a). The content of this subsection is based on [92].

We start with some basic prerequisites that are necessary to understand the method. Let

$$\boldsymbol{A}\boldsymbol{w} = \boldsymbol{b} \tag{4.36}$$

be a linear system where $\boldsymbol{b} \in \mathbb{R}^n$, $n \in \mathbb{N}$, and $\boldsymbol{A} \in \mathbb{R}^{n \times n}$ is quadratic and invertible. Let $\boldsymbol{w}_0$ be an arbitrary approximation (initial guess) of (4.36) and L_m an m-dimensional subspace of $\mathbb{R}^n$. Furthermore, let $||\cdot||_2$ denote the Euclidean norm in $\mathbb{R}^n$.

Definition 4.3
A *Krylov subspace method* is a method for solving (4.36) by calculating approximate solutions $\boldsymbol{w}_m \in \boldsymbol{w}_0 + K_m$ by taking into account the Petrov-Galerkin condition

$$(\boldsymbol{b} - \boldsymbol{A}\boldsymbol{w}_m) \perp L_m, \tag{4.37}$$

where $\perp$ means orthogonal with respect to the Euclidean inner product in $\mathbb{R}^n$. The subspace K_m defined as

$$K_m = K_m(\boldsymbol{A}, \boldsymbol{r}_0) = \text{span}\{\boldsymbol{r}_0, \boldsymbol{A}\boldsymbol{r}_0, \dots, \boldsymbol{A}^{m-1}\boldsymbol{r}_0\}, \quad \boldsymbol{r}_0 = \boldsymbol{b} - \boldsymbol{A}\boldsymbol{w}_0,$$

is called the order-m Krylov subspace.

The GMRES method was developed by Saad and Schultz in 1986, see [107], and can be applied to general linear systems with an invertible system matrix $\boldsymbol{A}$. It is a Krylov subspace method with $L_m = \boldsymbol{A}K_m$ which in step m minimizes the norm of the residuum $||\boldsymbol{b} - \boldsymbol{A}\boldsymbol{w}_m||_2$. One can show that minimizing the norm of the residuum is equivalent to fulfilling the Petrov-Galerkin condition (4.37), see [92].

The foundation of the GMRES method is calculating an orthonormal basis $\{\boldsymbol{v}_1, \dots, \boldsymbol{v}_m\}$ of K_m with the *Arnoldi algorithm* for which we refer to [92]. The reason for this is that

the vectors $\boldsymbol{r}_0, \boldsymbol{A}\boldsymbol{r}_0, \ldots, \boldsymbol{A}^{m-1}\boldsymbol{r}_0$ which would be an obvious choice for the basis might be close to be linearly dependent. In particular, the first vector $\boldsymbol{v}_1$ is given through

$$\boldsymbol{v}_1 = \frac{\boldsymbol{r}_0}{||\boldsymbol{r}_0||_2}. \tag{4.38}$$

With the orthonormal basis $\{\boldsymbol{v}_1, \ldots, \boldsymbol{v}_m\}$ we then can write each $\boldsymbol{w}_m \in \boldsymbol{w}_0 + K_m$ as

$$\boldsymbol{w}_m = \boldsymbol{w}_0 + \boldsymbol{V}_m \boldsymbol{\alpha}_m, \quad \boldsymbol{\alpha}_m \in \mathbb{R}^m, \tag{4.39}$$

where $\boldsymbol{V}_m = (\boldsymbol{v}_1, \ldots, \boldsymbol{v}_m) \in \mathbb{R}^{n\times m}$. The Arnoldi algorithm also produces an upper Hessenberg matrix $\boldsymbol{H}_m \in \mathbb{R}^{m\times m}$ which gives the following relation between the $\boldsymbol{V}$ matrices

$$\boldsymbol{A}\boldsymbol{V}_m = \boldsymbol{V}_{m+1}\overline{\boldsymbol{H}}_m, \tag{4.40}$$

where

$$\overline{\boldsymbol{H}}_m = \begin{pmatrix} \boldsymbol{H}_m \\ 0 \cdots 0\ h_{m+1,m} \end{pmatrix} = \begin{pmatrix} h_{1,1} & h_{1,2} & h_{1,3} & \cdots & h_{1,m} \\ h_{2,1} & h_{2,2} & h_{2,3} & \cdots & h_{2,m} \\ 0 & h_{3,2} & h_{3,3} & \cdots & h_{3,m} \\ \vdots & \ddots & \ddots & \ddots & \vdots \\ \vdots & & 0 & h_{m,m-1} & h_{m,m} \\ 0 & \cdots & \cdots & 0 & h_{m+1,m} \end{pmatrix} \in \mathbb{R}^{(m+1)\times m}$$

is formed by adding an extra row to $\boldsymbol{H}_m$ in which only the last entry is nonzero. By using (4.38), (4.39) and (4.40), the norm of the residuum in step m is then given through

$$\begin{aligned} \|\boldsymbol{b} - \boldsymbol{A}\boldsymbol{w}_m\|_2 &= \|\boldsymbol{b} - \boldsymbol{A}(\boldsymbol{w}_0 + \boldsymbol{V}_m\boldsymbol{\alpha}_m)\|_2 = \|\boldsymbol{r}_0 - \boldsymbol{A}\boldsymbol{V}_m\boldsymbol{\alpha}_m\|_2 = \|\|\boldsymbol{r}_0\|_2\,\boldsymbol{v}_1 - \boldsymbol{A}\boldsymbol{V}_m\boldsymbol{\alpha}_m\|_2 \\ &= \left\|\|\boldsymbol{r}_0\|_2\,\boldsymbol{v}_1 - \boldsymbol{V}_{m+1}\overline{\boldsymbol{H}}_m\boldsymbol{\alpha}_m\right\|_2 = \left\|\|\boldsymbol{r}_0\|_2\,\boldsymbol{V}_{m+1}\boldsymbol{e}_1 - \boldsymbol{V}_{m+1}\overline{\boldsymbol{H}}_m\boldsymbol{\alpha}_m\right\|_2 \\ &= \left\|\boldsymbol{V}_{m+1}(\|\boldsymbol{r}_0\|_2\,\boldsymbol{e}_1 - \overline{\boldsymbol{H}}_m\boldsymbol{\alpha}_m)\right\|_2, \end{aligned}$$

where $\boldsymbol{e}_1 = (1, 0, \ldots, 0)^\top \in \mathbb{R}^{m+1}$. Since $\boldsymbol{V}_{m+1}$ is an orthogonal matrix, the Euclidean norm of the matrix product is preserved and it follows

$$\|\boldsymbol{b} - \boldsymbol{A}\boldsymbol{w}_m\|_2 = \left\|\|\boldsymbol{r}_0\|_2\,\boldsymbol{e}_1 - \overline{\boldsymbol{H}}_m\boldsymbol{\alpha}_m\right\|_2. \tag{4.41}$$

Hence $\boldsymbol{w}_m$ can be determined by minimizing (4.41). The advantage of minimizing this norm is that during the iteration one can calculate the residuum without determining the approximation $\boldsymbol{w}_m$. Only when the norm is smaller than a given tolerance, the solution $\boldsymbol{w}_m$ is calculated by using (4.39).

The GMRES method has two disadvantages. The first one is the computational effort for determining the orthonormal basis which grows with the dimension of the Krylov space. The second disadvantage is a large memory requirement for saving the basis vectors. It can happen that even for a sparse matrix $\boldsymbol{A} \in \mathbb{R}^{n\times n}$ a dense matrix $\boldsymbol{V}_n \in \mathbb{R}^{n\times n}$ has to be saved. Thus, often a restarted version of the method, also called *restarted GMRES*, is used. It avoids the disadvantages by limiting the maximal dimension of the Krylov subspace. In the case that after this given maximal number of iterations the norm of the

residuum $\|\boldsymbol{r}_m\|_2$ is not smaller than the given tolerance, the approximation $\boldsymbol{w}_m$ is still calculated and then used as the initial guess for another run of the GMRES method.

To speed up the convergence of iterative methods often preconditioning is used. In fact, the convergence of the GMRES method highly depends on the choice of the preconditioner. With an incomplete LU factorization (ILU) the method performs robustly. In general, preconditioning reformulates the linear system equivalently in such a way that the condition number of the problem is reduced which has a positive effect on the convergence speed of the iterative method, see [92]. The condition number $\text{cond}(\boldsymbol{A})$ is a property of the matrix which can be seen as the rate at which the solution $\boldsymbol{w}$ will change concerning a change in $\boldsymbol{b}$ and is given through

$$\text{cond}(\boldsymbol{A}) = \left\|\boldsymbol{A}^{-1}\right\| \|\boldsymbol{A}\| .$$

It is desirable to have a small condition number since for a large condition number $\text{cond}(\boldsymbol{A})$ even a small error in $\boldsymbol{b}$ may cause a large error in $\boldsymbol{w}$. The main idea of the ILU preconditioning is a decomposition of the form $\boldsymbol{A} = \boldsymbol{L}\boldsymbol{U} + \boldsymbol{F}$, where $\boldsymbol{L}$ is a lower left triangular matrix and $\boldsymbol{U}$ is an upper right triangular matrix. Neglecting the matrix $\boldsymbol{F}$, one obtains a matrix $\tilde{\boldsymbol{A}} = \boldsymbol{L}\boldsymbol{U}$ that can easily be inverted. The inverse $\tilde{\boldsymbol{A}}^{-1}$ is an approximation of $\boldsymbol{A}^{-1}$ and can be used as preconditioner for system (4.36) by multiplication with this matrix. For more details on the ILU preconditioner we refer to [92].

For more details on the GMRES method, we refer the reader to [92], where the derivation is nicely carried out and even a pseudo code as well as a reference to a MATLAB code can be found.

Remark 4.4*:* To solve (4.31) and (4.32) we use the restarted GMRES method with ILU preconditioning from the scientific toolkit PETSc (portable, extensible toolkit for scientific computation).

4.2.6 Time step restrictions

For the approximation of the fully discrete scheme, we need to take care of stability conditions for the advection and diffusion terms which are approximated explicitly in time.

Advection terms: For the nonlinear advection we take the CFL condition into account which is a necessary condition for a finite volume method to become stable and converge towards the exact solution as $h, \Delta t^n \to 0$, cf. [23]. It states that the numerical domain of dependence of the method should include the analytical domain of dependence of the PDE, at least as $h, \Delta t^n \to 0$. Thereby, the analytical domain of dependence of a point y is the maximal subset $D_y \subset \Omega$ such that the PDE solution $w(y, t+\Delta t^n)$ depends only on $w(x,t)$ for $x \in D_y$ in time t. Its numerical analogon considers the stencil around a mesh point x_i at time t on which the value of the approximation in $(x_i, t + \Delta t^n)$ depends.

In the case of the scalar conservation law (4.1), the condition leads to $u_{\max}\Delta t^n = \mathcal{O}(h)$ for a finite volume method which is explicit in time, where $u_{\max}$ is the maximal wave propagation speed. This is due to the fact that the solution stays constant along characteristic lines, cf. Figure 4.5 and Remark 4.1. Since we will treat some nonlinear advection

terms explicitly in time, we will use a condition of the form

$$u_{\max}\frac{\Delta t^n}{h} \leq \mathrm{CFL},$$

where $0 \leq \mathrm{CFL} \leq 1$ denotes a fixed number depending on the problem and on the method, see (4.47) and (4.48). For the central method we will use $\mathrm{CFL} \leq 1/2$, cf. Figure 4.5.

Diffusion terms: For parabolic equations, like the Navier-Stokes equation in (2.48), the analytical domain of dependence covers the full computational domain. Therefore, one needs an additional condition to explicitly approximate the second derivatives in a stable manner.

When choosing explicit central differences to approximate the diffusion equation, the time step needs to be chosen as $\Delta t^n = \mathcal{O}(h^2)$ to be stable, see [54]. This is not the case for an implicit method since there the numerical domain of dependence in a grid point includes the whole computational domain. However, due to the nonlinearity of the diffusion terms in (M1), an implicit method would require costly computational methods. Hence, we chose a fully explicit treatment which is straightforward but requires the additional time step restriction $\Delta t^n = \mathcal{O}(h^2)$ on top of the CFL condition, cf. (4.47) and (4.48).

4.3 Numerical scheme for the deterministic model

The numerical approximation of the coupled model (M1) is based on the second-order Strang operator splitting, see Section 4.2.2. Therefore, we split the whole system into the macroscopic Navier-Stokes flow equations and the microscopic cloud equations. The Navier-Stokes equations (3.7), i.e. the part describing dynamics of fluids (M1.a), are approximated by an IMEX finite-volume method, see Section 4.2.3, and the cloud equations (2.50), i.e. the cloud dynamics part (M1.b), are approximated by a finite-volume method in space and an explicit Runge-Kutta method with an enlarged stability region in time, namely the Dumka 3 method that was introduced in Section 4.2.4. The description in this section is based on [21].

4.3.1 Operator form

Let $\boldsymbol{w} := (\rho', \rho\boldsymbol{u}, (\rho\theta)')^\top$ and $\boldsymbol{w}_q := (\rho q_v, \rho q_c, \rho q_r)^\top$ denote the solution vectors of (M1.a) and (M1.b), respectively. Then, the coupled system can be written as

$$\begin{aligned}\boldsymbol{w}_t &= -\nabla\cdot\boldsymbol{F}(\boldsymbol{w}) + \mathfrak{D}(\boldsymbol{w}) + \mathfrak{R}(\boldsymbol{w}),\\ (\boldsymbol{w}_q)_t &= -\nabla\cdot\boldsymbol{F}_q(\boldsymbol{w}_q) + \mathfrak{D}_q(\boldsymbol{w}_q) + \mathfrak{R}_q(\boldsymbol{w}_q),\end{aligned}$$

where $\boldsymbol{F}$ and $\boldsymbol{F}_q$ are advection fluxes and $\mathfrak{D}$, $\mathfrak{R}$ and $\mathfrak{D}_q$, $\mathfrak{R}_q$ denote the diffusion and reaction operators of the respective systems. They are given by

$$\begin{aligned}\boldsymbol{F}(\boldsymbol{w}) &:= (\rho\boldsymbol{u}, \rho\boldsymbol{u}\otimes\boldsymbol{u} + p'\,\mathrm{Id}, \rho\theta\boldsymbol{u})^\top,\\ \mathfrak{D}(\boldsymbol{w}) &:= \big(0, \nabla\cdot(\mu_m\rho(\nabla\boldsymbol{u} + (\nabla\boldsymbol{u})^\top)), \nabla\cdot(\mu_h\rho\nabla\theta)\big)^\top,\\ \mathfrak{R}(\boldsymbol{w}) &:= (0, -\rho' g\boldsymbol{e_d}, S_\theta)^\top,\end{aligned}$$

$$\begin{aligned}
\boldsymbol{F}_q(\boldsymbol{w}_q) &:= (\rho q_v \boldsymbol{u}, \rho q_c \boldsymbol{u}, \rho q_r \boldsymbol{u} - v_q \rho q_r \boldsymbol{e_d})^\top, \\
\mathfrak{D}_q(\boldsymbol{w}_q) &:= (\nabla \cdot (\mu_q \rho \nabla q_v), \nabla \cdot (\mu_q \rho \nabla q_c), \nabla \cdot (\mu_q \rho \nabla q_r))^\top, \\
\mathfrak{R}_q(\boldsymbol{w}_q) &:= (-C + E, C - A_1 - A_2, A_1 + A_2 - E)^\top.
\end{aligned}$$

In order to derive an asymptotically stable, accurate and computationally efficient scheme for the Navier-Stokes equations, we first split the equations (except the diffusion terms) into linear and nonlinear parts, see [14, 79] and references therein. Consequently, we introduce

- $\boldsymbol{F}(\boldsymbol{w}) = \boldsymbol{F}_L(\boldsymbol{w}) + \boldsymbol{F}_N(\boldsymbol{w})$
  with $\boldsymbol{F}_L(\boldsymbol{w}) := \left(\rho \boldsymbol{u}, p' \operatorname{Id}, \bar{\theta} \rho \boldsymbol{u}\right)^\top$ and $\boldsymbol{F}_N(\boldsymbol{w}) := (0, \rho \boldsymbol{u} \otimes \boldsymbol{u}, \theta' \rho \boldsymbol{u})^\top$;
- $\mathfrak{R}(\boldsymbol{w}) = \mathfrak{R}_L(\boldsymbol{w}) + \mathfrak{R}_N(\boldsymbol{w})$
  with $\mathfrak{R}_L(\boldsymbol{w}) := (0, -\rho' g \boldsymbol{e_d}, 0)^\top$ and $\mathfrak{R}_N(\boldsymbol{w}) := (0, 0, S_\theta)^\top$.

We would like to point out that the choice of the linear and nonlinear operators is crucial. We choose the linear part to model linear acoustic and gravitational waves as well as linear viscous fluxes. The nonlinear part describes nonlinear advective effects together with the remaining nonlinear viscous fluxes and the influence of the latent heat. We will use the following notation:

$$\mathcal{L} := -\nabla \cdot \boldsymbol{F}_L(\boldsymbol{w}) + \mathfrak{R}_L(\boldsymbol{w}) \quad \text{and} \quad \mathcal{N} := -\nabla \cdot \boldsymbol{F}_N(\boldsymbol{w}) + \mathfrak{D}(\boldsymbol{w}) + \mathfrak{R}_N(\boldsymbol{w}). \tag{4.42}$$

4.3.2 Discretization in space

The spatial discretization is realized by a finite volume method, see Section 4.1. We take a cuboid computational domain $\Omega \subset \mathbb{R}^d$, which is divided into N uniform Cartesian cells. The cells are labeled using a single-index notation. For simplicity of notation, we assume that the cells are cubes with the sides of size h so that $|C_i| = h^d$. We also introduce the notation $S(i)$ for the set of all neighboring cells of cell C_i, $i = 1, \dots, N$.

Remark 4.5*:* If the domain Ω is not cuboid, we approximate it by a cuboid domain. This then leads to additional approximation errors. When applying the Galerkin method this domain approximation is called *geometric variational crime*. If the domain, for instance, has a smooth curved boundary, it cannot be decomposed exactly by rectangles or even triangles, which as consequence violates assumptions for the Galerkin formulation. Nevertheless, these approximations are a practical necessity and the numerical computations converge just fine. These observations were pointed out by Strang who quantified the additional errors introduced by these approximations in [116]. For more details, we also refer to [17].

We assume that at a any time t the piecewise constant approximate solution is given by cell averages

$$\boldsymbol{w}_i(t) \approx \frac{1}{h^d} \int_{C_i} \boldsymbol{w}(\boldsymbol{x}, t) \, \mathrm{d}\boldsymbol{x} \quad \text{and} \quad (\boldsymbol{w}_q)_i(t) \approx \frac{1}{h^d} \int_{C_i} \boldsymbol{w}_q(\boldsymbol{x}, t) \, \mathrm{d}\boldsymbol{x}, \quad i = 1, \dots, N.$$

In order to simplify the notation, we will now omit the time dependence of $\boldsymbol{w}_i(t)$ and $(\boldsymbol{w}_q)_i(t)$. Next, we introduce the notation $\boldsymbol{w}_h := \{\boldsymbol{w}_i\}_{i=1}^N$ and $(\boldsymbol{w}_q)_h := \{(\boldsymbol{w}_q)_i\}_{i=1}^N$ and consider the following approximation of the advection, diffusion and reaction operators:

$$\begin{aligned}\mathcal{A}_i(\boldsymbol{w}_h) = (\mathcal{A}_L)_i(\boldsymbol{w}_h) + (\mathcal{A}_N)_i(\boldsymbol{w}_h) &\approx \frac{1}{h^d}\int_{C_i} \nabla\cdot\boldsymbol{F}_L(\boldsymbol{w}(\boldsymbol{x},t))\,\mathrm{d}\boldsymbol{x} \\ &\quad + \frac{1}{h^d}\int_{C_i} \nabla\cdot\boldsymbol{F}_N(\boldsymbol{w}(\boldsymbol{x},t))\,\mathrm{d}\boldsymbol{x},\\ \mathcal{D}_i(\boldsymbol{w}_h) &\approx \frac{1}{h^d}\int_{C_i} \mathfrak{D}(\boldsymbol{w}(\boldsymbol{x},t))\,\mathrm{d}\boldsymbol{x},\\ \mathcal{R}_i(\boldsymbol{w}_h) = (\mathcal{R}_L)_i(\boldsymbol{w}_h) + (\mathcal{R}_N)_i(\boldsymbol{w}_h) &\approx \frac{1}{h^d}\int_{C_i} \mathfrak{R}_L(\boldsymbol{w}(\boldsymbol{x},t))\,\mathrm{d}\boldsymbol{x} + \frac{1}{h^d}\int_{C_i} \mathfrak{R}_N(\boldsymbol{w}(\boldsymbol{x},t))\,\mathrm{d}\boldsymbol{x}.\end{aligned}$$

An analogous notation will be used for the approximations of the cloud operators, $(\mathcal{A}_q)_i(\boldsymbol{w}_h)$, $(\mathcal{D}_q)_i(\boldsymbol{w}_h)$ and $(\mathcal{R}_q)_i(\boldsymbol{w}_h)$.

Advection

The advection terms are discretized using numerical flux functions as follows:

$$\begin{aligned}(\mathcal{A}_L)_i(\boldsymbol{w}_h) &= \frac{1}{h}\sum_{j\in S(i)} H_{ij}^L(\boldsymbol{w}_h)\sum_{k=1}^d n_{ij}^{(k)},\\ (\mathcal{A}_N)_i(\boldsymbol{w}_h) &= \frac{1}{h}\sum_{j\in S(i)} H_{ij}^N(\boldsymbol{w}_h)\sum_{k=1}^d n_{ij}^{(k)},\\ (\mathcal{A}_q)_i((\boldsymbol{w}_q)_h) &= \frac{1}{h}\sum_{j\in S(i)} (H_q)_{ij}((\boldsymbol{w}_q)_h)\sum_{k=1}^d n_{ij}^{(k)},\end{aligned}$$

where the numerical fluxes H_{ij}^L, H_{ij}^N and $(H_q)_{ij}$ approximate the corresponding fluxes between the computational cells C_i and C_j, and $n_{ij}^{(k)}$ denotes the k-th component of the outer unit normal vector of cell C_i in the direction of cell C_j. We use the Rusanov numerical flux for H_{ij}^N and $(H_q)_{ij}$ and the central flux for H_{ij}^L. Note that the central flux already yields a second order of accuracy in space. To increase the accuracy for $(\mathcal{A}_N)_i(\boldsymbol{w}_h)$ and $(\mathcal{A}_q)_i((\boldsymbol{w}_q)_h)$ a discretization is obtained via a MUSCL-type approach using piecewise linear reconstructions with the minmod limiter. It is well-known that this approach yields an approximation, which is almost second-order accurate as its accuracy deteriorates only at sudden changes, i.e. jumps, discontinuities or large curvatures. The numerical fluxes are given by

$$\begin{aligned}H_{ij}^L(\boldsymbol{w}_h) &= \frac{1}{2}\left(\boldsymbol{F}_L(\boldsymbol{w}_j) + \boldsymbol{F}_L(\boldsymbol{w}_i)\right),\\ H_{ij}^N(\boldsymbol{w}_h) &= \frac{1}{2}\left(\boldsymbol{F}_N(\boldsymbol{w}_{ij}^+) + \boldsymbol{F}_N(\boldsymbol{w}_{ij}^-)\right) - \frac{\lambda_{ij}}{2}\left(\boldsymbol{w}_{ij}^+ - \boldsymbol{w}_{ij}^-\right),\\ (H_q)_{ij}((\boldsymbol{w}_q)_h) &= \frac{1}{2}\left(\boldsymbol{F}_q((\boldsymbol{w}_q)_{ij}^+) + \boldsymbol{F}_q((\boldsymbol{w}_q)_{ij}^-)\right) - \frac{(\lambda_q)_{ij}}{2}\left((\boldsymbol{w}_q)_{ij}^+ - (\boldsymbol{w}_q)_{ij}^-\right).\end{aligned} \tag{4.43}$$

Here, $\boldsymbol{w}_{ij}^-$, $\boldsymbol{w}_{ij}^+$ and $(\boldsymbol{w}_q)_{ij}^-$, $(\boldsymbol{w}_q)_{ij}^+$ denote the corresponding interface values, which are computed using a piecewise linear reconstruction so that

$$\boldsymbol{w}_{ij}^- = \boldsymbol{w}_i + \boldsymbol{s}_{ij}\frac{h}{2}\sum_{k=1}^{d} n_{ij}^{(k)}, \quad \boldsymbol{w}_{ij}^+ = \boldsymbol{w}_j - \boldsymbol{s}_{ji}\frac{h}{2}\sum_{k=1}^{d} n_{ij}^{(k)},$$

where the slopes $\boldsymbol{s}_{ij}$ are computed by the minmod limiter,

$$\boldsymbol{s}_{ij} = \frac{1}{h}\text{minmod}\left(\boldsymbol{w}_j - \boldsymbol{w}_i, \boldsymbol{w}_i - \boldsymbol{w}_{j^*}\right)\sum_{k=1}^{d} n_{ij}^{(k)},$$

applied in a componentwise manner. The minmod limiter is defined as is (4.14) and $(\boldsymbol{w}_q)_{ij}^-$ and $(\boldsymbol{w}_q)_{ij}^+$ are obtained similarly. By C_{j*} the other neighboring cell of C_i in the opposite direction from C_j is denoted. Finally, the values λ_{ij} and $(\lambda_q)_{ij}$ are given by

$$\lambda_{ij} = \max\left\{\sigma\left(\frac{\partial \boldsymbol{F}_N(\boldsymbol{w}_{ij}^-)}{\partial \boldsymbol{w}}\right), \sigma\left(\frac{\partial \boldsymbol{F}_N(\boldsymbol{w}_{ij}^+)}{\partial \boldsymbol{w}}\right)\right\},$$
$$(\lambda_q)_{ij} = \max\left\{\sigma\left(\frac{\partial \boldsymbol{F}_q((\boldsymbol{w}_q)_{ij}^-)}{\partial \boldsymbol{w}_q}\right), \sigma\left(\frac{\partial \boldsymbol{F}_q((\boldsymbol{w}_q)_{ij}^+)}{\partial \boldsymbol{w}_q}\right)\right\},$$

where σ denotes the spectral radius of the corresponding Jacobians.

Remark 4.6*:* Note that in the computation of H_{ij}^L in (4.43), we use the cell averages rather than the point values at the cell interfaces for the following two reasons. As already mentioned above, the flux is second-order accurate. Further, in Section 4.3.3, we will treat the linear part of the flux implicitly and this is much easier to do when the numerical flux is linear as well.

Diffusion

The components of the discrete diffusion operators can be written as:

$$\begin{aligned}
\mathcal{D}_i(\boldsymbol{w}_h) &=: \left(0, \boldsymbol{\mathcal{D}}_i^2(\boldsymbol{w}_h), \mathcal{D}_i^3(\boldsymbol{w}_h)\right)^\top \\
&\approx \frac{1}{h^d}\int_{C_i} \left(0, \nabla\cdot(\mu_m\rho(\nabla\boldsymbol{u} + (\nabla\boldsymbol{u})^\top)), \nabla\cdot(\mu_h\rho\nabla\theta)\right)^\top \mathrm{d}\boldsymbol{x} \\
&= \frac{1}{h^d}\int_{C_i} \left(0, \mu_m\nabla\cdot(\rho(\nabla\boldsymbol{u} + (\nabla\boldsymbol{u})^\top)), \mu_h\left(\rho\Delta\theta + \nabla\rho\cdot\nabla\theta\right)\right)^\top \mathrm{d}\boldsymbol{x} \\
&= \frac{1}{h^d}\int_{C_i} \begin{pmatrix} 0 \\ \mu_m\left(\sum_{j=1}^d\left(\rho_{x_j}\left((u_1)_{x_j} + (u_j)_{x_1}\right)\right) + \rho\sum_{j=1}^d\left((u_1)_{x_j^2} + (u_j)_{x_1x_j}\right)\right) \\ \vdots \\ \mu_m\left(\sum_{j=1}^d\left(\rho_{x_j}\left((u_d)_{x_j} + (u_j)_{x_d}\right)\right) + \rho\sum_{j=1}^d\left((u_d)_{x_j^2} + (u_j)_{x_dx_j}\right)\right) \\ \mu_h\left(\rho\sum_{j=1}^d\theta_{x_j^2} + \sum_{j=1}^d\rho_{x_j}\theta_{x_j}\right) \end{pmatrix} \mathrm{d}\boldsymbol{x},
\end{aligned}$$

$$
\begin{aligned}
(\mathcal{D}_q)_i(\boldsymbol{w}_h) &=: ((\mathcal{D}_q)_i^v((\boldsymbol{w}_q)_h), (\mathcal{D}_q)_i^c((\boldsymbol{w}_q)_h), (\mathcal{D}_q)_i^r((\boldsymbol{w}_q)_h))^\top \\
&\approx \frac{1}{h^d} \int_{C_i} (\nabla \cdot (\mu_q \rho \nabla q_v), \nabla \cdot (\mu_q \rho \nabla q_c), \nabla \cdot (\mu_q \rho \nabla q_r))^\top \, \mathrm{d}\boldsymbol{x} \\
&= \frac{\mu_q}{h^d} \int_{C_i} (\rho \Delta q_v + \nabla \rho \cdot \nabla q_v, \rho \Delta q_c + \nabla \rho \cdot \nabla q_c, \rho \Delta q_r + \nabla \rho \cdot \nabla q_r)^\top \, \mathrm{d}\boldsymbol{x} \\
&= \frac{\mu_q}{h^d} \int_{C_i} \begin{pmatrix} \rho \sum_{j=1}^d (q_v)_{x_j^2} + \sum_{j=1}^d \rho_{x_j} (q_v)_{x_j} \\ \rho \sum_{j=1}^d (q_c)_{x_j^2} + \sum_{j=1}^d \rho_{x_j} (q_c)_{x_j} \\ \rho \sum_{j=1}^d (q_r)_{x_j^2} + \sum_{j=1}^d \rho_{x_j} (q_r)_{x_j} \end{pmatrix} \mathrm{d}\boldsymbol{x}.
\end{aligned}
$$

They are discretized in a straightforward manner using second-order central differences, which leads to

$$
\begin{aligned}
\mathcal{D}_i^2(\boldsymbol{w}_h)^{(l)} = \frac{\mu_m}{h^2} \Bigg(& \sum_{j=1}^d \left(\frac{1}{4} \left(\sum_{k \in S(i)} \rho_k n_{ik}^{(j)} \right) \left(\sum_{k \in S(i)} \left((u_l)_k n_{ik}^{(j)} + (u_j)_k n_{ik}^{(l)} \right) \right) \right) \\
& + \rho_i \sum_{j=1}^d \left(\sum_{k \in S(i)} (u_l)_k \left| n_{ik}^{(j)} \right| - 2(u_l)_i + \frac{1}{4} \sum_{k \in S(i)} \left(n_{ik}^{(l)} \sum_{s \in S(k)} (u_j)_s n_{ks}^{(j)} \right) \right) \Bigg),
\end{aligned}
$$

for $l = 1, \ldots, d$,

$$
\mathcal{D}_i^3(\boldsymbol{w}_h) = \frac{\mu_h}{h^2} \left(\rho_i \sum_{j=1}^d \left(\sum_{k \in S(i)} \theta_k \left| n_{ik}^{(j)} \right| - 2\theta_i \right) + \frac{1}{4} \sum_{j=1}^d \left(\sum_{k \in S(i)} \rho_k n_{ik}^{(j)} \right) \left(\sum_{k \in S(i)} \theta_k n_{ik}^{(j)} \right) \right)
$$

and

$$
\begin{aligned}
(\mathcal{D}_q)_i^\ell((\boldsymbol{w}_q)_h) = \frac{\mu_q}{h^2} \Bigg(& \rho_i \sum_{j=1}^d \left(\sum_{k \in S(i)} (q_\ell)_k \left| n_{ik}^{(j)} \right| - 2(q_l)_i \right) \\
& + \frac{1}{4} \sum_{j=1}^d \left(\sum_{k \in S(i)} \rho_k n_{ik}^{(j)} \right) \left(\sum_{k \in S(i)} (q_\ell)_k n_{ik}^{(j)} \right) \Bigg), \quad \ell \in \{v, c, r\}.
\end{aligned}
$$

Reaction

The reaction terms are discretized by a direct evaluation of the reaction operators using the cell-centered averages:

$$
\mathcal{R}_i(\boldsymbol{w}_h) = \mathfrak{R}_L(\boldsymbol{w}_i) + \mathfrak{R}_N(\boldsymbol{w}_i), \quad (\mathcal{R}_q)_i((\boldsymbol{w}_q)_h) = \mathfrak{R}_q((\boldsymbol{w}_q)_i).
$$

After the spatial discretization, we obtain the following system of time-dependent ODEs:

$$
\frac{\mathrm{d}}{\mathrm{d}t} \boldsymbol{w}_i = -\mathcal{A}_i(\boldsymbol{w}_h) + \mathcal{D}_i(\boldsymbol{w}_h) + \mathcal{R}_i(\boldsymbol{w}_h), \tag{4.44}
$$

$$
\frac{\mathrm{d}}{\mathrm{d}t} (\boldsymbol{w}_q)_i = -(\mathcal{A}_q)_i((\boldsymbol{w}_q)_h) + (\mathcal{D}_q)_i((\boldsymbol{w}_q)_h) + (\mathcal{R}_q)_i((\boldsymbol{w}_q)_h). \tag{4.45}
$$

This system has to be solved using an appropriate ODE solver as discussed in Section 4.3.3.

4.3.3 Discretization in time

Let $\boldsymbol{w}_h^n$ and $(\boldsymbol{w}_q)_h^n$ denote the numerical approximation of the solutions $\boldsymbol{w}_h(t)$ and $(\boldsymbol{w}_q)_h(t)$ at the discrete time level t^n. We evolve the solution at the next time level $t^{n+1} = t^n + \Delta t^n$, where Δt^n is the size of the Strang operator splitting time step. In the operator splitting approach, we first numerically solve the ODE system (4.44) with $\Delta t_{\mathrm{NS}}^n = {}^{\Delta t^n}/_2$, we then numerically integrate the ODE system (4.45) with Δt^n and finally we solve system (4.44) again with Δt_{NS}^n.

Notice that system (4.44) may be very stiff as the Navier-Stokes equations are in the weakly compressible regime. We therefore follow the approach from [14] (see also [13]) and employ the second-order ARS(2,2,2) IMEX method from [6]:

$$\begin{aligned}
\boldsymbol{w}_h^{n+\frac{1}{4}} &= \boldsymbol{w}_h^n + \beta \Delta t_{\mathrm{NS}}^n \left(\mathcal{L}\left(\boldsymbol{w}_h^{n+\frac{1}{4}} \right) + \mathcal{N}\left(\boldsymbol{w}_h^n \right) \right), \\
\boldsymbol{w}_h^{n+\frac{1}{2}} &= \boldsymbol{w}_h^n + \Delta t_{\mathrm{NS}}^n \left(\delta \mathcal{N}\left(\boldsymbol{w}_h^n \right) + (1-\delta) \mathcal{N}\left(\boldsymbol{w}_h^{n+\frac{1}{4}} \right) \right) \\
&\quad + \Delta t_{\mathrm{NS}}^n \left(\beta \mathcal{L}\left(\boldsymbol{w}_h^{n+\frac{1}{2}} \right) + (1-\beta) \mathcal{L}\left(\boldsymbol{w}_h^{n+\frac{1}{4}} \right) \right),
\end{aligned} \tag{4.46}$$

where $\beta = 1 - {}^1/_{\sqrt{2}}$, $\delta = 1 - {}^1/_{2\beta}$, $t^{n+\frac{1}{2}} = t^n + \Delta t_{\mathrm{NS}}^n$, $t^{n+\frac{1}{4}} = t^n + {}^{\Delta t_{\mathrm{NS}}^n}/_2$, and Δt_{NS}^n satisfies the following CFL condition:

$$\max\left(\frac{\max(\mu_h, \mu_m)}{h^2}, \max_{s=1,2,3} \max_{i=1,\dots,N} (|(u_s)_i|) \frac{d}{h} \right) \Delta t_{\mathrm{NS}}^n < 0.5. \tag{4.47}$$

We note that the time step has to be of order h^2 since we solve the diffusion terms explicitly in time, see Subsection 4.2.6.

For solving the linear systems arising in (4.46), we use the generalized minimal residual (GMRES) method combined with a preconditioner, the incomplete LU factorization (ILU), see Subsection 4.2.5. As shown in [14] (see also [13]), the resulting method is both accurate and efficient in the weakly compressible regime.

The ODE system (4.45) is also stiff, but its stiffness only originates from the diffusion and power-law-type source terms. We therefore efficiently solve it using the large stability domain third-order Runge-Kutta method from [91]. We have used the ODE solver DUMKA3, see Subsection 4.2.4, which is a free software that can be found in [90]. We note that DUMKA3 selects time steps automatically, but in order to improve its efficiency, one needs to provide the code with a time step stability restriction for the forward Euler method; see [90, 91]. This bound is obtained by $\min\{\Delta t^n, \Delta t_{\mathrm{cloud}}^n\}$, where $\Delta t_{\mathrm{cloud}}^n$ satisfies the following CFL condition for the cloud system:

$$\max\left(\frac{\mu_q}{h^2}, \max_{s=1,2} \max_{i=1,\dots,N} (|(u_s)_i|, |(u_3)_i + v_q|) \frac{d}{h} \right) \Delta t_{\mathrm{cloud}}^n < 0.5. \tag{4.48}$$

5 Numerical methods for the stochastic models

This chapter is devoted to the numerical approximation of the stochastic models (M2) and (M3) that will be presented in Section 5.3 and is based on [21]. We will start by providing a general overview of uncertainty quantification and possible uncertainty quantification methods for cloud modeling and related physical models in Section 5.1 and then focus on stochastic spectral methods in Section 5.2 based on [68, 113, 144]. In Subsections 5.2.2 and 5.2.1, we introduce two spectral methods, the stochastic collocation and the stochastic Galerkin method, respectively. In Subsection 5.2.3 we give a comparison of both methods. We apply the method of our choice, the stochastic Galerkin method, to the model with stochastic cloud dynamics (M2) in Subsection 5.3.1 and the fully stochastic model (M3) in Subsection 5.3.2. By making some comments on the combination of the stochastic approximation with the space-time approximations of the models in Section 5.4, we conclude the chapter.

5.1 General overview of uncertainty quantification

Uncertainty quantification has become an interdisciplinary field with explosive growth. Reasons for that are an increasing emphasis on models with quantified uncertainties for large-scale applications, novel algorithm development and new as well as powerful computational architectures which enable implementation of these algorithms. In this section, we will motivate uncertainty quantification for physical models in the context of cloud/weather modeling, characterize sources of uncertainty and give a general overview of methods to tackle these uncertainties. The content of this section is based on [113] and [144].

A broad definition of uncertainty quantification is the science of identifying, quantifying and reducing uncertainties associated with models, numerical algorithms and predicted quantities of interest. Some parts of this field are already well understood and addressed by classical statistics and numerical analysis theory. These include for example the quantification of measurement uncertainties (often taken as the standard deviation of a known probability distribution over the possible values that could be assigned to a measured quantity) and numerical errors. However, the analysis of uncertainty propagation in complex models and its impact on predicted quantities of interest is more recent and

forms an active and innovative area of research. The goal is to systematically quantify uncertainties and errors in models, simulations and experiments.

We start by introducing different natures and sources of arising uncertainties. In our application of cloud modeling, as well as in related physical models, uncertainties and errors arise in the modeling, simulation and experimental components. The following distinction of uncertainties depending on their different sources can be made:

- **Experimental uncertainties:** Two main sources of uncertainty and errors in experiments are incomplete data and limited accuracy or the resolution of sensors.
- **Model and input uncertainties:** Model uncertainties arise from model errors and input uncertainties due to, for example, uncertain parameters and initial and boundary conditions. The modeling errors are due to an approximate or imprecise representation of underlying physical processes and the input uncertainties are due to the fact that all models contain parameters that must be specified before the model can be used, e.g., initial or boundary conditions for differential equation models. These are uncertainties that must be quantified and propagated through the models. Estimating input uncertainties for a model using measured data is often referred to as *inverse uncertainty quantification*. In this work, we will focus on the *forward uncertainty quantification*, where various sources of uncertainty are propagated through the model. Especially in coupled models or models with a coupling of multiscale or multiphysics phenomena, as in cloud modeling, this is a challenging task and an active area of research.
- **Numerical uncertainties:** Numerical uncertainties are, for example, roundoff errors as well as coding errors and hardware failures. They belong to the least uncertain component of predictive sciences.

The scope of this chapter will be to quantify model and input uncertainties in cloud modeling. We consider sampling methods and spectral representations to propagate uncertainties through models. For different techniques such as direct evaluation for linearly parameterized models or perturbation methods, we refer to [113]. In the sequel, we will focus on the stochastic Galerkin method to establish numerical methods for the stochastic models (M2) and (M3). Since we want to further compare the stochastic Galerkin method to the Monte Carlo and the stochastic collocation approach in Section 7.3, we will also briefly address these approaches.

Sampling methods

These methods are widely used to propagate uncertainties in nonlinear problems. They include the well-known *Monte Carlo method*. The sampling technique has the advantage of being independent of the number of parameters and being *nonintrusive* in the sense that existing codes do not need to be modified. This approach is very intuitive and is implemented by randomly sampling from the measurement error and joint input distributions to construct an ensemble of responses from which response statistics can be computed. Additionally, the efficiency is independent of the number of parameters since one can simultaneously sample from each parameter distribution. A drawback of

sampling methods is that they typically exhibit relatively slow convergence rates such as $1/\sqrt{M}$ for the Monte Carlo method, where M is the number of simulations, which is due to the solely statistical nature of the method and the fact that it does not exploit regularity associated with the parameter space. Thus, a large number of response realizations are required to construct a reasonable statistical ensemble. The Latin hypercube, see, e.g., [77, 114], and quasi-Monte Carlo sampling methods, see, e.g., [96, 99], exhibit higher convergence rates, but they are often infeasible for computationally complex problems such as applications involving coupled physics. Still, for problems with large parameter dimensions and with correlated parameters, sampling methods may be the best choice.

Spectral representations

Spectral methods, like the stochastic Galerkin and stochastic collocation method, have better convergence rates. In addition, they represent uncertain inputs in a way that facilitates the evaluation of moments and distributions of the quantities of interest. This is achieved by employing spectral expansions in the stochastic space. Due to the breadth of spectral representation methods, we devote Section 5.2 to this topic. Our main focus will be on the method of our choice, the stochastic Galerkin method.

5.2 Stochastic spectral methods

The objective of spectral methods is to significantly reduce the number of deterministic model simulations required to construct moments of quantities of interest. This is achieved by employing a spectral expansion in the stochastic space which exploits the smoothness and leads to convergence rates faster than the Monte Carlo rates $1/\sqrt{M}$, where M is the number of simulations, for moderate parameter dimensions. The content of this section is based on [113], [144] and [68].

Remark 5.1*:* In this thesis, we will just consider the case of a single random input and thus only present the respective methods for this case. In general, stochastic spectral methods can also be applied to the case with multiple random input parameters. We note that the spectral techniques then require either mutually independent parameters or a representation of the joint posterior density for the implementation. For more details on the case with multiple input parameters, we refer to [113].

Remark 5.2*:* A widely used spectral expansion is the *Karhunen-Loève* expansion which represents a random field according to a spectral decomposition of its correlation function. The Karhunen-Loève expansion is also known as proper orthogonal decomposition or principal component analysis in finite-dimensional settings. The decomposition is bi-orthogonal since the random field is decomposed in terms of components that are both orthogonal over the spatio-temporal domain as well as the underlying probability space. A favorable property is the optimality of the expansion: There is no approximation with the same number of terms which results in a smaller mean-square error. However, the expansion is only applicable to problems where the covariance function of the solution field is known a priori. Since this is not the case for our problem, we will not further discuss this method and refer for more details to [68, 113, 118, 144].

As already mentioned in Chapter 3, the solutions to the stochastic systems (M2) and (M3) are random fields, see Definition 3.6. We construct now a spectral expansion to represent these random fields which facilitates the construction of their moments. Dating back to Wiener, these expansions are often termed *polynomial chaos* or *generalized polynomial chaos* (gPC) expansions, since he first introduced them for constructing a physical theory of chaos, see [142]. Although most of the systems investigated by uncertainty quantification are not chaotic, including ours, the terminology has become established (nonetheless) and also in this work we will utilize it. Thus, in what follows the gPC expansion will refer to the spectral expansion in the stochastic space. To begin with, we will introduce the gPC expansion for the random nonlinear conservation law from (4.1). In Subsections 5.3.1 and 5.3.2, we then extend the approach to the stochastic models (M2) and (M3) and the respective random fields $(\rho q_\ell)(\boldsymbol{x}, t, \omega)$, $\ell \in \{v, c, r\}$, $\rho'(\boldsymbol{x}, t, \omega)$, $(\rho \boldsymbol{u})(\boldsymbol{x}, t, \omega)$ and $(\rho\theta)'(\boldsymbol{x}, t, \omega)$.

Thus, we consider again the nonlinear conservation law from (4.1)

$$w_t + F(w)_x = 0.$$

In the stochastic setting its solution $w(x, t, \omega)\,(= w(x, t, X(\omega)))$ will be a random field. We separate spatio-temporal and random dependencies to obtain in our case of a single random variable the following finite-dimensional representation

$$w^M(x, t, \omega) := \sum_{k=0}^{M} \widehat{w}_k(x, t)\Phi_k(\omega) \approx w(x, t, \omega) \quad \text{with} \quad M \geq 0, \tag{5.1}$$

where $\widehat{w}_k(x, t)$ are deterministic coefficients and $\Phi_k(\omega)(= \Phi_k(X(\omega)))$, $k = 0, \ldots, M$, are polynomials of k-th degree that are orthogonal. This means that they fulfill the following property

$$\int_\Gamma \Phi_k(\omega)\Phi_{k'}(\omega)\,\mathrm{d}P(\omega) = c_k\delta_{kk'} \quad \text{for} \quad 0 \leq k, k' \leq M, \tag{5.2}$$

where $\delta_{kk'}$ is the Kronecker symbol, Γ is the sample space and c_k a constant depending on the probability density function μ.

Remark 5.3*:* Applying the following property of the pushforward measure to (5.2) gives

$$\begin{aligned}\int_\Gamma \Phi_k(\omega)\Phi_{k'}(\omega)\,\mathrm{d}P(\omega) &= \int_{\mathbb{R}} \Phi_k(y)\Phi_{k'}(y)\,\mathrm{d}(P \circ X^{-1})(y) \\ &= \int_{\mathbb{R}} \Phi_k(z)\Phi_{k'}(z)\mu(z)\,\mathrm{d}z = c_k\delta_{kk'} \quad \text{for} \quad 0 \leq k, k' \leq M.\end{aligned}$$

Thus, the polynomials are orthogonal with respect to the probability density function. In general, the pushforward can be used to calculate explicitly integrals over Γ, when the distribution of the random variable X is chosen. In what follows, we will, for simplicity, often omit this pushforward when explicitly calculating the integrals over Γ.

Consequently, the choice of the orthogonal polynomials $\{\Phi_k(\omega)\}_{k=0}^M$ depends on the distribution of the random variable X. As a matter of fact, for many distributions (of X)

	Distribution of X	gPC basis polynomials	Support
Continuous	Gaussian	Hermite	$(-\infty, +\infty)$
	Gamma	Laguerre	$[0, \infty)$
	Beta	Jacobi	$[a, b]$
	Uniform	Legendre	$[a, b]$
Discrete	Poisson	Charlier	$\{0, 1, 2, \dots\}$
	Binomial	Krawtchouck	$\{0, 1, \dots, N\}$
	Negative binomial	Meixner	$\{0, 1, 2, \dots\}$
	Hypergeometric	Hahn	$\{0, 1, \dots, N\}$

Table 5.1: Correspondence of the distribution of a random variable X and the gPC basis polynomials, see [144] and [146], where $a, b \in \mathbb{R}$ and $N \in \mathbb{N}$.

corresponding sets of orthogonal polynomials are known. Table 5.1 states the correspondence of the distribution and the gPC basis polynomials for some common distributions.

The orthogonality (5.2) ensures that the polynomials $\{\Phi_k(\omega)\}_{k=0}^M$ can be used as basis functions to approximate functions in terms of the random variable X. The nature of the approximations was investigated in detail in [144]. Here, we will summarize the most important concepts.

Definition 5.1
Let $w(\omega)$ be a function of a random variable $X(\omega)$ whose probability distribution is given through $\mathcal{F}_X(x) = P(X \leq x)$ and whose support is denoted by I_X. Then w^M is a *strong gPC approximation* if $\|w(\omega) - w^M(\omega)\| \to 0$ as $M \to \infty$ in a proper norm defined on I_X.

An example of a strong approximation is the orthogonal projection. We denote the space of all mean-square integrable functions by

$$L^2_{d\mathcal{F}_X}(I_X) = \{w : I_X \to \mathbb{R} \,|\, \mathbb{E}\left[w^2\right] < \infty\}$$

and then the corresponding norm is given through $\|w\|_{L^2_{d\mathcal{F}_X}} := \sqrt{\mathbb{E}\left[w^2\right]}$. We define the Mth-degree gPC orthogonal projection of $w \in L^2_{d\mathcal{F}_X}(I_X)$ as

$$P_M w := \sum_{k=0}^{M} \widehat{w}_k \Phi_k(\omega) \quad \text{with} \quad \widehat{w}_k = \frac{1}{c_k} \mathbb{E}\left[w(\omega)\Phi_k(\omega)\right],$$

cf. the discrete transforms (5.16) and (5.18). This leads to a mean-square convergence

$$\|w - P_M w\|_{L^2_{d\mathcal{F}_X}} \to 0 \quad \text{as} \quad M \to \infty.$$

Hence the requirement for convergence is L^2-integrability. The rate of convergence will depend on the smoothness of w in terms of the random variable X. More precisely, the smoother w is, the faster is the convergence. For more details on these results, we refer to [144].

A strong gPC approximation also converges in probability.

Definition 5.2
A sequence of random variables $\{X_M\}$ *converges in probability* to the random variable X if for all $\varepsilon > 0$ the following holds

$$\lim_{M\to\infty} P\left(|X_M - X| > \varepsilon\right) = 0.$$

An in probability converging sequence of random variables also converges in distribution.

Definition 5.3
A sequence of random variables $\{X_M\}$ *converges in distribution* or *weakly* to the random variable X if for all points of continuity x of the distribution function $\mathcal{F}_X$ it holds $\mathcal{F}_{X_M}(x) \to \mathcal{F}_X(x)$ as $M \to \infty$.

In practice, the explicit form of $w(\omega)$ in terms of $X(\omega)$ is unknown in most cases. This means that a gPC expansion that converges strongly cannot be constructed. In some cases, however, the distribution of w is known and the approximation can be made to converge in a weak sense, meaning in probability.

Definition 5.4
An approximation w^M is a *weak gPC approximation* of w if w^M converges to w in probability.

A strong gPC approximation is also a weak gPC approximation but not vice versa. We also note that the weak gPC approximation is not unique. If the gPC polynomials can be constructed, as in the case for the distributions listed in Table 5.1, then it is best to use these basis polynomials, since a proper first-order expansion, i.e. $M = 1$, can produce the given distribution exactly. Using a different polynomial basis can still lead to the convergence of the expansion series, but one gets additional approximation errors and a more complex gPC representation. For more details and examples we refer to [144].

In this thesis, we will focus on two distributions of X that are important for meteorological applications:

1. A *uniformly distributed* $X \sim \mathcal{U}(-1, 1)$. In this case, we work with the Legendre polynomials

$$\Phi_k(z) = \sum_{j=0}^{\lfloor \frac{k}{2} \rfloor} (-1)^j \frac{(2k-2j)!}{(k-j)!(k-2j)!j!2^k} z^{k-2j}, \tag{5.3}$$

where $\lfloor \cdot \rfloor$ is the floor function which is given through

$$\left\lfloor \frac{k}{2} \right\rfloor = \begin{cases} \frac{n}{2} & \text{for even } n, \\ \frac{n-1}{2} & \text{for odd } n. \end{cases}$$

For the Legendre polynomials (5.3) the following equality holds

$$\int_{-1}^{1} \Phi_k(z)\Phi_{k'}(z)\,\mathrm{d}z = \frac{2}{2k+1}\delta_{kk'} \quad \text{for} \quad 0 \le k, k' \le M.$$

Since the property of the pushforward measure gives

$$\begin{aligned}\int_\Gamma \Phi_k(X(\omega))\Phi_{k'}(X(\omega))\,\mathrm{d}P(\omega) &= \int_{\mathbb{R}} \Phi_k(y)\Phi_{k'}(y)\,\mathrm{d}(P\circ X^{-1})(y)\\ &= \int_{-1}^{1} \Phi_k(y)\Phi_{k'}(y)\,\mathrm{d}\mathcal{U}(-1,1)(y)\\ &= \int_{-1}^{1} \Phi_k(z)\Phi_{k'}(z)\mu(z)\,\mathrm{d}z\\ &= \frac{1}{2}\int_{-1}^{1} \Phi_k(z)\Phi_{k'}(z)\,\mathrm{d}z,\end{aligned}$$

the coefficient in the orthogonality property (5.2) is given through

$$c_k = \frac{1}{2k+1}. \tag{5.4}$$

2. A *normally distributed* $X \sim \mathcal{N}(\mu_H, \sigma_H^2)$. In this case, we use the following Hermite polynomials

$$\Phi_k(z) = 2^{-\frac{1}{2}k} H_k\left(\frac{z-\mu_H}{\sqrt{2}\sigma_H}\right) \quad \text{with} \quad H_k(z) = (-1)^k \boldsymbol{e}^{z^2}\frac{d^k}{dz^k}\boldsymbol{e}^{-z^2}, \tag{5.5}$$

where μ_H and σ_H are the mean value and the standard deviation of the normal distribution. For the polynomials H_k, $0 \le k \le M$, it holds that

$$\int_{-\infty}^{\infty} H_k(z)H_{k'}(z)\boldsymbol{e}^{-z^2}\,\mathrm{d}z = 2^k\sqrt{\pi}k!\delta_{kk'} \quad \text{for} \quad 0 \le k,k' \le M. \tag{5.6}$$

Using (5.6) and the substitution $\bar{z} = \sqrt{2}\sigma_H z + \mu_H$, we get

$$\begin{aligned}\int_{-\infty}^{\infty} H_k(z)H_{k'}(z)\boldsymbol{e}^{-z^2}\,\mathrm{d}z &= \int_{-\infty}^{\infty} H_k\left(\frac{\bar{z}-\mu_H}{\sqrt{2}\sigma_H}\right) H_{k'}\left(\frac{\bar{z}-\mu_H}{\sqrt{2}\sigma_H}\right)\boldsymbol{e}^{-\frac{(\bar{z}-\mu_H)^2}{2\sigma_H^2}}\frac{1}{\sqrt{2}\sigma_H}\,\mathrm{d}\bar{z}\\ &= 2^k\sqrt{\pi}k!\delta_{kk'} \quad \text{for} \quad 0 \le k,k' \le M.\end{aligned}$$

Dividing the above equation by $2^k\sqrt{\pi}$ leads to

$$\begin{aligned}\int_{-\infty}^{\infty} 2^{-k} H_k\left(\frac{\bar{z}-\mu_H}{\sqrt{2}\sigma_H}\right) H_{k'}\left(\frac{\bar{z}-\mu_H}{\sqrt{2}\sigma_H}\right)\boldsymbol{e}^{-\frac{(\bar{z}-\mu_H)^2}{2\sigma_H^2}}\frac{1}{\sqrt{2\pi\sigma_H^2}}\,\mathrm{d}\bar{z}&\\ = \int_{-\infty}^{\infty} \Phi_k(\bar{z})\,\Phi_{k'}(\bar{z})\,\mu(\bar{z})\,\mathrm{d}\bar{z}&\\ = k!\delta_{kk'} \quad \text{for} \quad 0 \le k,k' \le M.&\end{aligned}$$

From that it follows with

$$\begin{aligned}\int_\Gamma \Phi_k(X(\omega))\Phi_{k'}(X(\omega))\,\mathrm{d}P(\omega) &= \int_{\mathbb{R}} \Phi_k(y)\Phi_{k'}(y)\,\mathrm{d}(P\circ X^{-1})(y)\\ &= \int_{-\infty}^{\infty} \Phi_k(y)\Phi_{k'}(y)\,\mathrm{d}\mathcal{N}(\mu_H,\sigma_H^2)(y)\\ &= \int_{-\infty}^{\infty} \Phi_k(z)\Phi_{k'}(z)\mu(z)\,\mathrm{d}z\end{aligned}$$

that the coefficient in the orthogonality property (5.2) is given through

$$c_k = k!. \tag{5.7}$$

Remark 5.4*:* It is possible to consider other distributions. One just needs to adjust the choice of the polynomials and re-compute the constants c_k, $k = 0,\dots,M$.

The gPC expansion (5.1) has the advantage that statistical and sensitivity analysis can be performed with minimal computational effort once the coefficients have been determined. We state the characterization of the mean and the variance. Higher-order moments and correlation functions can then be computed in a similar manner.

- *Mean*:

$$\begin{aligned}\mathbb{E}[w^M(x,t,\omega)] &= \int_\Gamma w^M(x,t,\omega)\,\mathrm{d}P(\omega) = \int_\Gamma \sum_{k=0}^{M} \widehat{w}_k(x,t)\Phi_k(\omega)\,\mathrm{d}P(\omega)\\ &= \sum_{k=0}^{M} \widehat{w}_k(x,t)\int_\Gamma \Phi_k(\omega)\,\mathrm{d}P(\omega)\\ &= \sum_{k=0}^{M} \widehat{w}_k(x,t)\int_{\mathbb{R}} \Phi_k(y)\,\mathrm{d}(P\circ X^{-1})(y)\\ &= \sum_{k=0}^{M} \widehat{w}_k(x,t)\int_{\mathbb{R}} \Phi_k(z)\mu(z)\,\mathrm{d}z\\ &= \sum_{k=0}^{M} \widehat{w}_k(x,t)\int_{\mathbb{R}} \Phi_k(z)1\mu(z)\,\mathrm{d}z\\ &= \sum_{k=0}^{M} \widehat{w}_k(x,t)\int_{\mathbb{R}} \Phi_k(z)\Phi_0(z)\mu(z)\,\mathrm{d}z\\ &= \sum_{k=0}^{M} \widehat{w}_k(x,t)c_k\delta_{k0}\\ &= \widehat{w}_0(x,t).\end{aligned} \tag{5.8}$$

- *Variance*:

$$
\begin{aligned}
\mathrm{Var}(w^M(x,t,\omega)) = \sigma^2(w^M(x,t,\omega)) &= \mathbb{E}\left[\left(w^M(x,t,\omega) - \mathbb{E}[w^M(x,t,\omega)]\right)^2\right] \\
&= \mathbb{E}\left[\left(w^M(x,t,\omega) - \widehat{w}_0(x,t)\right)^2\right] \\
&= \mathbb{E}\left[\left(\sum_{k=0}^{M} \widehat{w}_k(x,t)\Phi_k(\omega) - \widehat{w}_0(x,t)1\right)^2\right] \\
&= \mathbb{E}\left[\left(\sum_{k=0}^{M} \widehat{w}_k(x,t)\Phi_k(\omega) - \widehat{w}_0(x,t)\Phi_0(\omega)\right)^2\right] \\
&= \mathbb{E}\left[\left(\sum_{k=1}^{M} \widehat{w}_k(x,t)\Phi_k(\omega)\right)^2\right] \\
&= \int_\Gamma \left(\sum_{k=1}^{M} \widehat{w}_k(x,t)\Phi_k(\omega)\right)\left(\sum_{j=1}^{M} \widehat{w}_j(x,t)\Phi_j(\omega)\right) \mathrm{d}P(\omega) \\
&= \int_{\mathbb{R}} \left(\sum_{k=1}^{M} \widehat{w}_k(x,t)\Phi_k(z)\right)\left(\sum_{j=1}^{M} \widehat{w}_j(x,t)\Phi_j(z)\right) \mu(z)\,\mathrm{d}z \\
&= \sum_{k=1}^{M}\sum_{j=1}^{M} \widehat{w}_k(x,t)\widehat{w}_j(x,t) \int_{\mathbb{R}} \Phi_k(z)\Phi_j(z)\mu(z)\,\mathrm{d}z \\
&= \sum_{k=1}^{M}\sum_{j=1}^{M} \widehat{w}_k(x,t)\widehat{w}_j(x,t) c_k \delta_{kj} \\
&= \sum_{k=1}^{M} \left(\widehat{w}_k(x,t)\right)^2 c_k.
\end{aligned}
\tag{5.9}
$$

To determine the coefficients $\{\widehat{w}_k(x,t)\}_{k=0}^M$ in (5.1), we present the stochastic Galerkin method in Subsection 5.2.1 and the stochastic collocation method in Subsection 5.2.2. They work analogously as their deterministic counterparts. In the Galerkin framework, one projects the governing equations onto a finite-dimensional subspace spanned by the polynomial basis functions and ends up with deterministic equations for the spectral expansion coefficients. It is an intrusive method in the sense that existing codes must be modified since the projection step requires discrete transformations for the inner products. In the collocation framework, one approximates the solution of the governing equations at a discrete set of points termed collocation points. These points are typical values in the random variable space used to represent inputs or parameters in the model. Collocation methods are nonintrusive because existing codes can be used to determine the approximate solutions at the collocation points.

5.2.1 Stochastic Galerkin method

The strategy for stochastic Galerkin methods is to project the governing equations onto a finite-dimensional space spanned by appropriate basis functions. Here, we employ polynomials that are orthogonal with respect to the density $\mu(\omega)$ as stated in (5.2). Thus, we are looking for functions $w^M(x,t,\omega)$ which satisfy

$$\left\langle w_t^M(x,t,\omega) + F\left(w^M(x,t,\omega)\right)_x, \Phi_k(\omega)\right\rangle = 0 \quad \text{for} \quad 0 \le k \le M, \tag{5.10}$$

where $\langle\cdot,\cdot\rangle$ is the inner product in our probability space which is given through

$$\langle u, v\rangle = \int_\Gamma u(\omega)v(\omega)\,\mathrm{d}P(\omega) = \int_{\mathbb{R}} u(z)v(z)\mu(z)\,\mathrm{d}z. \tag{5.11}$$

Using (5.1) and (5.2), we can rewrite (5.10) as

$$\begin{aligned}
0 &= \left\langle w_t^M(x,t,\omega) + F\left(w^M(x,t,\omega)\right)_x, \Phi_k(\omega)\right\rangle \\
&= \int_\Gamma \left(w_t^M(x,t,\omega) + F\left(w^M(x,t,\omega)\right)_x \Phi_k(\omega)\right)\,\mathrm{d}P(\omega) \\
&= \int_{\mathbb{R}} \sum_{j=0}^{M} (\widehat{w}_j)_t(x,t)\Phi_j(z)\Phi_k(z)\mu(z)\,\mathrm{d}z + \int_\Gamma F\left(w^M(x,t,\omega)\right)_x \Phi_k(\omega)\,\mathrm{d}P(\omega) \\
&= c_k(\widehat{w}_k)_t(x,t) + \int_\Gamma F\left(w^M(x,t,\omega)\right)_x \Phi_k(\omega)\,\mathrm{d}P(\omega) \quad \text{for} \quad 0 \le k \le M.
\end{aligned} \tag{5.12}$$

To compute the inner product of the nonlinear advection flux F, we will use the discrete transform (DT) and inverse discrete transform (IDT) described below. Their precise definitions depend on the particular choice of polynomials (in our case Legendre or Hermite), but their basic mode of operation is always the same.

- *Discrete transform (DT)*

  The discrete transform starts with the expansion of a function f in the stochastic space

  $$f(\boldsymbol{x},t,\omega) = \sum_{i=0}^{M} \widehat{f}_i(\boldsymbol{x},t)\Phi_i(\omega) \tag{5.13}$$

  and at the end gives the expansion coefficients $\widehat{f}_i(\boldsymbol{x},t)$, $i = 0,\ldots,M$.

The idea is to use the orthogonality property (5.2) as follows

$$\begin{aligned}\int_\Gamma f(\boldsymbol{x},t,\omega)\Phi_k(\omega)\,\mathrm{d}P(\omega) &= \int_\Gamma \sum_{i=0}^{M} \widehat{f}_i(\boldsymbol{x},t)\Phi_i(\omega)\Phi_k(\omega)\,\mathrm{d}P(\omega)\\ &= \sum_{i=0}^{M} \widehat{f}_i(\boldsymbol{x},t)\int_{\mathbb{R}} \Phi_i(z)\Phi_k(z)\mu(z)\,\mathrm{d}z\\ &= \sum_{i=0}^{M} \widehat{f}_i(\boldsymbol{x},t)c_k\delta_{ki}\\ &= c_k\widehat{f}_k(\boldsymbol{x},t).\end{aligned} \tag{5.14}$$

Dividing (5.14) by c_k gives then

$$\begin{aligned}\widehat{f}_k(\boldsymbol{x},t) &= \frac{1}{c_k}\int_\Gamma f(\boldsymbol{x},t,\omega)\Phi_k(\omega)\,\mathrm{d}P(\omega)\\ &= \frac{1}{c_k}\int_{\mathbb{R}} f(\boldsymbol{x},t,z)\Phi_k(z)\mu(z)\,\mathrm{d}z \quad \text{for} \quad 0\le k\le M.\end{aligned} \tag{5.15}$$

We approximate the above integral now by using the respective Gauss quadrature rules depending on the choice of polynomials. For that we will now distinguish between the two cases considered in this thesis, Legendre and Hermite polynomials.

1. Legendre polynomials: In this case the distribution is uniform with the probability density $1/2$. Then (5.15) reduces with (5.4) to

$$\widehat{f}_k(\boldsymbol{x},t) = \frac{2k+1}{2}\int_{-1}^{1} f(\boldsymbol{x},t,z)\Phi_k(z)\,\mathrm{d}z \quad \text{for} \quad 0\le k\le M.$$

   Approximating the integral using the Gauss-Legendre quadrature leads to

$$\begin{aligned}\mathrm{DT}\left[\{f(\boldsymbol{x},t,z_\ell)\}_{\ell=0}^{L}\right] &= \left\{\widehat{f}_k(\boldsymbol{x},t)\right\}_{k=0}^{M}\\ &= \left\{\frac{2k+1}{2}\sum_{l=0}^{L}\beta_\ell f(\boldsymbol{x},t,z_\ell)\Phi_k(z_\ell)\right\}_{k=0}^{M},\end{aligned} \tag{5.16}$$

   where $L+1$ is the number of quadrature points, z_ℓ is the ℓ-th root of Φ_{L+1} and β_ℓ are the Gauss-Legendre quadrature weights, that is

$$\beta_\ell = \frac{2}{(1-z_\ell^2)\left[\frac{\partial}{\partial z}\Phi_{L+1}(z_\ell)\right]^2}.$$

2. Hermite polynomials: Here, we use a general normal distribution with

$$\mu(z) = \frac{1}{\sqrt{2\pi\sigma_H^2}}\boldsymbol{e}^{-\frac{(z-\mu_H)^2}{2\sigma_H^2}}. \tag{5.17}$$

Applying (5.17) and (5.7) to (5.15) leads to

$$\widehat{f}_k(\boldsymbol{x},t) = \frac{1}{k!\sqrt{2\pi\sigma_H^2}} \int_{-\infty}^{\infty} f(\boldsymbol{x},t,z)\Phi_k(z)\boldsymbol{e}^{-\frac{(z-\mu_H)^2}{2\sigma_H^2}}\,\mathrm{d}z \quad \text{for} \quad 0 \le k \le M.$$

Approximating the integral using the Gauss-Hermite quadrature leads to

$$\begin{aligned} \mathrm{DT}\left[\{f(\boldsymbol{x},t,z_\ell)\}_{\ell=0}^{L}\right] &= \left\{\widehat{f}_k(\boldsymbol{x},t)\right\}_{k=0}^{M} \\ &= \left\{\frac{1}{k!\sqrt{2\pi\sigma_H^2}}\sum_{l=0}^{L}\beta_\ell f(\boldsymbol{x},t,z_\ell)\Phi_k(z_\ell)\boldsymbol{e}^{-\frac{(z_\ell-\mu_H)^2}{2\sigma_H^2}+z_\ell^2}\right\}_{k=0}^{M}, \end{aligned} \tag{5.18}$$

where $L+1$ is the number of quadrature points, z_ℓ is the ℓ-th root of Φ_{L+1} and β_ℓ are the Gauss-Hermite quadrature weights, that is

$$\beta_\ell = \frac{2^L(L+1)!\sqrt{\pi}}{(L+1)^2\left[\Phi_L(z_\ell)\right]^2}.$$

- *Inverse discrete transform (IDT)*

  The inverse discrete transform starts with the expansion coefficients $\{\widehat{f}_k(\boldsymbol{x},t)\}_{k=0}^{M}$ and gives as a result the expansion function (5.13). For this direction we just compute the function f straightforwardly through the gPC expansion

$$\mathrm{IDT}\left[\left\{\widehat{f}_k(\boldsymbol{x},t)\right\}_{k=0}^{M}\right] = \{f(\boldsymbol{x},t,\omega_\ell)\}_{l=0}^{L} = \left\{\sum_{k=0}^{M}\widehat{f}_k(\boldsymbol{x},t)\Phi_k(z_\ell)\right\}_{\ell=0}^{L}. \tag{5.19}$$

Remark 5.5*:* The number L can be chosen equal to M, or even higher for a more accurate approximation.

Remark 5.6*:* We stress that the values $\Phi_k(z_\ell)$, $0 \le k \le M$, $0 \le \ell \le L$, which are needed every time either DT or IDT is applied, can be pre-computed for the code efficiency.

Expanding now also F as

$$F(w^M(x,t,\omega)) =: \tilde{F}(x,t,\omega) = \sum_{j=0}^{M}\widehat{\tilde{F}}_j(x,t)\Phi_j(\omega)$$

and using IDT and DT for the inner product as well as the orthogonality property (5.2)

leads to

$$\begin{aligned}\int_\Gamma F\left(w^M(x,t,\omega)\right)_x \Phi_k(\omega)\,\mathrm{d}P(\omega) &= \int_\Gamma F\left(\mathrm{IDT}\left[\{\widehat{w}_j\}_{j=0}^M\right]\right)_x \Phi_k(\omega)\,\mathrm{d}P(\omega)\\ &= \int_\Gamma \left(\sum_{j=0}^M \widehat{\widetilde{F}}_j(x,t)\Phi_j(\omega)\right)_x \Phi_k(\omega)\,\mathrm{d}P(\omega)\\ &= \sum_{j=0}^M \left(\widehat{\widetilde{F}}_j(x,t)\right)_x \int_{\mathbb{R}} \Phi_j(z)\Phi_k(z)\mu(z)\,\mathrm{d}z\\ &= c_k\left(\widehat{\widetilde{F}}_k(x,t)\right)_x.\end{aligned}$$

Then (5.12) simplifies to

$$0 = (\widehat{w}_k)_t(x,t) + \left(\widehat{\widetilde{F}}_k(x,t)\right)_x \quad \text{for} \quad 0 \le k \le M. \tag{5.20}$$

This means that we end up with $M+1$ deterministic equations for the expansion coefficients $\{\widehat{w}_k(x,t)\}_{k=0}^M$.

Remark 5.7*:* The initial conditions for (5.20) are constructed by similarly applying the Galerkin projection as above, see, for example, the projected Dirichlet boundary conditions (7.4) in the case of 2D Rayleigh-Bénard convection.

Remark 5.8*:* There are not many results on the convergence rate of stochastic Galerkin methods, since the numerical analysis of these methods began only recently. For now, the results are restricted to stochastic elliptic partial differential equations. Nevertheless, we briefly want to summarize some achievements. Babuška, Tempone and Zouraris have shown in [7] that the error between w and w^M decreases exponentially with respect to M. In [123], Todor and Schwab have proven exponential convergence rates which are independent of M under the assumption that the expansion coefficients decay exponentially to 0 in the L^∞-norm. Cohen, DeVore and Schwab show in [22] an algebraic decay rate of the gPC expansion under the weaker assumption that the expansion coefficients only have an algebraic decay. Their decay rate only depends on the decay rate of the expansion coefficients and not on M.

Applications of stochastic Galerkin methods to flows in porous media and incompressible and compressible flows can be found in [98, 147] and applications to other problems in physics and engineering can be found in [25, 102, 125, 135, 146].

5.2.2 Stochastic collocation method

The idea of the collocation method is to generate $K+1$ samples $\{z_i\}_{i=0}^K$, the collocation points, from the parameter space with the deterministic code/methods and then enforce the following condition

$$w(x,t,z_i) = w^M(x,t,z_i) \quad \text{for} \quad 0 \le i \le K. \tag{5.21}$$

This provides the necessary constraints to solve for $\{\widehat{w}_k(x,t)\}_{k=0}^M$, since

$$w^M(x,t,z_i) = \sum_{k=0}^{M} \widehat{w}_k(x,t)\Phi_k(z_i) \quad \text{for} \quad 0 \leq i \leq K$$

which can equivalently be written as

$$\begin{pmatrix} \Phi_0(z_0) & \cdots & \Phi_M(z_0) \\ \vdots & & \vdots \\ \Phi_0(z_K) & \cdots & \Phi_M(z_K) \end{pmatrix} \begin{pmatrix} \widehat{w}_0(x,t) \\ \vdots \\ \widehat{w}_M(x,t) \end{pmatrix} = \begin{pmatrix} w^M(x,t,z_0) \\ \vdots \\ w^M(x,t,z_K) \end{pmatrix}.$$

To not obtain an underdetermined system one requires $K \geq M$. If $K > M$ the system is overdetermined and the solution can be found by, e.g., a least squares approximation. We choose $K = M$ and use the quadrature points from the DT as collocation points.

Stochastic collocation methods in the context of physical and engineering applications have been proposed in [82, 143, 145].

5.2.3 Stochastic Galerkin versus collocation method

The stochastic collocation method is an interpolation technique, cf. (5.21), and not a projection method as the stochastic Galerkin method. This is manifested by the fact that the approximation space of the collocation method changes as the number of collocation points changes. The stochastic Galerkin method ensures that the residual of the stochastic governing equations is orthogonal to the linear space spanned by the gPC polynomials. In this sense, its accuracy is optimal in an L^2-sense which can reduce the number of computations required. The accuracy of the stochastic collocation method is dictated by the accuracy of the approximating polynomials. The interpolation error for one parameter and K collocation points decreases with a rate of K^{-a}, where a depends on the regularity of the solution, see [113]. For a fixed accuracy, which is usually measured in terms of the polynomial exactness of the approximation, the collocation methods require the solution of a larger number of equations than the gPC Galerkin method. This suggests that the gPC Galerkin method offers the most accurate solutions involving the least number of equations (especially in multidimensional random spaces).

Disadvantages of the stochastic Galerkin method are that it can only be used for probability densities with associated orthogonal polynomials and that a new system associated with the projection must be developed and implemented. Moreover, it is an intrusive method, since existing codes typically need to be extended to construct the coefficients. In contrast, the collocation method can be applied to general probability densities and it is nonintrusive in the sense that one solves for the K specified collocation points K deterministic problems using the existing code, which can also be easily parallelized.

In general, it is very problem-dependent which method should be preferred. Since the exact cost comparison between the Galerkin and the collocation methods depends on many factors, including error analysis (which is largely unknown) and even coding efforts for the stochastic Galerkin code, it is not always clear which should be the method of choice. In this work, we apply the stochastic Galerkin method and present mostly results

for this method. In Subsection 7.3, we briefly compare the stochastic Galerkin with the stochastic collocation method in the case of a rising warm air bubble. A more extensive comparison is left for future research since this investigation goes beyond the scope of this work.

5.3 Numerical scheme for the stochastic models

In this section, we present our numerical scheme for the stochastic models (M2), see Section 5.3.1, and (M3), see Section 5.3.2. The numerical approximation in the stochastic space is based on a polynomial chaos stochastic Galerkin method which was introduced in Section 5.2.1.

5.3.1 Stochastic cloud microphysics

Here, we describe a generalized polynomial chaos stochastic Galerkin (gPC-SG) method for the model with stochastic cloud dynamics (M2) based on [21]. Such a method belongs to the class of intrusive methods and the use of the Galerkin expansion leads to a system of deterministic equations for the expansion coefficients, see Section 5.2. In the gPC-SG method, the solution is sought in the form of a polynomial expansion

$$\rho q_\ell(\boldsymbol{x},t,\omega) = \sum_{k=0}^{M} (\widehat{\rho q_\ell})_k(\boldsymbol{x},t)\Phi_k(\omega) \quad \text{with} \quad \ell \in \{v,c,r\},\ M \geq 0, \tag{5.22}$$

where $\Phi_k(\omega)$, $k = 0,\dots,M$, fulfill the orthogonality property (5.2).

We use the same expansion for the uncertain coefficients,

$$k_1(\omega) = \sum_{k=0}^{M} (\widehat{k_1})_k \Phi_k(\omega), \quad k_2(\omega) = \sum_{k=0}^{M} (\widehat{k_2})_k \Phi_k(\omega), \quad \alpha(\omega) = \sum_{k=0}^{M} \widehat{\alpha}_k \Phi_k(\omega), \tag{5.23}$$

for the source terms on the RHS of (3.11),

$$\begin{aligned}
\rho\left(-C(\boldsymbol{x},t,\omega) + E(\boldsymbol{x},t,\omega)\right) &=: R_1(\boldsymbol{x},t,\omega) = \sum_{k=0}^{M} (\widehat{r_1})_k(\boldsymbol{x},t)\Phi_k(\omega),\\
\rho\left(C(\boldsymbol{x},t,\omega) - A_1(\boldsymbol{x},t,\omega) - A_2(\boldsymbol{x},t,\omega)\right) &=: R_2(\boldsymbol{x},t,\omega) = \sum_{k=0}^{M} (\widehat{r_2})_k(\boldsymbol{x},t)\Phi_k(\omega),\\
\rho\left(A_1(\boldsymbol{x},t,\omega) + A_2(\boldsymbol{x},t,\omega) - E(\boldsymbol{x},t,\omega)\right) &=: R_3(\boldsymbol{x},t,\omega) = \sum_{k=0}^{M} (\widehat{r_3})_k(\boldsymbol{x},t)\Phi_k(\omega),
\end{aligned} \tag{5.24}$$

as well as for the raindrop fall velocity,

$$v_q(\boldsymbol{x},t,\omega) = \sum_{k=0}^{M} (\widehat{v_q})_k(\boldsymbol{x},t)\Phi_k(\omega). \tag{5.25}$$

Since the Navier-Stokes equations stay deterministic, $\rho(\boldsymbol{x},t) = \widehat{\rho}_0(\boldsymbol{x},t)$ and thus we also obtain

$$\begin{aligned} q_\ell(\boldsymbol{x},t,\omega) &= \sum_{k=0}^{M} (\widehat{q_\ell})_k(\boldsymbol{x},t)\Phi_k(\omega) \\ \text{with} \quad (\widehat{q_\ell})_k(\boldsymbol{x},t) &= \frac{(\widehat{\rho q_\ell})_k(\boldsymbol{x},t)}{\rho(\boldsymbol{x},t)} \quad \text{for } \ell \in \{v,c,r\},\ k = 0,\dots,M. \end{aligned} \tag{5.26}$$

We note that in the case in which $\rho(\boldsymbol{x},t)$ is very small, the computation of the coefficients $(\widehat{q_\ell})_k(\boldsymbol{x},t)$ should be desingularized, e.g., by

$$(\widehat{q_\ell})_k(\boldsymbol{x},t) = \begin{cases} \frac{(\widehat{\rho q_\ell})_k(\boldsymbol{x},t)}{\rho(\boldsymbol{x},t)} & \text{if } \rho(\boldsymbol{x},t) \geq \varepsilon, \\ 0 & \text{otherwise,} \end{cases} \quad \text{for } \ell \in \{v,c,r\},\ k = 0,\dots,M,$$

where ε is a small a priori chosen positive number. The choice of ε depends on which values of $\rho(\boldsymbol{x},t)$ may be considered negligible for the problem at hand. In our case, $\varepsilon = 10^{-16}$ is a possible choice. For further details we refer to [66, formulae (5.16)–(5.18)] and references therein.

Applying the Galerkin projection to (3.11) yields

$$\begin{aligned} \langle (\rho q_v)_t + \nabla\cdot(\rho q_v \boldsymbol{u} - \mu_q \rho \nabla q_v)\,, \Phi_k\rangle &= \langle \rho(-C+E), \Phi_k\rangle\,, \\ \langle (\rho q_c)_t + \nabla\cdot(\rho q_c \boldsymbol{u} - \mu_q \rho \nabla q_c)\,, \Phi_k\rangle &= \langle \rho(C-A_1-A_2), \Phi_k\rangle\,, \\ \langle (\rho q_r)_t + \nabla\cdot(\rho q_r(-v_q \boldsymbol{e_d} + \boldsymbol{u}) - \mu_q \rho \nabla q_r)\,, \Phi_k\rangle &= \langle \rho(A_1+A_2-E), \Phi_k\rangle\,, \end{aligned} \tag{5.27}$$

for $k = 0,\dots,M$. We now substitute (5.22), (5.24)–(5.26) into (5.27) and use the orthogonality property (5.2) to obtain the following $3(M+1)$ deterministic equations for the gPC coefficients of the cloud variables:

$$\begin{aligned} \frac{\partial}{\partial t}(\widehat{\rho q_v})_k + \sum_{s=1}^{d}\left[\frac{\partial}{\partial x_s}\left((\widehat{\rho q_v})_k u_s\right) - \mu_q\left(\frac{\partial \rho}{\partial x_s}\frac{\partial}{\partial x_s}(\widehat{q_v})_k + \rho\frac{\partial^2}{\partial x_s^2}(\widehat{q_v})_k\right)\right] &= (\widehat{r_1})_k, \\ \frac{\partial}{\partial t}(\widehat{\rho q_c})_k + \sum_{s=1}^{d}\left[\frac{\partial}{\partial x_s}\left((\widehat{\rho q_c})_k u_s\right) - \mu_q\left(\frac{\partial \rho}{\partial x_s}\frac{\partial}{\partial x_s}(\widehat{q_c})_k + \rho\frac{\partial^2}{\partial x_s^2}(\widehat{q_c})_k\right)\right] &= (\widehat{r_2})_k, \\ \frac{\partial}{\partial t}(\widehat{\rho q_r})_k + \sum_{s=1}^{d}\left[\frac{\partial}{\partial x_s}\left((\widehat{\rho q_r})_k u_s - \delta_{sd}\widehat{a}_k\right) - \mu_q\left(\frac{\partial \rho}{\partial x_s}\frac{\partial (\widehat{q_r})_k}{\partial x_s} + \rho\frac{\partial^2 (\widehat{q_r})_k}{\partial x_s^2}\right)\right] &= (\widehat{r_3})_k, \end{aligned} \tag{5.28}$$

for $k = 0,\dots,M$. Here, the coefficients $\{\widehat{a}_k\}_{k=0}^{M}$ are obtained using the following expansion:

$$\begin{aligned} v_q(\boldsymbol{x},t,\omega)(\rho q_r)(\boldsymbol{x},t,\omega) &= \sum_{j=0}^{M}(\widehat{v_q})_j(\boldsymbol{x},t)\Phi_j(\omega)\sum_{m=0}^{M}(\widehat{\rho q_r})_m(\boldsymbol{x},t)\Phi_m(\omega) \\ &=: \sum_{k=0}^{M}\widehat{a}_k(\boldsymbol{x},t)\Phi_k(\omega). \end{aligned}$$

The coefficients $\{(\widehat{r_1})_k, (\widehat{r_2})_k, (\widehat{r_3})_k, \widehat{a}_k\}_{k=0}^M$ are calculated via discrete transform (DT), see (5.16), (5.18), and inverse discrete transform (IDT), see (5.19), which were introduced in Subsection 5.2.1. To be precise,

$$\{(\widehat{r_1})_k\}_{k=0}^M = \mathrm{DT}\left[R_1\left(\mathrm{IDT}\left[\{(\widehat{\rho q_v})_k\}_{k=0}^M\right], \mathrm{IDT}\left[\{(\widehat{\rho q_c})_k\}_{k=0}^M\right], \mathrm{IDT}\left[\{(\widehat{\rho q_r})_k\}_{k=0}^M\right]\right)\right], \tag{5.29}$$

and the coefficients $\{(\widehat{r_2})_k, (\widehat{r_3})_k, \widehat{a}_k\}_{k=0}^M$ are computed analogously. Thus, the system for the expansion coefficients of the cloud variables (5.28) is fully determined.

What is left to discuss is the coupling to the Navier-Stokes equations. As already stated in (3.12), this is realized by using the expected values of the cloud variables in the energy source term. We compute the expected values as in (5.8).

5.3.2 Fully stochastic model

In this subsection, we apply the gPC-SG method to the fully stochastic cloud model (M3). We follow the approach of the previous Subsection 5.3.1 for the stochastic cloud microphysics and add the approach for the Navier-Stokes equations. Due to this, some of the steps and notations of Subsection 5.3.1 will be repeated and for others, we will refer to the respective equations and explanations in Subsection 5.3.1.

We start again by representing the solution in the form of a polynomial expansion, that is,

$$\begin{aligned} \rho'(\boldsymbol{x},t,\omega) &= \sum_{k=0}^M (\widehat{\rho'})_k(\boldsymbol{x},t)\Phi_k(\omega), \quad \rho\boldsymbol{u}(\boldsymbol{x},t,\omega) = \sum_{k=0}^M (\widehat{\rho\boldsymbol{u}})_k(\boldsymbol{x},t)\Phi_k(\omega), \\ (\rho\theta)'(\boldsymbol{x},t,\omega) &= \sum_{k=0}^M (\widehat{(\rho\theta)'})_k(\boldsymbol{x},t)\Phi_k(\omega) \end{aligned} \tag{5.30}$$

and

$$\rho q_\ell(\boldsymbol{x},t,\omega) = \sum_{k=0}^M (\widehat{\rho q_\ell})_k(\boldsymbol{x},t)\Phi_k(\omega) \quad \text{with} \quad \ell \in \{v,c,r\},\ M \geq 0, \tag{5.31}$$

where $\Phi_k(\omega)$, $k = 0,\dots,M$, are polynomials of k-th degree that are orthogonal with respect to the probability density function μ. This implies that the orthogonality property (5.2) holds.

We use the same expansion for the source term S_θ of the energy equation in the Navier-Stokes system (5.35), see (3.2) for its definition,

$$S_\theta(\boldsymbol{x},t,\omega) = \sum_{k=0}^M (\widehat{S_\theta})_k(\boldsymbol{x},t)\Phi_k(\omega), \tag{5.32}$$

for the uncertain coefficients,

$$k_1(\omega) = \sum_{k=0}^M (\widehat{k_1})_k\Phi_k(\omega), \quad k_2(\omega) = \sum_{k=0}^M (\widehat{k_2})_k\Phi_k(\omega), \quad \alpha(\omega) = \sum_{k=0}^M \widehat{\alpha}_k\Phi_k(\omega),$$

for the source terms on the RHS of the cloud microphysics equations

$$\begin{aligned}
\rho\left(-C(\boldsymbol{x},t,\omega)+E(\boldsymbol{x},t,\omega)\right) &=: R_1(\boldsymbol{x},t,\omega) = \sum_{k=0}^{M}(\widehat{r_1})_k(\boldsymbol{x},t)\Phi_k(\omega),\\
\rho\left(C(\boldsymbol{x},t,\omega)-A_1(\boldsymbol{x},t,\omega)-A_2(\boldsymbol{x},t,\omega)\right) &=: R_2(\boldsymbol{x},t,\omega) = \sum_{k=0}^{M}(\widehat{r_2})_k(\boldsymbol{x},t)\Phi_k(\omega),\\
\rho\left(A_1(\boldsymbol{x},t,\omega)+A_2(\boldsymbol{x},t,\omega)-E(\boldsymbol{x},t,\omega)\right) &=: R_3(\boldsymbol{x},t,\omega) = \sum_{k=0}^{M}(\widehat{r_3})_k(\boldsymbol{x},t)\Phi_k(\omega),
\end{aligned} \tag{5.33}$$

as well as for the raindrop fall velocity,

$$v_q(\boldsymbol{x},t,\omega) = \sum_{k=0}^{M}(\widehat{v_q})_k(\boldsymbol{x},t)\Phi_k(\omega). \tag{5.34}$$

Applying the Galerkin projection to (M3) yields

$$\begin{aligned}
\left\langle (\rho')_t + \nabla\cdot\left(\rho\boldsymbol{u}\right), \Phi_k\right\rangle &= 0,\\
\left\langle (\rho\boldsymbol{u})_t + \nabla\cdot\left(\rho\boldsymbol{u}\otimes\boldsymbol{u} + p'\mathrm{Id} - \mu_m\rho\left(\nabla\boldsymbol{u}+(\nabla\boldsymbol{u})^T\right)\right), \Phi_k\right\rangle &= \left\langle -\rho' g\boldsymbol{e_d}, \Phi_k\right\rangle,\\
\left\langle ((\rho\theta)')_t + \nabla\cdot\left(\rho\theta\boldsymbol{u} - \mu_h\rho\nabla\theta\right), \Phi_k\right\rangle &= \left\langle S_\theta, \Phi_k\right\rangle
\end{aligned} \tag{5.35}$$

and

$$\begin{aligned}
\left\langle (\rho q_v)_t + \nabla\cdot\left(\rho q_v\boldsymbol{u} - \mu_q\rho\nabla q_v\right), \Phi_k\right\rangle &= \left\langle \rho(-C+E), \Phi_k\right\rangle,\\
\left\langle (\rho q_c)_t + \nabla\cdot\left(\rho q_c\boldsymbol{u} - \mu_q\rho\nabla q_c\right), \Phi_k\right\rangle &= \left\langle \rho(C-A_1-A_2), \Phi_k\right\rangle,\\
\left\langle (\rho q_r)_t + \nabla\cdot\left(\rho q_r(-v_q\boldsymbol{e_d}+\boldsymbol{u}) - \mu_q\rho\nabla q_r\right), \Phi_k\right\rangle &= \left\langle \rho(A_1+A_2-E), \Phi_k\right\rangle,
\end{aligned} \tag{5.36}$$

for $k = 0,\dots,M$, where $\langle\cdot,\cdot\rangle$ is the scalar product in our probability space which is given through (5.11).

We now substitute (5.30), (5.32) into (5.35) and (5.31), (5.33), (5.34) into (5.36) and use the orthogonality property (5.2) to obtain the following $(d+2)(M+1)$ deterministic equations for the gPC coefficients of the fluid variables

$$\begin{aligned}
\frac{\partial}{\partial t}(\widehat{\rho'})_k + \nabla\cdot(\widehat{\rho\boldsymbol{u}})_k &= 0,\\
\frac{\partial}{\partial t}(\widehat{\rho\boldsymbol{u}})_k + \nabla\cdot\left((\widehat{\boldsymbol{\eta_1}})_k + (\widehat{p'})_k\mathrm{Id}\right) - \mu_m(\widehat{\boldsymbol{d_1}})_k &= -(\widehat{\rho'})_k g\boldsymbol{e_d},\\
\frac{\partial}{\partial t}(\widehat{(\rho\theta)'})_k + \nabla\cdot\left(\bar{\theta}(\widehat{\rho\boldsymbol{u}})_k + (\widehat{\boldsymbol{\eta_2}})_k\right) - \mu_h(\widehat{d_2})_k &= (\widehat{S_\theta})_k,
\end{aligned} \tag{5.37}$$

and $3(M+1)$ deterministic equations for the gPC coefficients of the cloud variables

$$\begin{aligned}
\frac{\partial}{\partial t}(\widehat{\rho q_v})_k + \nabla\cdot((\widehat{\boldsymbol{\eta_1^q}})_k) - \mu_q(\widehat{d_1^q})_k &= (\widehat{r_1})_k,\\
\frac{\partial}{\partial t}(\widehat{\rho q_c})_k + \nabla\cdot((\widehat{\boldsymbol{\eta_2^q}})_k) - \mu_q(\widehat{d_2^q})_k &= (\widehat{r_2})_k,\\
\frac{\partial}{\partial t}(\widehat{\rho q_r})_k + \nabla\cdot((\widehat{\boldsymbol{\eta_3^q}})_k) - \mu_q(\widehat{d_3^q})_k &= (\widehat{r_3})_k,
\end{aligned} \tag{5.38}$$

for $k = 0, \dots, M$. Here, we linearize the pressure by using the expected values for q_v, q_c and q_r when computing R_m, that is,

$$p' = \frac{\mu_m p_0}{\overline{\rho\theta}} \left(\frac{R\overline{\rho\theta}}{p_0} \right)^{\gamma_m} (\rho\theta)' = \frac{\mu_m p_0}{\overline{\rho\theta}} \left(\frac{R\overline{\rho\theta}}{p_0} \right)^{\gamma_m} \sum_{k=0}^{M} (\widehat{(\rho\theta)'})_k \Phi_k$$

with $\gamma_m = \frac{c_p}{c_p - R_m}$ and $R_m = (1 - (\widehat{q_v})_0 - (\widehat{q_c})_0 - (\widehat{q_r})_0)R + (\widehat{q_v})_0 R_v$. In this way the pressure term can still be computed implicitly in time.

Remark 5.9*:* Since the density ρ is stochastic, too, we compute the coefficients $\{(\widehat{q_\ell})_k(\boldsymbol{x}, t)\}_{k=0}^M$, $\ell \in \{v, c, r\}$, in the following way

$$\{(\widehat{q_\ell})_k(\boldsymbol{x}, t)\}_{k=0}^M = \mathrm{DT} \left[\frac{\mathrm{IDT}\left[\{(\widehat{\rho q_\ell})_k(\boldsymbol{x}, t)\}_{k=0}^M\right]}{\mathrm{IDT}\left[\{\widehat{\rho'}_k(\boldsymbol{x}, t)\}_{k=0}^M\right] + \bar{\rho}(\boldsymbol{x})} \right], \tag{5.39}$$

where DT and IDT are the discrete and inverse discrete transforms described in Subsection 5.2.1.

The coefficients $\{(\widehat{r_1})_k, (\widehat{r_2})_k, (\widehat{r_3})_k\}_{k=0}^M$ are calculated as in (5.29) and analogously also the source term $\{(\widehat{S_\theta})_k\}_{k=0}^M$ in the energy equation is determined.

Additionally, we have the coefficients $\{(\widehat{\boldsymbol{\eta_1}})_k\}_{k=0}^M = \{\{(\widehat{\boldsymbol{\eta_1}})_k^s\}_{s=1}^d\}_{k=0}^M$, $\{(\widehat{\boldsymbol{\eta_2}})_k\}_{k=0}^M$ and $\{(\widehat{\boldsymbol{d_1}})_k\}_{k=0}^M$, $\{(\widehat{d_2})_k\}_{k=0}^M$ resulting from the nonlinear terms of the Navier-Stokes system. They are obtained through DT and IDT in a similar manner as in (5.39). Here, $\{(\widehat{\underline{\boldsymbol{\eta_1}}})_k\}_{k=0}^M$ and $\{(\widehat{\boldsymbol{\eta_2}})_k\}_{k=0}^M$ denote the nonlinear advection coefficients which are given by

$$\begin{aligned}
\nabla \cdot (\rho \boldsymbol{u} \otimes \boldsymbol{u}) &= \left(\sum_{s=1}^{d} \frac{\partial(\rho u_l u_s)}{\partial x_s} \right)_{l=1}^{d} \overset{\mathrm{IDT,\,DT}}{=:} \sum_{s=1}^{d} \sum_{k=0}^{M} \frac{\partial(\widehat{\boldsymbol{\eta_1}})_k^s}{\partial x_s} \Phi_k \\
&= \sum_{k=0}^{M} \nabla \cdot (\widehat{\underline{\boldsymbol{\eta_1}}})_k \Phi_k, \\
\nabla \cdot (\theta' \rho \boldsymbol{u}) &= \sum_{s=1}^{d} \frac{\partial(\theta' \rho u_s)}{\partial x_s} = \sum_{s=1}^{d} \frac{\partial}{\partial x_s} \left(\sum_{j=0}^{M} (\widehat{\theta'})_j \Phi_j \sum_{m=0}^{M} (\widehat{\rho u_s})_m \Phi_m \right) \\
&\overset{\mathrm{IDT,\,DT}}{=:} \sum_{s=1}^{d} \frac{\partial}{\partial x_s} \sum_{k=0}^{M} \left((\widehat{\eta_2})_k \right)_s \Phi_k = \sum_{k=0}^{M} \nabla \cdot (\widehat{\boldsymbol{\eta_2}})_k \Phi_k
\end{aligned} \tag{5.40}$$

and $\{(\widehat{\boldsymbol{d_1}})_k\}_{k=0}^M$ and $\{(\widehat{d_2})_k\}_{k=0}^M$ denote the nonlinear diffusion coefficients which are obtained through

$$\begin{aligned}
\nabla \cdot \left(\rho \left(\nabla \boldsymbol{u} + (\nabla \boldsymbol{u})^T \right) \right) &\overset{\mathrm{IDT,\,DT}}{=:} \sum_{k=0}^{M} (\widehat{\boldsymbol{d_1}})_k \Phi_k, \\
\nabla \cdot (\rho \nabla \theta) &\overset{\mathrm{IDT,\,DT}}{=:} \sum_{k=0}^{M} (\widehat{d_2})_k \Phi_k.
\end{aligned} \tag{5.41}$$

The coefficients $\{(\widehat{\boldsymbol{\eta_1^q}})_k, (\widehat{\boldsymbol{\eta_2^q}})_k, (\widehat{\boldsymbol{\eta_3^q}})_k\}_{k=0}^M$ and $\{(\widehat{d_1^q})_k, (\widehat{d_2^q})_k, (\widehat{d_3^q})_k\}_{k=0}^M$ are the coefficients of the nonlinear terms of the cloud equations which are also obtained through DT and IDT analogously to (5.39). The nonlinear advection coefficients $\{(\widehat{\boldsymbol{\eta_1^q}})_k, (\widehat{\boldsymbol{\eta_2^q}})_k, (\widehat{\boldsymbol{\eta_3^q}})_k\}_{k=0}^M$ are given by

$$\begin{aligned}
\nabla \cdot (\rho q_v \boldsymbol{u}) &= \sum_{s=1}^{d} \frac{\partial(\rho q_v u_s)}{\partial x_s} = \sum_{s=1}^{d} \frac{\partial}{\partial x_s} \left(\sum_{j=0}^{M} (\widehat{\rho q_v})_j \Phi_j \sum_{m=0}^{M} (\widehat{u_s})_m \Phi_m \right) \\
&=: \sum_{k=0}^{M} \nabla \cdot (\widehat{\boldsymbol{\eta_1^q}})_k \Phi_k, \\
\nabla \cdot (\rho q_c \boldsymbol{u}) &=: \sum_{k=0}^{M} \nabla \cdot (\widehat{\boldsymbol{\eta_2^q}})_k \Phi_k, \\
\nabla \cdot (\rho q_r \boldsymbol{u} - \rho q_r v_q \boldsymbol{e_d}) &=: \sum_{k=0}^{M} \nabla \cdot (\widehat{\boldsymbol{\eta_3^q}})_k \Phi_k
\end{aligned} \tag{5.42}$$

and the nonlinear diffusion coefficients $\{(\widehat{d_1^q})_k, (\widehat{d_2^q})_k, (\widehat{d_3^q})_k\}_{k=0}^M$ through

$$\begin{aligned}
\nabla \cdot (\rho \nabla q_v) &=: \sum_{k=0}^{M} (\widehat{d_1^q})_k \Phi_k, \\
\nabla \cdot (\rho \nabla q_c) &=: \sum_{k=0}^{M} (\widehat{d_2^q})_k \Phi_k, \\
\nabla \cdot (\rho \nabla q_r) &=: \sum_{k=0}^{M} (\widehat{d_3^q})_k \Phi_k.
\end{aligned} \tag{5.43}$$

Remark 5.10*:* The expansions (5.40) and (5.42) mean that we first compute the coefficients $\{(\widehat{\boldsymbol{\eta_1}})_k\}_{k=0}^M$, $\{(\widehat{\boldsymbol{\eta_2}})_k\}_{k=0}^M$ and $\{(\widehat{\boldsymbol{\eta_1^q}})_k, (\widehat{\boldsymbol{\eta_2^q}})_k, (\widehat{\boldsymbol{\eta_3^q}})_k\}_{k=0}^M$ through the transforms and then we are able to apply the appropriate approximation of the fluxes as in the deterministic case. In the case of the diffusion (5.41) and (5.43), we apply the discretization for the respective evaluated functions obtained by IDT and then perform DT to get the diffusion coefficients $\{(\widehat{\boldsymbol{d_1}})_k\}_{k=0}^M$, $\{(\widehat{d_2})_k\}_{k=0}^M$ and $\{(\widehat{d_1^q})_k, (\widehat{d_2^q})_k, (\widehat{d_3^q})_k\}_{k=0}^M$.

Remark 5.11*:* In [25] it has been shown that the systems for the expansion coefficients of stochastic hyperbolic conservation laws are not always hyperbolic. The nonlinearity of the hyberbolic system can generate ill-posedness even for some reasonable data. This loss of hyperbolicity could be fixed by the authors through an entropy closure method. The idea is to reformulate the system in terms of entropy variables and then perform an entropy-based spectral discretization. In [25] it was shown that this entropy method always preserves the hyperbolicity of the original stochastic system. Another recent contribution to the loss of hyperbolicity when applying the stochastic Galerkin method to hyperbolic conservation laws was done by the authors in [41]. There the same approach as in [25] was considered, i.e. the entropy closure method or also called intrusive polynomial moment method, to ensure hyperbolicity. Additionally, the authors

proposed a realizability-preserving spatial discretization to handle the case in which the moment vector leaves the so-called realizable set and in which the closure method was not applicable before. In [41] also two techniques to accelerate the method have been presented. The first one uses adaptivity in the number of moments so that only a few moments are used in parts of the domain, where the solutions are well-approximated by low-order moments. This avoids high-order moment representations and costly corresponding high-order quadrature rules. The other technique is applicable for steady state problems and its key idea is to rewrite the intrusive polynomial moment method in a way that some computations can be performed in parallel. In our work we did not observe any stability issues when simulation the benchmark test of a moist smooth air bubble, see Section 7.1, neither with the stochastic cloud dynamics model (M2) nor with the fully stochastic model (M3). But we noticed some loss of stability when simulating Rayleigh-Bénard convection in Section 7.2 with the fully stochastic model (M3). The issue could be resolved by setting modes of the vertical velocity (despite the expected value) to zero when the values are smaller than 10^{-16}. We did not further investigate if this was due to a loss of hyperbolicity or due to some errors close to machine precision.

5.4 Combination with the space-time approximation

We emphasize again that the systems (5.28) and (5.37), (5.38) resulting from (M2) and (M3), respectively, are deterministic, since they are written for the expansion coefficients. This allows us to apply the same finite volume method as in Section 4.3.2 and the same large stability domain explicit time integration method mentioned in Section 4.3.3 for the spatial and temporal discretizations. As mentioned in Remark 5.10, one just has to take care of the transforms DT and IDT for the nonlinear terms.

The time step stability restrictions (4.47) and (4.48) are updated in the following way:

- In the case of the semi-stochastic model (M2), we impose the same stability condition on the time steps as in the deterministic case for the Navier-Stokes equations, see (4.47), and the following one for the cloud equations

$$\max\left(\frac{\mu_q}{h^2}, \max_{s=1,..,d-1}\max_{i=1,...,N}(|(u_s)_i|, |(u_d)_i + v_q(\omega_l)|)\,\frac{d}{h}\right)\,\Delta t^n_{\text{cloud}} < 0.5,$$

  which should be satisfied for all of the roots (Legendre or Hermite) ω_ℓ, $\ell = 0, \ldots, L$.

- In the case of the fully stochastic model (M3), we use two stability conditions, namely,

$$\max\left(\frac{\max(\mu_h, \mu_m)}{h^2}, \max_{s=1,..,d}\max_{i=1,...,N}(|(u_s)_i(\omega_l)|)\,\frac{d}{h}\right)\,\Delta t^n_{\text{NS}} < 0.5$$

  for the Navier-Stokes equations and

$$\max\left(\frac{\mu_q}{h^2}, \max_{s=1,..,d-1}\max_{i=1,...,N}(|(u_s)_i(\omega_l)|, |(u_d)_i(\omega_l) + v_q(\omega_l)|)\,\frac{d}{h}\right)\,\Delta t^n_{\text{cloud}} < 0.5$$

  for the cloud microphysics. Both conditions should be satisfied for all of the roots (Legendre or Hermite) ω_ℓ, $\ell = 0, \ldots, L$.

6 Deterministic numerical experiments

In this chapter, we test the numerical method described in Section 4.3 for the deterministic cloud model (M1). We start by investigating the experimental convergence in Section 6.1 for the benchmark test of the so-called free convection of a moist warm air bubble in 2D in Example 6.1 and 3D in Example 6.2. In Section 6.2, we investigate the structure formation in cloud dynamics through the Rayleigh-Bénard convection. We compare dry and moist Rayleigh-Bénard convection in 2D and 3D by comparing solutions of the Navier-Stokes equations (M1.a) against solutions of the full cloud model (M1). Some of the experiments and results are based on [21].

6.1 Experimental convergence of the numerical scheme

We investigate the convergence of our numerical scheme experimentally with the well-known meteorological benchmark describing the free convection of a smooth warm air bubble, see, e.g., [19, 24]. In Example 6.1, we consider the 2D case and in Example 6.2 the 3D case.

Example 6.1 (**Convergence in time and space in 2D**)

In this experiment, we simulate free convection of a smooth warm air bubble in 2D. Due to the shear friction with the surrounding air at the warm/cold air interface, the warm air bubble rises and deforms axisymmetrically and gradually forms a mushroom-like shape. The bubble is placed at $(2500\,\mathrm{m}, 2000\,\mathrm{m})$ in a domain $\Omega = [0, 5000] \times [0, 5000]\, m^2$ with the initial perturbation:

$$\rho'(\boldsymbol{x}, 0) = -\bar{\rho}(\boldsymbol{x}) \frac{\theta'(\boldsymbol{x}, 0)}{\bar{\theta}(\boldsymbol{x}) + \theta'(\boldsymbol{x}, 0)}, \quad \bar{\rho}(\boldsymbol{x}) = \frac{p_0}{R\bar{\theta}(\boldsymbol{x})} \pi_e(\boldsymbol{x})^{\frac{1}{\gamma-1}}, \quad \pi_e(\boldsymbol{x}) = 1 - \frac{g x_2}{c_p \bar{\theta}},$$

$$\boldsymbol{u}(\boldsymbol{x}, 0) = 0,$$

$$\theta'(\boldsymbol{x}, 0) = \begin{cases} 2\cos^2\left(\frac{\pi r}{2}\right), & r := \sqrt{(x_1 - 2500)^2 + (x_2 - 2000)^2} \leq 2000, \\ 0, & \text{otherwise}, \end{cases}$$

where $\bar{\theta} = 285\,\mathrm{K}$ and $p_0 = \bar{p} = 10^5\,\mathrm{Pa}$. The experiment was simulated in a domain $\Omega = [0, 5000] \times [0, 5000]\,\mathrm{m}^2$. For the cloud variables we choose the following initial

conditions:

$$q_v(\boldsymbol{x},0) = 5\cdot 10^{-3}\,\theta'(\boldsymbol{x},0), \quad q_c = 10^{-4}\,\theta'(\boldsymbol{x},0), \quad q_r = 10^{-6}\,\theta'(\boldsymbol{x},0).$$

We start here with nonzero values for the cloud drops concentration q_c and the rain concentration q_r to avoid values close to machine precision since the main purpose of the test is the convergence study. Furthermore, we apply the no-slip boundary conditions, see (4.21), for the velocities and zero Neumann boundary conditions, see (4.20), for the remaining variables, i.e. $\nabla\rho'\cdot\boldsymbol{n}=0$, $\nabla(\rho\theta)'\cdot\boldsymbol{n}=0$, $\nabla(\rho q_\ell)\cdot\boldsymbol{n}=0$, $\ell\in\{v,c,r\}$.

In Figure 6.3, we show the potential temperature θ and cloud variables q_v, q_c and q_r, computed on a 320×320 mesh at $t=0$ and $100s$ and in Figure 6.4 the same variables at $t=150$ and $200s$. One can clearly observe condensation taking place on the interface between cold and warm air, leading to cloud formation in this region. In consequence, rain forms in the clouds and falls towards the surface. The experimental convergence study for the cloud and flow variables is presented in Tables 6.1 and 6.2, respectively. The experimental order of convergence (EOC) has been computed in the following way:

$$EOC = \log_2\left(\frac{\|v_{N,\Delta t} - v_{2N,\Delta t/2}\|_{L^1(\Omega)}}{\|v_{2N,\Delta t/2} - v_{4N,\Delta t/4}\|_{L^1(\Omega)}}\right),$$

where $v_{N,\Delta t}$ is the numerical solution computed with a fixed time step Δt on a grid with $N\times N$ grid cells. As one can clearly see, the expected second order of accuracy has been achieved. For comparison, we present in Figures 6.1 and 6.2 the errors measured in the L^1-norm, L^2-norm and L^∞-norm. They all give similar results.

Remark 6.1*:* In the following studies, we will thus just present the error plots of the L^1-norms.

N	ρq_v	EOC	ρq_c	EOC	ρq_r	EOC
10	2.89e-01	–	2.49e-01	–	3.22e-02	–
20	8.90e-02	1.80	8.33e-02	1.77	7.98e-03	1.97
40	2.60e-02	1.83	2.16e-02	2.22	2.09e-03	1.93
80	1.07e-02	1.53	7.55e-03	1.79	5.50e-04	1.93
160	4.39e-03	1.74	2.37e-03	1.83	1.41e-04	1.99
320	1.75e-03	1.84	7.38e-04	1.85	3.56e-05	2.00

Table 6.1: Example 6.1: L^1-errors and EOC for the cloud variables computed at time $t=10s$ using $\Delta t = {}^{256}/_{100N}$.

N	ρ'	EOC	ρu_1	EOC	ρu_2	EOC	$(\rho\theta)'$	EOC
10	1.52e+01	–	3.97e+03	–	3.38e+03	–	4.36e+03	–
20	6.72e+00	1.27	1.29e+03	1.75	1.39e+03	1.33	1.90e+03	1.31
40	2.39e+00	1.44	5.09e+02	1.41	5.57e+02	1.41	6.77e+02	1.46
80	7.49e-01	1.73	1.57e+02	1.74	1.53e+02	1.87	2.08e+02	1.76
160	2.00e-01	1.92	4.16e+01	1.91	4.44e+01	1.75	5.54e+01	1.92
320	5.90e-02	1.77	1.14e+01	1.87	1.37e+01	1.69	1.61e+01	1.78

Table 6.2: Example 6.1: L^1-errors and EOC for the Navier-Stokes variables computed at time $t = 10s$ using $\Delta t = {}^{256}/_{100N}$.

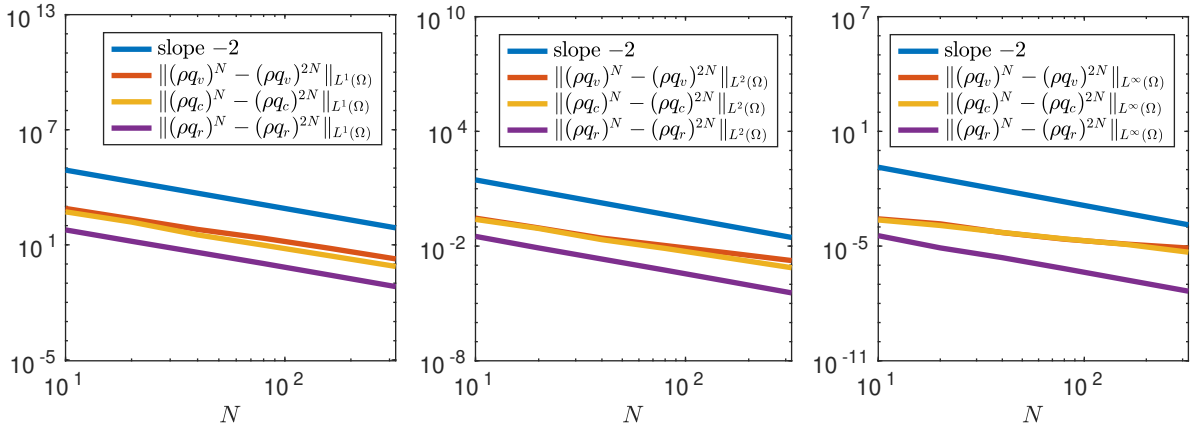

Figure 6.1: Example 6.1: Comparison of different error norms for the cloud variables q_v, q_c and q_r computed at time $t = 10s$ using $\Delta t = {}^{256}/_{100N}$.

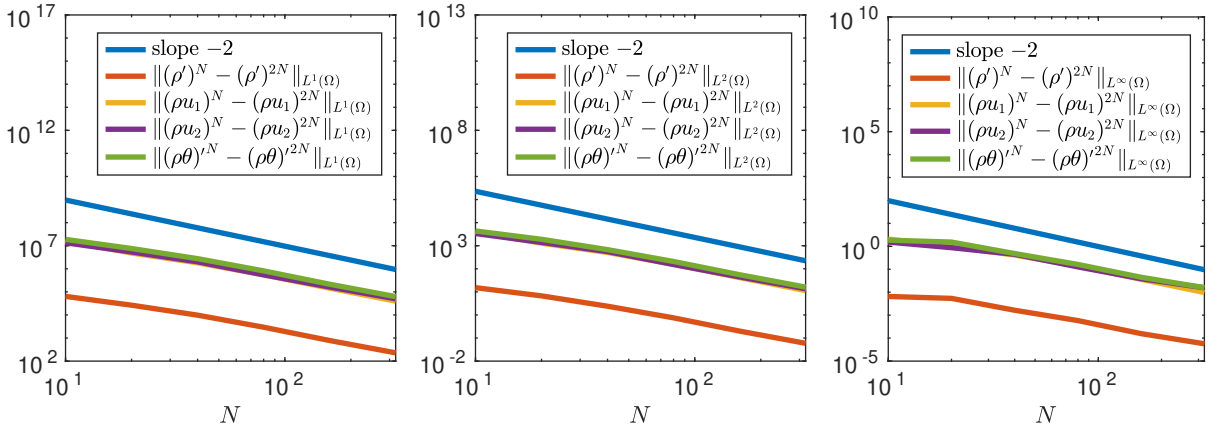

Figure 6.2: Example 6.1: Comparison of different error norms for the flow variables ρ', ρu_1, ρu_2 and $(\rho\theta)'$ at time $t = 10s$ using $\Delta t = {}^{256}/_{100N}$.

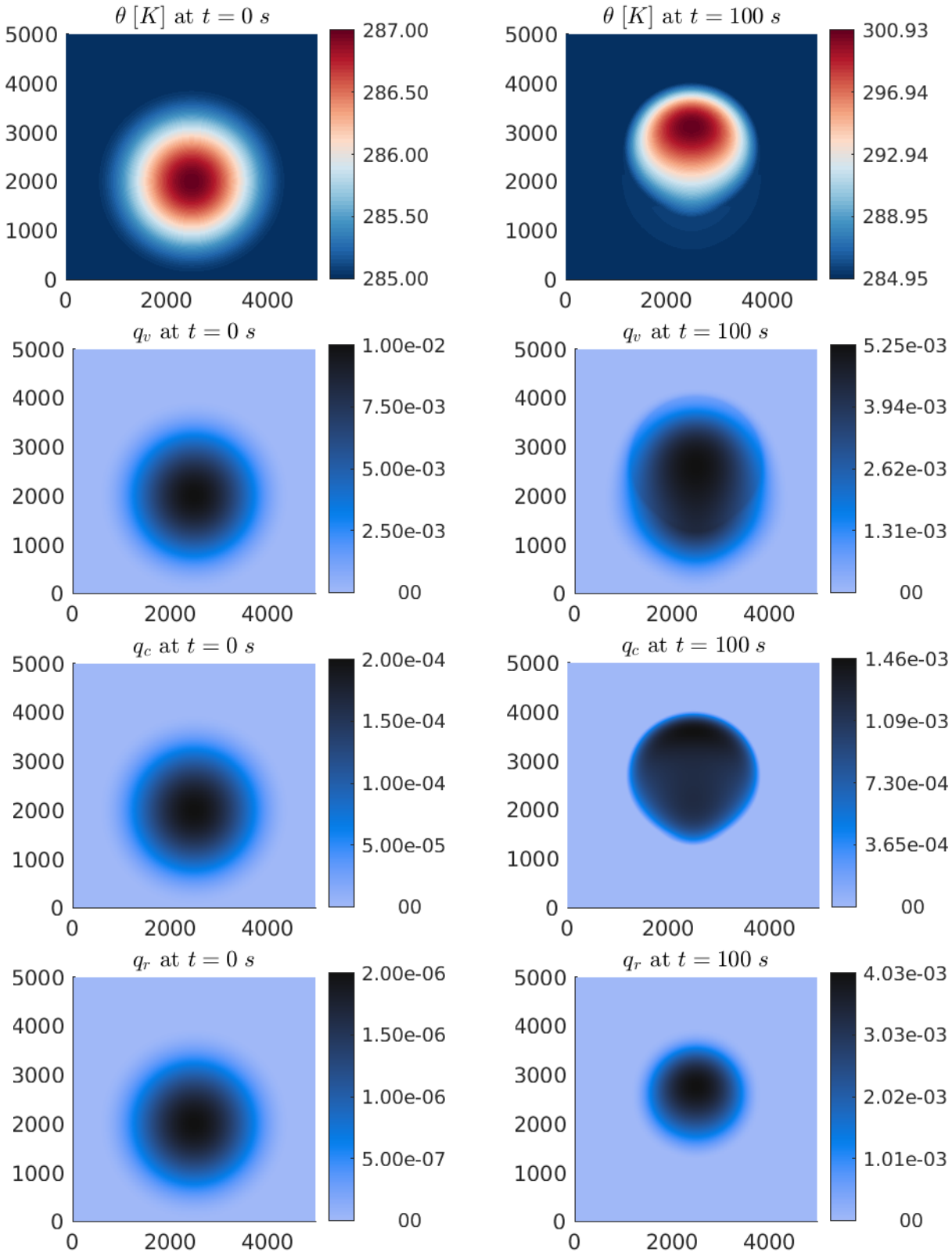

Figure 6.3: Example 6.1: Potential temperature θ, water vapor concentration q_v, cloud drops concentration q_c and rain concentration q_r at times $t = 0$ (left column) and $100s$ (right column) simulated on a 320×320 mesh.

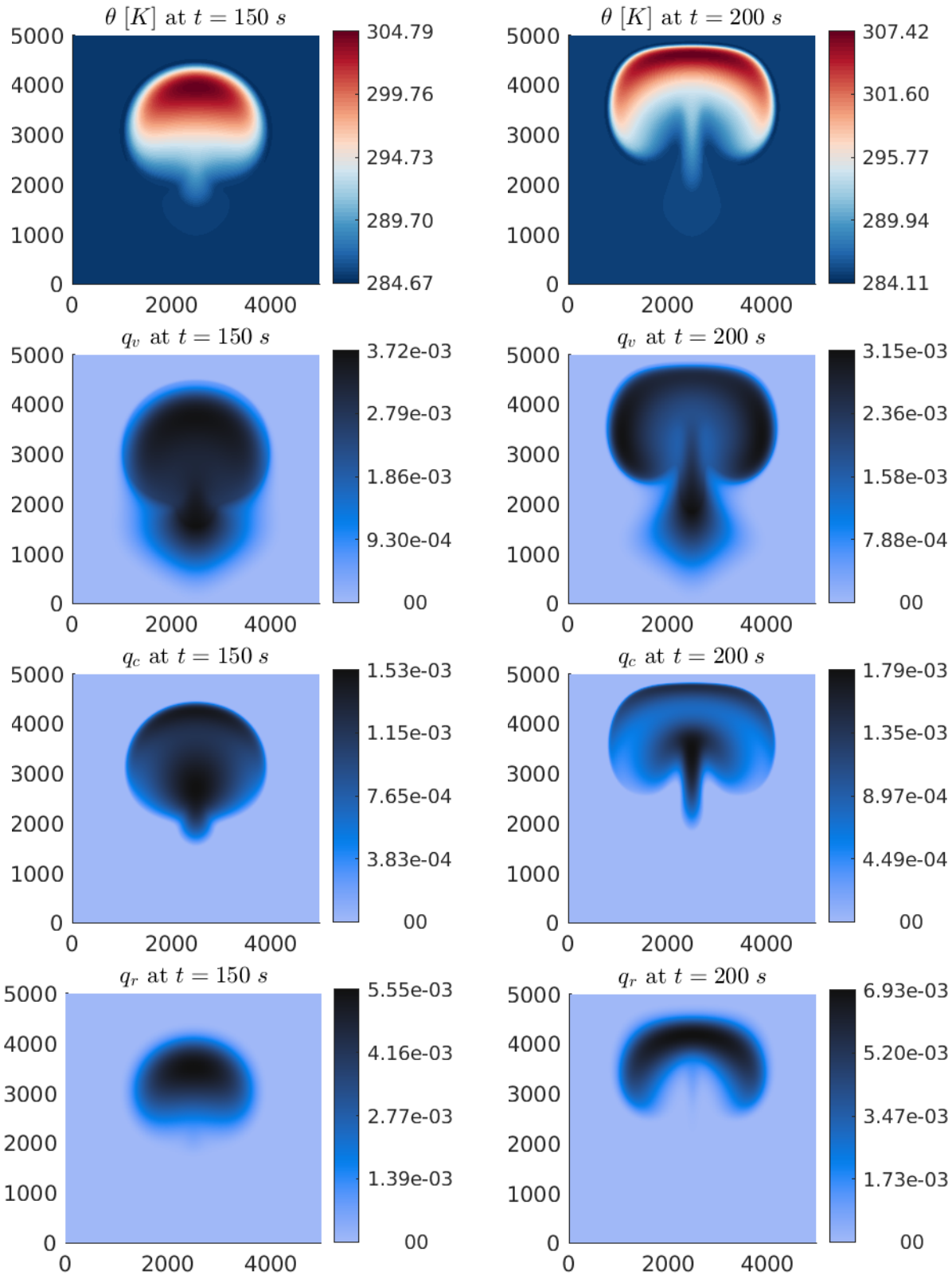

Figure 6.4: Example 6.1: Potential temperature θ, water vapor concentration q_v, cloud drops concentration q_c and rain concentration q_r at times $t = 150$ (left column) and $200s$ (right column) simulated on a 320×320 mesh.

Example 6.2 (**Convergence in time and space in 3D**)

We investigate the convergence of our deterministic numerical scheme in 3D. The test case is the same as in Example 6.1, that is, the free convection of a smooth warm air bubble. The initial and boundary conditions are chosen as in Example 6.1, just extended in an analogous way to 3D, meaning that the bubble is placed at (2500 m, 2500 m, 2000 m) in a domain $\Omega = [0, 5000] \times [0, 5000] \times [0, 5000]\, m^3$.

In Figure 6.5, the errors in time and space are presented. The experimental study shows that the solutions of both systems, the Navier-Stokes (M1.a) and the cloud equations (M1.b), converge with second order accuracy.

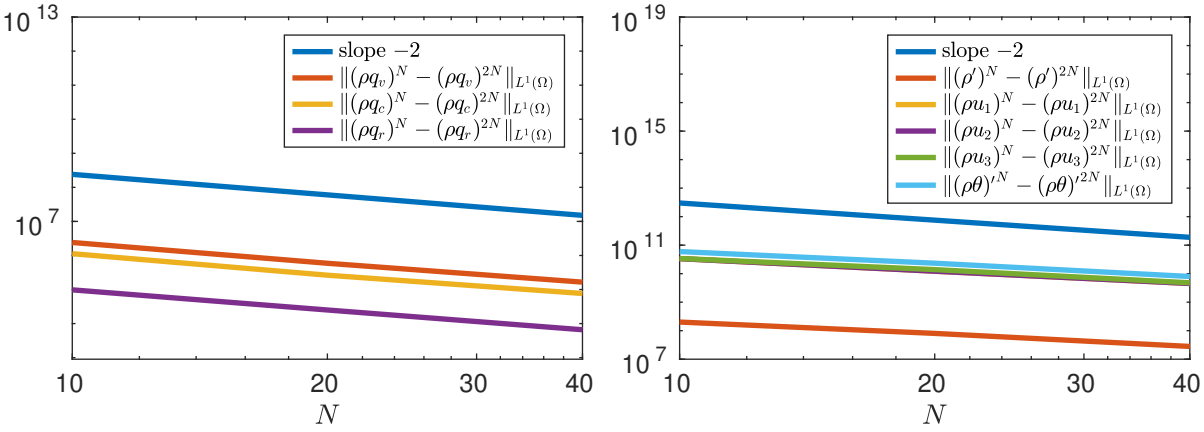

Figure 6.5: Example 6.2: Convergence study for the cloud variables $(\rho q_\ell), \ell \in \{v, c, r\}$, and the flow variables ρ', ρu_1, ρu_2, ρu_3 and $(\rho\theta)'$ in 3D computed at time $t = 10s$ using $\Delta t = {}^{256}/_{100N}$.

6.2 Rayleigh-Bénard convection

In the numerical experiments of this section, we study a natural convection that is used to model structure formation. It occurs in a planar flow between two horizontal plates, where the lower one is heated from below and the upper one is cooled from above. Due to the presence of buoyancy the fluid develops a regular pattern of convection rolls, known as the Bénard cells. In 3D, these convection rolls form additionally hexagonal structures, see, e.g., [5, 43, 100]. In Figure 6.6, the two categories of patterns, rolls and hexagons, are shown. For more details on the Rayleigh-Bénard convection, we refer to the overview paper of Manneville, see [84].

While for the dry case phase diagrams for resulting patterns, as e.g. rolls and hexagons, are available, see, e.g., [15], only little is known about patterns in moist Rayleigh-Bénard convection. Few studies with reduced order models indicate the possibility of roll-like structures or the formation of hexagons, see, e.g., [139], but no results for compressible Navier-Stokes equations coupled with full cloud microphysics are available, at least to our knowledge. Thus, we would expect patterns similar to those evolving in the case of dry convection, although the latent heat release might change these patterns partially. This

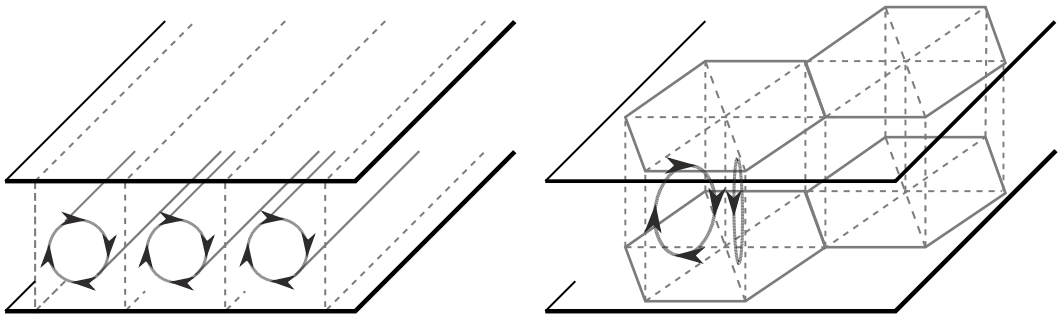

Figure 6.6: Illustration of roll and hexagonal patterns in the Rayleigh-Bénard convection.

effect of moisture is investigated in the experiments of this section. The initial conditions were set up with the help of F. Otto, see [1], and are inspired by the experiments in the works [138, 148]. We start with an initial perturbation of the potential temperature and the velocity in the vertical direction. This perturbation is given by a sine or cosine function which ensures that it is independent of the mesh resolution.

In Example 6.3, we consider dry Rayleigh-Bénard convection in 2D using the Navier-Stokes equations (M1.a) with $S_\theta = 0$. The numerical results show characteristic rolls forming over time. To illustrate the effect of moisture, we repeat the experiment for the full cloud model (M1) including the liquid water phases in Example 6.4. In Example 6.5, we then depict numerical results for two setups of dry Rayleigh-Bénard convection in 3D in which one can clearly observe the formation of cell and roll structures, respectively. In this experiment, we also investigate the effect of different grid resolutions on the structures. The effect on patterns and the influence of moisture in 3D is investigated in Example 6.6.

Remark 6.2*:* Let us note that the Rayleigh-Bénard convection can be understood as a very simplified model for atmospheric convection in the turbulent planetary boundary layer. In [100, 140], numerical simulations for moist Rayleigh-Bénard convection have been realized using the Boussinesq approximation, a simplified equation of state, and the rigid-lid boundary conditions at the top and bottom of the domain. Our mathematical model is more general and takes weakly compressible effects into account.

Example 6.3 (**Dry Rayleigh-Bénard convection in 2D**)

In this experiment, we simulate dry Rayleigh-Bénard convection in 2D by using the Navier-Stokes equations (M1.a). The numerical solutions are computed on a domain $\Omega = [0, 5000] \times [0, 1000]\, m^2$ that has been discretized using 160×160 mesh cells. As initial conditions we used

$$\begin{aligned}
&\rho'(\boldsymbol{x}, 0) = \frac{-\bar{\rho}(\boldsymbol{x})\theta'(\boldsymbol{x}, 0)}{\bar{\theta}(\boldsymbol{x}) + \theta'(\boldsymbol{x}, 0)}, \quad \bar{\rho}(\boldsymbol{x}) = \frac{p_0}{R\bar{\theta}(\boldsymbol{x})}\pi_e(\boldsymbol{x})^{\frac{1}{\gamma-1}}, \quad \pi_e(\boldsymbol{x}) = 1 - \frac{g x_2}{c_p \bar{\theta}(\boldsymbol{x})}, \\
&u_1(\boldsymbol{x}, 0) = 0.001, \quad u_2(\boldsymbol{x}, 0) = \sin\left(2\pi \frac{x_2}{1000}\right), \\
&\theta'(\boldsymbol{x}, 0) = 0.6 \sin\left(2\pi \frac{x_2}{1000}\right), \quad \bar{\theta}(\boldsymbol{x}) = 284 - \frac{x_2}{1000}
\end{aligned} \tag{6.1}$$

and applied Dirichlet boundary conditions, see (4.19), for the potential temperature

$$\theta(x_2 = 0) = 284\,\mathrm{K} \quad \text{and} \quad \theta(x_2 = 1000) = 283\,\mathrm{K}, \tag{6.2}$$

as well as periodic boundary conditions for all variables in horizontal direction, see (4.18), no-slip boundary conditions, see (4.21), for the velocities at the vertical boundaries and zero Neumann conditions, see (4.20), for the remaining variables in vertical direction, i.e. $\nabla\rho' \cdot \boldsymbol{n} = 0$. Since we have an equation for $(\rho\theta)'$ and not for θ, we implement the above Dirichlet boundary conditions (6.2) using $\rho\theta(\boldsymbol{x}, t) = (\rho\theta)'(\boldsymbol{x}, t) + \overline{\rho\theta}(\boldsymbol{x})$ in the following way

$$\begin{aligned}
&(\rho\theta)'(x_2 = 0, t) - \rho'(x_2 = 0, t)\theta(x_2 = 0, t) = \bar{\rho}(x_2 = 0)\theta(x_2 = 0, t) - \overline{\rho\theta}(x_2 = 0) \\
&\Leftrightarrow (\rho\theta)'(x_2 = 0, t) - \rho'(x_2 = 0, t)284 = \bar{\rho}(x_2 = 0)284 - \overline{\rho\theta}(x_2 = 0)
\end{aligned}$$

and

$$\begin{aligned}
(\rho\theta)'(x_2 = 1000, t) - \rho'(x_2 = 1000, t)\theta(x_2 = 1000, t) &= \bar{\rho}(x_2 = 1000)\theta(x_2 = 1000, t) \\
&\quad - \overline{\rho\theta}(x_2 = 1000) \\
\Leftrightarrow (\rho\theta)'(x_2 = 1000, t) - \rho'(x_2 = 1000, t)283 &= \bar{\rho}(x_2 = 1000)283 - \overline{\rho\theta}(x_2 = 1000).
\end{aligned}$$

In Figure 6.7, we present time snapshots of the numerical solution for the potential temperatures at times $t = 3000$, 4000, 5000 and $6000s$. We can clearly see the formation and evolution of a roll pattern. At an early time $t = 3000s$, one can observe the formation of small finger-like structures reaching towards the top of the domain. At later times, more roll dynamics can be seen which then ends in two stable rolls at $t = 6000s$.

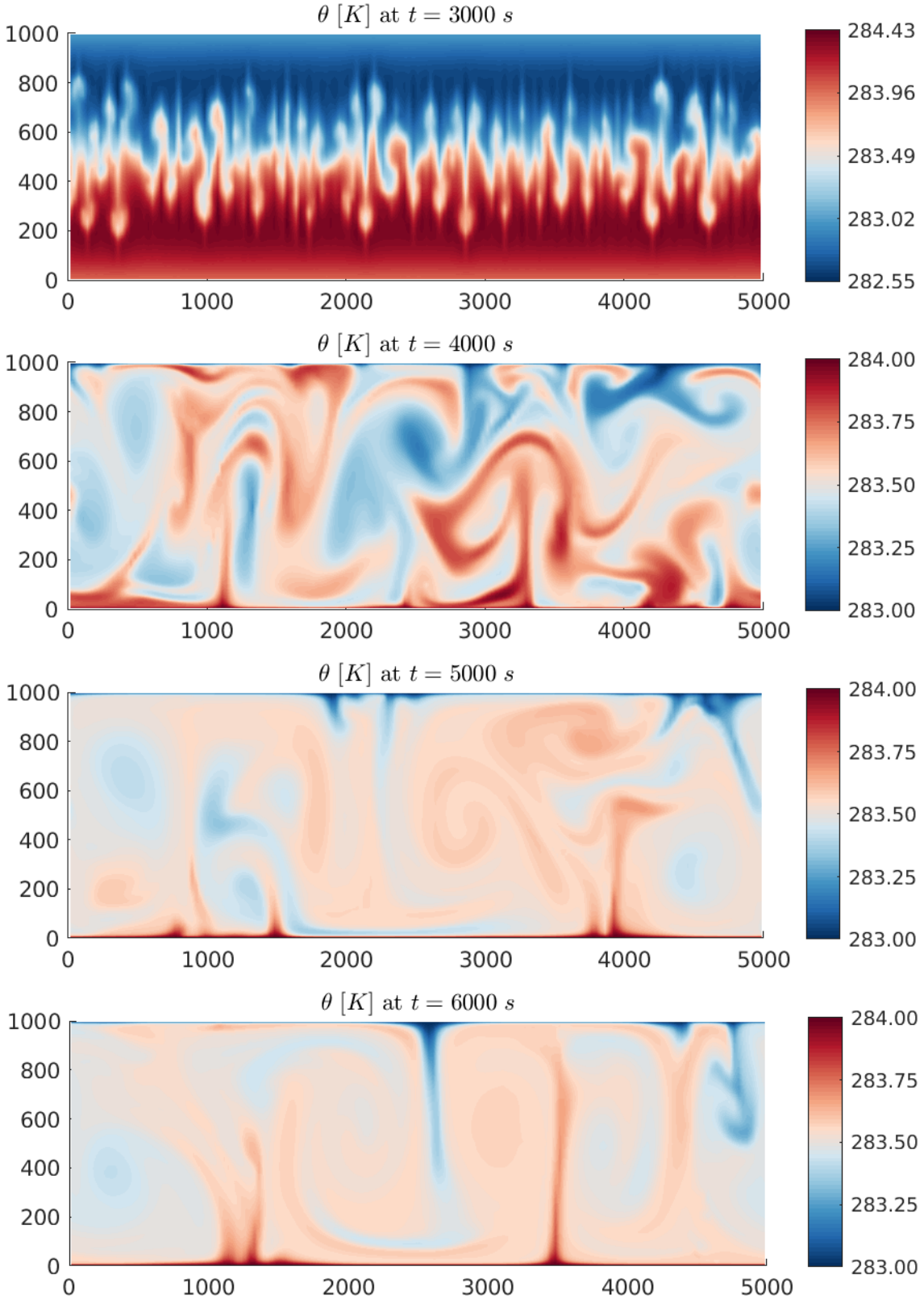

Figure 6.7: Example 6.3: Potential temperature θ at times $t = 3000$, 4000, 5000 and 6000s simulated on a 160×160 mesh.

Example 6.4 (**Moist Rayleigh-Bénard convection in 2D**)

In this example, we investigate the effect of moisture for two-dimensional Rayleigh-Bénard convection with the full cloud model (M1). For this purpose, we apply the same initial and boundary conditions for the Navier-Stokes equations (M1.a) as in the previous Example 6.3, see (6.1). For the cloud variables we add the following initial conditions

$$q_v(\boldsymbol{x},0) = 0.025(\theta'(\boldsymbol{x},0))_+,\ q_c(\boldsymbol{x},0) = 10^{-4}(\theta'(\boldsymbol{x},0))_+,\ q_r(\boldsymbol{x},0) = 10^{-6}(\theta'(\boldsymbol{x},0))_+, \quad (6.3)$$

as well as periodic boundary conditions in horizontal direction and zero Neumann conditions, see (4.20), vertically, i.e. $\nabla(\rho q_\ell)\cdot\boldsymbol{n} = 0$, $\ell \in \{v,c,r\}$. The numerical solution is again computed on a domain $\Omega = [0,5000]\times[0,1000]\,m^2$ that has been discretized using 160×160 mesh cells.

Remark 6.3*:* The chosen initial data for the cloud variables (6.3) is physically not very realistic. To investigate more realistic atmospheric scenarios one would start with no cloud drops and rain concentrations and also the choice of q_v would depend on the saturation mixing ratio q_*. Here, we still chose the above data because we wanted to choose the same initial conditions for all the Rayleigh-Bénard test cases to demonstrate the applicability and effects of the stochasticity. Starting with no cloud drops and rain concentrations was not applicable because the initialization of convection takes too long and thus is computationally too expensive (especially in 3D).

In Figures 6.8 and 6.10–6.12, we present time snapshots of the potential temperature, water vapor mixing ratio, cloud mass and rain mass concentration at times $t = 1000$, 2000, 3000 and $6000s$. In Figure 6.9, we additionally depict snapshots of the difference of the water vapor concentration to the saturation mixing ratio $q_v - q_*$ to highlight the oversaturated and undersaturated regions. One can observe a clear effect of the moisture on the structure formation when comparing the results to those obtained in Example 6.3. The potential temperature is overall much higher due to the latent heating and the formation of convection cells happens much faster, already at time $t = 1000s$, due to a strong buoyancy term. Inside these cells, the potential temperature is enhanced, partly due to the upward transport of higher values from below and partly due to phase changes and thus latent heat release. Also the mass concentrations of water vapor and cloud water follow the structure and show enhanced values inside the finger-like structures reaching to the top of the domain. Clouds form inside the finger-like structures because of oversaturation which can be seen in Figure 6.9. This leads to a high enough cloud water concentration for autoconversion and accretion to take place. Thus, even at this early stage, rain can form. At a later time $t = 2000s$, much larger roll structures, which are similar to the structures in the dry case, see Example 6.3, have formed. In the variables θ, q_v and q_c the spatial convection cells clearly can be seen at time $t = 3000s$ and they stay stable until $t = 6000s$. When comparing Figures 6.9 and 6.11, it can be nicely observed that clouds form and stay in oversaturated regions. In contrast, rain water is not following the convective structure although some larger features can be seen. This is because the rain drops mostly fall down and do not follow so much the vertical motion. In general, smearing due to sedimentation is a major feature of the rain mass concentration. Another feature that can be observed when comparing the potential

temperature at times $t = 2000$ and $t = 6000s$ in Figure 6.8 is the cooling of lower levels due to sedimenting rain water.

All in all, the formation of structure is comparable to the dry case seen in Example 6.3. We can clearly see convection rolls forming. Due to the latent heating, we now observe higher potential temperatures on the top of the domain and the roll structures are more smeared and not as clear as in the dry case. One can also observe more convection cells being formed than just the two stable ones obtained in Example 6.3.

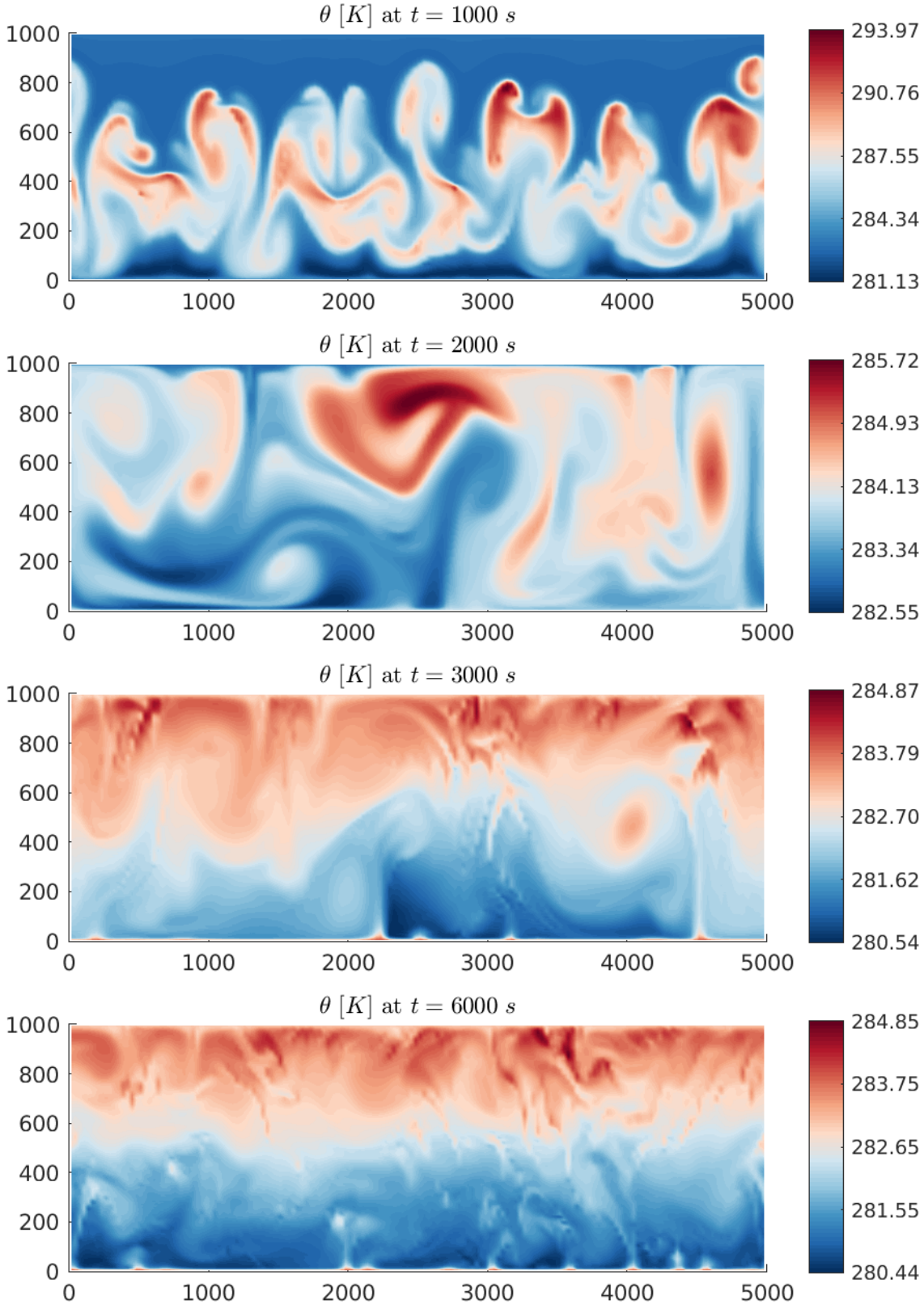

Figure 6.8: Example 6.4: Potential temperature θ at times $t = 1000$, 2000, 3000 and $6000s$ simulated on a 160×160 mesh.

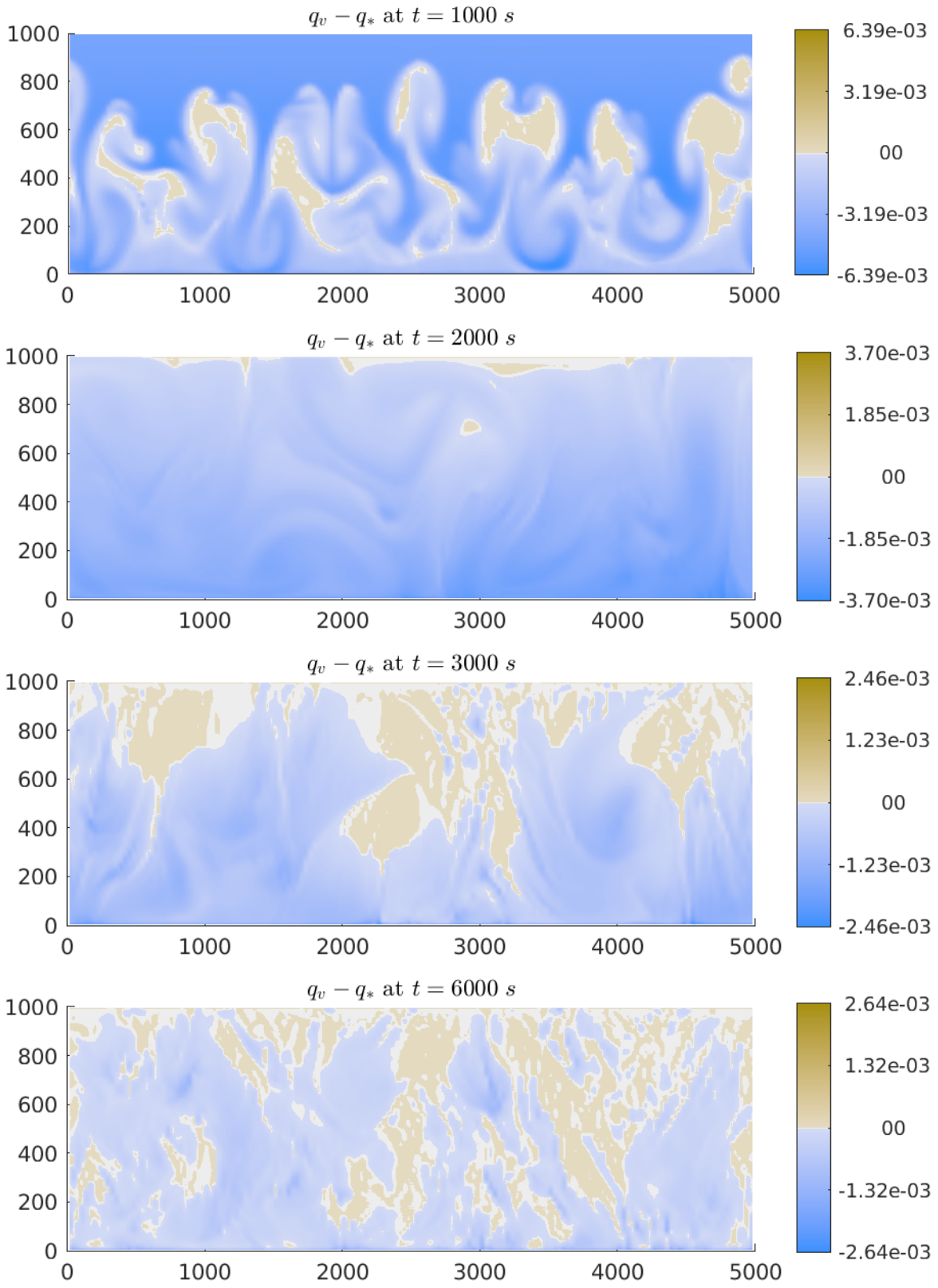

Figure 6.9: Example 6.4: Difference of water vapor to the saturation mixing ratio $q_v - q_*$ at times $t = 1000$, 2000, 3000 and $6000s$ simulated on a 160×160 mesh.

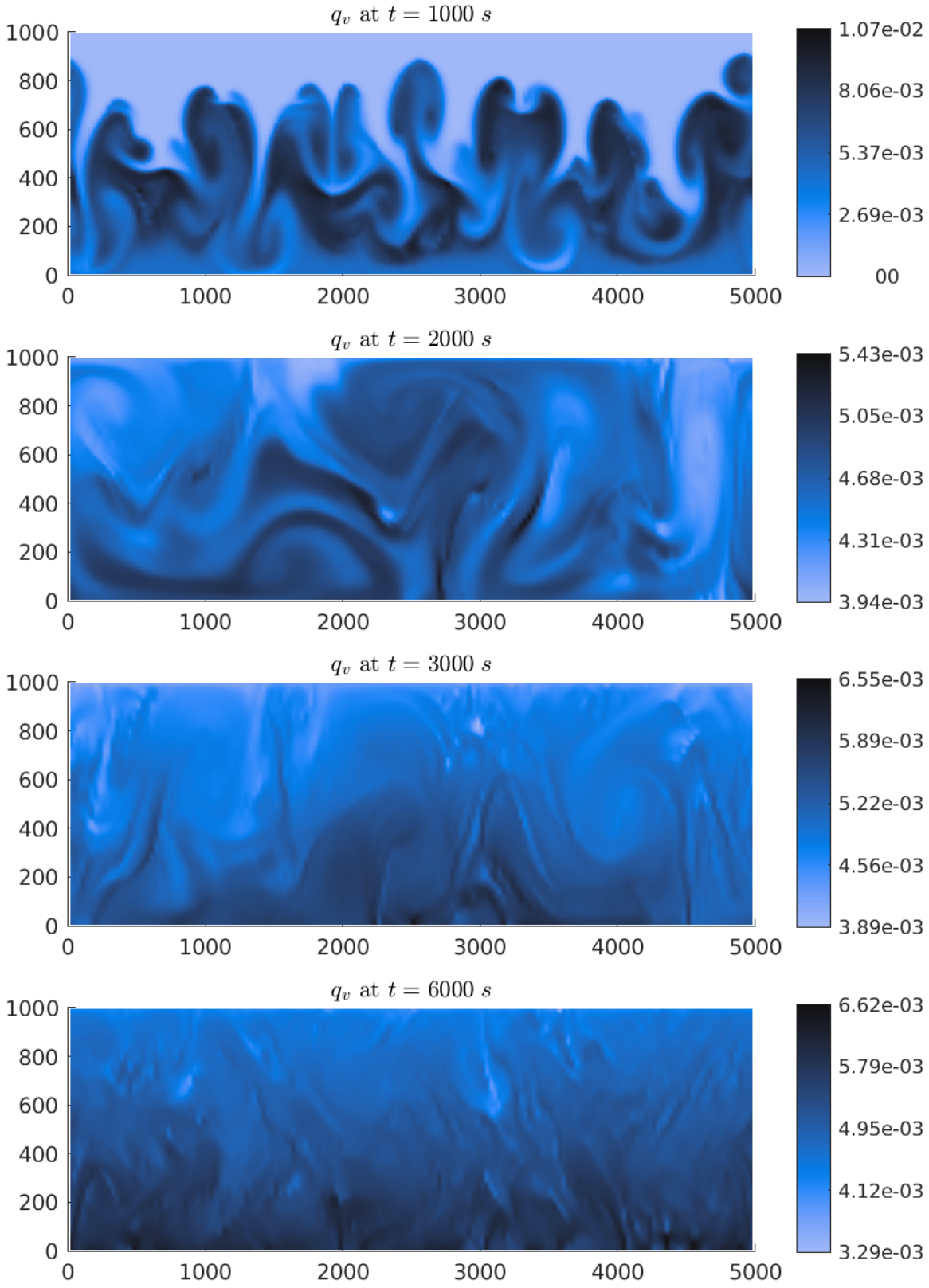

Figure 6.10: Example 6.4: Water vapor concentration q_v at times $t = 1000$, 2000, 3000 and $6000s$ simulated on a 160×160 mesh.

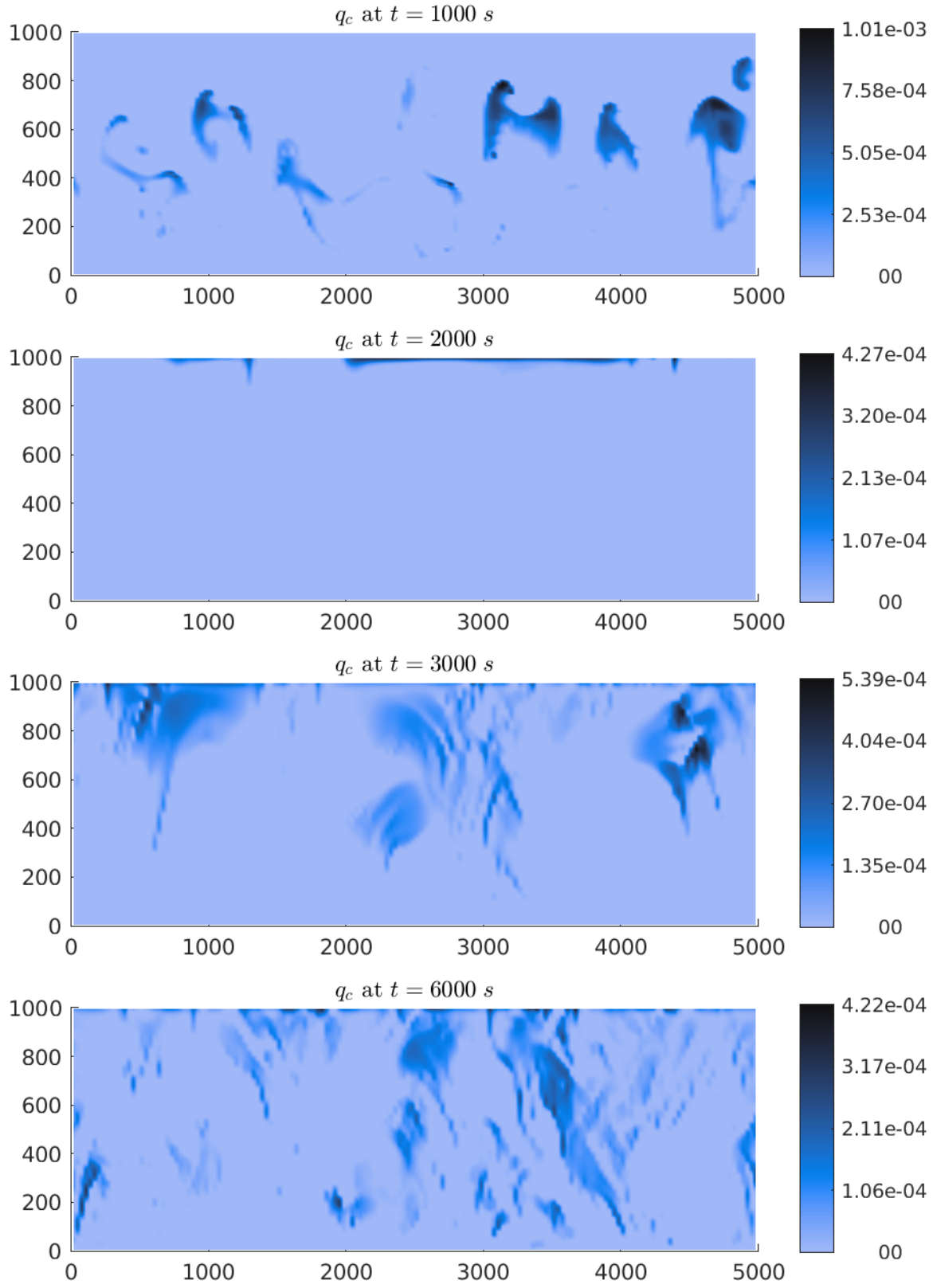

Figure 6.11: Example 6.4: Cloud drops concentration q_c at times $t = 1000$, 2000, 3000 and $6000s$ simulated on a 160×160 mesh.

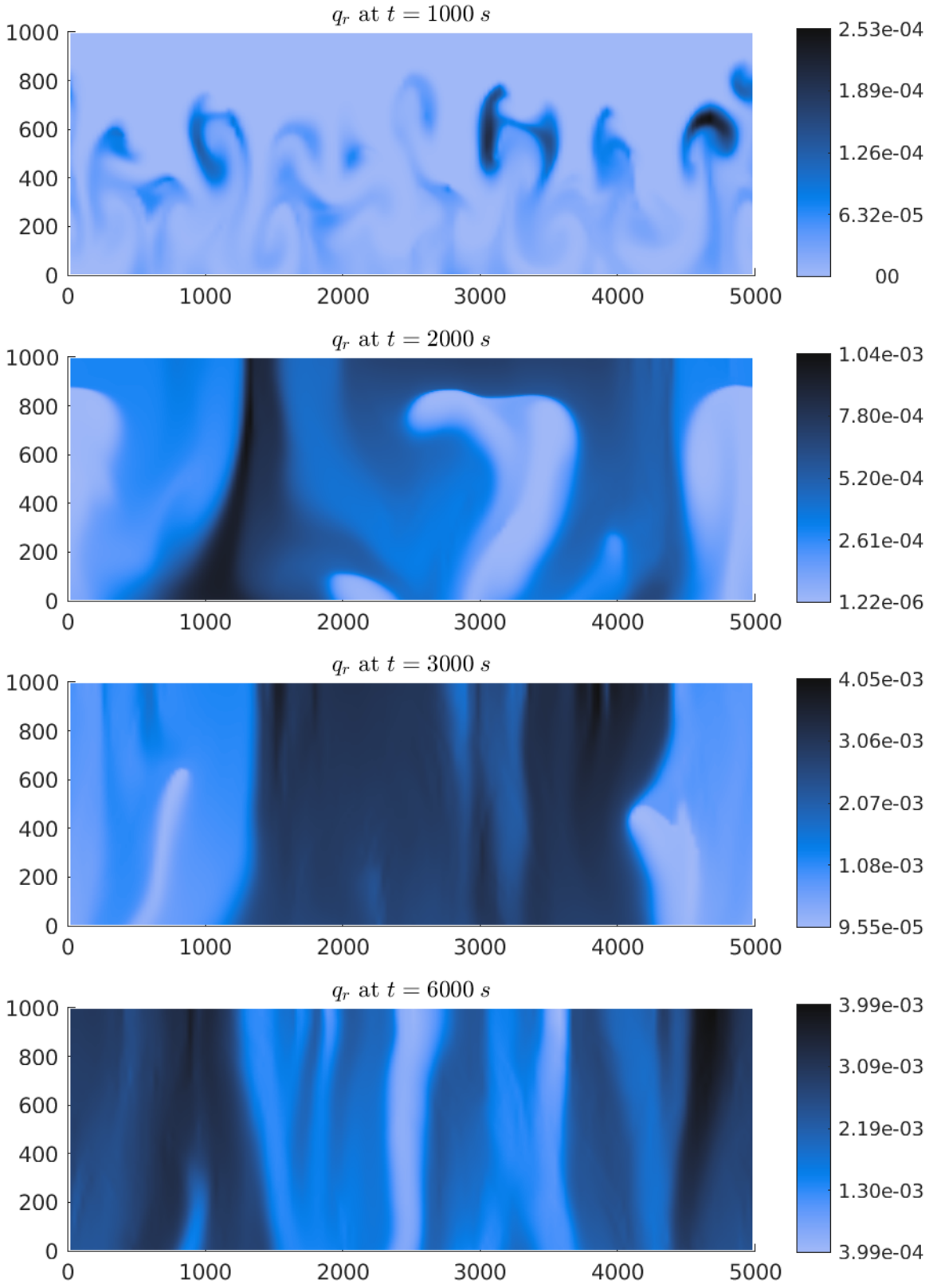

Figure 6.12: Example 6.4: Rain concentration q_r at times $t = 1000$, 2000, 3000 and $6000s$ simulated on a 160×160 mesh.

Example 6.5 (Dry Rayleigh-Bénard convection in 3D)

In this example, we investigate the formation of cells, the influence of the grid resolution of the numerical spatial discretization on the cells and the formation of rolls in dry Rayleigh-Bénard convection in 3D simulated with the Navier-Stokes equations (M1.a). The influence of the grid resolution on the cell structure and size was suggested by R. Klein and was an outcome of a personal discussion, [2].

1. **Formation of cells:** To obtain cells, we realized Example 6.3 in 3D with the following initial conditions

$$\begin{aligned} &\rho'(\boldsymbol{x},0) = \frac{-\bar{\rho}(\boldsymbol{x})\theta'(\boldsymbol{x},0)}{\bar{\theta}(\boldsymbol{x})+\theta'(\boldsymbol{x},0)}, \quad \bar{\rho}(\boldsymbol{x}) = \frac{p_0}{R\bar{\theta}(\boldsymbol{x})}\pi_e(\boldsymbol{x})^{\frac{1}{\gamma-1}}, \quad \pi_e(\boldsymbol{x}) = 1 - \frac{gx_3}{c_p\bar{\theta}(\boldsymbol{x})}, \\ &u_1(\boldsymbol{x},0) = 0.001, \quad u_2(\boldsymbol{x},0) = 0.001, \quad u_3(\boldsymbol{x},0) = \sin\left(2\pi\frac{x_3}{1000}\right), \\ &\theta'(\boldsymbol{x},0) = 0.6\sin\left(2\pi\frac{x_3}{1000}\right), \quad \bar{\theta}(\boldsymbol{x}) = 284 - \frac{x_3}{1000} \end{aligned} \tag{6.4}$$

and the same boundary conditions as in Example 6.3. The numerical solution is computed in a domain $\Omega = [0,5000] \times [0,5000] \times [0,1000]\, m^3$ that has been discretized using $50 \times 50 \times 50$ mesh cells. In Figure 6.13 we depict the potential temperature at times $t = 3000$, 4000, 5000 and $6000s$. As in the 2D case, we can observe small finger-like structures developing at $t = 3000s$, which then reach to the top of the domain at $t = 4000s$. The dynamics stabilized in cell/hexagonal structures at $t = 5000$ and $6000s$.

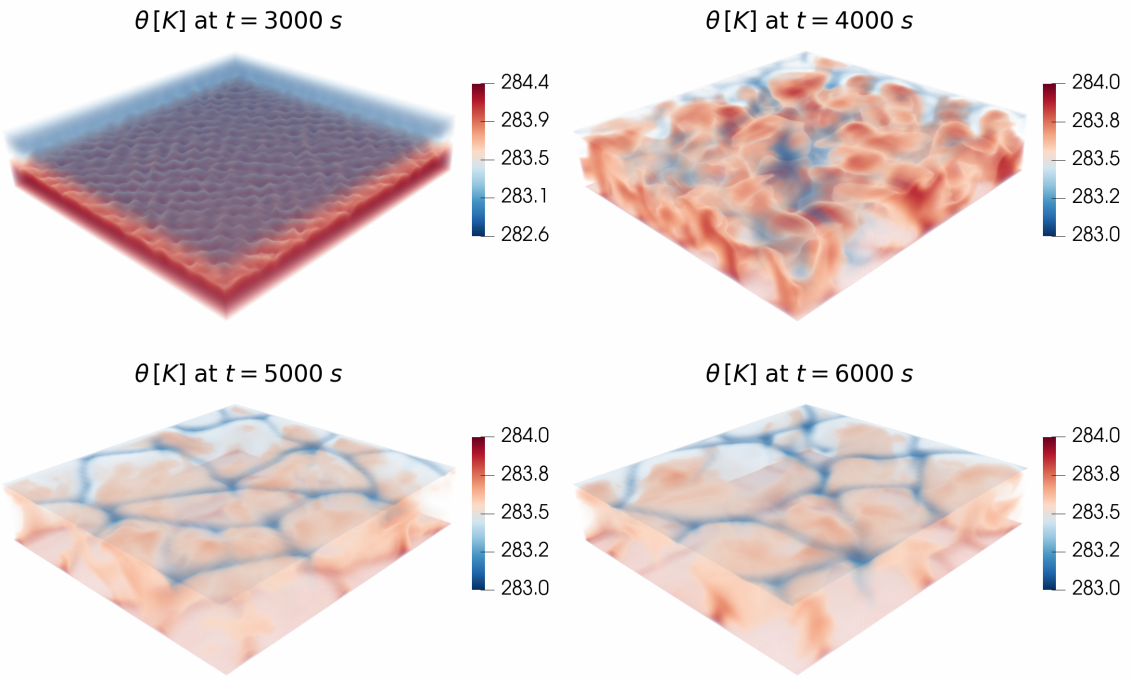

Figure 6.13: Example 6.5: Potential temperature θ at times $t = 3000$, 4000, 5000 and $6000s$ simulated on a $50 \times 50 \times 50$ mesh.

2. **Influence of the grid resolution on the cell pattern:** In this experiment, we investigate the effect of the grid resolution of the numerical spatial discretization on the cell structure and size. Thus, we compare the numerical solutions of the previous experiment (6.4) on different grids. In Figure 6.14, the potential temperature is shown at $t = 6000s$ simulated with $40 \times 40 \times 40$, $50 \times 50 \times 50$, $60 \times 60 \times 60$ and $70 \times 70 \times 70$ mesh cells. One can observe some changes of the solution, but the size and type of the structure stay the same with all the different meshes. Thus, the formation and the size of the cells is not mesh-dependent. In what follows, we will always use $50 \times 50 \times 50$ mesh cells for 3D simulations.

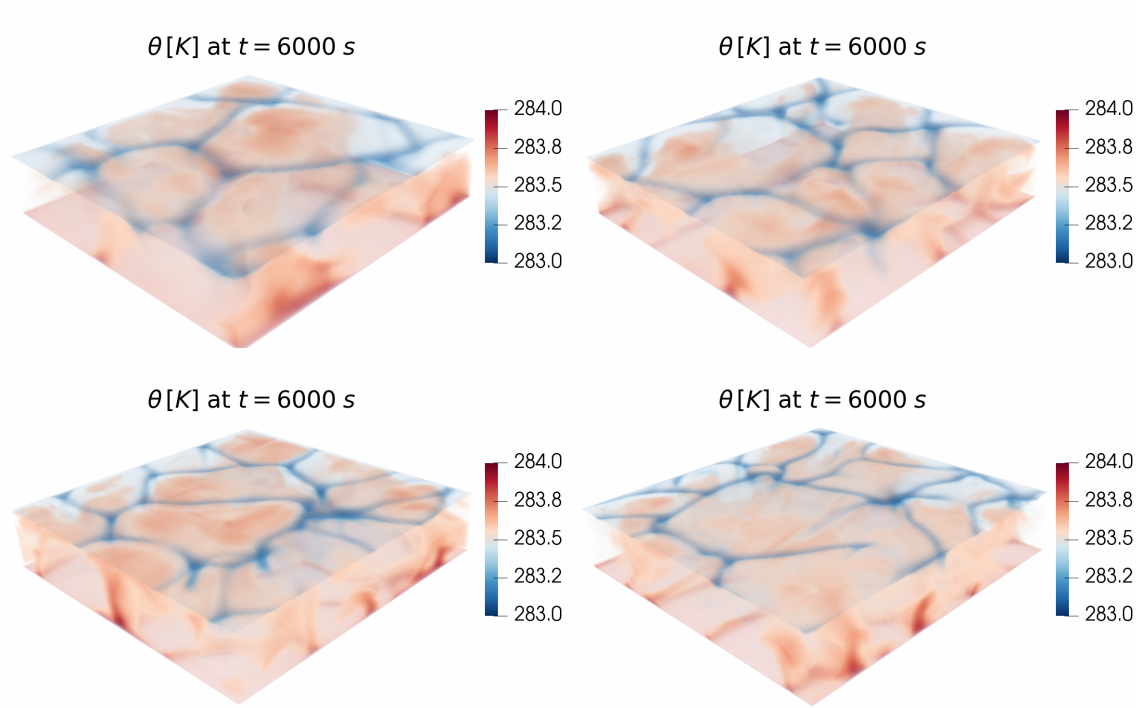

Figure 6.14: Example 6.5: Potential temperature θ at time $t = 6000s$ simulated on a $40 \times 40 \times 40$ (top left), $50 \times 50 \times 50$ (top right), $60 \times 60 \times 60$ (bottom left) and $70 \times 70 \times 70$ (bottom right) mesh.

3. **Formation of rolls:** In this example, we look at the roll pattern which is achieved by considering the same initial and boundary conditions as for the cells, see (6.4), but replacing the potential temperature perturbation by

$$\theta'(\boldsymbol{x}, 0) = 0.6 \sin\left(2\pi \frac{x_3}{1000}\right) \sin\left(4\pi \frac{x_2}{5000}\right). \tag{6.5}$$

The numerical solution is computed on a domain $\Omega = [0, 5000] \times [0, 5000] \times [0, 1000]\, m^3$ that has been discretized using $50 \times 50 \times 50$ mesh cells. In Figure 6.15, the potential temperature is depicted at times $t = 2000$, 3000, 4000 and $6000s$. We can clearly observe roll structures forming at time $t = 2000s$ which then end up in three rolls at time $t = 3000s$. At $t = 6000s$ it is already noticeable that the rolls start deforming with some finer structures. Thus, we suspect that the rolls are not stable over time and probably change into cell like structures.

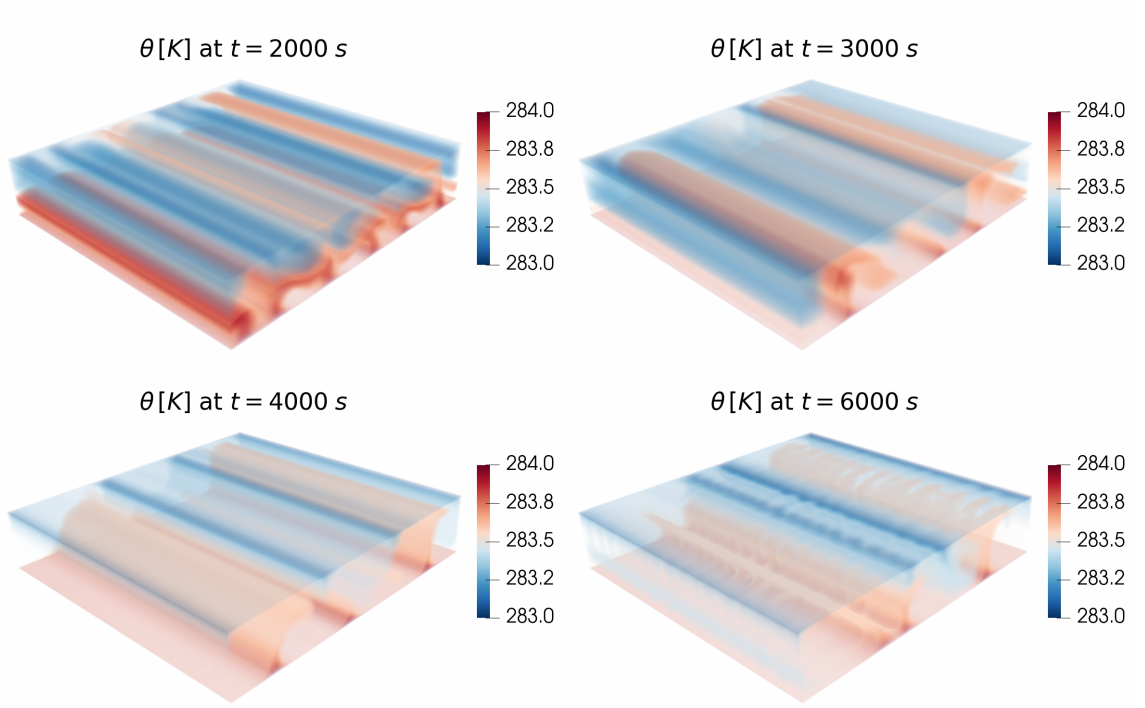

Figure 6.15: Example 6.5: Potential temperature θ at times $t = 2000$, 3000, 4000 and $6000s$ simulated on a $50 \times 50 \times 50$ mesh.

Example 6.6 (**Moist Rayleigh-Bénard convection in 3D**)

Here, we investigate the influence of moisture on the dynamics and pattern formation in 3D Rayleigh-Bénard convection. We do that by simulating the full cloud model (M1) for the initial conditions in the cases of cell and roll formation of the previous Example 6.5 and adding the conditions for the liquid water phases. Both experiments where simulated on a domain $\Omega = [0, 5000] \times [0, 5000] \times [0, 1000]\, m^3$ that has been discretized using $50 \times 50 \times 50$ mesh cells.

1. **Formation of cells:** We consider the same initial conditions for the Navier-Stokes variables as in the dry case for the formation of cells, see (6.4), and add as initial conditions for the cloud variables the ones from the moist two-dimensional case, see (6.3). As in the 2D case, different structures form in the different variables. Figures 6.16–6.20 show the potential temperature, the difference of water vapor to the saturation mixing ratio and the water vapor, cloud drops and rain concentration computed at times $t = 1000$, 2000, 3000 and $6000s$. In Figures 6.21–6.25, we additionally depict 2D slices of these solutions at $x_3 = 700$ and $x_1 = 3000$ at times $t = 1000$ and $6000s$. The moisture leads, as in the 2D case in Example 6.4, to higher values of the potential temperature due to the latent heating and to an overall much faster convection taking place due to stronger buoyancy. At an earlier time $t = 1000s$, smaller convection cells can be seen at the top layer of the domain, especially in the potential temperature, see Figures 6.16 and 6.21, and cloud water, see Figures 6.19 and 6.24. As time progresses, these structures aggregate and reorganize into

larger cells. These structures in potential temperature seem to be quite robust as the overall scales and pattern do not change from time $t = 2000s$ to time $t = 6000s$. As one can see in Figure 6.19, the structures in the cloud water are very similar since the variables θ and q_c are closely connected; the structures are mainly visible in horizontal planes as shown in Figures 6.21 and 6.24. These structures naturally can also be observed in the oversaturated regions in Figures 6.17 and 6.22 in which, due to the high water vapor content and the higher temperature, clouds are formed. For the rain distribution, the evolved structures are quite different since rain forms in regions with high cloud water (that is, at the top layers) and is then transported by sedimentation. This leads to a more pronounced pattern in the vertical direction since sedimentation is the dominant process after the rain has formed which can nicely be observed in Figure 6.25. Overall, we can see a clear effect of the moisture on the structure formation, though in this case the cell-like structures from the dry case can still be recognized.

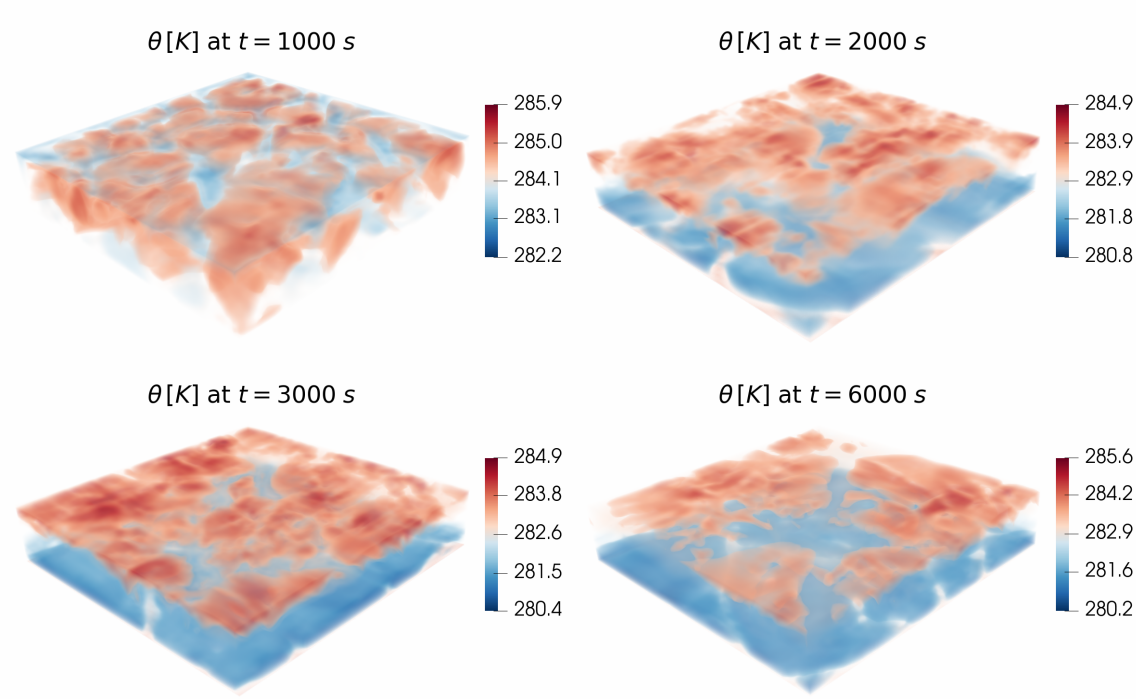

Figure 6.16: Example 6.6: Potential temperature θ at times $t = 1000$, 2000, 3000 and $6000s$ simulated on a $50 \times 50 \times 50$ mesh.

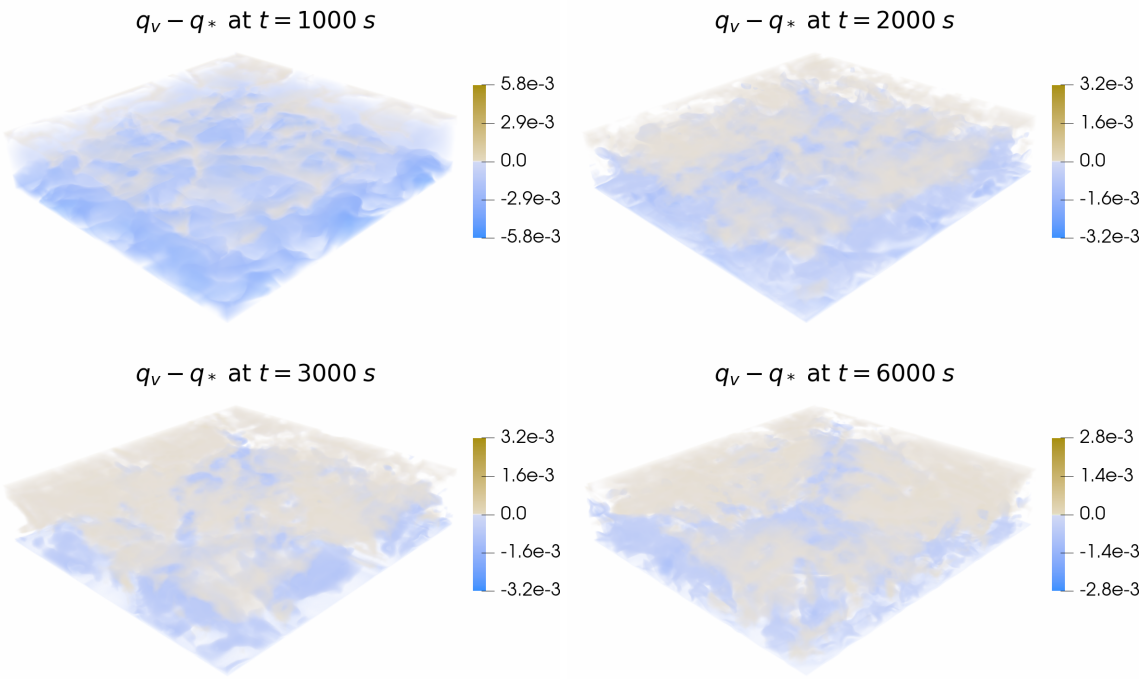

Figure 6.17: Example 6.6: Difference of water vapor to the saturation mixing ratio $q_v - q_*$ at times $t = 1000$, 2000, 3000 and $6000s$ simulated on a $50 \times 50 \times 50$ mesh.

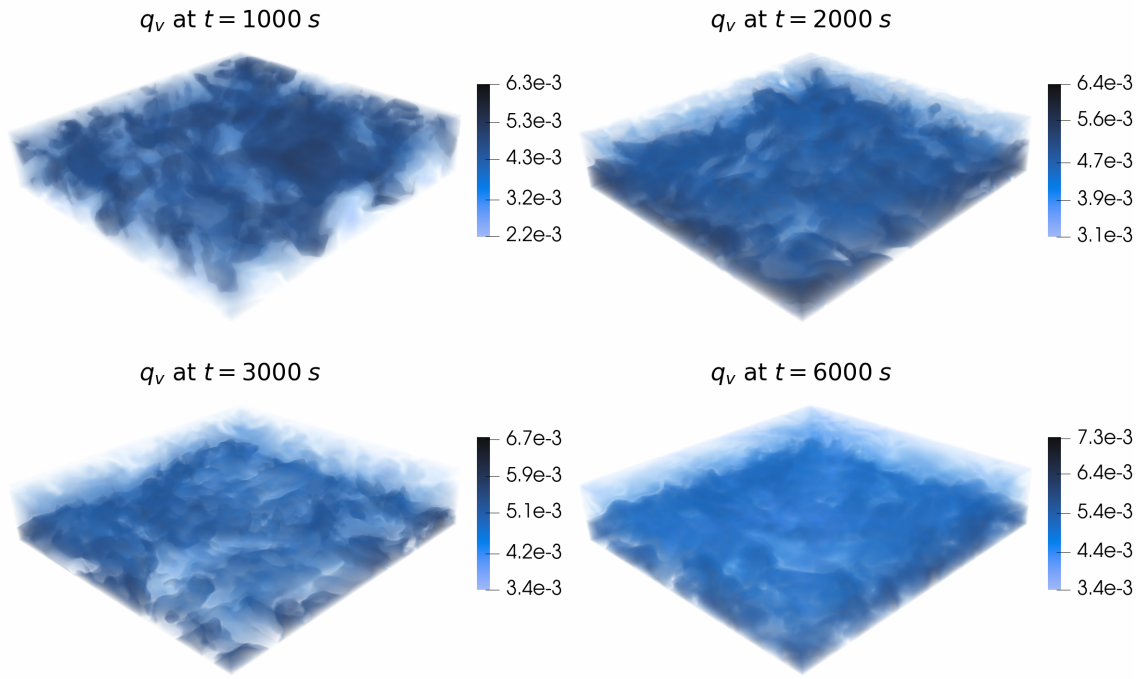

Figure 6.18: Example 6.6: Water vapor concentration q_v at times $t = 1000$, 2000, 3000 and $6000s$ simulated on a $50 \times 50 \times 50$ mesh.

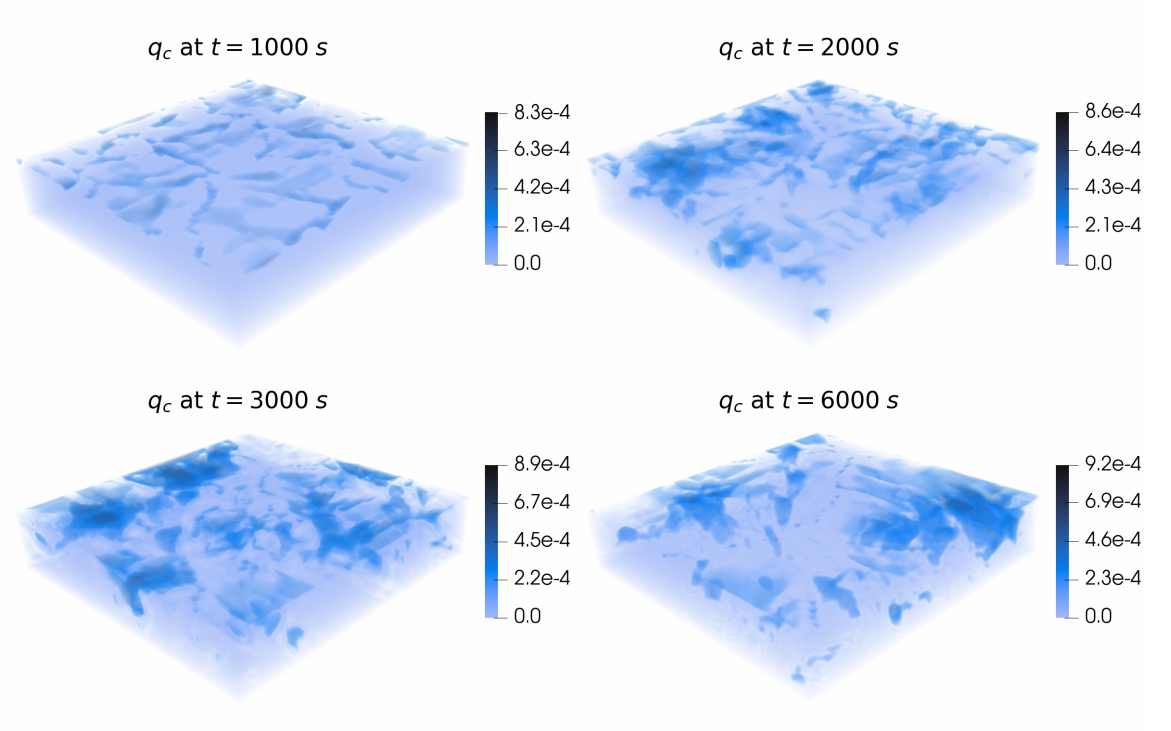

Figure 6.19: Example 6.6: Cloud drops concentration q_c at times $t = 1000$, 2000, 3000 and $6000s$ simulated on a $50 \times 50 \times 50$ mesh.

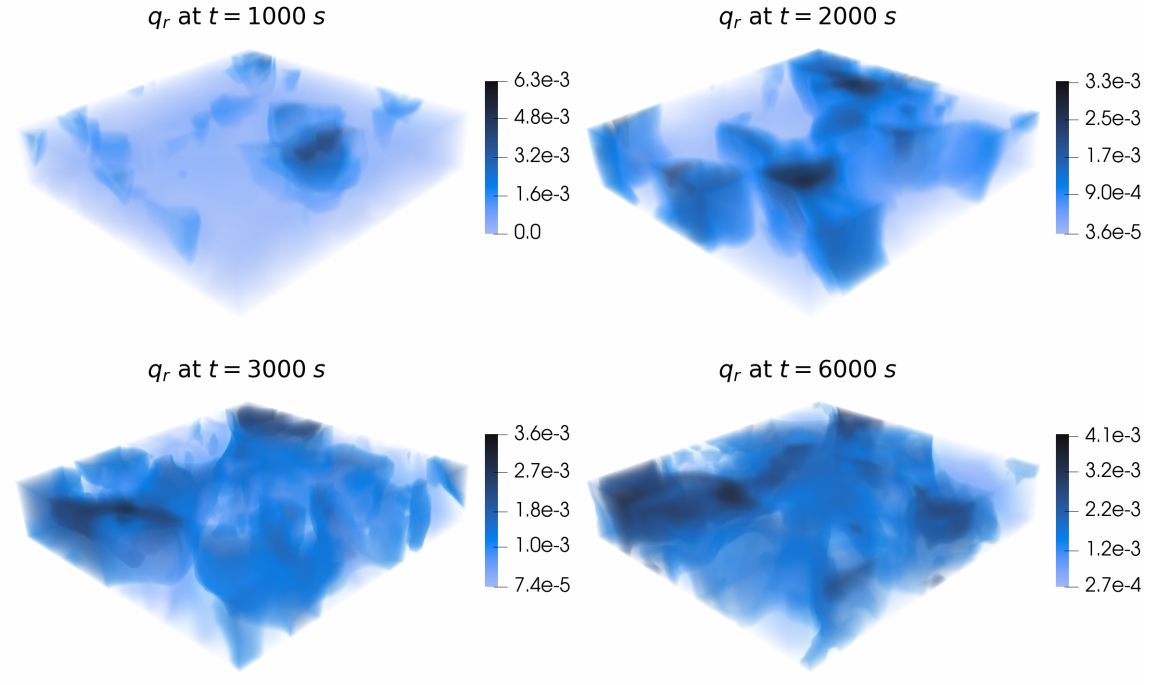

Figure 6.20: Example 6.6: Rain concentration q_r at times $t = 1000$, 2000, 3000 and $6000s$ simulated on a $50 \times 50 \times 50$ mesh.

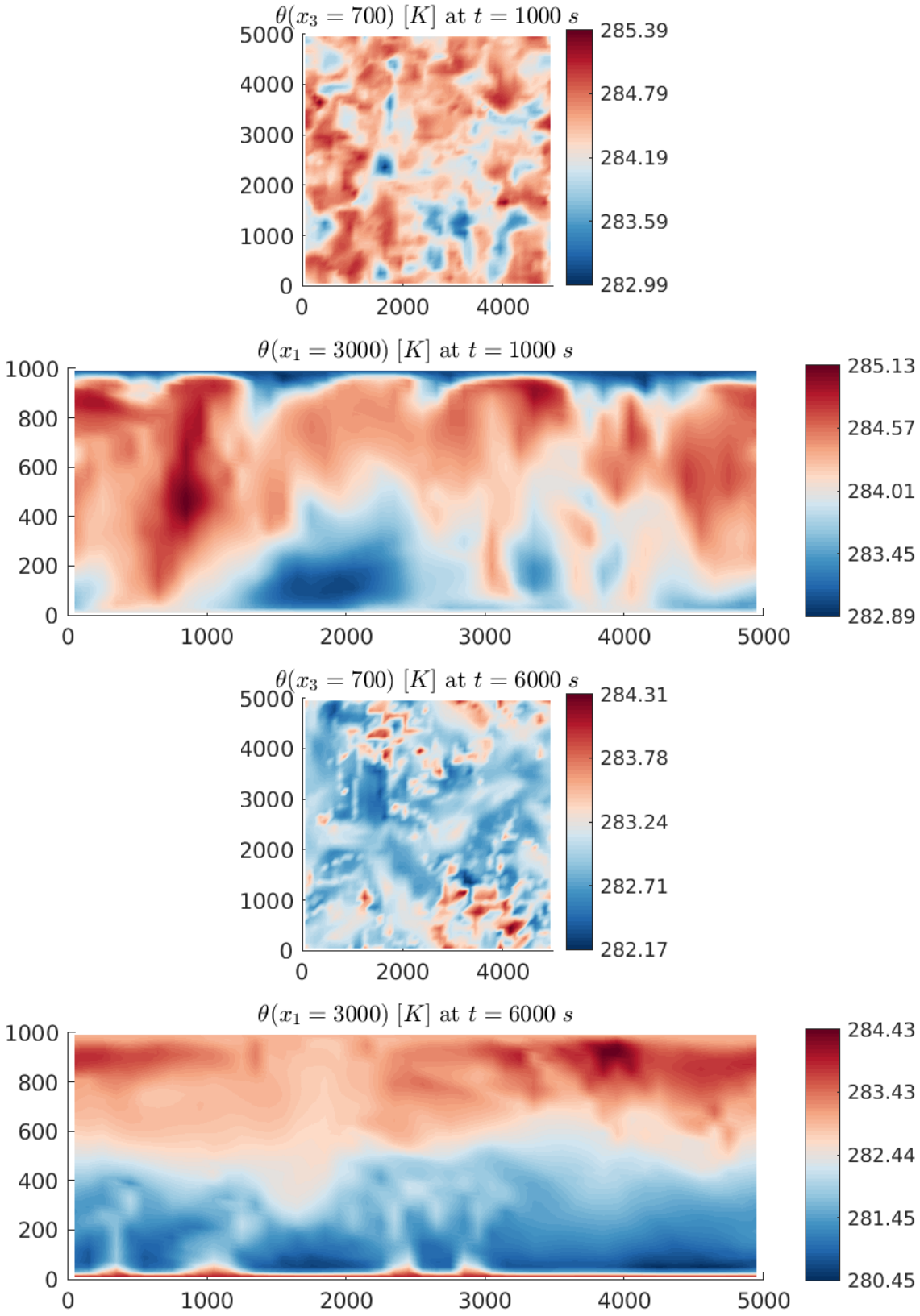

Figure 6.21: Example 6.6: Slices of the potential temperature θ at $x_3 = 700$ and $x_1 = 3000$ at times $t = 1000$ and $6000s$ simulated on a $50 \times 50 \times 50$ mesh.

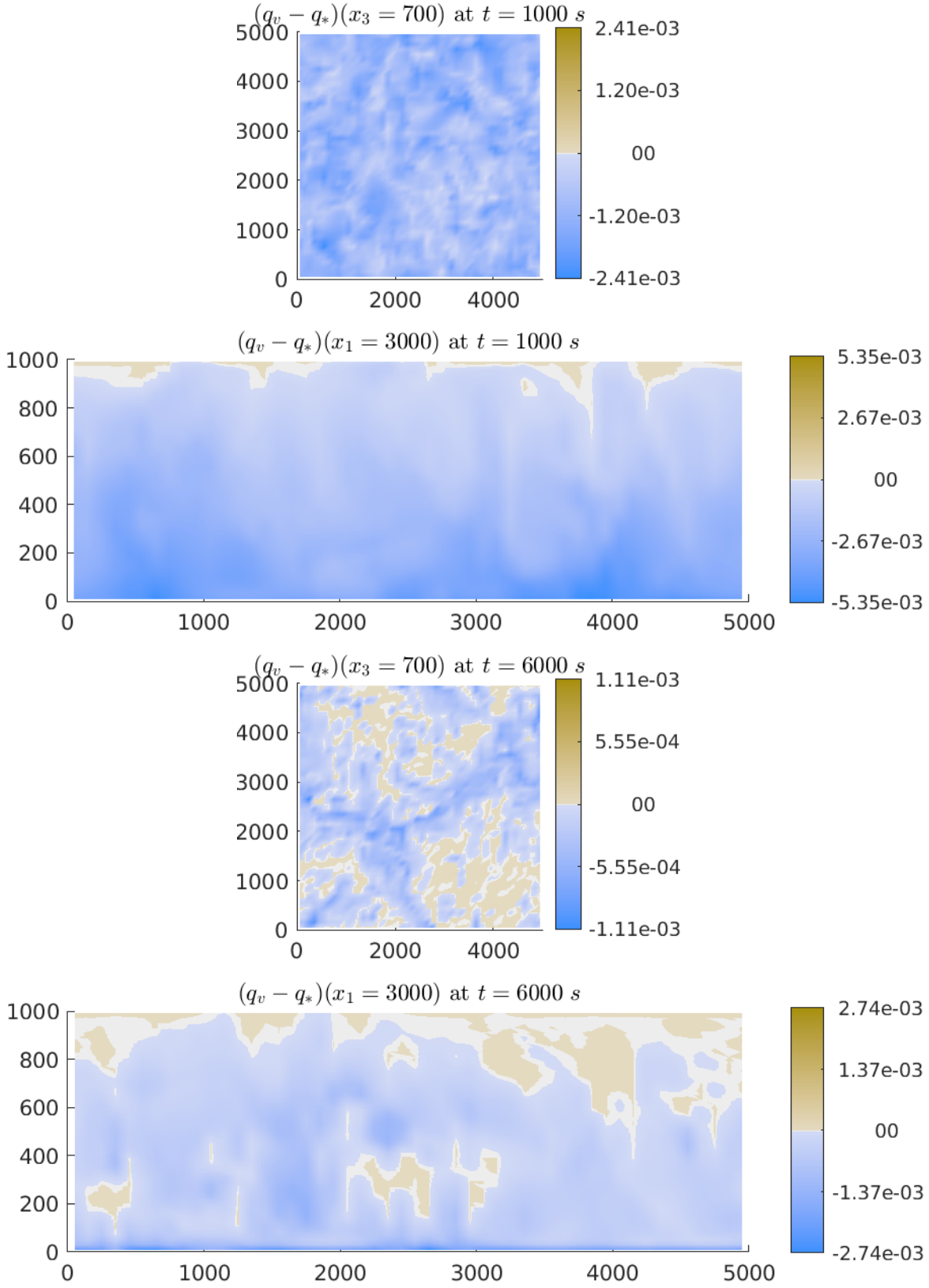

Figure 6.22: Example 6.6: Slices of the difference of water vapor to the saturation mixing ratio $q_v - q_*$ at $x_3 = 700$ and $x_1 = 3000$ at times $t = 1000$ and $6000s$ simulated on a $50 \times 50 \times 50$ mesh.

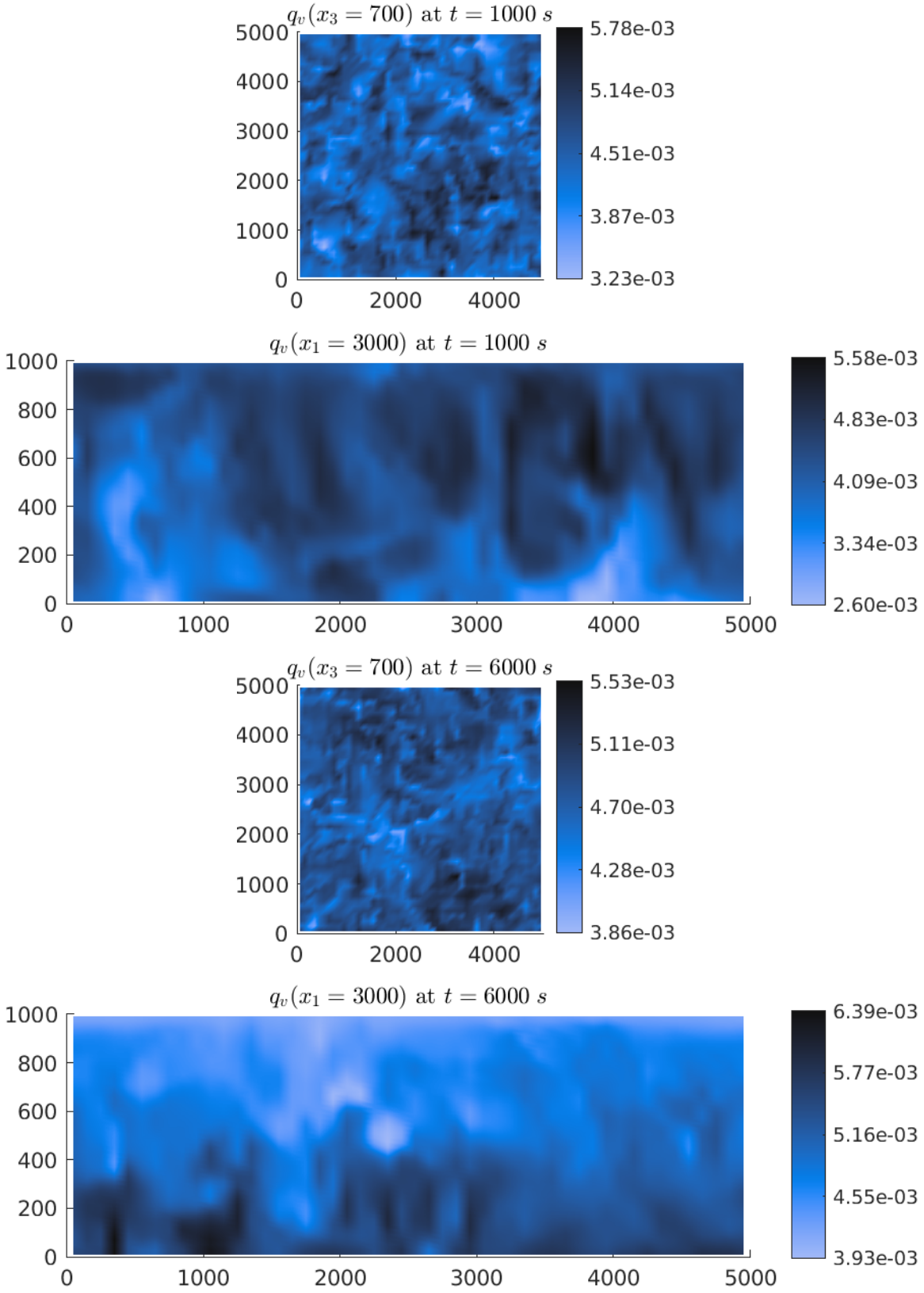

Figure 6.23: Example 6.6: Slices of the water vapor concentration q_v at $x_3 = 700$ and $x_1 = 3000$ at times $t = 1000$ and $6000s$ simulated on a $50 \times 50 \times 50$ mesh.

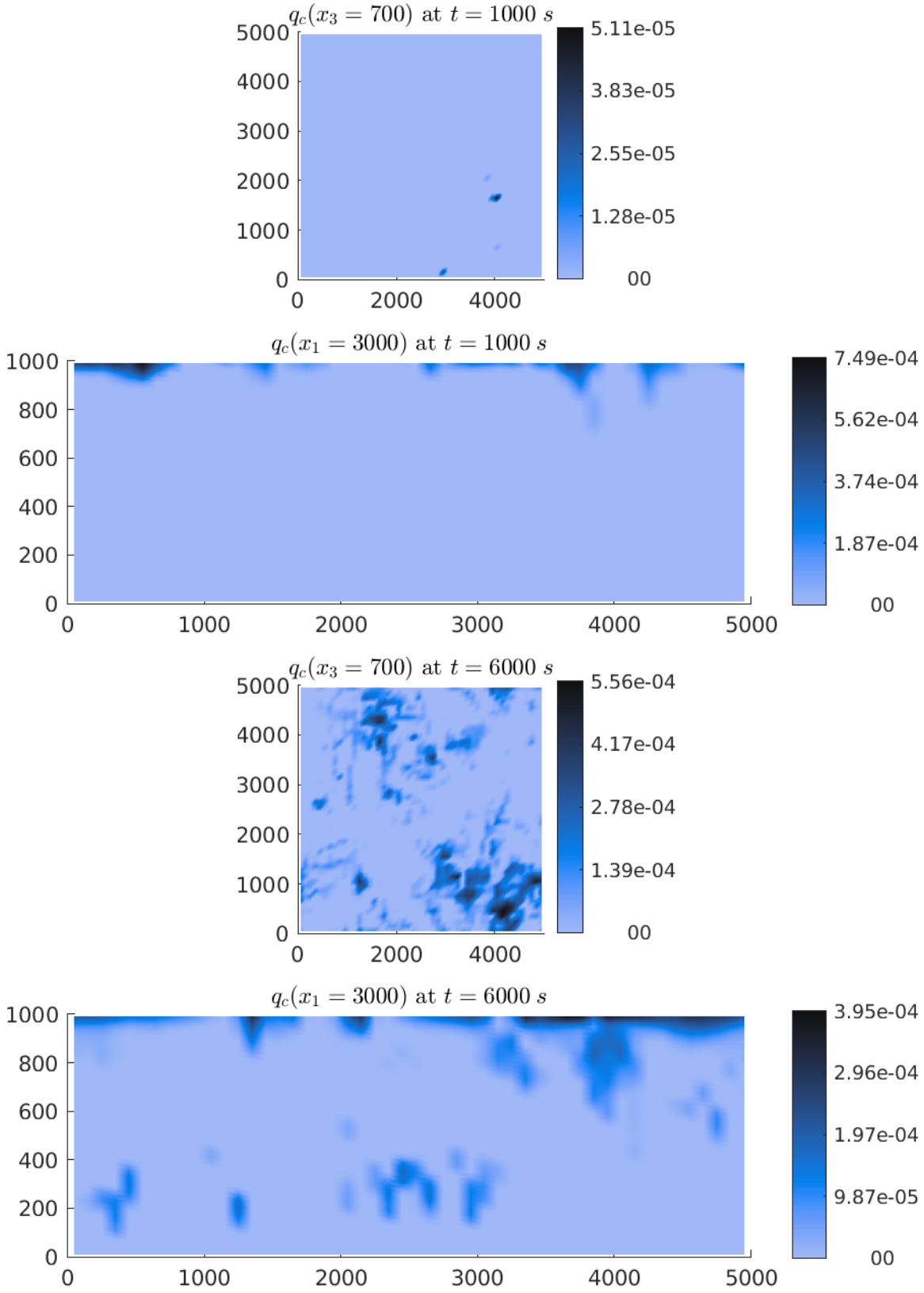

Figure 6.24: Example 6.6: Slices of the cloud drops concentration q_c at $x_3 = 700$ and $x_1 = 3000$ at times $t = 1000$ and $6000s$ simulated on a $50 \times 50 \times 50$ mesh.

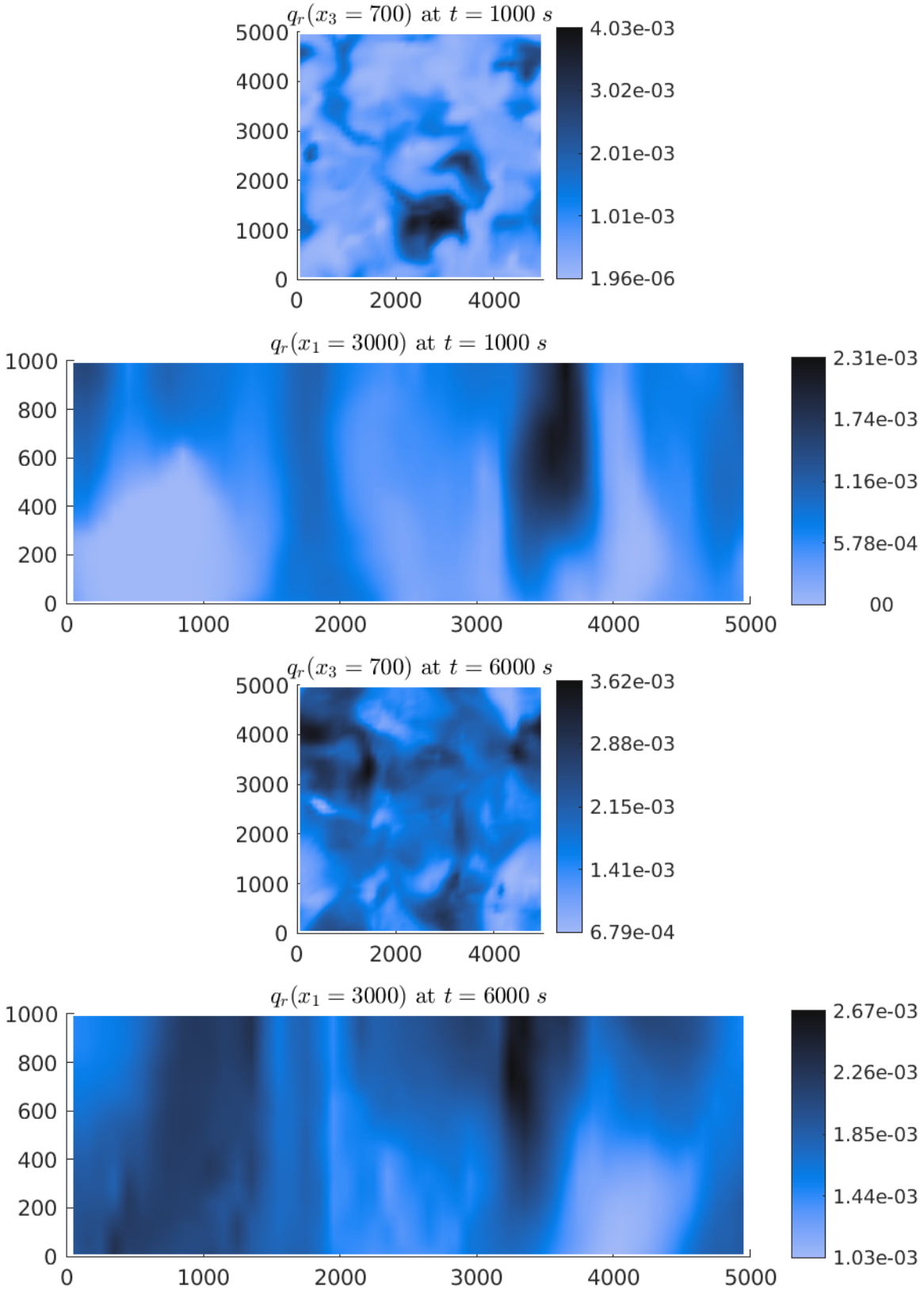

Figure 6.25: Example 6.6: Slices of the rain concentration q_r at $x_3 = 700$ and $x_1 = 3000$ at times $t = 1000$ and $6000s$ simulated on a $50 \times 50 \times 50$ mesh.

2. **Formation of rolls:** For this experiment, we choose as initial conditions for the Navier-Stokes variables the ones from the dry roll formation case, see (6.5), and add as initial conditions for the cloud variables the ones from the moist two-dimensional case, see (6.3). In Figures 6.26 and 6.27, the numerical solutions of the potential temperature and the water vapor, cloud drops and rain concentration and the difference of the water vapor to the saturation mixing ratio $q_v - q_*$ are depicted at times $t = 1000$ and $6000s$. In Figures 6.28–6.32, we additionally present 2D slices of these solutions at $x_3 = 700$ and $x_1 = 3000$ at the same times. At the early time $t = 1000s$, one can observe that also in the moist case three rolls have formed –however, much faster than in the dry case, cf. Figure 6.15. One can nicely observe that also the liquid water concentrations follow this roll structure. Clouds formed on the top of the rolls as stripes, see Figure 6.31, because of the oversaturation, see Figure 6.29. At one roll the cloud water content was so high that it rained out leading to a roll/stripe rain pattern which can be seen in Figure 6.32. At a later time $t = 6000s$, one can observe that the roll pattern vanished and by examining the potential temperature one can rather identify a cell-like structure starting from the bottom. This is also the case for the cloud variables in which one can see convection cells and rain fields. This change of pattern can also be nicely observed in the 2D slices of the solutions. Thus, the rolls are not stable over time, as already expected in the dry case in Example 6.5. Here, the vertical velocity is higher because of the moisture and leads to a much faster change from rolls to patterns than in the dry case.

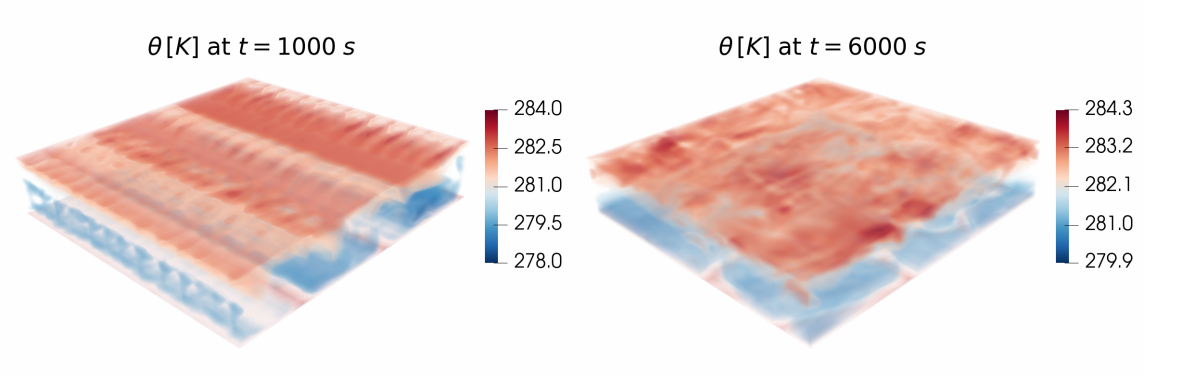

Figure 6.26: Example 6.6: Potential temperature θ at times $t = 1000$ and $6000s$ simulated on a $50 \times 50 \times 50$ mesh.

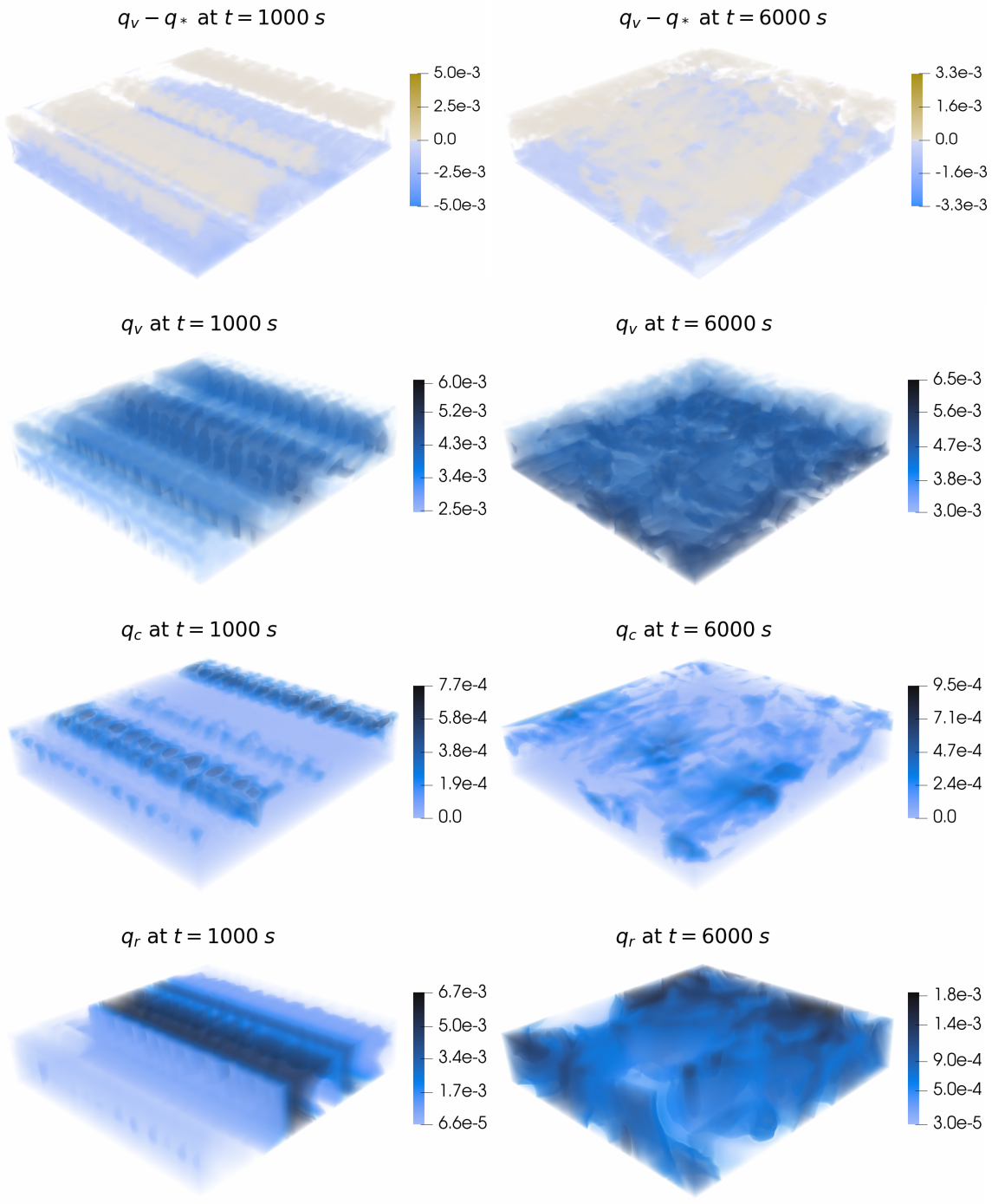

Figure 6.27: Example 6.6: Difference of water vapor to the saturation mixing ratio $q_v - q_*$ and cloud variables q_v, q_c and q_r at times $t = 1000$ and $6000s$ simulated on a $50 \times 50 \times 50$ mesh.

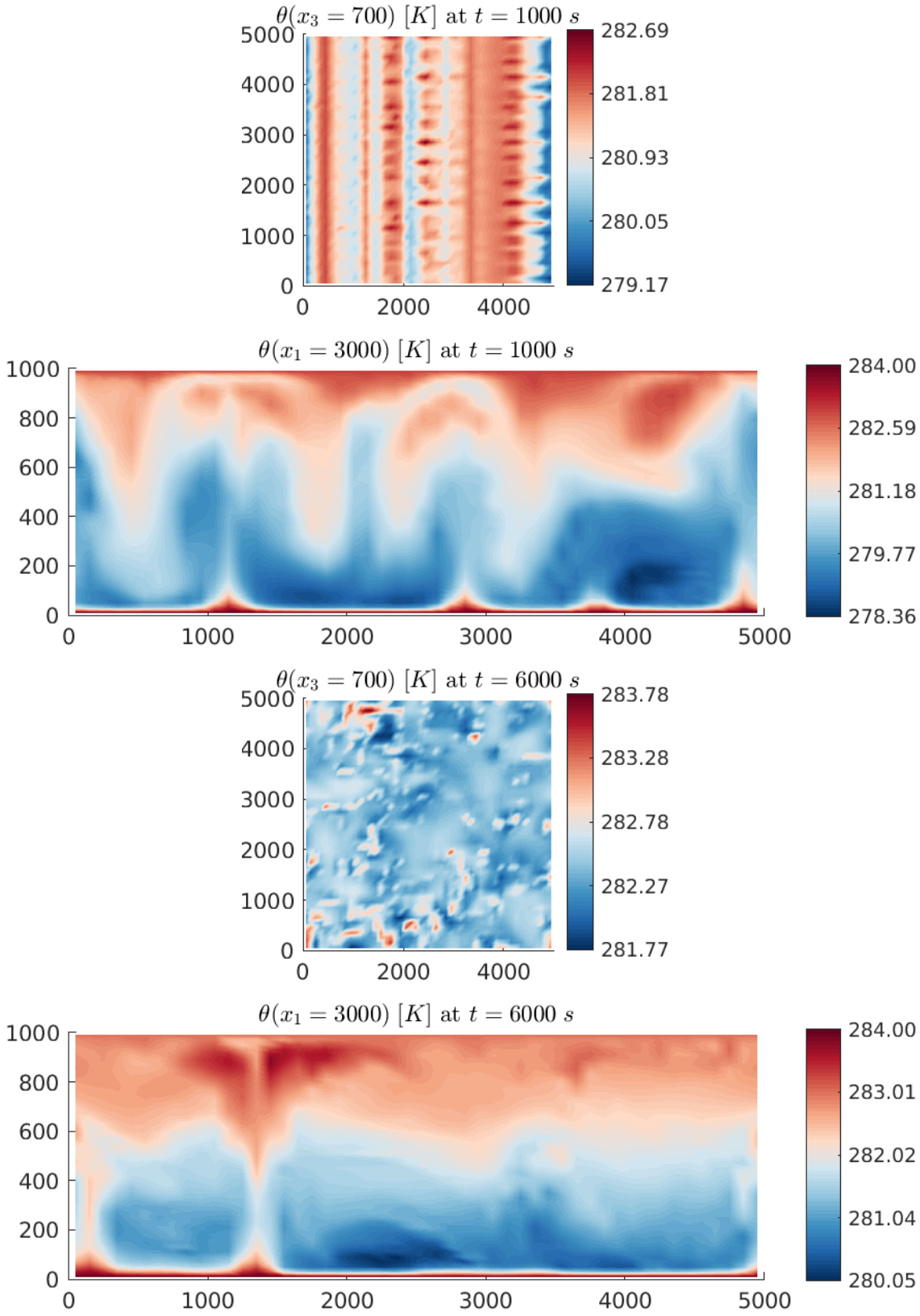

Figure 6.28: Example 6.6: Slices of the potential temperature θ at $x_3 = 700$ and $x_1 = 3000$ at times $t = 1000$ and $6000s$ simulated on a $50 \times 50 \times 50$ mesh.

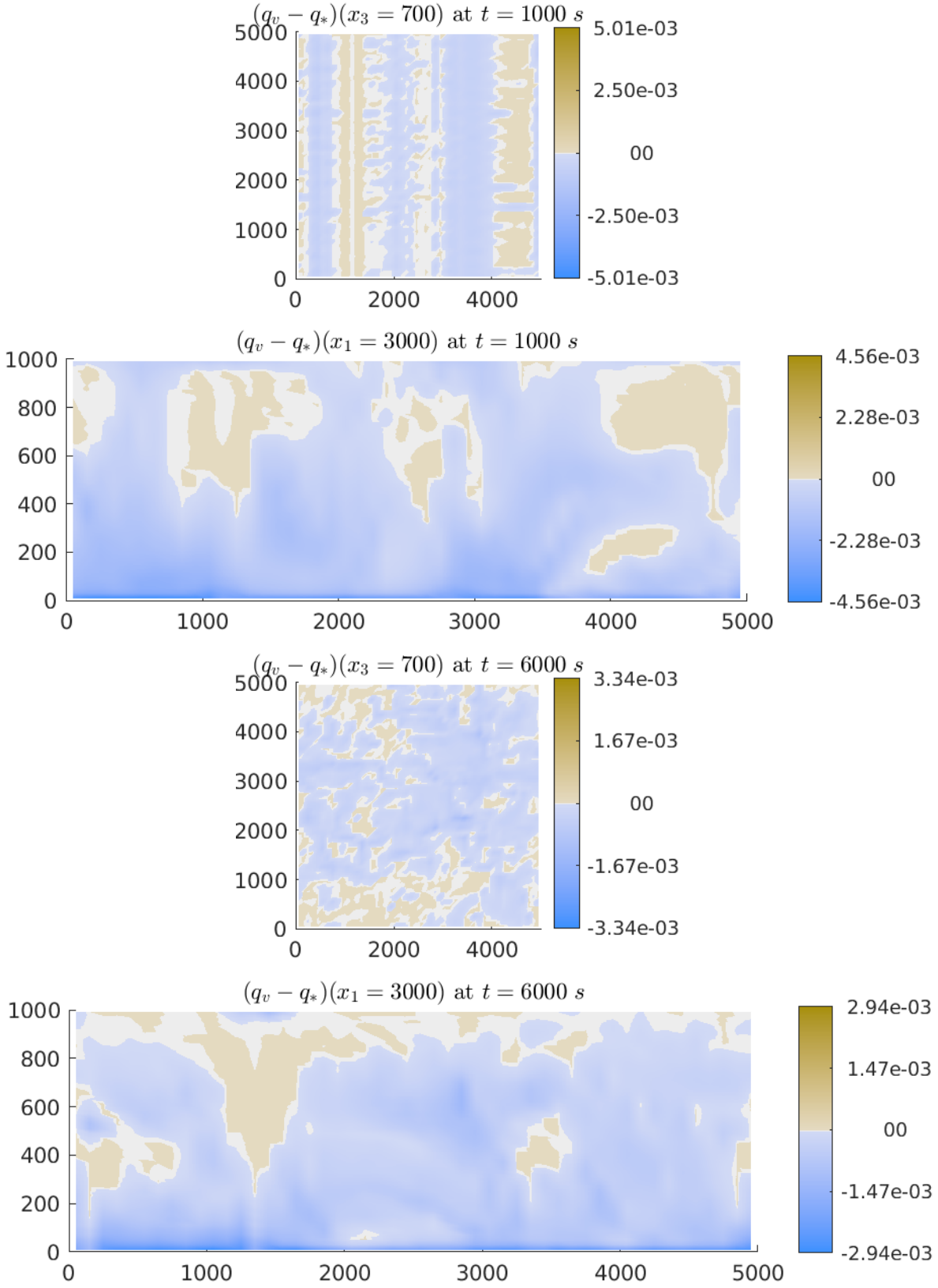

Figure 6.29: Example 6.6: Slices of the difference of water vapor to the saturation mixing ratio $q_v - q_*$ at $x_3 = 700$ and $x_1 = 3000$ at times $t = 1000$ and $6000s$ simulated on a $50 \times 50 \times 50$ mesh.

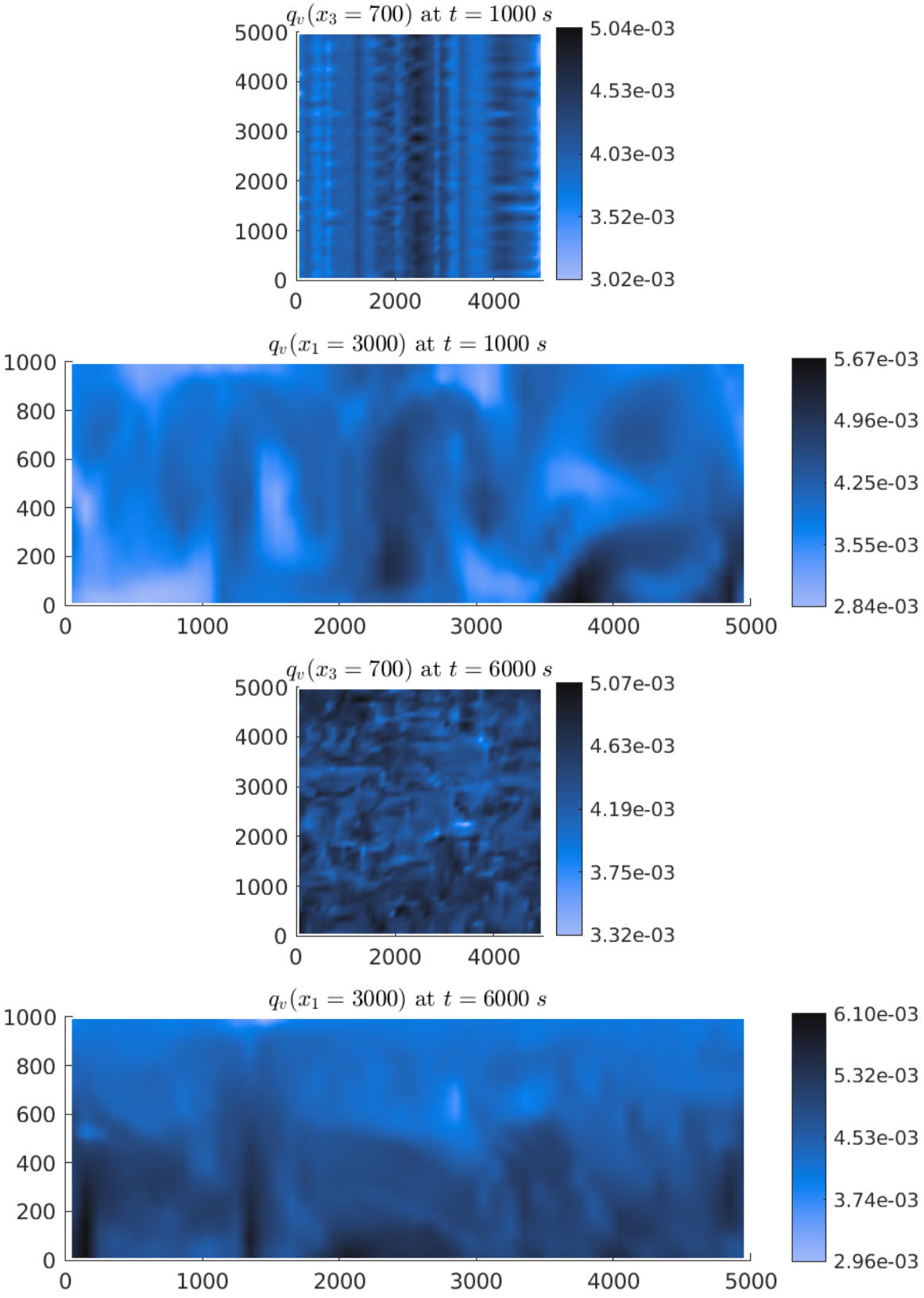

Figure 6.30: Example 6.6: Slices of the water vapor concentration q_v at $x_3 = 700$ and $x_1 = 3000$ at times $t = 1000$ and $6000s$ simulated on a $50 \times 50 \times 50$ mesh.

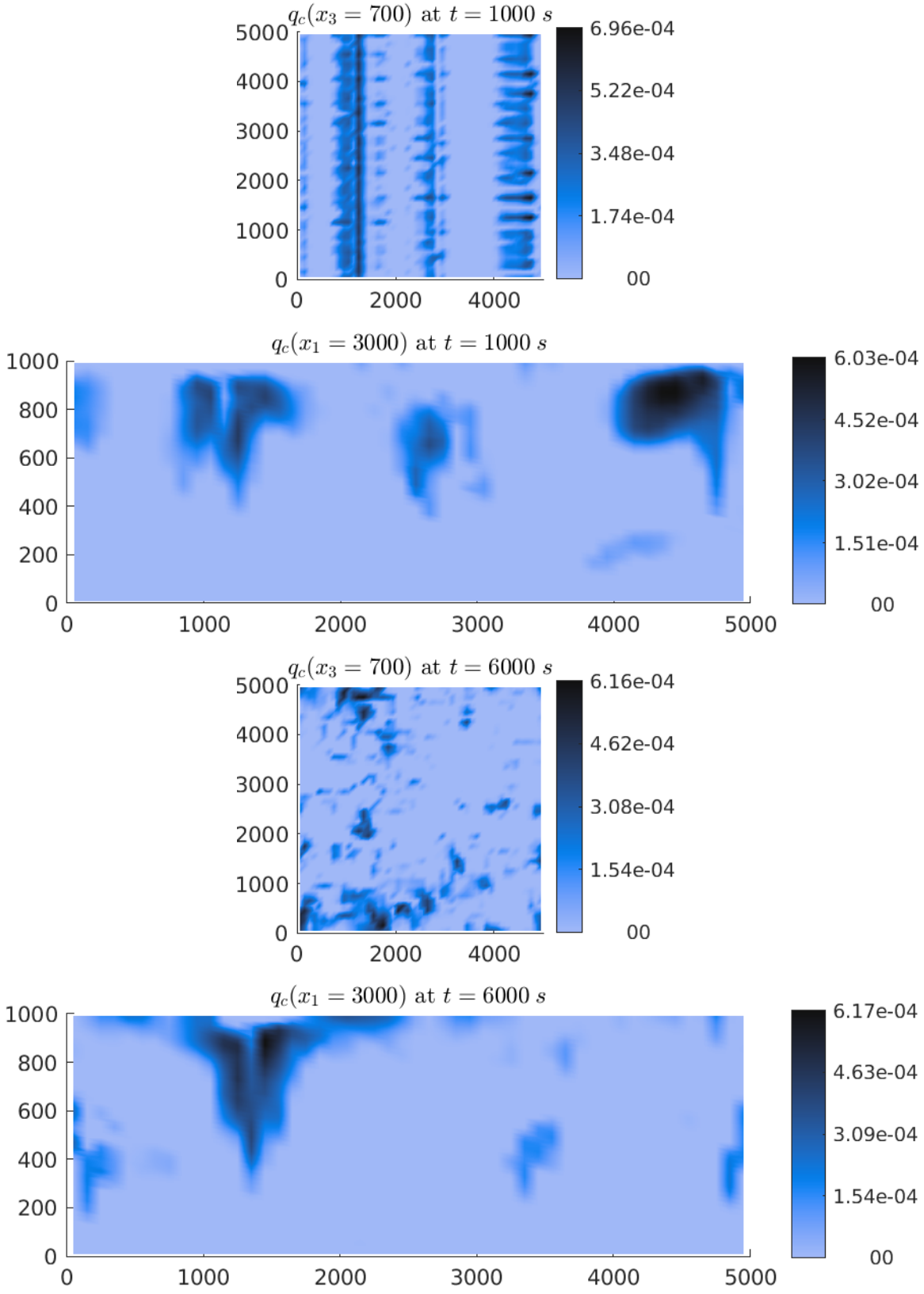

Figure 6.31: Example 6.6: Slices of the cloud drops concentration q_c at $x_3 = 700$ and $x_1 = 3000$ at times $t = 1000$ and $6000s$ simulated on a $50 \times 50 \times 50$ mesh.

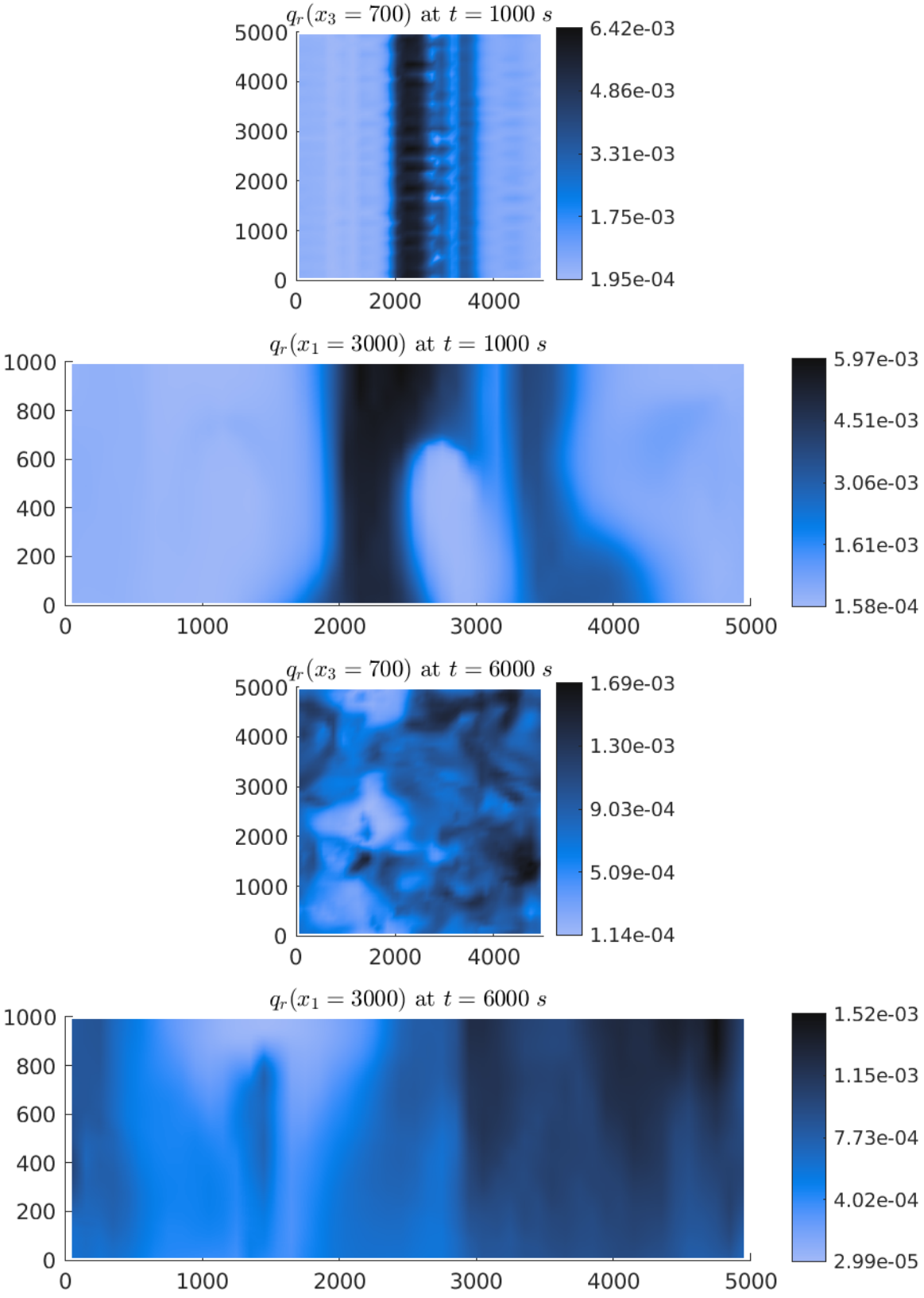

Figure 6.32: Example 6.6: Slices of the rain concentration q_r at $x_3 = 700$ and $x_1 = 3000$ at times $t = 1000$ and $6000s$ simulated on a $50 \times 50 \times 50$ mesh.

7 Stochastic numerical experiments

In this chapter, we present numerical results for the methods introduced in Subsections 5.3.1 and 5.3.2 for the respective stochastic models, i.e., the stochastic microphysics model (M2) and the fully stochastic model (M3). We begin by investigating the experimental convergence in Section 7.1 for the benchmark test of the free convection of a moist warm air bubble as introduced in Example 6.1 for the deterministic convergence tests. In Subsection 7.1.1, we study the experimental convergence for the stochastic microphysics scheme as introduced in 5.3.1 and in Subsection 7.1.2 we study the experimental convergence for the fully stochastic scheme as introduced in 5.3.2. Then we present results on the stochastic Rayleigh-Bénard convection in Section 7.2, where we depict the results obtained by the different stochastic models (M2) and (M3) in 2D and 3D. In Section 7.3, we compare the results of the stochastic Galerkin method, see Section 5.2.1, on which our numerical schemes for the stochastic models are based, with the Monte Carlo and the stochastic collocation method, see Section 5.2.2.

7.1 Experimental convergence of the numerical scheme

Here, we investigate the experimental convergence of our numerical schemes for different uncertainties. In Subsection 7.1.1, we state different examples for studying the experimental convergence of the numerical scheme introduced in Subsection 5.3.1 for the stochastic cloud microphysics model (M2). In Subsection 7.1.2, we depict some experimental convergence results for the scheme introduced in Subsection 5.3.2 for the fully stochastic cloud model (M3).

7.1.1 Stochastic cloud microphysics

In this subsection, we modify Example 6.1 by randomly perturbing either the initial data or selected model parameters of (M2) with a uniformly or normally distributed $X(\omega)$ and present the experimental convergence results. The experiments and results are based on [21].

In Example 7.1, we perturb the initial water vapor concentration q_v by 10% which is realized with a uniformly distributed $X(\omega)$. For that experiment, we present the con-

vergence in the stochastic space as well as the convergence in time and space. For the remaining experiments in this subsection, we will just compute the experimental order of convergence in the stochastic space since the method in time and space does not change. In Example 7.2, we use the same setup as in 7.1 but this time with a normally distributed $X(\omega)$ and demonstrate that the convergence of the method does not change with a different choice of distribution. In Example 7.3, we perturb some well-chosen uncertain coefficients in the source terms on the RHS of the cloud microphysics equations, see (5.23), and show that also in this case the method converges.

Example 7.1 (**Stochastic initial data with uniformly distributed** $X(\omega)$)

Here, we consider the following modification of Example 6.1 with a 10% perturbation of the initial water vapor concentration which is realized in the following way in the case of a uniformly distributed $X(\omega)$:

$$
\begin{aligned}
&(\widehat{q_v})_0(\boldsymbol{x},0) = 0.005\,\theta'(\boldsymbol{x},0),\ (\widehat{q_v})_1(\boldsymbol{x},0) = 0.1\,(\widehat{q_v})_0(\boldsymbol{x},0),\ (\widehat{q_v})_k(\boldsymbol{x},0) = 0 \quad \text{for } 2 \le k \le M,\\
&(\widehat{q_c})_0(\boldsymbol{x},0) = 10^{-4}\,\theta'(\boldsymbol{x},0),\ (\widehat{q_c})_k(\boldsymbol{x},0) = 0 \quad \text{for } 1 \le k \le M,\\
&(\widehat{q_r})_0(\boldsymbol{x},0) = 10^{-6}\,\theta'(\boldsymbol{x},0),\ (\widehat{q_r})_k(\boldsymbol{x},0) = 0 \quad \text{for } 1 \le k \le M.
\end{aligned}
$$

The initial data for the Navier-Stokes variables as well as the boundary conditions are the same as in Example 6.1. In Figure 7.6, we show the potential temperature θ and the expected values of the cloud variables $(\rho q_\ell), \ell \in \{v, c, r\}$, computed on a 160×160 mesh at $t = 0$ and $100s$ and in Figure 7.7 the same variables at $t = 150$ and $200s$. The solutions were computed with $M = L = 3$. In Figure 7.8, we depict the difference of the obtained result to the deterministic ones of Example 6.1. For a better comparison, we have used the same range of values for the different simulations. We can observe that in the stochastic case vortices have developed beneath the bubble. This is probably a feature of the higher moments and is caused because there is no feedback to the dynamics, see (3.12), since this feature is not present in the fully stochastic Examples 7.4 and 7.5.

The experimental convergence study in time and space for the cloud and flow variables is presented in Figure 7.1 at the time $t = 10s$. We computed the solutions on different meshes with $M = L = 3$. Similarly to the deterministic case, one can observe a second-order convergence in space and time.

To test the convergence in the stochastic space, we obtain a reference solution computed by the stochastic Galerkin method with 20 stochastic modes. The convergence study in the stochastic space is presented in Figures 7.2, 7.3 and 7.4, where we plot the difference in the L^1-norm, the L^2-norm and the L^∞-norm between the reference solution and approximate solutions computed with different numbers of modes M and $L = M$. All the solutions are computed using a mesh with 160×160 cells and $\Delta t = 0.01$ at time $t = 10s$. One can see a spectral convergence with an approximate rate of $e^{-0.3M}$. Since the results with different norms are qualitatively the same, we will from now on just show the errors in the L^1-norm.

In Figure 7.5, the convergence in the stochastic space is computed by taking $L = 19$ for all the computed solutions with different numbers of modes M, i.e., the accuracy for

the quadrature increases, see (5.16). Again, all the solutions are computed using a mesh with 160×160 cells and $\Delta t = 0.01$ at time $t = 10s$. As expected, one can see that the errors are smaller in general and that the errors are already quite small even with a low number of modes M. In the following convergence studies, we will always use $M = L$, since the computational time is much higher for $L = 19$ and already with $M = L$ one obtains very similar results and an exponential decay of the same rate.

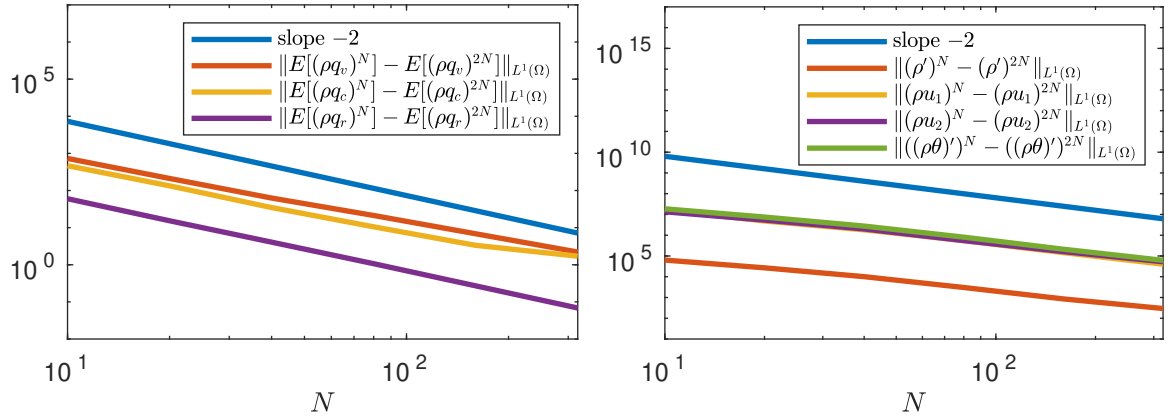

Figure 7.1: Example 7.1: Convergence study in time and space for the cloud variables $(\rho q_\ell), \ell \in \{v, c, r\}$, and the flow variables ρ', ρu_1, ρu_2 and $(\rho\theta)'$ computed at time $t = 10s$ using $\Delta t = {}^{256}/_{100N}$ and $M = L = 3$.

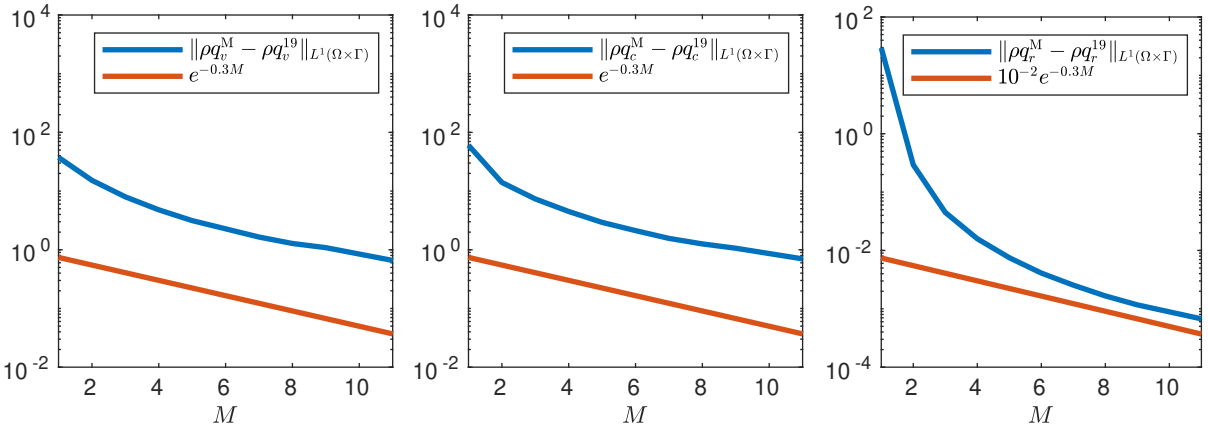

Figure 7.2: Example 7.1: Convergence study for the cloud variables $(\rho q_\ell), \ell \in \{v, c, r\}$, in the stochastic space computed with the L^1-norm at time $t = 10s$ using $\Delta t = 0.01$ and $M = L$.

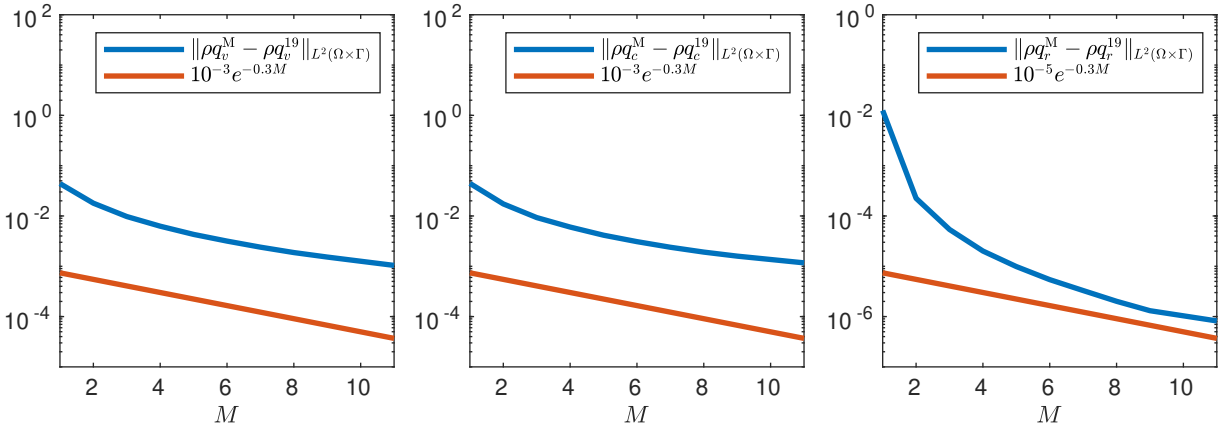

Figure 7.3: Example 7.1: Convergence study for the cloud variables $(\rho q_\ell), \ell \in \{v, c, r\}$, in the stochastic space computed with the L^2-norm at time $t = 10s$ using $\Delta t = 0.01$ and $M = L$.

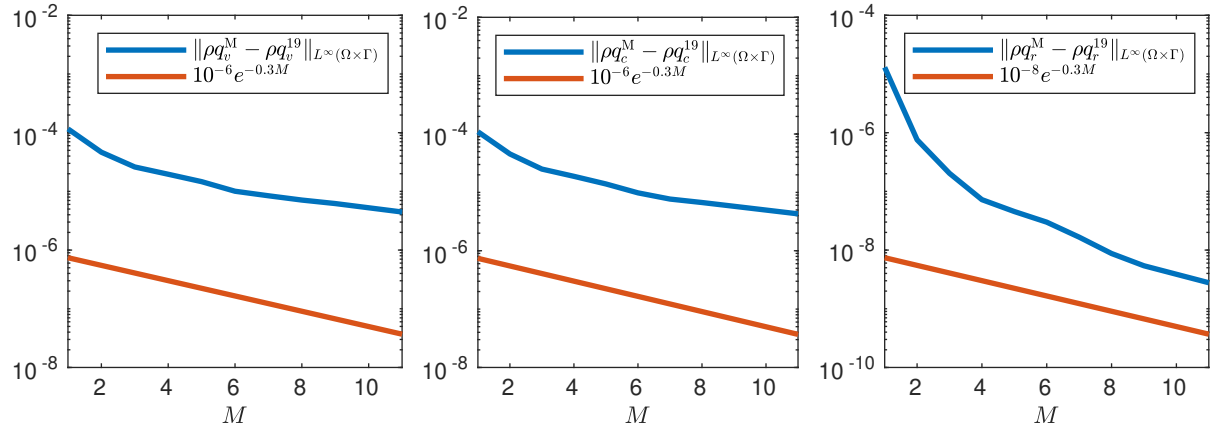

Figure 7.4: Example 7.1: Convergence study for the cloud variables $(\rho q_\ell), \ell \in \{v, c, r\}$, in the stochastic space computed with the L^∞-norm at time $t = 10s$ using $\Delta t = 0.01$ and $M = L$.

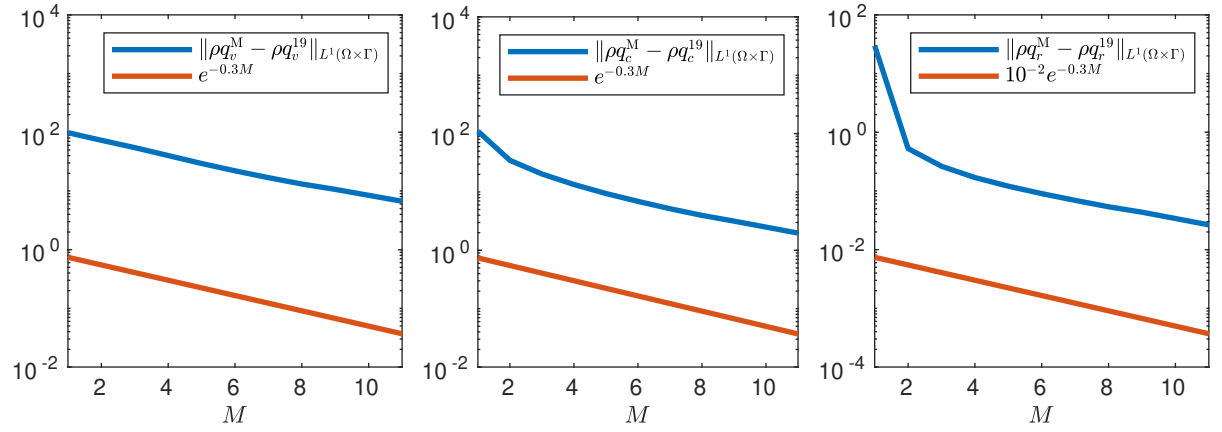

Figure 7.5: Example 7.1: Convergence study for the cloud variables $(\rho q_\ell), \ell \in \{v, c, r\}$, in the stochastic space computed with the L^1-norm at time $t = 10s$ using $\Delta t = 0.01$ and $L = 19$.

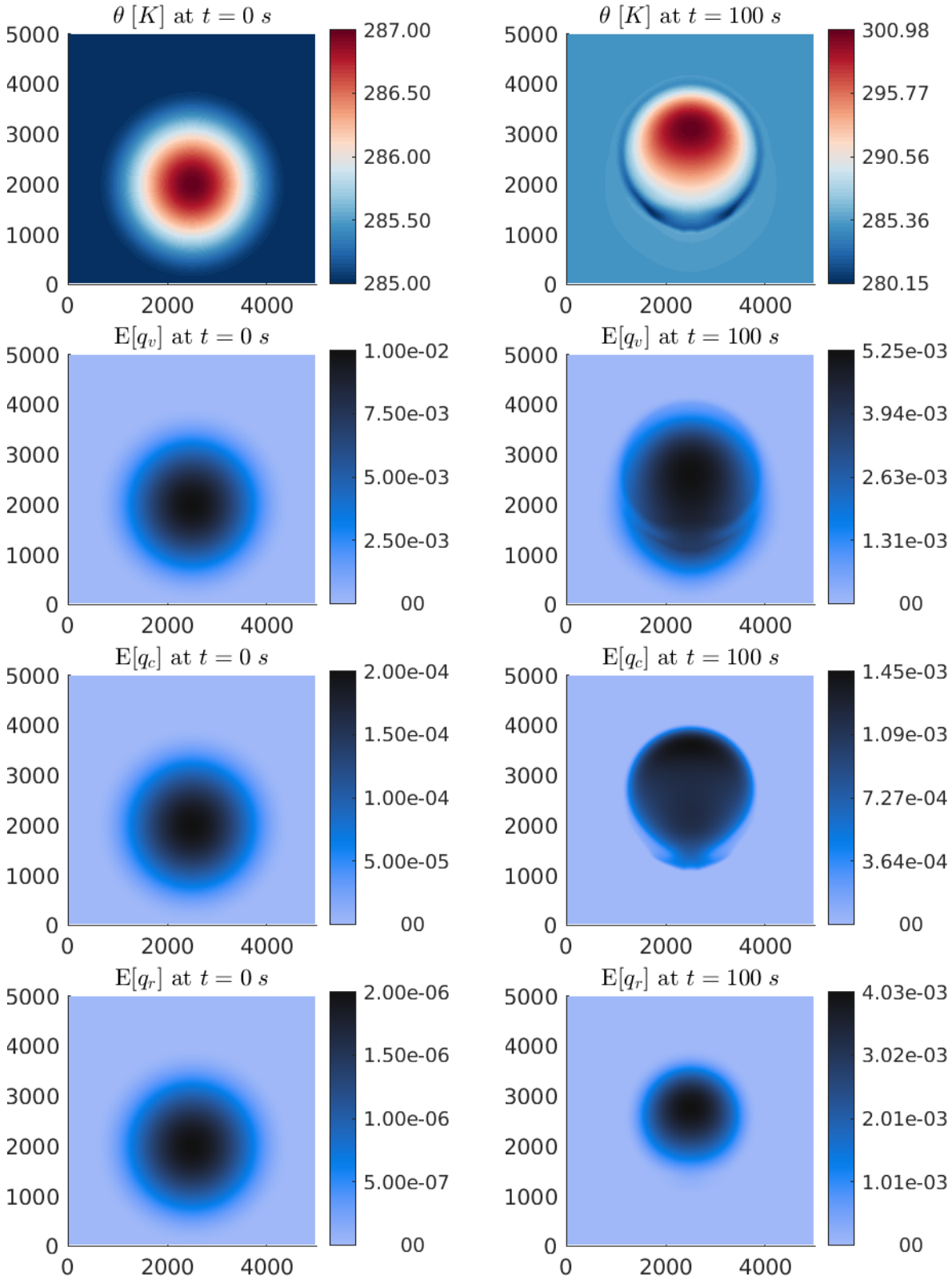

Figure 7.6: Example 7.1: Potential temperature θ, expected values of the water vapor concentration q_v, cloud drops concentration q_c and rain concentration q_r at times $t = 0$ (left column) and $100s$ (right column) simulated on a 160×160 mesh with $M = L = 3$.

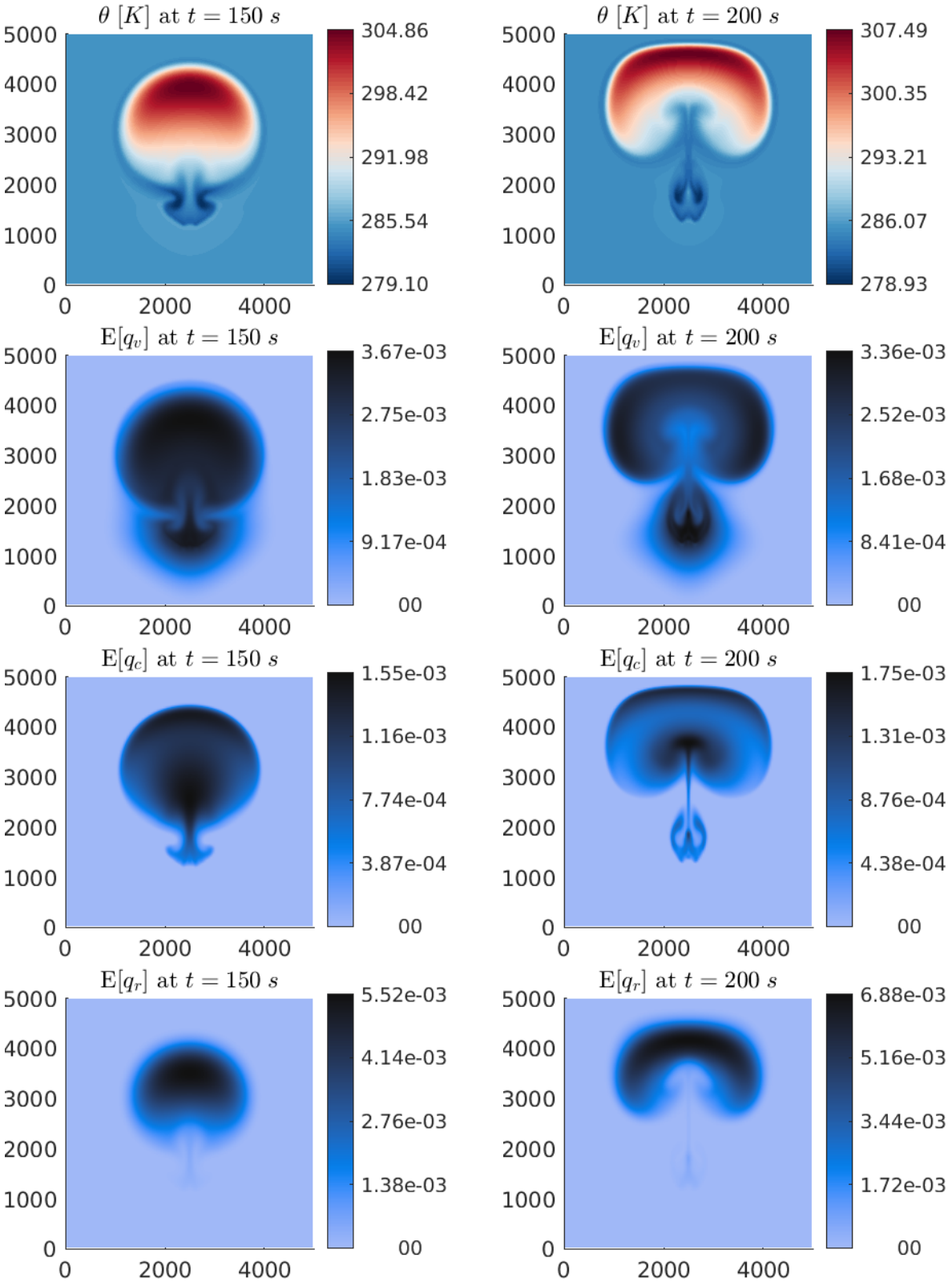

Figure 7.7: Example 7.1: Potential temperature θ, expected values of the water vapor concentration q_v, cloud drops concentration q_c and rain concentration q_r at times $t = 150$ (left column) and $200s$ (right column) simulated on a 160×160 mesh with $M = L = 3$.

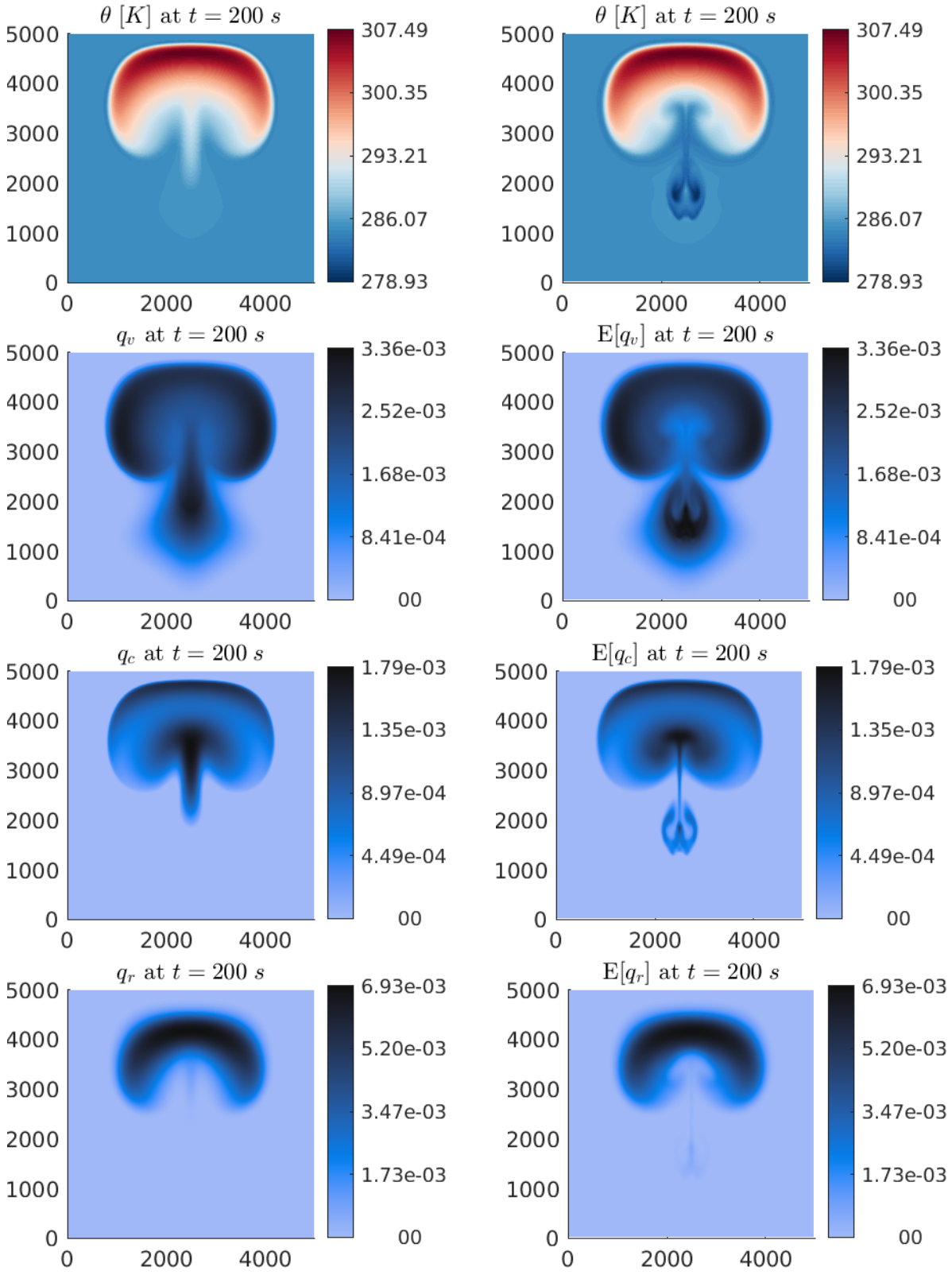

Figure 7.8: Example 7.1: Comparison of the potential temperature θ, expected values of the water vapor concentration q_v, cloud drops concentration q_c and rain concentration q_r (right column) with the respective solutions of the deterministic experiment of Example 6.1 (left column) at time $t = 200s$.

Example 7.2 (**Stochastic initial data with normally distributed** $X(\omega)$)

In this experiment, we demonstrate that the convergence does not depend on the choice of the distribution of $X(\omega)$. For this purpose, we choose the same initial data as in Example 7.1 just with a normally distributed $X(\omega)$. We use $X \sim \mathcal{N}(0,1)$. Thus, the difference to Example 7.1 is that instead of a basis with Legendre polynomials, we have a basis with Hermite polynomials of the stochastic space, see (5.3) and (5.5).

In Figure 7.10, we depict the potential temperature θ and the expected values of the cloud variables $(\rho q_\ell), \ell \in \{v, c, r\}$, computed on a 160×160 mesh at $t = 150$ and $200s$ with $M = L = 3$. In Figure 7.11, we depict the difference of the obtained result to the deterministic ones of Example 6.1. For a better comparison, we have used the same range of values for the different simulations. As in the previous example, the development of vortices beneath the bubble can be observed which is probably a feature of the higher moments and is caused because there is no feedback to the dynamics, see (3.12) since this feature is not present in the fully stochastic Examples 7.4 and 7.5.

To examine the convergence, we compute a reference solution by means of the stochastic Galerkin method with 12 stochastic modes and then analyze its difference to approximate solutions with different numbers of modes M and $L = M$. For all computations we used a mesh with 160×160 cells and $\Delta t = 0.01$. The convergence study in the stochastic space is presented in Figure 7.9 at time $t = 10s$. As in the case with a uniformly distributed $X(\omega)$ in Example 7.1, one can see a spectral convergence.

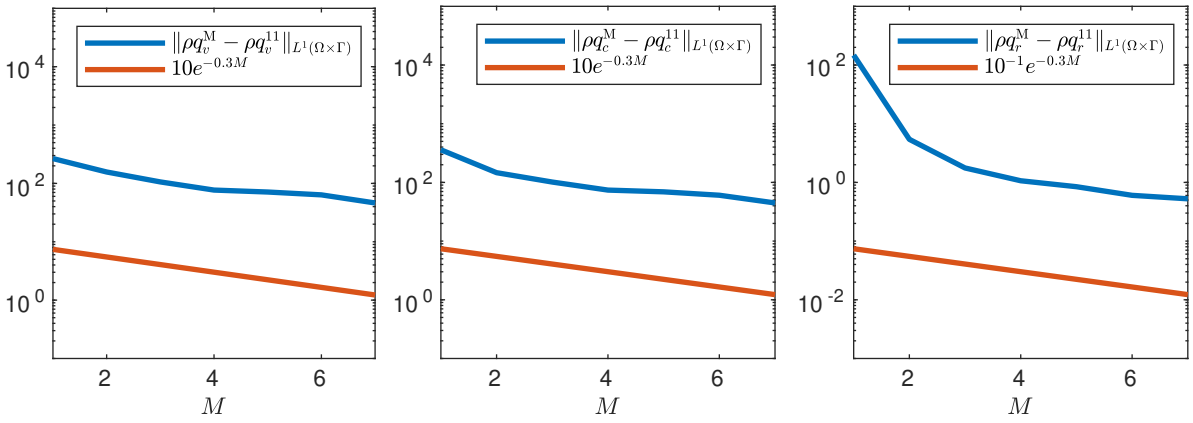

Figure 7.9: Example 7.2: Convergence study for the cloud variables $(\rho q_\ell), \ell \in \{v, c, r\}$, in the stochastic space computed with the L^1-norm at time $t = 10s$ using $\Delta t = 0.01$ and $M = L$.

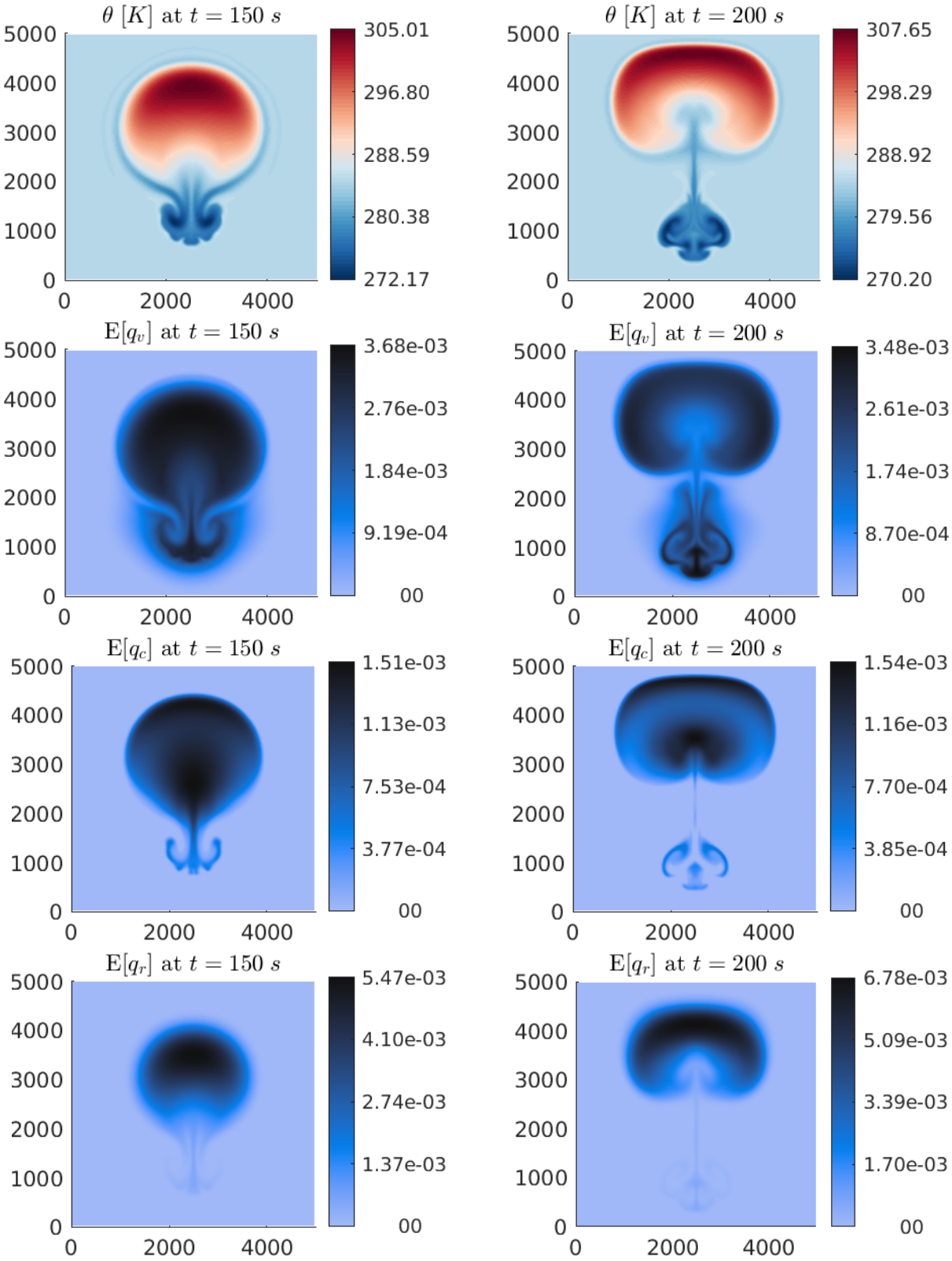

Figure 7.10: Example 7.2: Potential temperature θ, expected values of the water vapor concentration q_v, cloud drops concentration q_c and rain concentration q_r at times $t = 150$ (left column) and $200s$ (right column) simulated on a 160×160 mesh with $M = L = 3$.

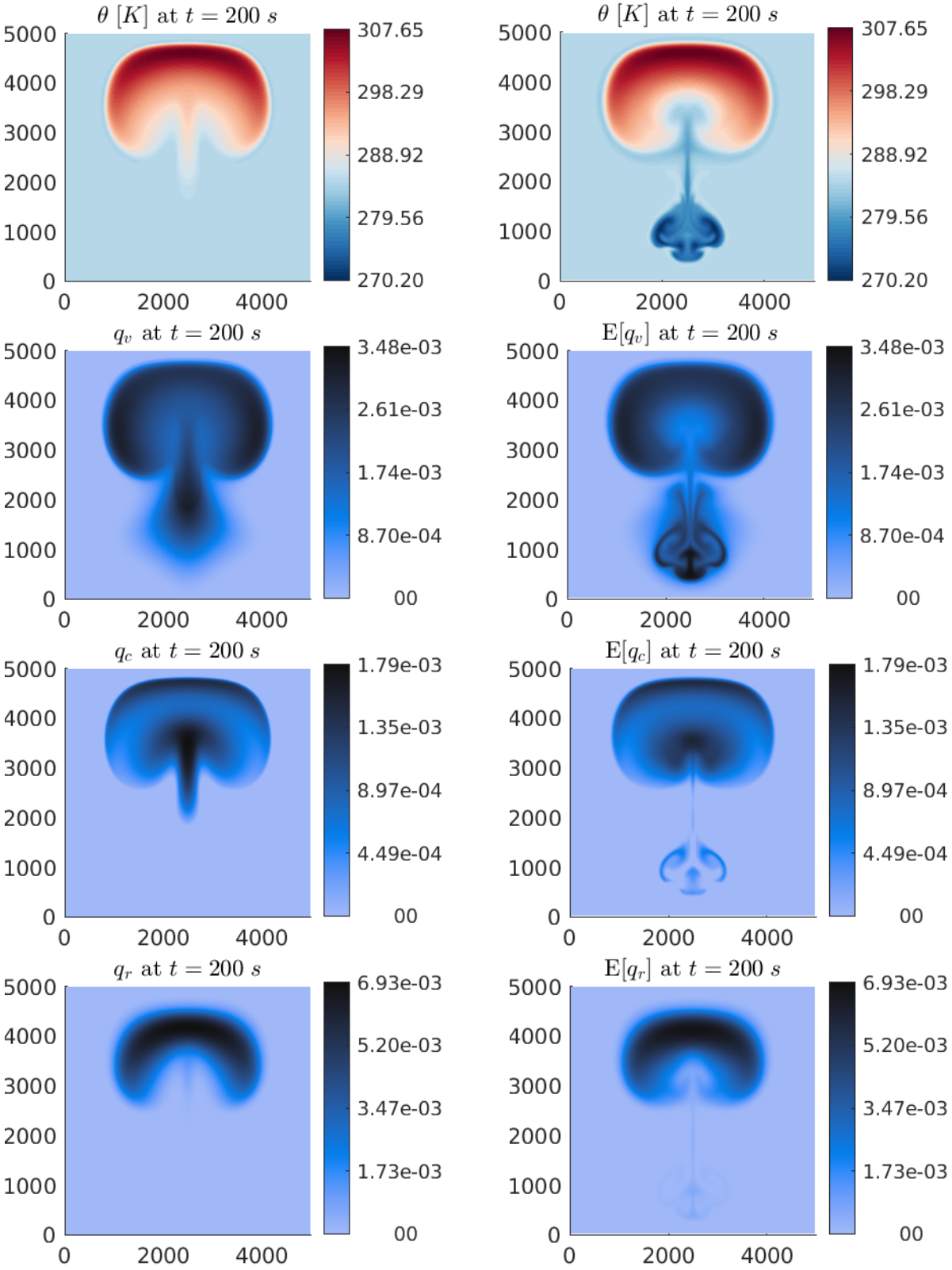

Figure 7.11: Example 7.2: Comparison of the potential temperature θ, expected values of the water vapor concentration q_v, cloud drops concentration q_c and rain concentration q_r (right column) with the respective solutions of the deterministic experiment of Example 6.1 (left column) at time $t = 200s$

Example 7.3 (**Stochastic parameters with uniformly distributed** $X(\omega)$)

In this experiment, we demonstrate that the stochastic Galerkin method also convergences experimentally when one considers perturbed parameter, see (5.23). Thus, we modify Example 6.1 with a 10% perturbation of the parameters k_1, k_2, α which is realized in the following way in the case of a uniformly distributed $X(\omega)$:

$$
\begin{aligned}
(\widehat{k_1})_0(\boldsymbol{x},0) = 4083,\ (\widehat{k_1})_1(\boldsymbol{x},0) = 0.1(\widehat{k_1})_0(\boldsymbol{x},0),\ (\widehat{k_1})_k(\boldsymbol{x},0) = 0 \quad \text{for } 2 \le k \le M,\\
(\widehat{k_2})_0(\boldsymbol{x},0) = 0.8,\ (\widehat{k_2})_1(\boldsymbol{x},0) = 0.1(\widehat{k_2})_0(\boldsymbol{x},0),\ (\widehat{k_2})_k(\boldsymbol{x},0) = 0 \quad \text{for } 2 \le k \le M,\\
\widehat{\alpha}_0(\boldsymbol{x},0) = 190.3,\ \widehat{\alpha}_1(\boldsymbol{x},0) = 0.1\widehat{\alpha}_0(\boldsymbol{x},0),\ \widehat{\alpha}_k(\boldsymbol{x},0) = 0 \quad \text{for } 2 \le k \le M,
\end{aligned}
$$

$$
\begin{aligned}
(\widehat{q_v})_0(\boldsymbol{x},0) = 0.005\,\theta'(\boldsymbol{x},0),\ (\widehat{q_v})_k(\boldsymbol{x},0) = 0 \quad \text{for } 1 \le k \le M,\\
(\widehat{q_c})_0(\boldsymbol{x},0) = 10^{-4}\,\theta'(\boldsymbol{x},0),\ (\widehat{q_c})_k(\boldsymbol{x},0) = 0 \quad \text{for } 1 \le k \le M,\\
(\widehat{q_r})_0(\boldsymbol{x},0) = 10^{-6}\,\theta'(\boldsymbol{x},0),\ (\widehat{q_r})_k(\boldsymbol{x},0) = 0 \quad \text{for } 1 \le k \le M,.
\end{aligned}
$$

The chosen perturbations of the parameters serve to demonstrate the convergence for this test case. A complete and meaningful parameter study is left for future works. The initial data for the Navier-Stokes variables as well as the boundary conditions are the same as in Example 6.1.

In Figure 7.13, we show the potential temperature θ and the expected values of the cloud variables $(\rho q_\ell), \ell \in \{v, c, r\}$, computed on a 160×160 mesh at $t = 150$ and $200s$. The solutions were computed with $M = L = 3$. In Figure 7.14, we depict the difference of the obtained result to the deterministic ones of Example 6.1. For a better comparison, we have used the same range of values for the different simulations. The solutions obtained with the stochastic parameters look almost the same as the deterministic ones. Thus, the model is not sensitive to a small perturbation of the chosen parameters. In addition, we do not see vortices forming beneath the bubble which could be observed in the previous examples. This is probably due to the fact, that the change of parameters was too small to cause a significantly different behavior compared to the deterministic case.

To test the convergence in the stochastic space, we compute a reference solution by means of the stochastic Galerkin method with 20 stochastic modes. The convergence study in the stochastic space is presented in Figure 7.12, where we plot the difference in the L^1-norm between the reference solution and approximate solutions computed with different numbers of modes M and $L = M$. All the solutions are computed using a mesh with 160×160 cells and $\Delta t = 0.01$ at time $t = 10s$. As in the case with a uniformly distributed perturbation $X(\omega)$ of the initial data in Example 7.1, one can see a spectral convergence with an exponential rate.

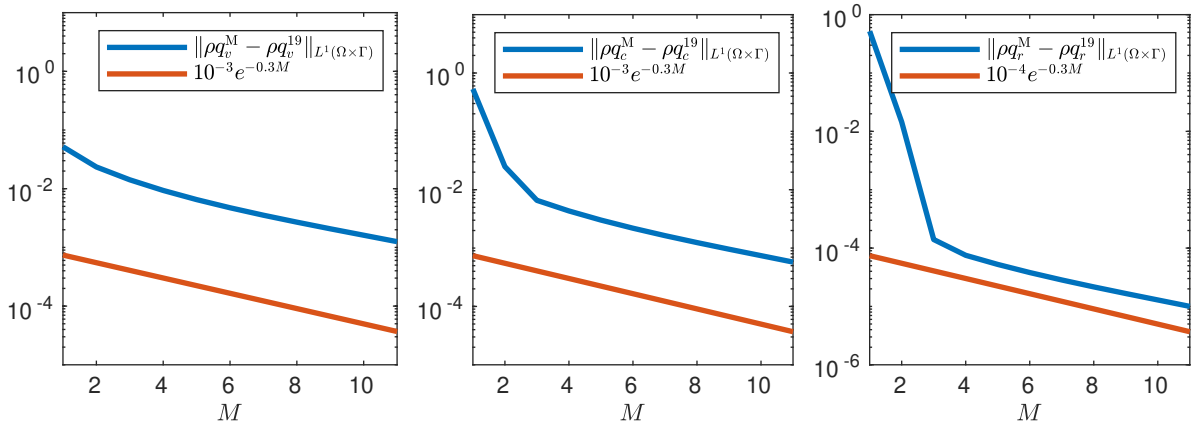

Figure 7.12: Example 7.3: Convergence study for the cloud variables $(\rho q_\ell), \ell \in \{v, c, r\}$, in the stochastic space computed with the L^1-norm at time $t = 10s$ using $\Delta t = 0.01$ and $M = L$.

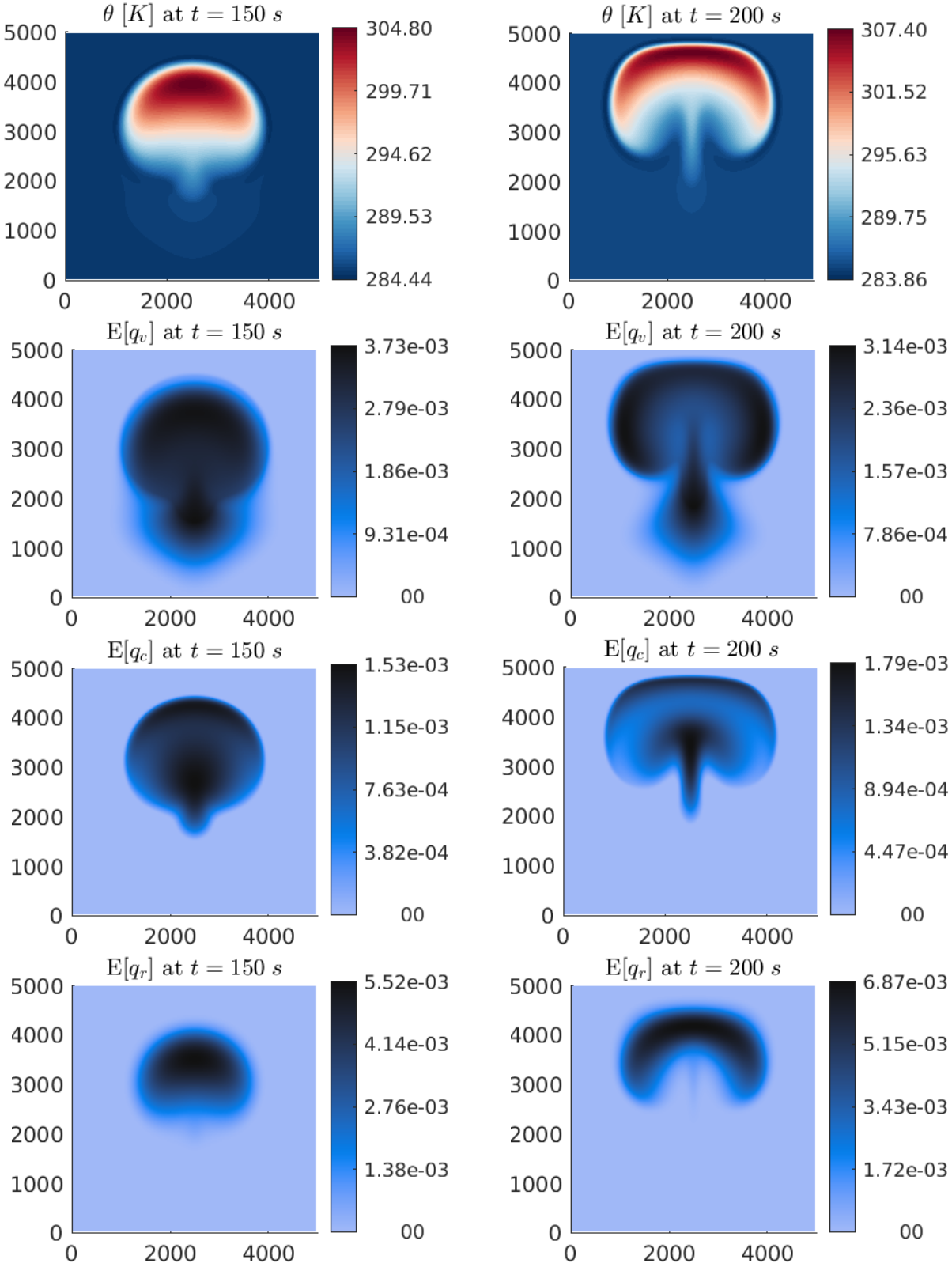

Figure 7.13: Example 7.3: Potential temperature θ, expected values of the water vapor concentration q_v, cloud drops concentration q_c and rain concentration q_r at times $t = 150$ (left column) and $200s$ (right column) simulated on a 160×160 mesh with $M = L = 3$.

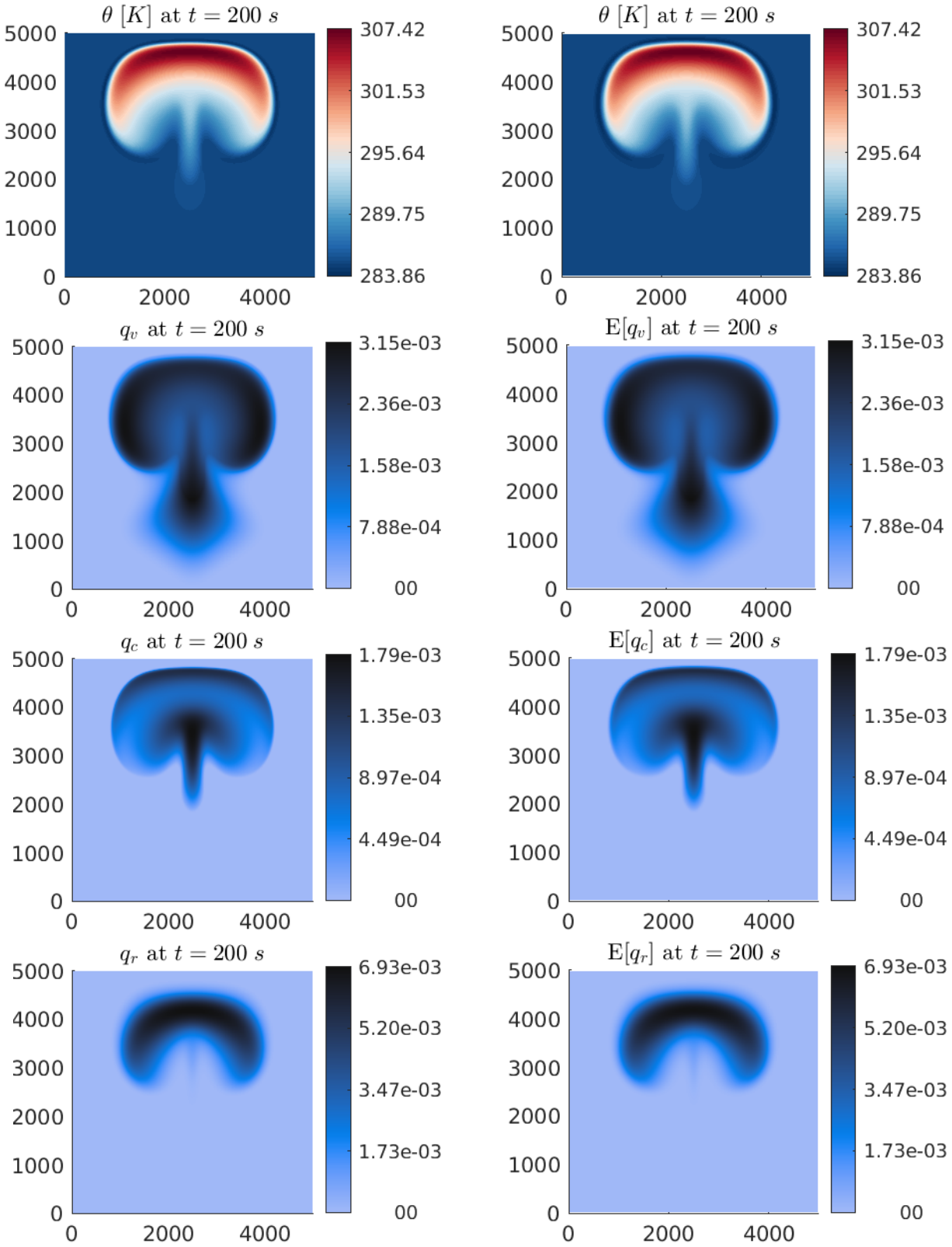

Figure 7.14: Example 7.3: Comparison of the potential temperature θ, expected values of the water vapor concentration q_v, cloud drops concentration q_c and rain concentration q_r (right column) with the respective solutions of the deterministic experiment of Example 6.1 (left column) at time $t = 200s$.

7.1.2 Fully stochastic model

In this subsection, we present experimental convergence results for the fully stochastic model (M3). We modify Example 6.1 by randomly perturbing the initial data of the model (M3) with a uniformly or normally distributed $X(\omega)$.

In Example 7.4, we present the spatio-temporal convergence as well as the convergence in the stochastic space for the case in which the initial vapor concentration q_v is perturbed by 10% which is realized with a uniformly distributed $X(\omega)$. The setup is the same as in Example 7.1 with the addition that now also the Navier-Stokes variables are random. In Example 7.5, we then investigate the convergence for the same setup as in Example 7.4 but this time with a normally distributed $X(\omega)$ and demonstrate that the convergence of the method does not change with a different choice of distribution. Since we use the same numerical method for the space and time discretization as in Example 7.4, we just investigate the convergence in the stochastic space in Example 7.5.

Example 7.4 (Stochastic initial data with uniformly distributed $X(\omega)$)

In this example, we consider a 10% perturbation of the initial water vapor concentration in the fully stochastic model (M3). This is realized through the following modification of Example 6.1 in the case of a uniformly distributed $X(\omega)$ for the cloud variables

$$
\begin{aligned}
&(\widehat{q_v})_0(\boldsymbol{x},0) = 0.005\,\theta'(\boldsymbol{x},0),\ (\widehat{q_v})_1(\boldsymbol{x},0) = 0.1\,(\widehat{q_v})_0(\boldsymbol{x},0),\ (\widehat{q_v})_k(\boldsymbol{x},0) = 0 \quad \text{for } 2 \le k \le M,\\
&(\widehat{q_c})_0(\boldsymbol{x},0) = 10^{-4}\,\theta'(\boldsymbol{x},0),\ (\widehat{q_c})_k(\boldsymbol{x},0) = 0 \quad \text{for } 1 \le k \le M,\\
&(\widehat{q_r})_0(\boldsymbol{x},0) = 10^{-6}\,\theta'(\boldsymbol{x},0),\ (\widehat{q_r})_k(\boldsymbol{x},0) = 0 \quad \text{for } 1 \le k \le M
\end{aligned}
$$

and for the Navier-Stokes variables

$$
\begin{aligned}
&(\widehat{\rho'})_0(\boldsymbol{x},0) = -\bar{\rho}(\boldsymbol{x})\frac{(\widehat{\theta'})_0(\boldsymbol{x},0)}{\bar{\theta}(\boldsymbol{x}) + (\widehat{\theta'})_0(\boldsymbol{x},0)},\ (\widehat{\rho'})_k(\boldsymbol{x},0) = 0 \quad \text{for } 1 \le k \le M,\\
&(\widehat{\rho\boldsymbol{u}})_k(\boldsymbol{x},0) = 0 \quad \text{for } 0 \le k \le M,\\
&\widehat{((\rho\theta)')}_0(\boldsymbol{x},0) = \bar{\rho}(\boldsymbol{x})(\widehat{\theta'})_0(\boldsymbol{x},0) + \bar{\theta}(\widehat{\rho'})_0(\boldsymbol{x},0) + (\widehat{\theta'})_0(\boldsymbol{x},0)(\widehat{\rho'})_0(\boldsymbol{x},0),\\
&\qquad\qquad \widehat{((\rho\theta)')}_k(\boldsymbol{x},0) = 0 \quad \text{for } 1 \le k \le M,
\end{aligned}
$$

where

$$
\begin{aligned}
&(\widehat{\theta'})_0(\boldsymbol{x},0) = \begin{cases} 2\cos^2\left(\frac{\pi r}{2}\right), & r := \sqrt{(x_1-2500)^2 + (x_2-2000)^2} \le 2000,\\ 0, & \text{otherwise} \end{cases}\\
&(\widehat{\theta'})_k(\boldsymbol{x},0) = 0 \quad \text{for } 1 \le k \le M.
\end{aligned}
$$

As in Example 6.1, it is $\bar{\theta} = 285\,\mathrm{K}$ and $p_0 = \bar{p} = 10^5\,\mathrm{Pa}$ and

$$
\bar{\rho}(\boldsymbol{x}) = \frac{p_0}{R\bar{\theta}(\boldsymbol{x})}\pi_e(\boldsymbol{x})^{\frac{1}{\gamma-1}}, \quad \pi_e(\boldsymbol{x}) = 1 - \frac{g x_2}{c_p\bar{\theta}}.
$$

In Figure 7.18, we depict the expected values of the potential temperature θ and the cloud variables $(\rho q_\ell), \ell \in \{v, c, r\}$, computed on a 160×160 mesh at times $t = 150$

and $200s$ with $M = L = 3$. A comparison with the solutions of the experiment with stochastic cloud dynamics of Example 7.1 and the deterministic ones of Example 6.1 is shown in Figures 7.19 and 7.20. For a better comparison, we have used the same range of values for the different simulations. We can observe that in the fully stochastic experiment no additional vortices beneath the bubble have developed and the results are slight variations of the deterministic results, which is to be expected. Thus, the vortex features of the solutions obtained with the stochastic cloud dynamic scheme seem to result from the missing feedback to the dynamics of the fluid. Additionally, it can be observed that the fully stochastic results are more smeared compared to the deterministic ones, which can be seen especially well for the potential temperature θ and the cloud drops concentration q_c.

The spatio-temporal convergence study for the expected values of the cloud and flow variables is presented in Figure 7.15 at the time $t = 10s$, where we computed the solutions on different meshes with $M = L = 3$. As in the deterministic case, one can clearly see a second-order convergence in space and time.

The stochastic convergence studies are presented in Figures 7.16 and 7.17 for the cloud and Navier-Stokes variables, respectively, at time $t = 10s$ using a mesh with 160×160 cells and $\Delta t = 0.01$. We computed the difference of approximate solutions with different numbers of modes M and $L = M$ to a reference solution with 20 stochastic modes. One can see a spectral convergence with an approximate rate of $e^{-0.3M}$ as in the convergence experiments for model (M2). The error of the rain drops in Figure 7.16 stays basically constant at some point because in this case we already approach machine precision.

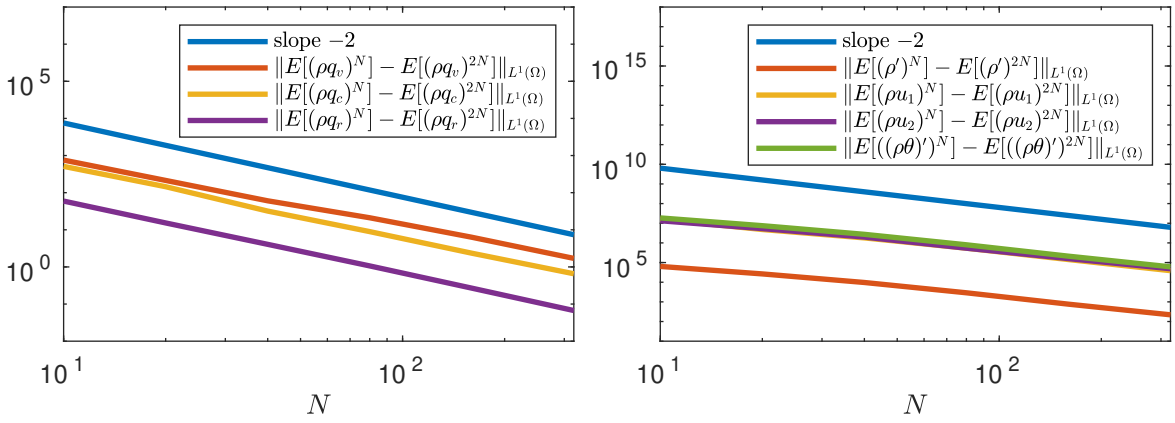

Figure 7.15: Example 7.4: Convergence study in time and space for the cloud variables $(\rho q_\ell), \ell \in \{v, c, r\}$, and the flow variables ρ', ρu_1, ρu_2 and $(\rho\theta)'$ computed at time $t = 10s$ using $\Delta t = {}^{256}/_{100N}$ and $M = L = 3$.

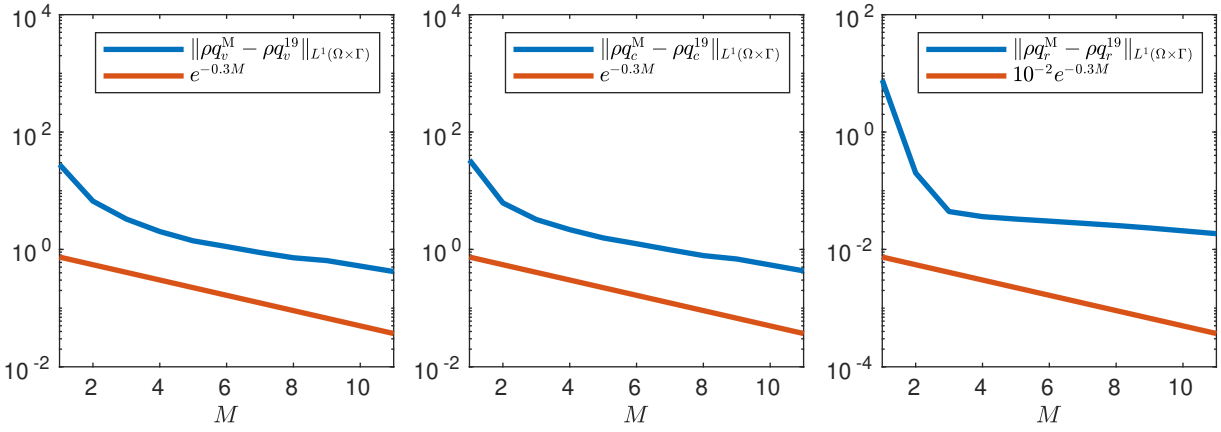

Figure 7.16: Example 7.4: Convergence study for the cloud variables $(\rho q_\ell), \ell \in \{v, c, r\}$, in the stochastic space computed with the L^1-norm at time $t = 10s$ using $\Delta t = 0.01$ and $M = L$.

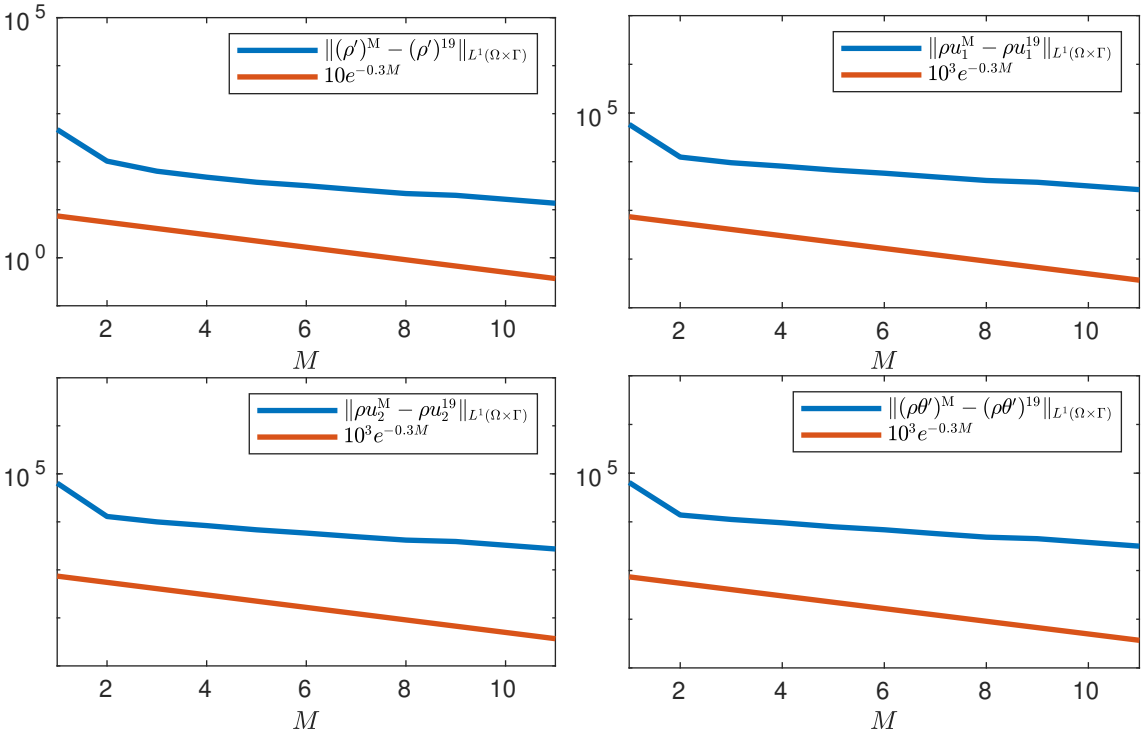

Figure 7.17: Example 7.4: Convergence study for the Navier-Stokes variables ρ', ρu_1, ρu_2 and $(\rho\theta)'$ in the stochastic space computed with the L^1-norm at time $t = 10s$ using $\Delta t = 0.01$ and $M = L$.

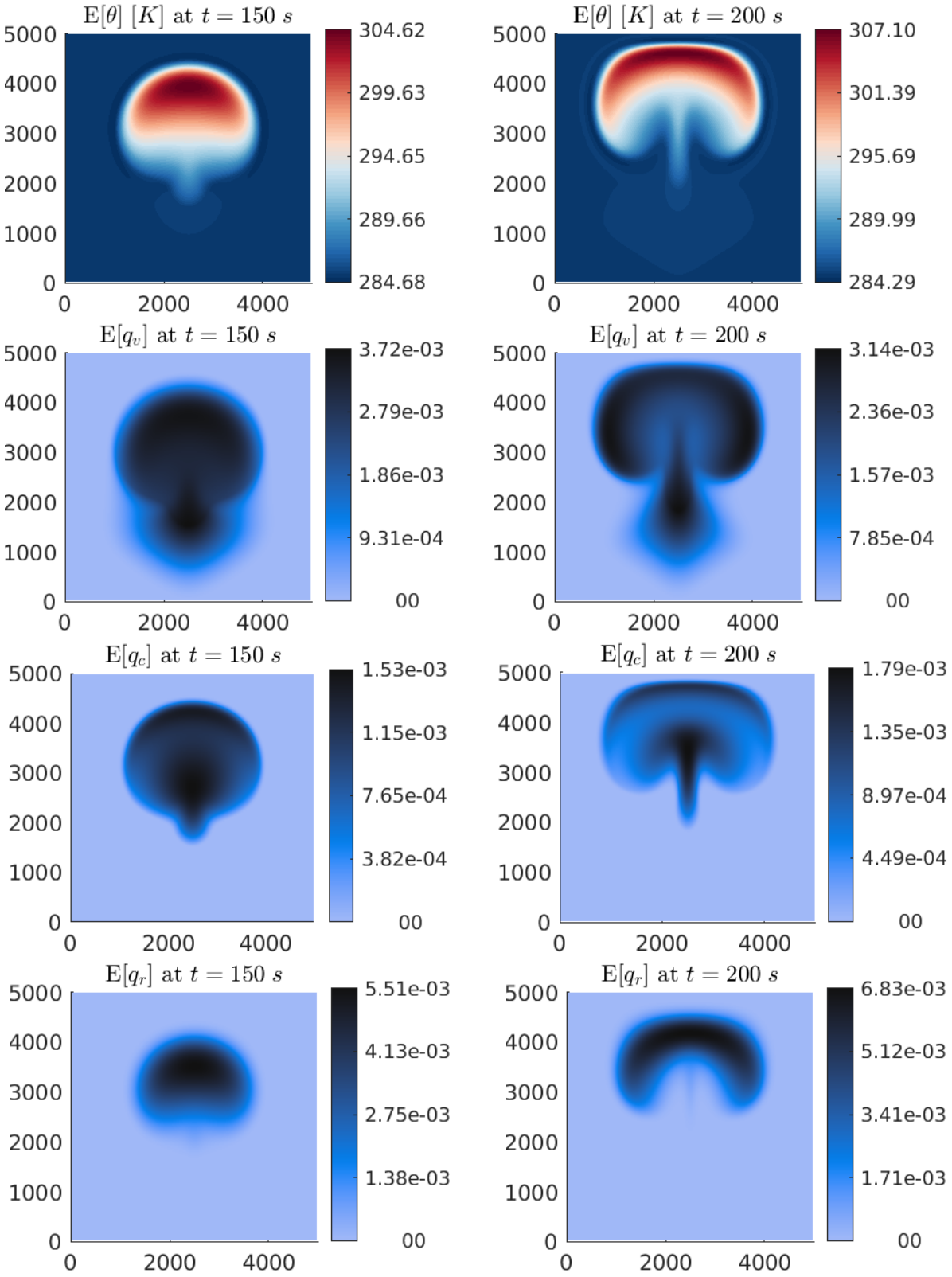

Figure 7.18: Example 7.4: Expected values of the potential temperature θ, the water vapor concentration q_v, cloud drops concentration q_c and rain concentration q_r at times $t = 150$ (left column) and $200s$ (right column) simulated on a 160×160 mesh with $M = L = 3$.

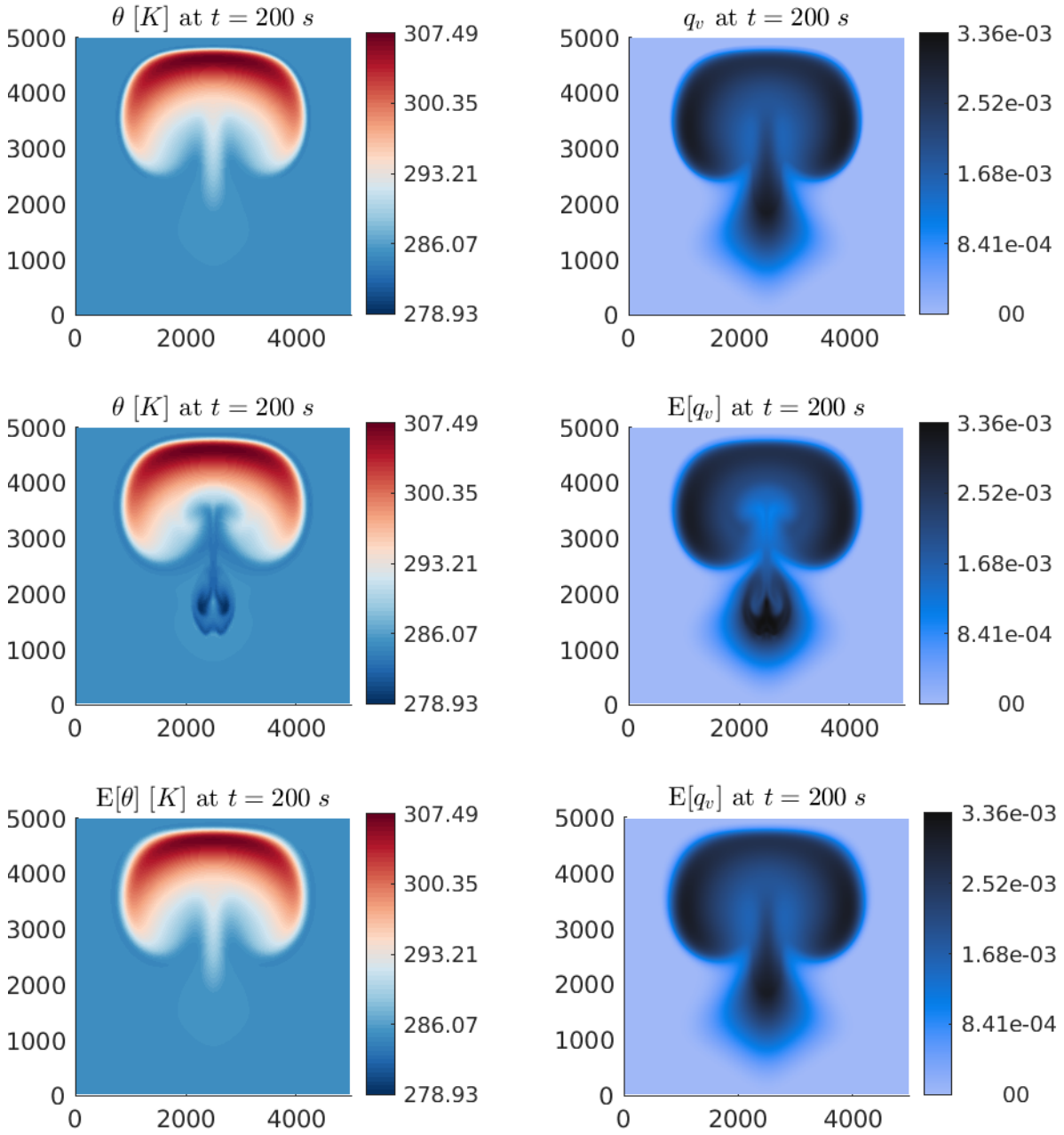

Figure 7.19: Example 7.4: Comparison of the expected values of the potential temperature θ and the water vapor concentration q_v (third row) with the respective solutions of the experiment with stochastic cloud dynamics of Example 7.1 (second row) and the respective solutions of the deterministic experiment of Example 6.1 (first row) at time $t = 200s$.

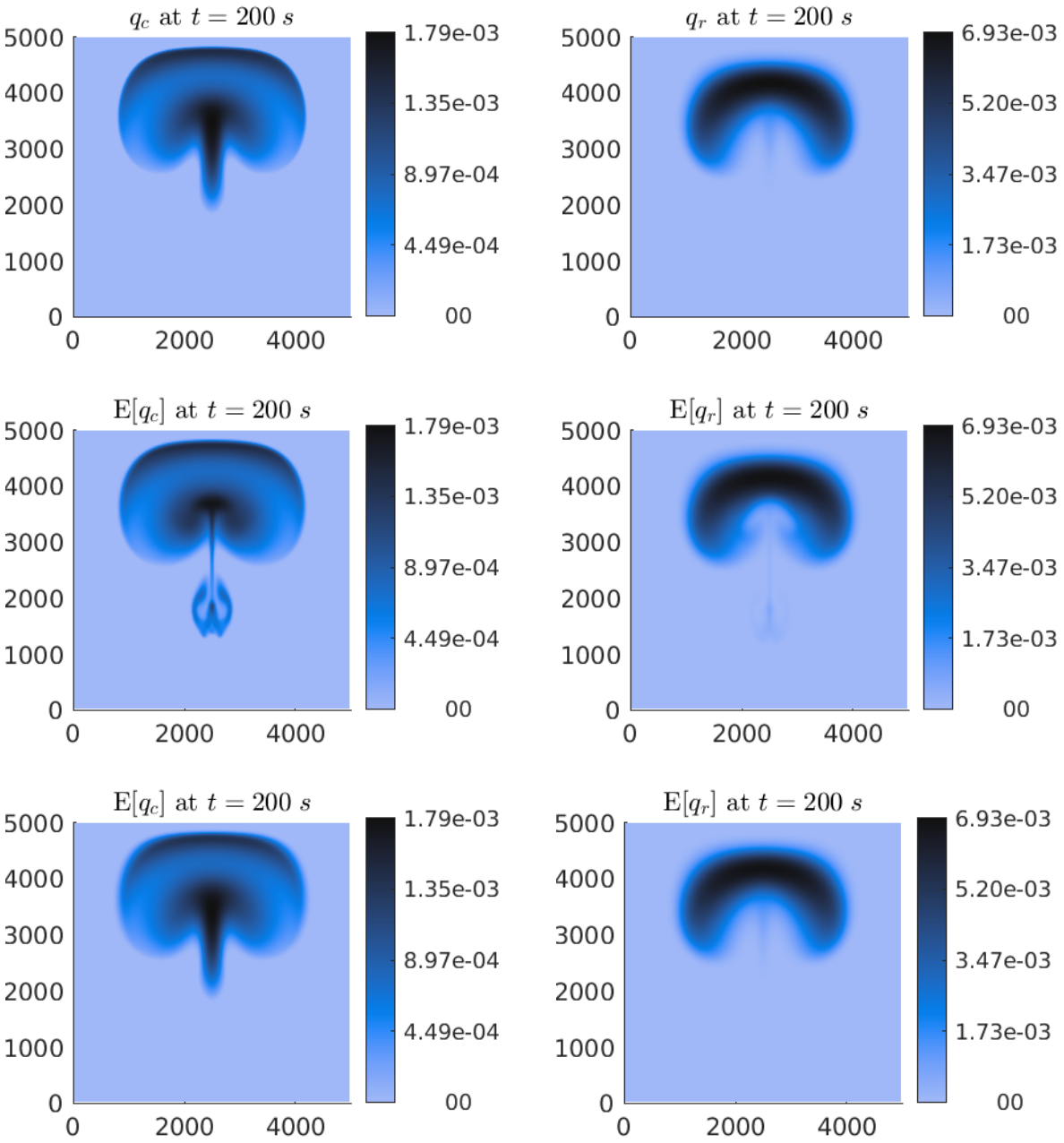

Figure 7.20: Example 7.4: Comparison of the expected values of the cloud drops concentration q_c and rain concentration q_r (third row) with the respective solutions of the experiment with stochastic cloud dynamics of Example 7.1 (second row) and the respective solutions of the deterministic experiment of Example 6.1 (first row) at time $t = 200s$.

Example 7.5 (**Stochastic initial data with normally distributed** $X(\omega)$)

In this experiment, we demonstrate that the convergence of the stochastic Galerkin method for the fully stochastic model (M3) does not depend on the choice of the distribution of $X(\omega)$. For this purpose, we choose the same initial conditions as in the previous Example 7.4, but this time with a normally distributed $X(\omega)$. We use $X \sim \mathcal{N}(0,1)$.

In Figure 7.23, the mean values of the potential temperature θ and the cloud variables $(\rho q_\ell), \ell \in \{v, c, r\}$, computed on a 160×160 mesh at times $t = 150$ and $200s$ with $M = L = 3$ are depicted. A comparison with the solutions of the experiment with stochastic cloud dynamics of Example 7.1 and the deterministic ones of Example 6.1 is shown in Figures 7.24 and 7.25. For a better comparison, we have used the same range of values for the different simulations. As in the previous example, we can observe that in the fully stochastic experiment no additional vortices beneath the bubble have developed and the results are slight variations of the deterministic results, which is to be expected. Thus, the vortex features of the solutions obtained with the stochastic cloud dynamic scheme are independent of the distributions of the initial perturbation and result from the missing feedback to the dynamics of the fluid.

In Figure 7.26, we investigated the influence of the choice of distribution for the initial perturbation. We depict the results obtained with the initial normally distributed perturbation of this experiment with the one obtained with the uniformly distributed ones of Example 7.4. For a better comparison, we have used again the same range of values for both of the simulations. Since the initial perturbation was rather small, the results look very similar. In general, both simulations smear the boundaries of the bubble. However, the smearing with the normal distribution is not as strong as with the uniform distribution, which can be seen for the cloud drops concentration q_c. This effect is due to the concentrated shape of the normal distribution around the expected value.

The convergence studies in the stochastic space are presented in Figures 7.21 and 7.22 for the cloud and Navier-Stokes variables, respectively, at time $t = 10s$. We computed the difference of approximate solutions with different numbers of modes M and $L = M$ to a reference solution with 12 stochastic modes. As in the case with a uniformly distributed $X(\omega)$ in Example 7.4, one can see a spectral convergence with an exponential decay rate.

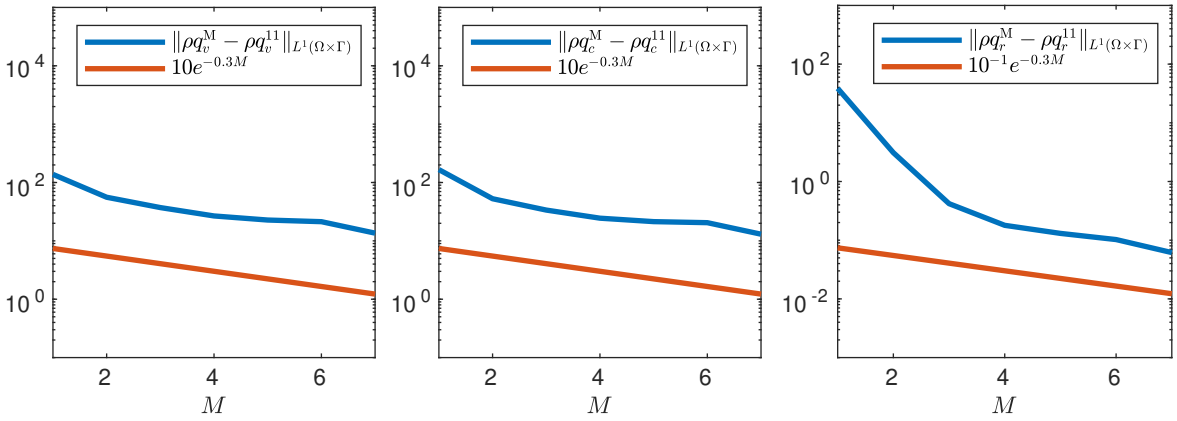

Figure 7.21: Example 7.5: Convergence study for the cloud variables $(\rho q_\ell), \ell \in \{v, c, r\}$, in the stochastic space computed with the L^1-norm at time $t = 10s$ using $\Delta t = 0.01$ and $M = L$.

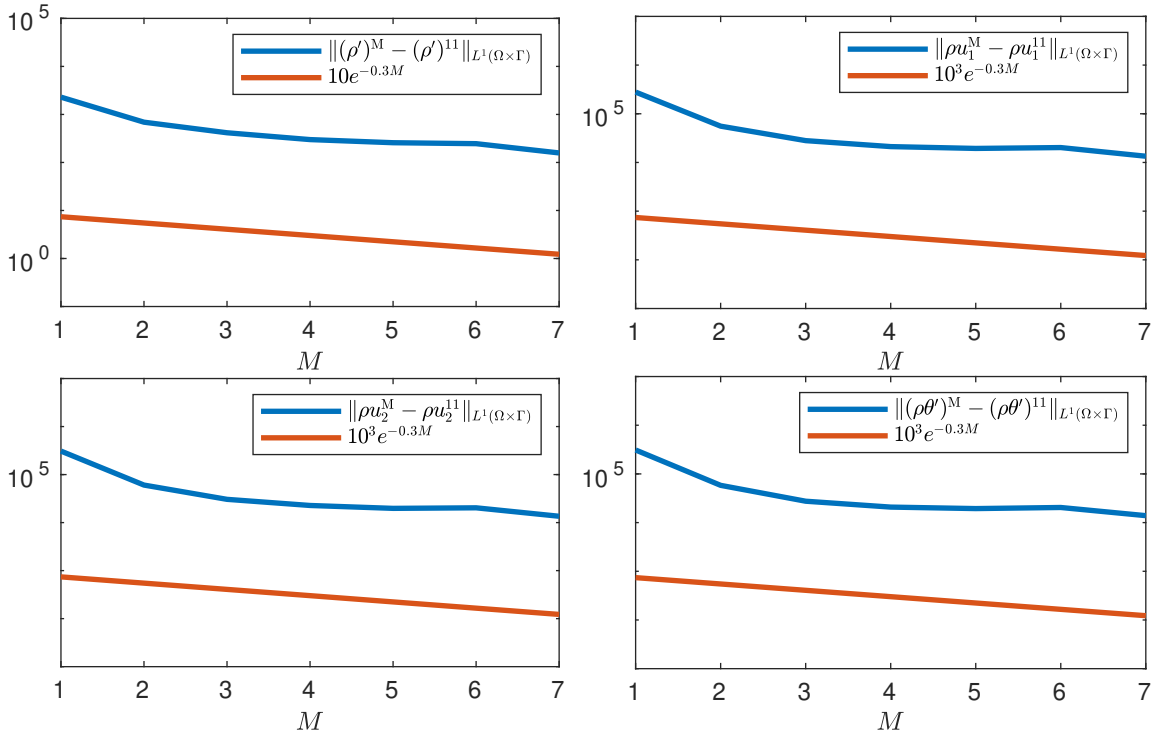

Figure 7.22: Example 7.5: Convergence study for the Navier-Stokes variables ρ', ρu_1, ρu_2 and $(\rho\theta)'$ in the stochastic space computed with the L^1-norm at time $t = 10s$ using $\Delta t = 0.01$ and $M = L$.

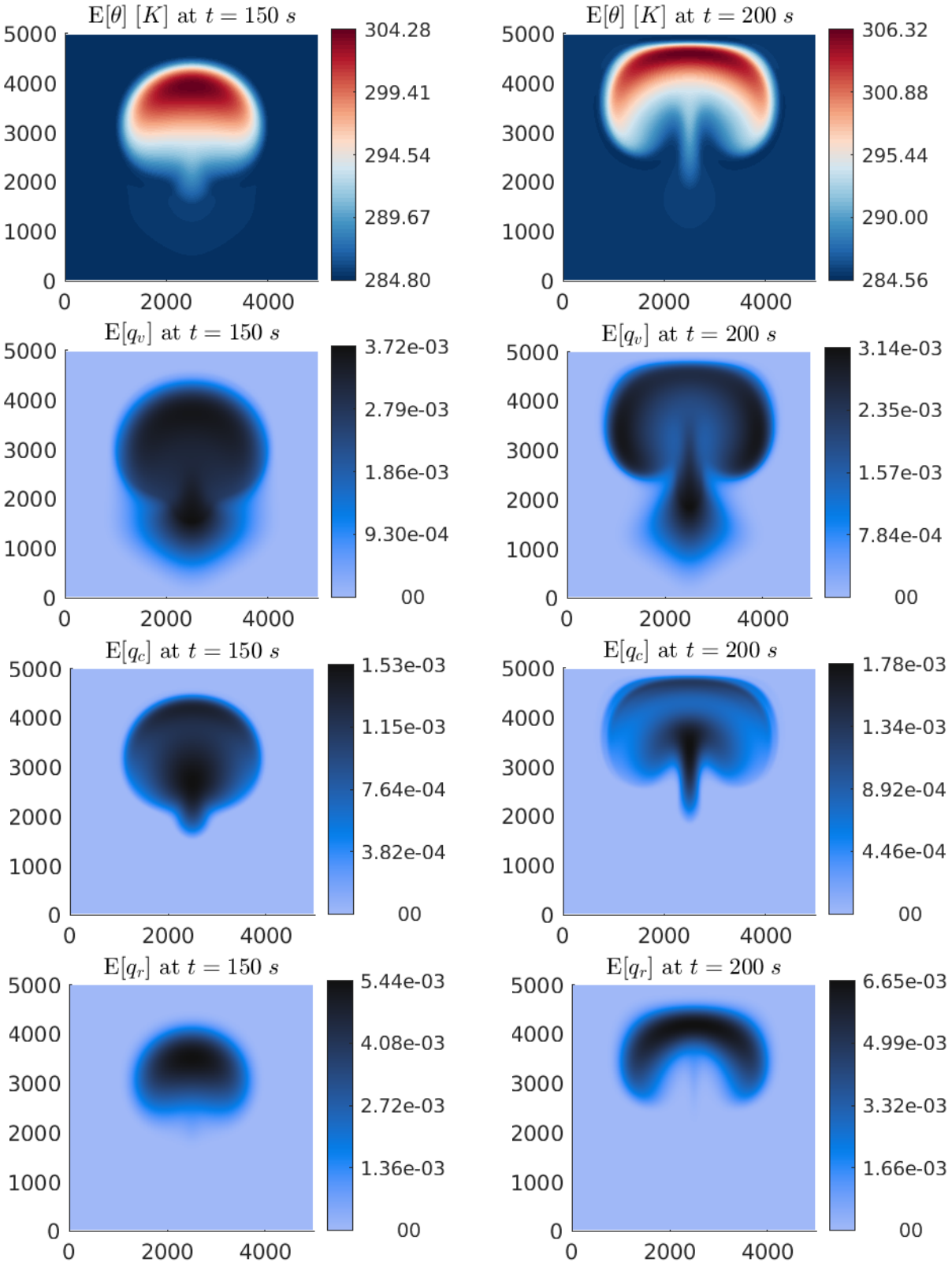

Figure 7.23: Example 7.5: Expected values of the temperature θ, the water vapor concentration q_v, cloud drops concentration q_c and rain concentration q_r at times $t = 150$ (left column) and $200s$ (right column) simulated on a 160×160 mesh with $M = L = 3$.

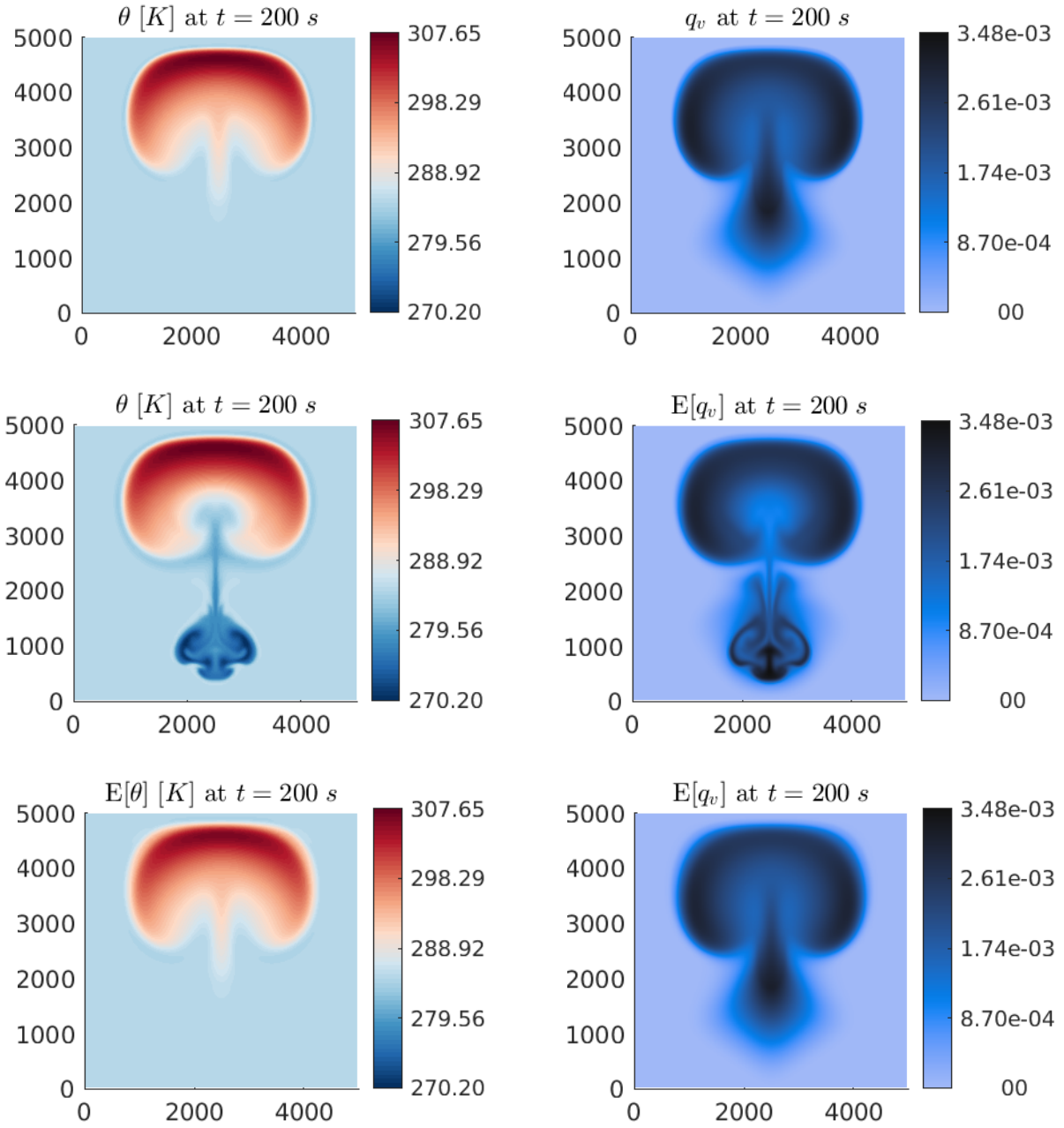

Figure 7.24: Example 7.5: Comparison of the expected values of the potential temperature θ and the water vapor concentration q_v (third row) with the respective solutions of the experiment with stochastic cloud dynamics of Example 7.1 (second row) and the respective solutions of the deterministic experiment of Example 6.1 (first row) at time $t = 200s$.

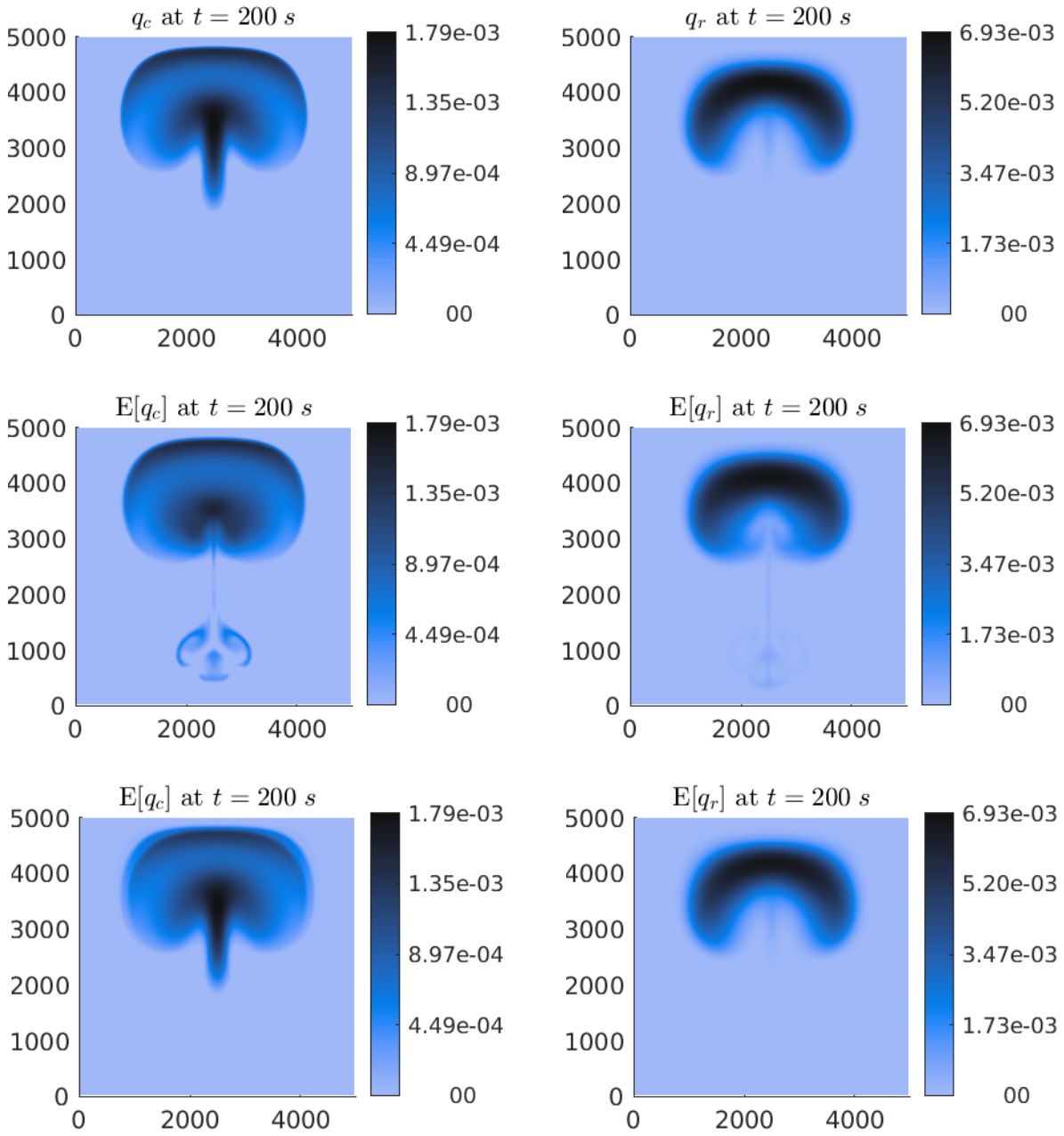

Figure 7.25: Example 7.5: Comparison of the expected values of the cloud drops concentration q_c and rain concentration q_r (third row) with the respective solutions of the experiment with stochastic cloud dynamics of Example 7.1 (second row) and the respective solutions of the deterministic experiment of Example 6.1 (first row) at time $t = 200s$.

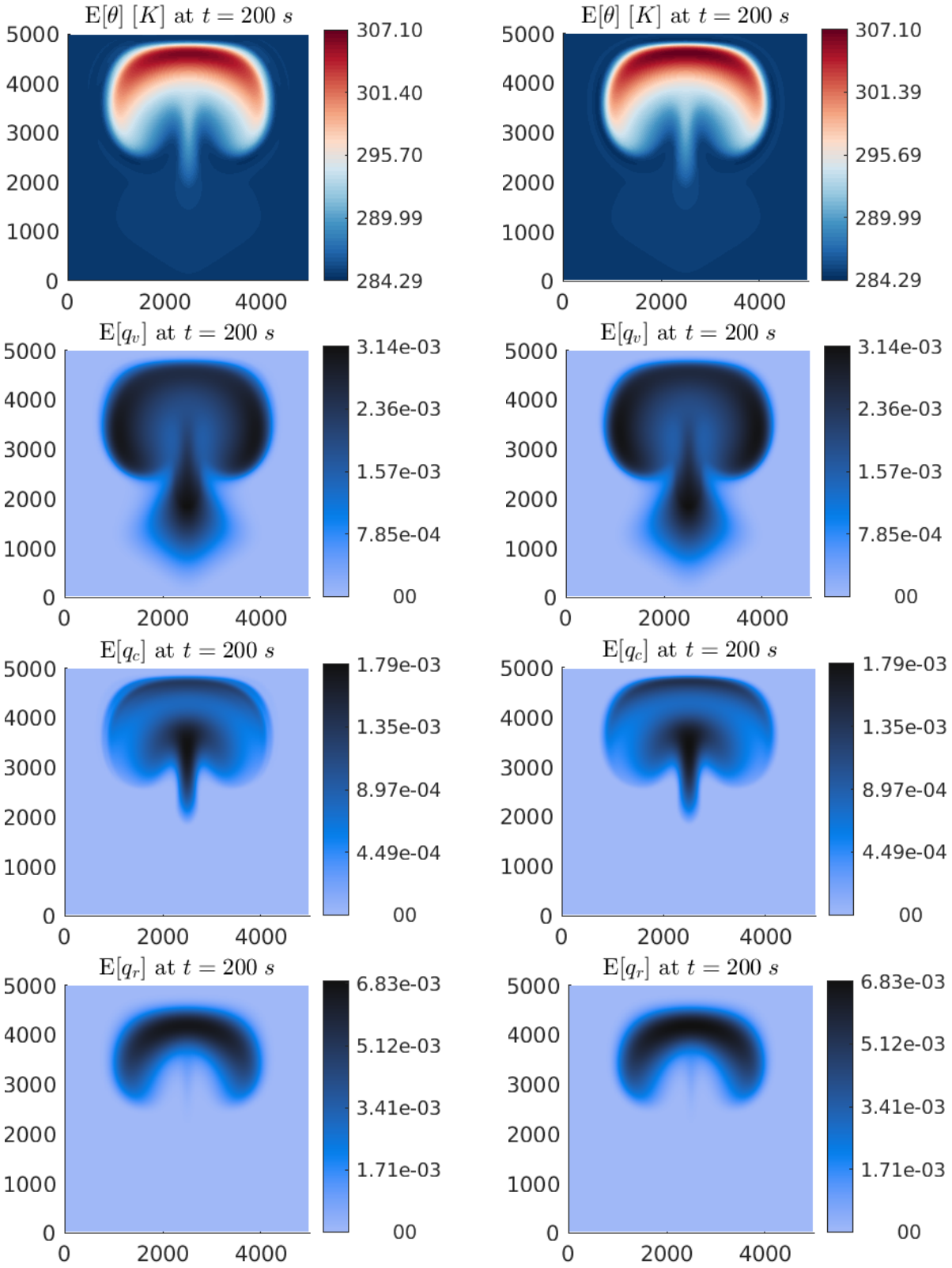

Figure 7.26: Example 7.5: Comparison of the expected values of the potential temperature θ, water vapor concentration q_v, cloud drops concentration q_c and rain concentration q_r with initial normally distributed perturbation (left column) with the respective solutions with initial uniformly distributed perturbation of Example 7.4 (right column) at time $t = 200s$.

7.2 Rayleigh-Bénard convection

In this section, we present the results of the uncertainty study for the Rayleigh-Bénard convection in both 2D and 3D. The experiments and results with stochastic cloud dynamics (M2) are based on [21], though the results differ due to the slightly modified cloud equations, see Remark 2.1. We investigate uncertainty propagation, which is triggered by the initial data of the water vapor concentration q_v. For the Rayleigh-Bénard experiments in this section, we always consider a uniform perturbation. A comparison with a normally distributed initial perturbation or even perturbations of certain parameters goes beyond the scope of this work and is left for future research.

It should be observed that uniform perturbations in the initial conditions for q_v may lead to either reduced or enhanced water vapor concentrations as compared to the deterministic simulations. Since the temperature gradient is quite small, a change in q_v translates to an (almost) linear change in saturation ratio, which directly controls cloud formation. Thus, in the case of positive perturbations, a higher water vapor concentration leads to earlier cloud formation and, in addition, a higher potential temperature change since more water is available in the system. The higher potential temperature change then results in stronger convection. On the other hand, lower values of q_v lead to a time delay in the formation of clouds, even if small convective cells are driven by the dry unstable situation. In a feedback cycle, a reduced or even delayed formation of cloud water propagates further to a weaker rain formation. Finally, the evaporation of rain water leads to a strong cooling effect of the lower layers of the domain, which also crucially depends on the amount of sedimenting rain water. These effects have to be taken into account for the evaluation of the different perturbation scenarios.

In Examples 7.6 and 7.7, we consider Rayleigh-Bénard convection in 2D with stochastic cloud dynamics using (M2) and fully stochastic dynamics using (M3), respectively. With these two experiments, we demonstrate that the two different stochastic models (M2) and (M3) lead to qualitatively different results, although starting with the same initial conditions and initial perturbation of q_v. In Examples 7.8 and 7.9, we then consider stochastic Rayleigh-Bénard convection in 3D using again the two stochastic models (M2) and (M3), respectively. We investigate the effect of the initial perturbation of q_v in both cases by considering a 0%, 10%, 20% and 50% perturbation of the initial water vapor concentration q_v. In terms of oversaturation, one reaches initial values of $q_v - q_*$ of $8.9 \cdot 10^{-3}$ for 10%, $1.1 \cdot 10^{-2}$ for 20% and $1.3 \cdot 10^{-2}$ for 50% of perturbation. Comparing the solutions in Example 7.8 with the ones in Example 7.9 one can again notice that the two stochastic models produce quite different solutions. Additionally, one can observe that the perturbation of the initial water vapor concentration has a clear effect on the formation of the pattern. The bigger the perturbations are, the more changes in patterns and solutions can be seen.

Example 7.6 (**Stochastic cloud dynamics Rayleigh-Bénard convection in 2D**)

In this experiment, we simulate Rayleigh-Bénard convection in 2D with stochastic cloud dynamics by using model (M2). The numerical solutions are computed on a domain

$\Omega = [0, 5000] \times [0, 1000]\, m^2$ that has been discretized using 160×160 mesh cells. As initial conditions we choose the ones from the deterministic case in Example 6.4 and perturb the initial water vapor concentration by 10%. This means that we use (6.1) for the Navier-Stokes variables and

$$\begin{aligned} (\widehat{q_v})_0(\boldsymbol{x}, 0) &= 0.025\,(\theta'(\boldsymbol{x}, 0))_+,\ (\widehat{q_v})_1(\boldsymbol{x}, 0) = 0.1\,(\widehat{q_v})_0(\boldsymbol{x}, 0), \\ &\qquad (\widehat{q_v})_k(\boldsymbol{x}, 0) = 0 \quad \text{for } 2 \le k \le M, \\ (\widehat{q_c})_0(\boldsymbol{x}, 0) &= 10^{-4}\,(\theta'(\boldsymbol{x}, 0))_+,\ (\widehat{q_c})_k(\boldsymbol{x}, 0) = 0 \quad \text{for } 1 \le k \le M, \\ (\widehat{q_r})_0(\boldsymbol{x}, 0) &= 10^{-6}\,(\theta'(\boldsymbol{x}, 0))_+,\ (\widehat{q_r})_k(\boldsymbol{x}, 0) = 0 \quad \text{for } 1 \le k \le M \end{aligned} \tag{7.1}$$

for the cloud variables. As boundary conditions we also use the same ones as in the deterministic case, that is Dirichlet boundary conditions for the potential temperature, see (6.2), as well as periodic boundary conditions for all variables in horizontal direction and no-slip boundary conditions, see (4.21), for the velocities at the vertical boundaries and zero Neumann conditions, see (4.20), for the remaining variables in vertical direction, i.e. $\nabla\rho' \cdot \boldsymbol{n} = 0$, $\nabla(\rho q_\ell) \cdot \boldsymbol{n} = 0$, $\ell \in \{v, c, r\}$. Since the cloud variables are stochastic, we need to project the periodic and zero Neumann conditions. The projection is straightforward since the term is linear in the cloud variables and one ends up with periodic and zero Neumann boundary conditions for all the expansion coefficients.

In Figure 7.27, we present time snapshots of the numerical solution for the potential temperature at times $t = 1000$, 2000, 3000 and $6000s$. The expected values and standard deviations of the cloud variables, see (5.8) and (5.9), are depicted in Figures 7.28–7.31 at times $t = 1000$ and $6000s$. In Figures 7.28 and 7.29, also the differences of the expected value of the water vapor concentration to the saturation mixing ratio $E[q_v] - q_*$ are shown. From the results presented in Figure 7.27 for the potential temperature θ, one can observe two major features. First, the perturbation leads to an earlier start in convection and rolls forming already at time $t = 1000s$. This feature can also be recognized for the water vapor concentration in Figure 7.28 and ends up in much more rain at time $t = 1000s$ than in the deterministic experiment at the same time. This is probably due to the fact that even small variations in water vapor have a strong impact on cloud formation since the activation of cloud droplets is a threshold process. For values closer to saturation, even small variations in vertical upward motions can trigger cloud formation and thus rain formation which is then sedimenting. The second feature is that the perturbation in the initial water vapor distribution leads to a stronger vertical gradient in potential temperature at the beginning of convection at times $t = 1000$ and $2000s$, that is, at low levels the temperature is much smaller than in the deterministic case. This feature is due to the cooling of sedimenting rain water. For simulations with a high water vapor loading, more clouds form and thus more rain falls into lower levels and cools the environment by evaporation. Since this process is very effective, the temperature can be reduced drastically. Note that this feature is well-known for the real atmosphere: Falling rain can cool lower levels efficiently so that a transition from melting rain droplets to snow can be possible for the winter seasons. The efficient formation of rain also leads to a strong reduction in cloud water since accretion can eat up cloud droplets in the lower levels, see Figure 7.30. For reduced values of initial water vapor, processes of cloud and precipitation formation are strongly reduced. However, on average the positive perturbations seem to dominate the statistical picture. The results

at time $t = 6000s$ are then very similar to the ones obtained in the deterministic case, see Example 6.4, both structure-wise and value-wise. One can even observe that the standard deviation of all cloud variables decreases by one order of magnitude compared to time $t = 1000s$. Thus, the main effect of the uncertainty in this example obtained with model (M2) seems to be at the starting point of convection.

Remark 7.1*:* For simplicity, the saturation mixing ratio q_* was calculated with the expected values of the cloud variables, that is $q_*(E[q_v], E[q_c], E[q_r])$. In the following stochastic experiments, we will always mean the saturation mixing ratio of the expected values when referring to q_*.

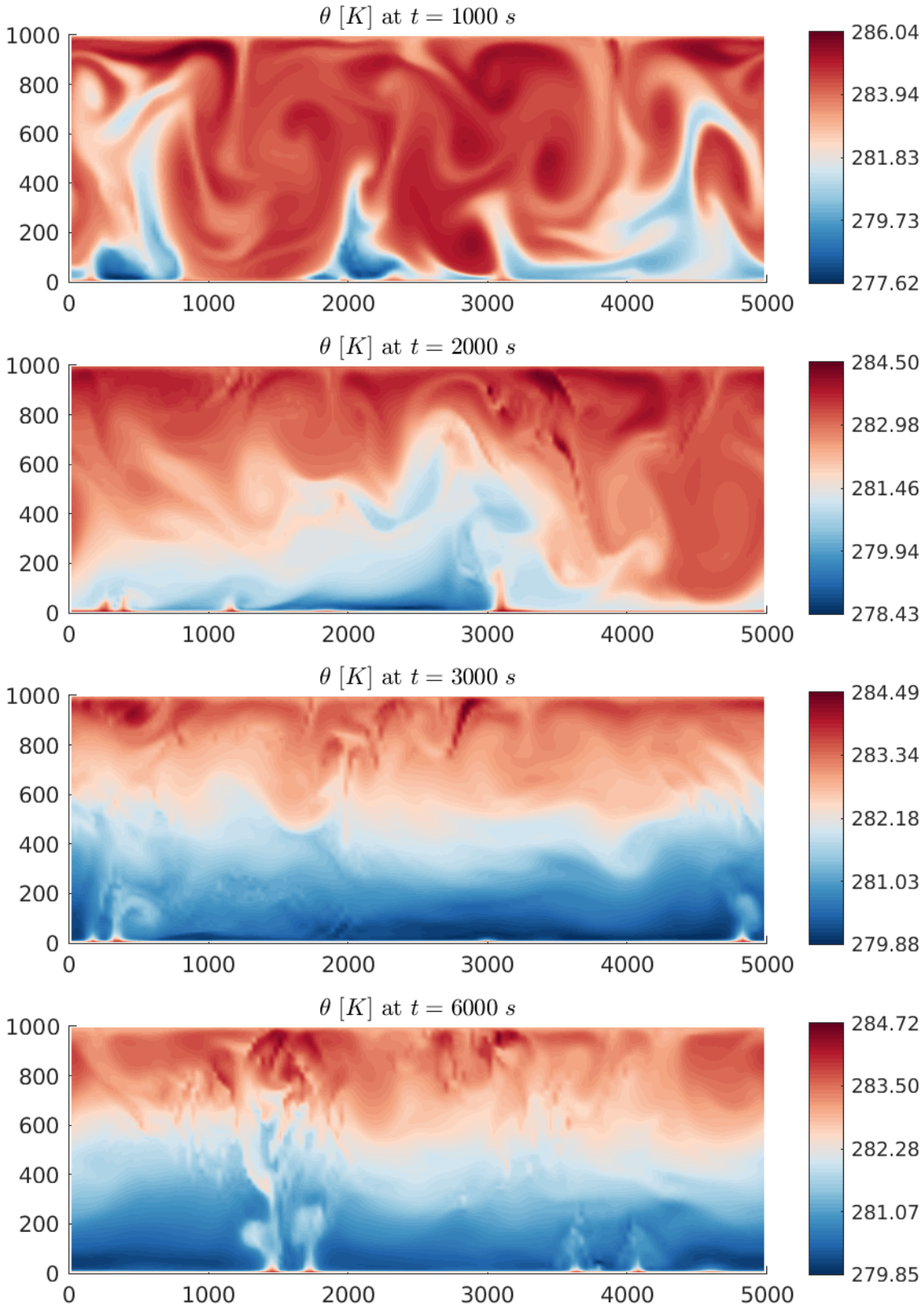

Figure 7.27: Example 7.6: Potential temperature θ at times $t = 1000$, 2000, 3000 and $6000s$ simulated on a 160×160 mesh.

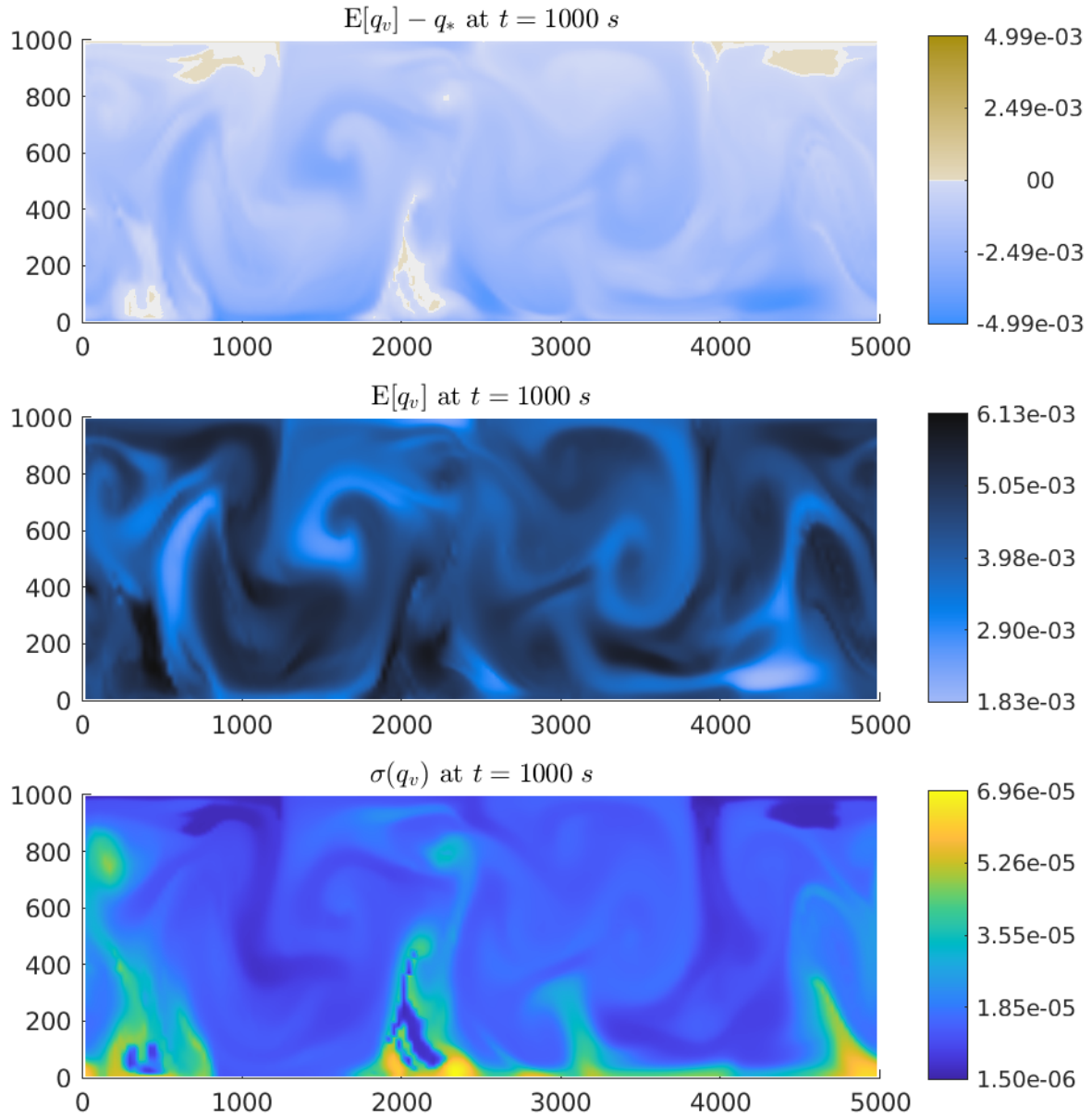

Figure 7.28: Example 7.6: Difference of the expected value of the water vapor concentration to the saturation mixing ratio $E[q_v] - q_*$ and the expected value and standard deviation of the water vapor concentration q_v at time $t = 1000s$ simulated on a 160×160 mesh.

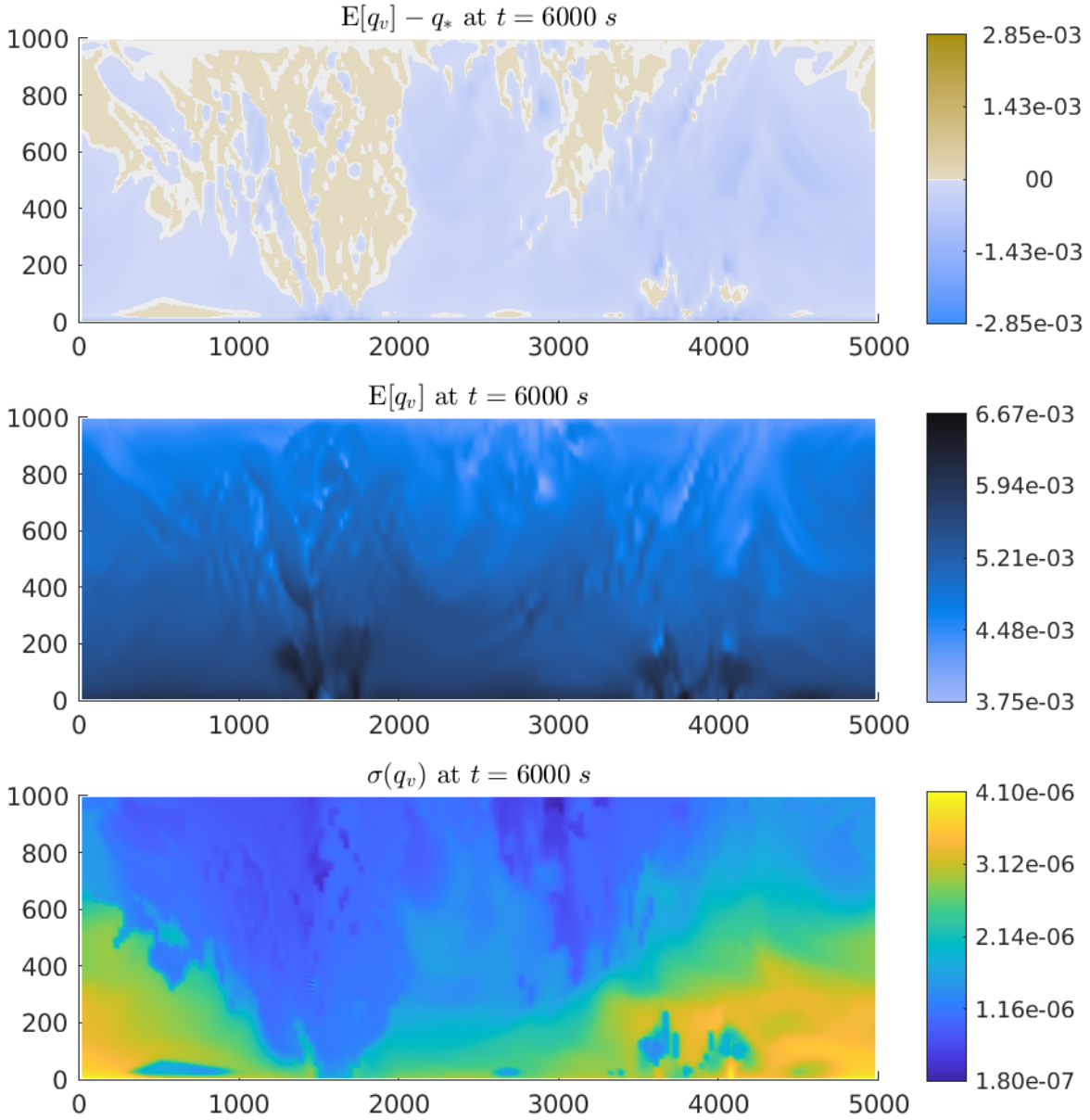

Figure 7.29: Example 7.6: Difference of the expected value of the water vapor concentration to the saturation mixing ratio $E[q_v] - q_*$ and the expected value and standard deviation of the water vapor concentration q_v at time $t = 6000s$ simulated on a 160×160 mesh.

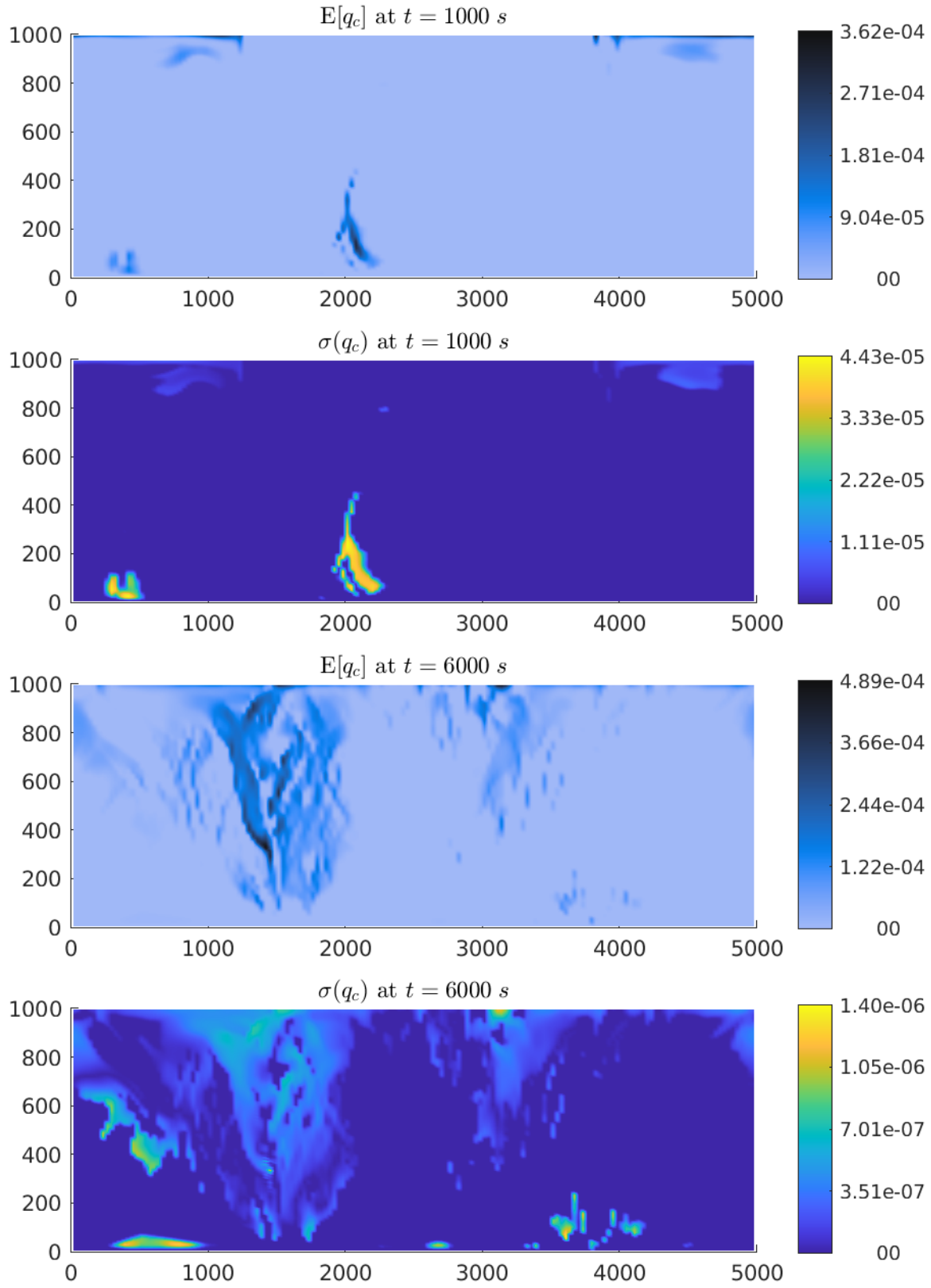

Figure 7.30: Example 7.6: Expected value and standard deviation of the cloud drops concentration q_c at times $t = 1000$ and $6000s$ simulated on a 160×160 mesh.

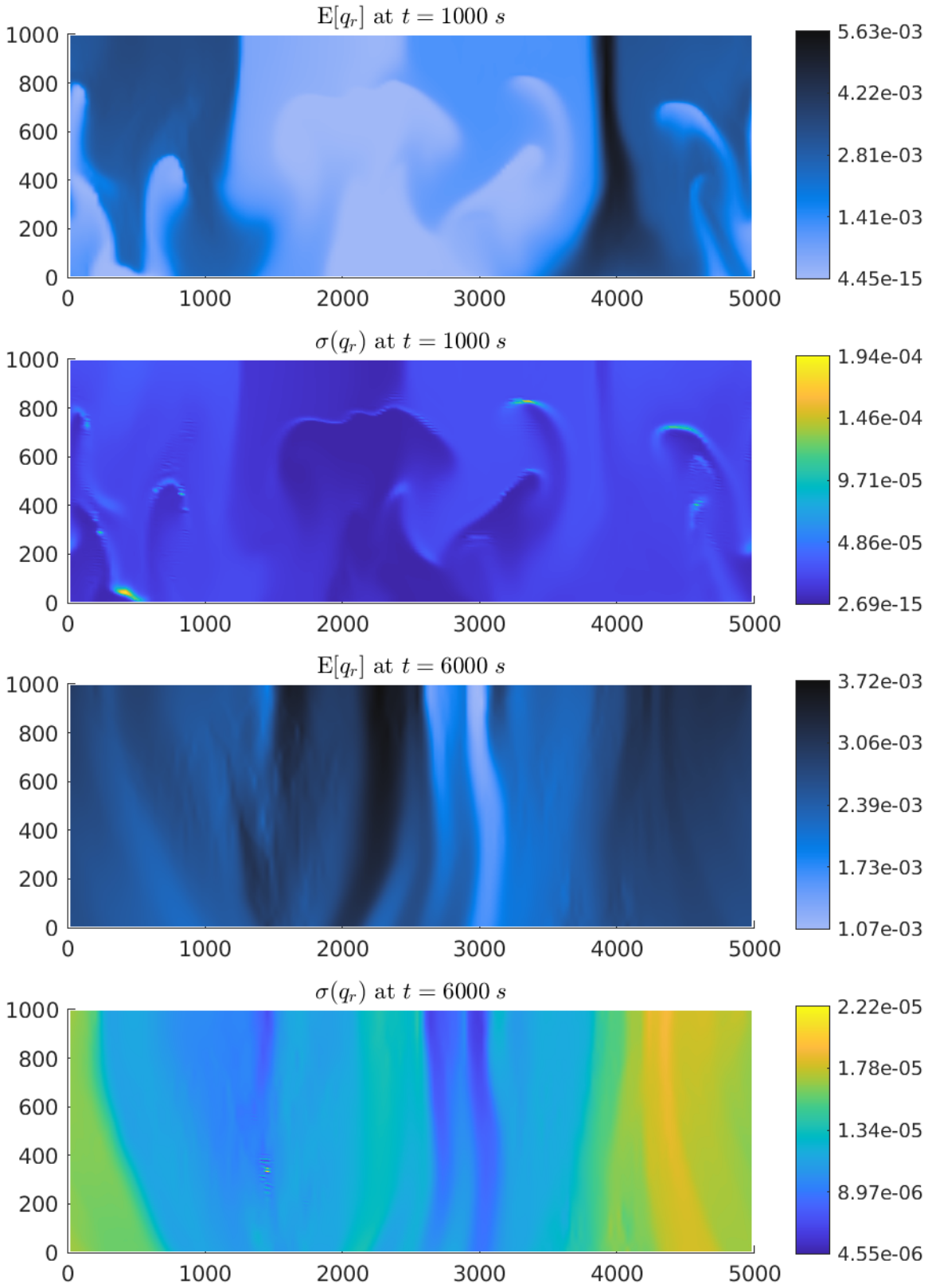

Figure 7.31: Example 7.6: Expected value and standard deviation of the rain concentration q_r at at times $t = 1000$ and $6000s$ simulated on a 160×160 mesh.

Example 7.7 (Fully stochastic Rayleigh-Bénard convection in 2D)

Here, we consider fully stochastic Rayleigh-Bénard convection in 2D simulated with (M3) on a domain $\Omega = [0, 5000] \times [0, 1000]\, m^2$ that has been discretized using 160×160 mesh cells. The initial conditions are the same as in the previous Example 7.6 with the only difference that now also the Navier-Stokes variables are stochastic. Thus, we use (7.1) as initial data for the cloud variables and the following conditions for the Navier-Stokes variables

$$\begin{aligned}
&(\widehat{\rho'})_0(\boldsymbol{x},0) = -\bar{\rho}(\boldsymbol{x})\frac{(\widehat{\theta'})_0(\boldsymbol{x},0)}{\bar{\theta}(\boldsymbol{x}) + (\widehat{\theta'})_0(\boldsymbol{x},0)},\ (\widehat{\rho'})_k(\boldsymbol{x},0) = 0 \quad \text{for } 1 \le k \le M,\\
&(\widehat{\rho u_1})_0(\boldsymbol{x},0) = 0.001\left((\widehat{\rho'})_0(\boldsymbol{x},0) + \bar{\rho}(\boldsymbol{x})\right),\ (\widehat{\rho u_1})_k(\boldsymbol{x},0) = 0 \quad \text{for } 1 \le k \le M,\\
&(\widehat{\rho u_2})_0(\boldsymbol{x},0) = \sin\left(2\pi\frac{x_2}{1000}\right)\left((\widehat{\rho'})_0(\boldsymbol{x},0) + \bar{\rho}(\boldsymbol{x})\right),\ (\widehat{\rho u_2})_k(\boldsymbol{x},0) = 0 \quad \text{for } 1 \le k \le M,\\
&(\widehat{(\rho\theta)'})_0(\boldsymbol{x},0) = \bar{\rho}(\boldsymbol{x})(\widehat{\theta'})_0(\boldsymbol{x},0) + \bar{\theta}(\widehat{\rho'})_0(\boldsymbol{x},0) + (\widehat{\theta'})_0(\boldsymbol{x},0)(\widehat{\rho'})_0(\boldsymbol{x},0),\\
&\qquad (\widehat{(\rho\theta)'})_k(\boldsymbol{x},0) = 0 \quad \text{for } 1 \le k \le M,
\end{aligned} \tag{7.2}$$

where

$$(\widehat{\theta'})_0(\boldsymbol{x},0) = 0.6\sin\left(2\pi\frac{x_2}{1000}\right),\ (\widehat{\theta'})_k(\boldsymbol{x},0) = 0 \quad \text{for } 1 \le k \le M \tag{7.3}$$

and $\bar{\theta}(\boldsymbol{x})$ and $\bar{\rho}(\boldsymbol{x})$ are chosen as in (6.1). Additionally, we have to project the Dirichlet boundary conditions onto the stochastic space. As already mentioned in Example 7.6 the projection of the periodic, the no-slip and the Neumann conditions is straightforward and one ends up with the same conditions as in the deterministic case for all the expansion coefficients of the respective variable. As in Example 6.3, we implement the Dirichlet boundary conditions for the potential temperature, see (6.2), using $\rho\theta(\boldsymbol{x},t,\omega) = (\rho\theta)'(\boldsymbol{x},t,\omega) + \overline{\rho\theta}(\boldsymbol{x})$. Rearranging and inserting the expansion for $\rho'(\boldsymbol{x},t,\omega)$ and $(\rho\theta)'(\boldsymbol{x},t,\omega)$ gives

$$\begin{aligned}
&(\rho\theta)'(\boldsymbol{x},t,\omega) - \rho'(\boldsymbol{x},t,\omega)\theta(\boldsymbol{x},t,\omega) = \bar{\rho}(\boldsymbol{x})\theta(\boldsymbol{x},t,\omega) - \overline{\rho\theta}(\boldsymbol{x})\\
\Leftrightarrow &\sum_{k=0}^{M}(\widehat{(\rho\theta)'})_k(\boldsymbol{x},t)\Phi_k(\omega) - \left(\sum_{k=0}^{M}(\widehat{\rho'})_k(\boldsymbol{x},t)\Phi_k(\omega)\right)\theta(\boldsymbol{x},t,\omega) = \bar{\rho}(\boldsymbol{x})\theta(\boldsymbol{x},t,\omega) - \overline{\rho\theta}(\boldsymbol{x}).
\end{aligned}$$

At the boundary θ is constant because of the Dirichlet conditions. Thus, applying the projections leads to

$$\begin{aligned}
&(\widehat{(\rho\theta)'})_0(x_2 = 0,t) - (\widehat{\rho'})_0(x_2 = 0,t)\theta(x_2 = 0) = \bar{\rho}(x_2 = 0)\theta(x_2 = 0) - \overline{\rho\theta}(x_2 = 0),\\
&(\widehat{(\rho\theta)'})_k(x_2 = 0,t) - (\widehat{\rho'})_k(x_2 = 0,t)\theta(x_2 = 0) = 0 \quad \text{for } 1 \le k \le M
\end{aligned} \tag{7.4}$$

and analogously for $x_2 = 1000$.

In Figures 7.32–7.36, we present the expected values and standard deviations of the potential temperature and the cloud variables at times $t = 1000$ and $6000s$. In Figures 7.33 and 7.34, also the differences of the expected value of the water vapor concentration to the saturation mixing ratio $E[q_v] - q_*$ are depicted. A comparison of the solutions

in this experiment obtained with the fully stochastic model (M3) at time $t = 6000s$ to the ones obtained with the stochastic cloud dynamics (M2) in Example 7.6 and the ones obtained with the deterministic model (M1) in Example 6.4 is shown in Figures 7.37–7.41. In this 2D experiment, the overall behavior of the three models (M1) – (M3) is very similar. As can be seen in Figure 7.32, the potential temperature also exhibits a strong vertical gradient at time $t = 1000s$, but with higher values than in the case with just stochastic cloud dynamics, cf. Figure 7.27 in Example 7.6. The convection cells are formed similarly and the solution at a later time $t = 6000s$ is comparable to the one in the deterministic case as well as to the stochastic cloud dynamics case, see Figure 7.37. The same behavior can be observed for the water vapor concentration in Figures 7.33 and 7.34. A difference to Example 7.6 with stochastic cloud dynamics can be seen in Figures 7.35 and 7.40 for the cloud drop concentration which is now one order of magnitude larger and exhibits a smaller standard deviation as in the case with just stochastic cloud dynamics. The cloud structure is basically the same as in the deterministic case and the one with stochastic cloud dynamics: we can observe that the clouds follow the roll-like flow structure. As shown in Figure 7.38 this is because the oversaturated regions are formed in the rolls where the convection takes place. The rain formation in this experiment is very similar to the one in Example 7.6 with stochastic cloud dynamics as can be seen in Figure 7.41, though more rain is formed due to more cloud formation and thus also the standard deviation at time $t = 6000s$ is much larger as for the case with stochastic cloud dynamics, cf. Figures 7.36 and 7.31 in Example 7.6.

In Figures 7.42 and 7.43 the time evolution of the mean expected value per m^2 as well as the mean standard deviation per m^2 for the cloud variables and the potential temperature are presented. In d space dimensions these quantities can be computed for uniformly distributed perturbations in the following way

$$\begin{aligned} \mathbb{E}\left[\frac{h^d}{|\Omega|}\sum_{i=1}^{N}(q_\ell)_i\right] &= \frac{h^d}{|\Omega|}\sum_{i=1}^{N}\mathbb{E}\left[(q_\ell)_i\right] = \frac{h^d}{|\Omega|}\sum_{i=1}^{N}\widehat{((q_\ell)_i)_0}, \\ \sigma\left(\frac{h^d}{|\Omega|}\sum_{i=1}^{N}(q_\ell)_i\right) &= \frac{h^d}{|\Omega|}\sqrt{\sum_{k=1}^{M}\left(\sum_{i=1}^{N}\widehat{((q_\ell)_i)_k}\right)^2\frac{1}{2k+1}}, \end{aligned} \tag{7.5}$$

where N is the number of mesh cells and $\ell \in \{v, c, r\}$. We compared the solutions using 0% and 10% of perturbation of the initial data in q_v, where for 10% of perturbation we compared the solutions obtained with the two different stochastic models (M2) and (M3). Also here, it can be seen that the standard deviation of all variables as well as the rain concentration increases with the perturbations. Another difference can be observed for the solutions simulated with the stochastic cloud dynamics model (M2). In that case, the potential temperature decreases faster than in the deterministic and fully stochastic cases. One reason for that is that at time $t = 1000s$ the water vapor concentration increases which leads to more clouds and also rain formation. This probably causes cooling of lower levels due to sedimenting rain water and results in a decrease of potential temperature. This suggests that the different behavior of the solutions obtained with the stochastic cloud dynamics model (M2) compared to the solutions obtained with the other two models (M1) and (M3) is due to the missing feedback to the potential temperature.

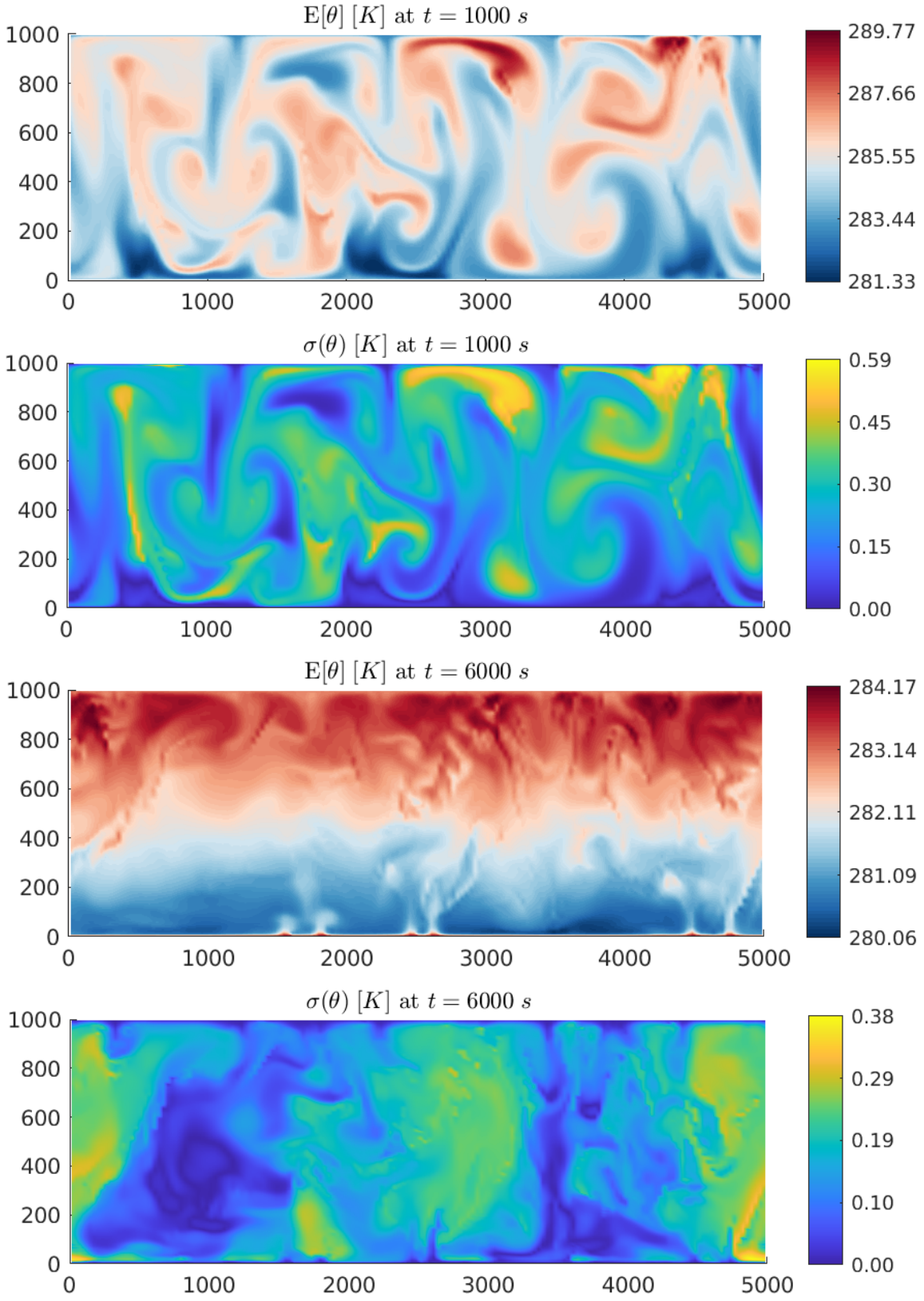

Figure 7.32: Example 7.7: Expected value and standard deviation of the potential temperature θ at times $t = 1000$ and $6000s$ simulated on a 160×160 mesh.

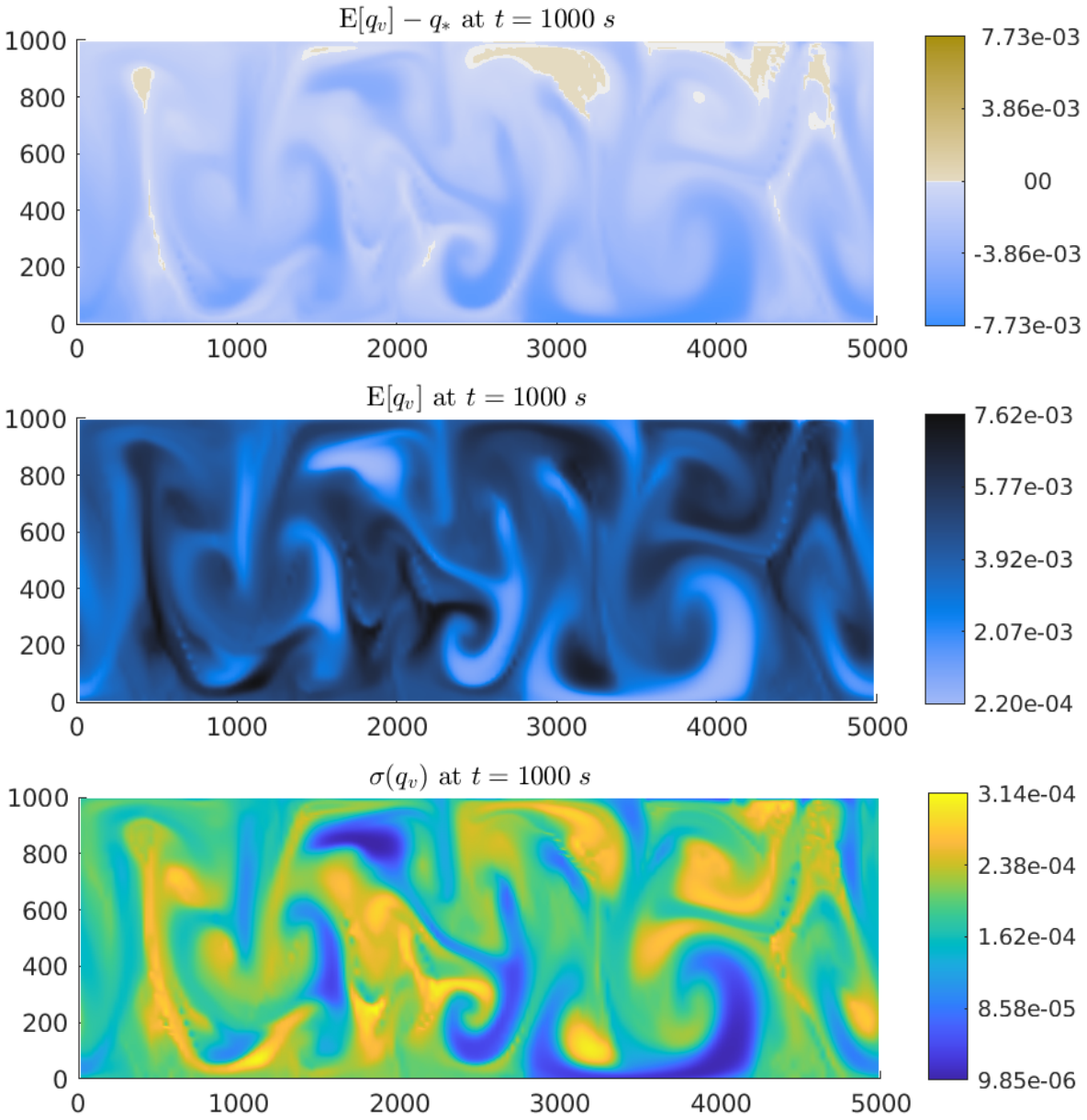

Figure 7.33: Example 7.7: Difference of the expected value of the water vapor concentration to the saturation mixing ratio $E[q_v] - q_*$ and expected value and standard deviation of the water vapor concentration q_v at time $t = 1000s$ simulated on a 160×160 mesh.

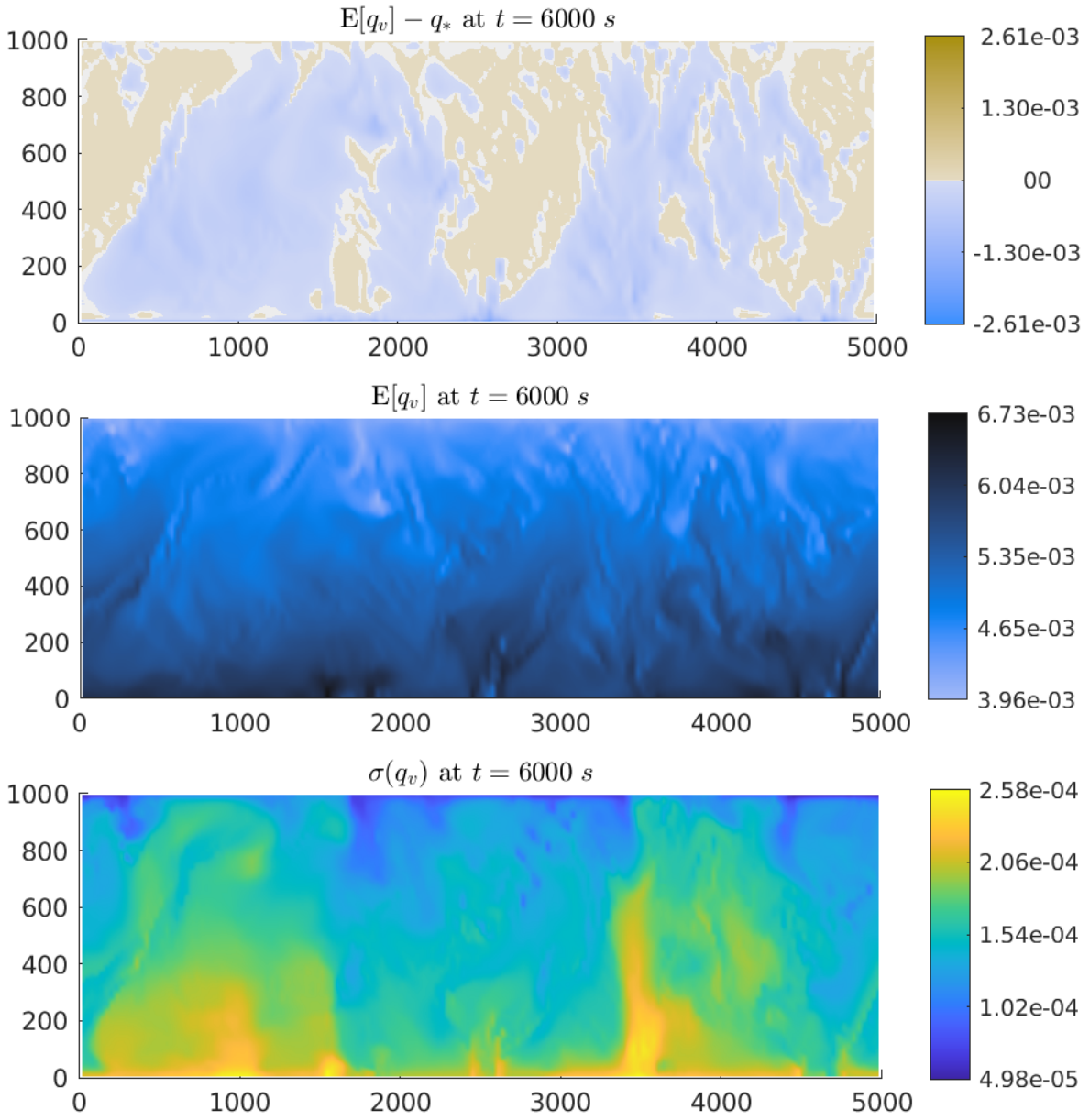

Figure 7.34: Example 7.7: Difference of the expected value of the water vapor concentration to the saturation mixing ratio $E[q_v] - q_*$ and expected value and standard deviation of the water vapor concentration q_v at time $t = 6000s$ simulated on a 160×160 mesh.

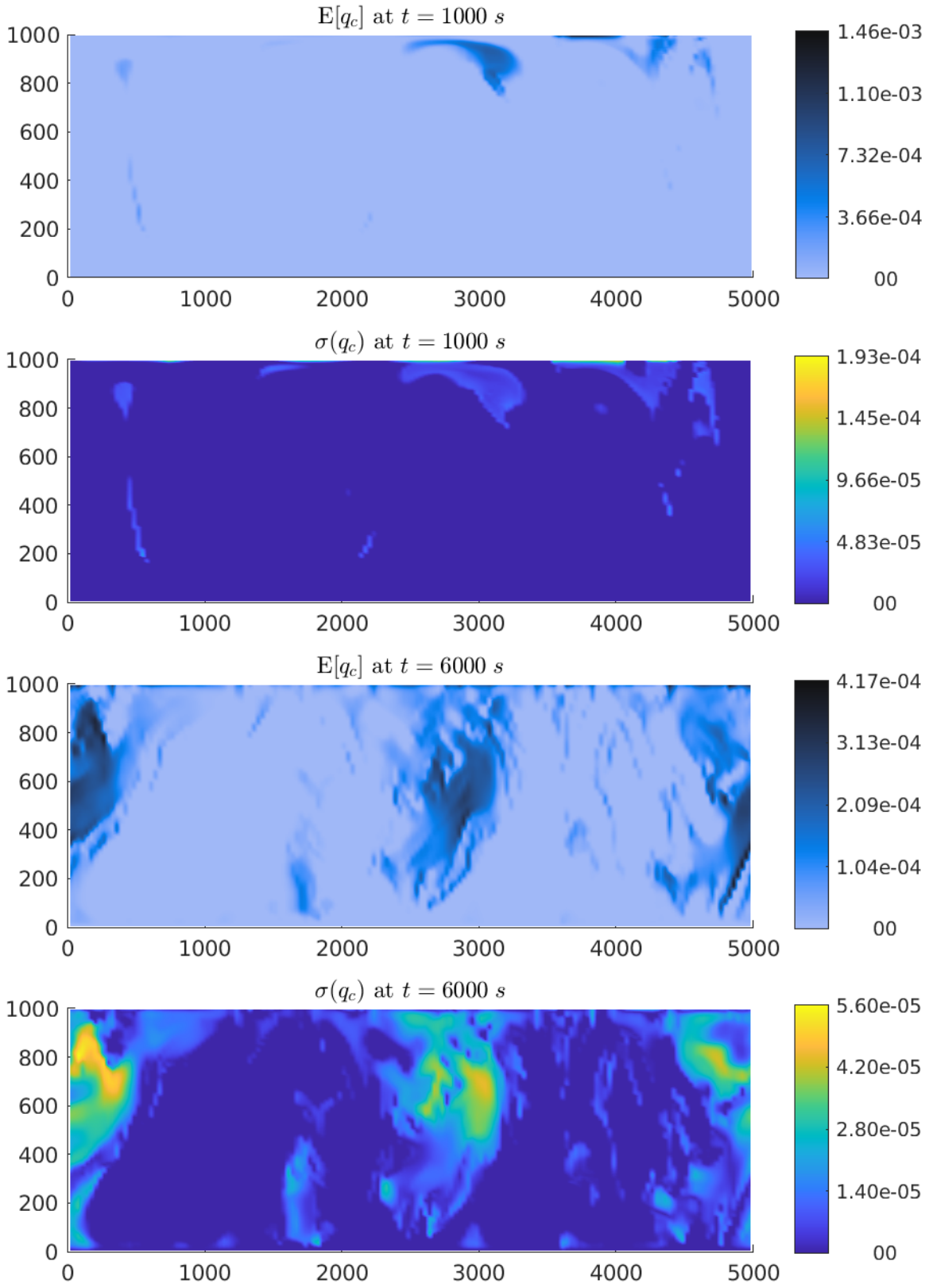

Figure 7.35: Example 7.7: Expected value and standard deviation of the cloud drops concentration q_c at times $t = 1000$ and $6000s$ simulated on a 160×160 mesh.

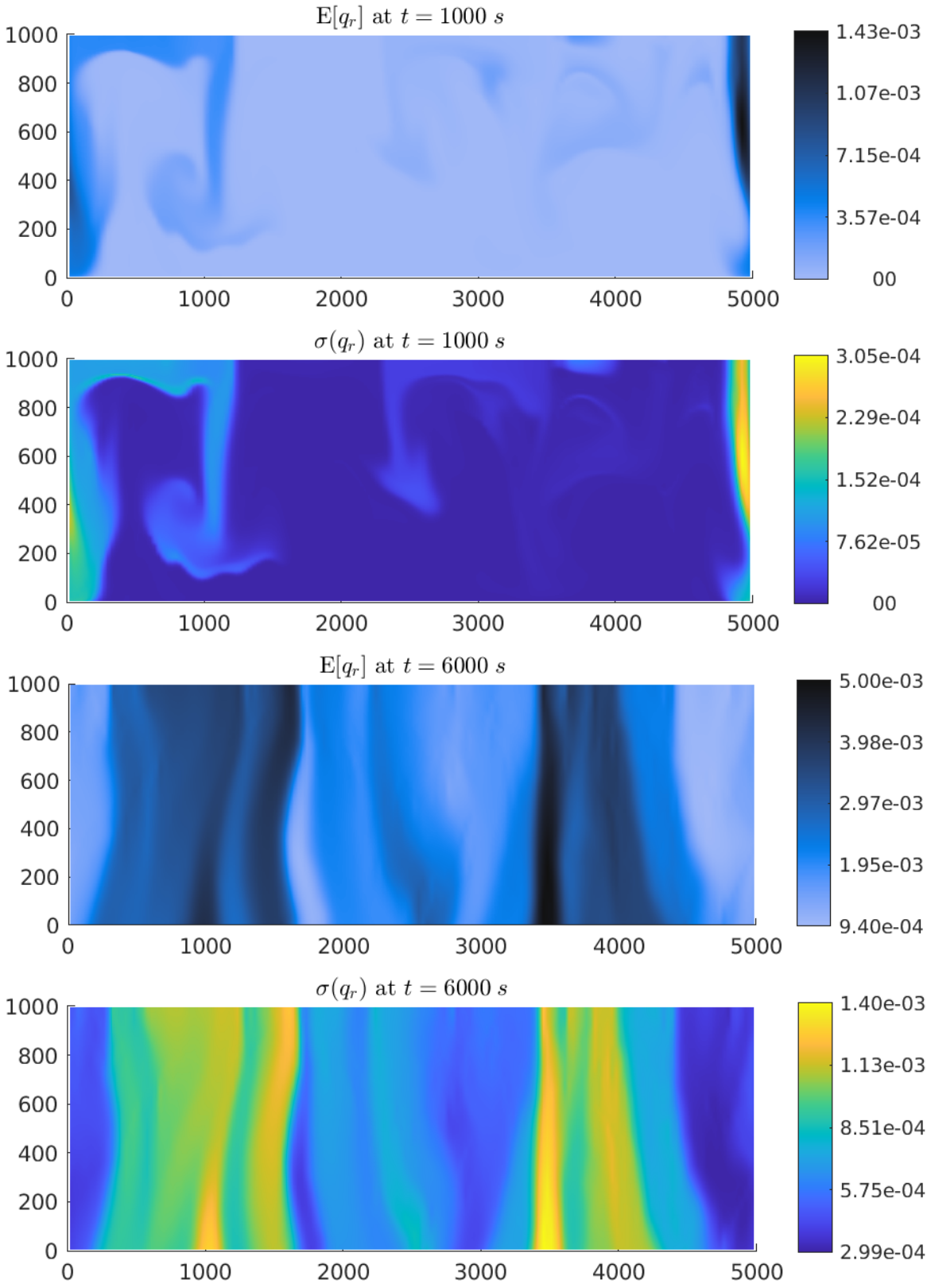

Figure 7.36: Example 7.7: Expected value and standard deviation of the rain concentration q_r at at times $t = 1000$ and $6000s$ simulated on a 160×160 mesh.

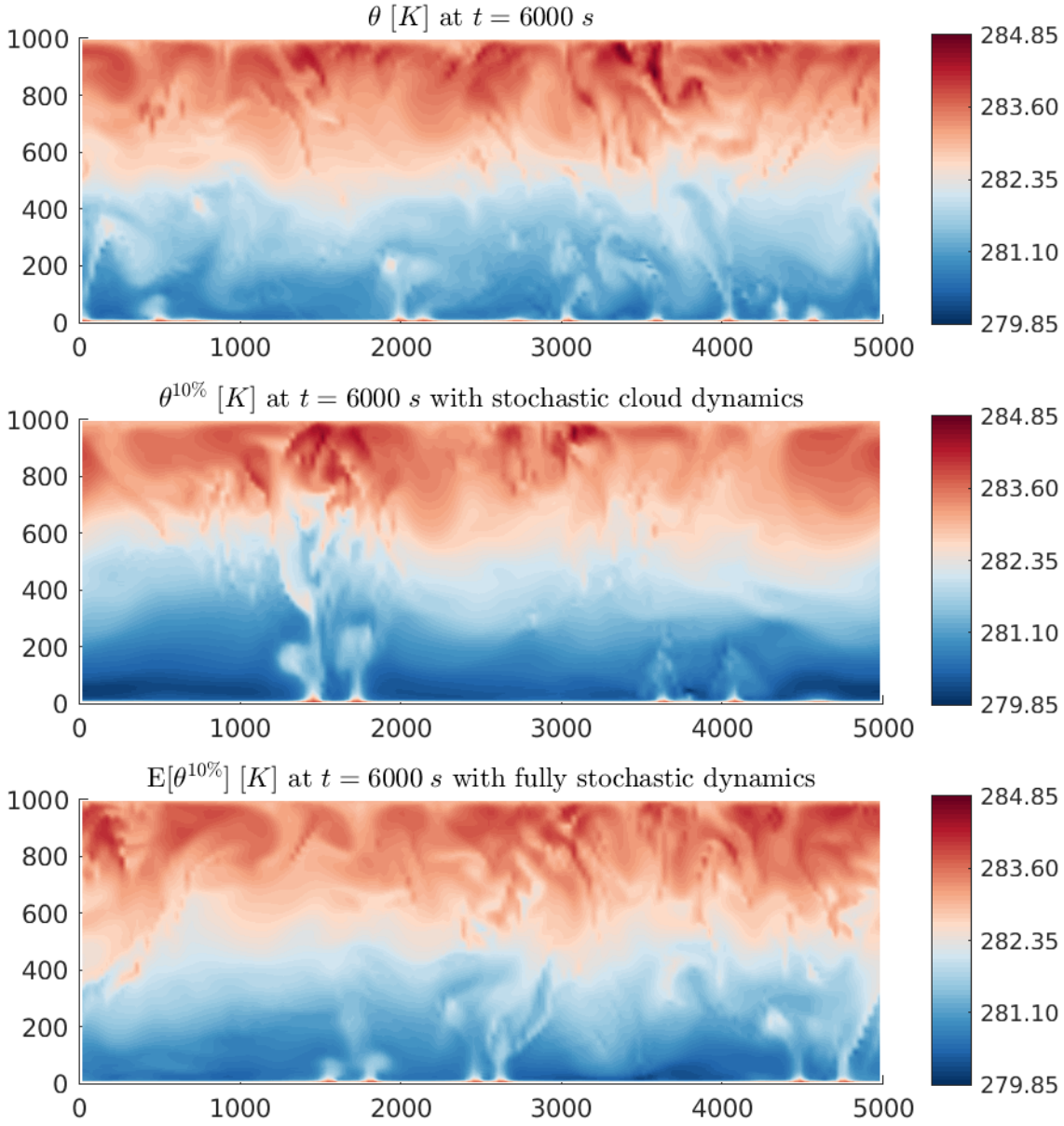

Figure 7.37: Example 7.7: Potential temperature θ at time $t = 6000s$ with 0% and 10% perturbation of the initial water vapor concentration, where the latter was simulated with stochastic cloud dynamics and the fully stochastic dynamics.

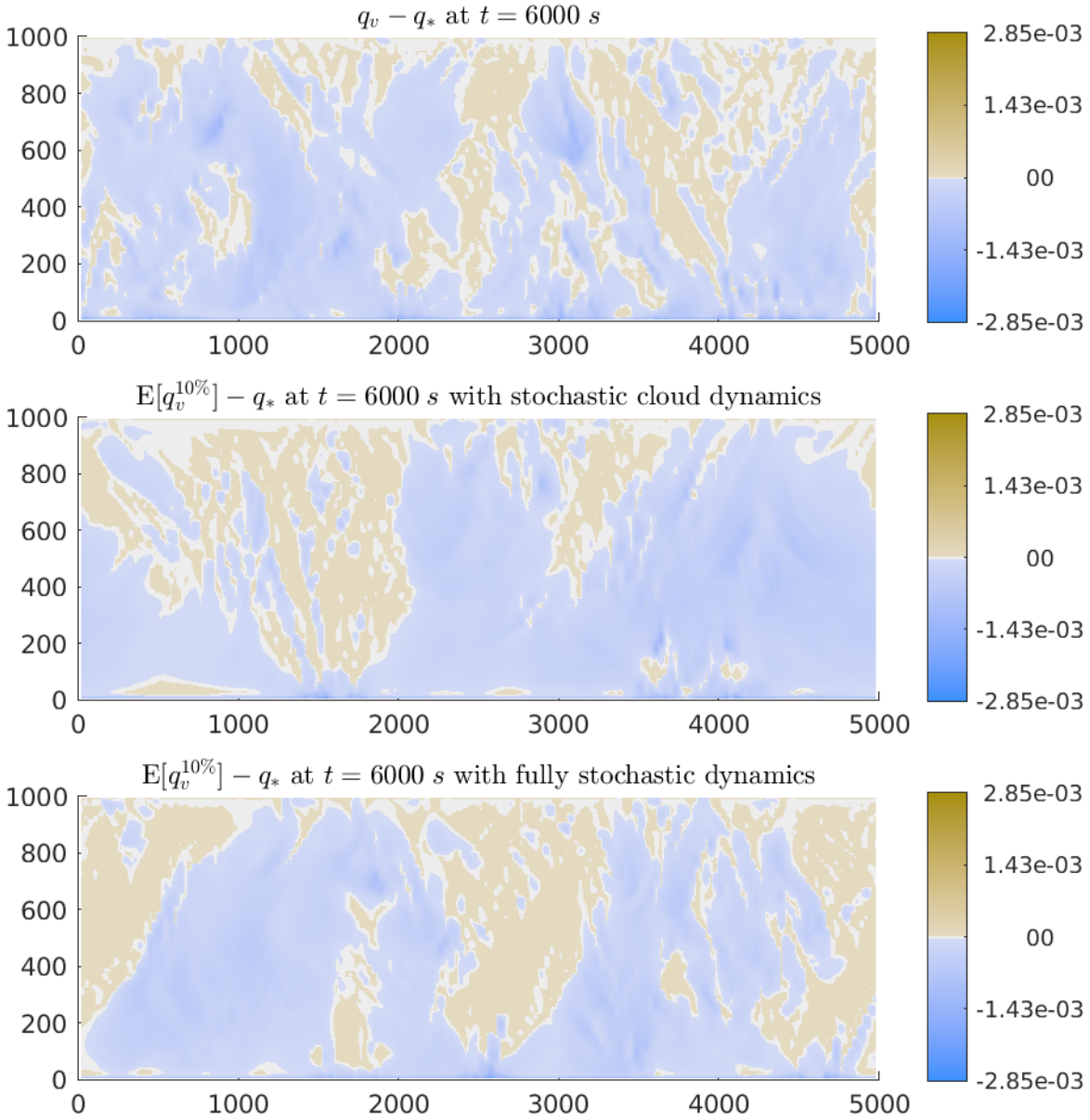

Figure 7.38: Example 7.7: Difference of the water vapor concentration to the saturation mixing ratio $q_v - q_*$ at time $t = 6000s$ with 0% and 10% perturbation of the initial water vapor concentration, where the latter was simulated with stochastic cloud dynamics and the fully stochastic dynamics.

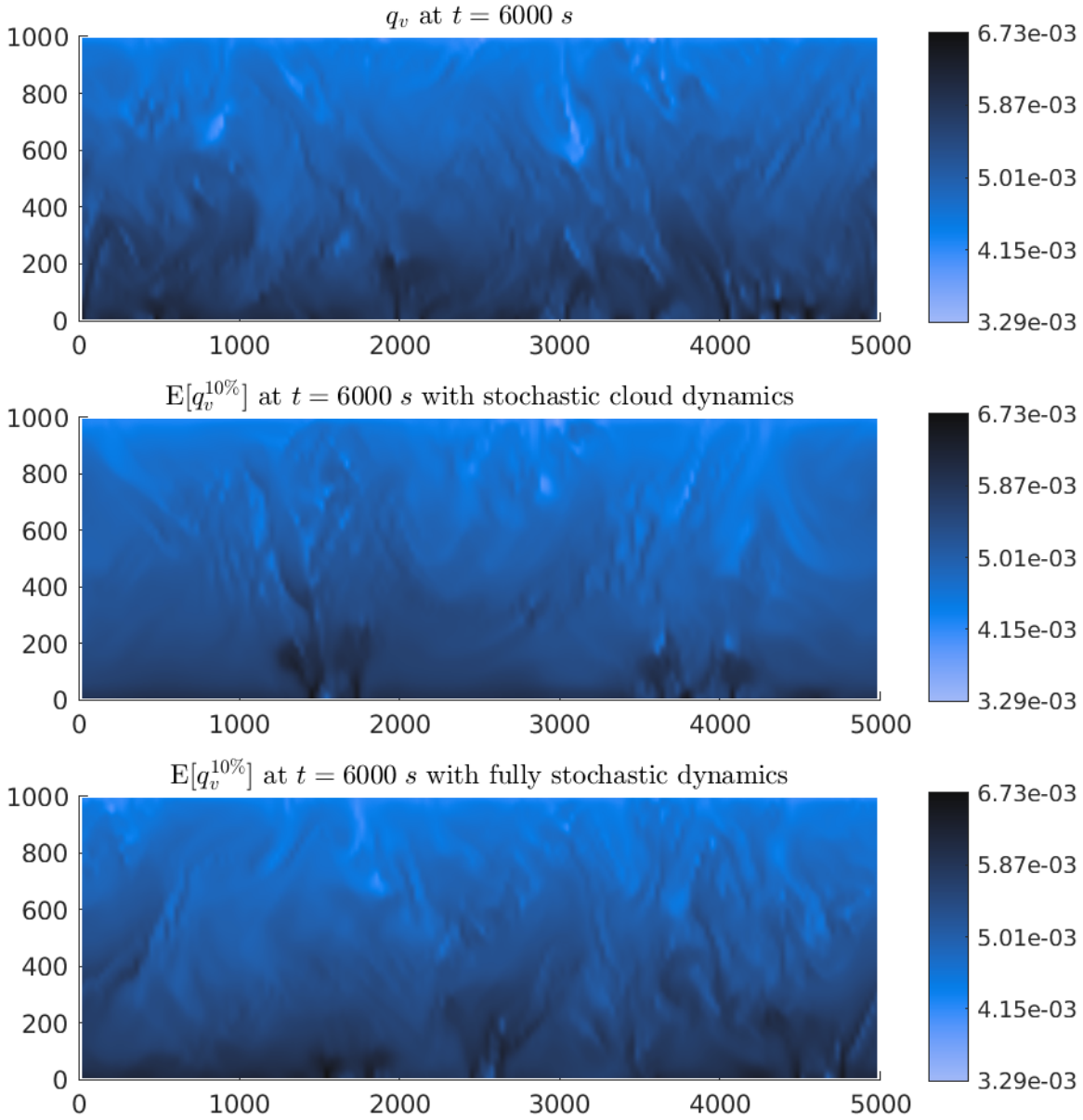

Figure 7.39: Example 7.7: Water vapor concentration q_v at time $t = 6000s$ with 0% and 10% perturbation of the initial water vapor concentration, where the latter was simulated with stochastic cloud dynamics and the fully stochastic dynamics.

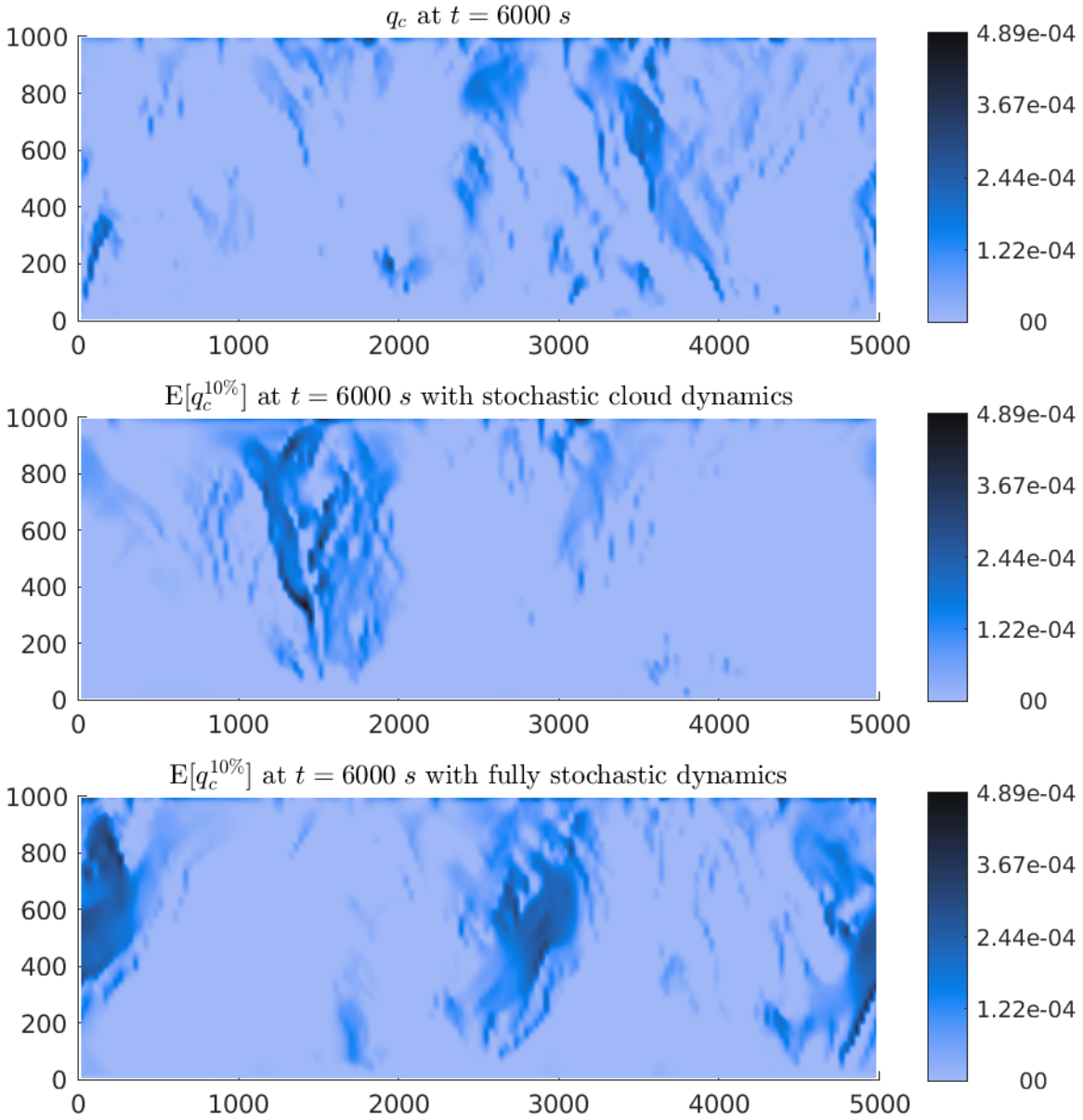

Figure 7.40: Example 7.7: Cloud drops concentration q_c at time $t = 6000s$ with 0% and 10% perturbation of the initial water vapor concentration, where the latter was simulated with stochastic cloud dynamics and the fully stochastic dynamics.

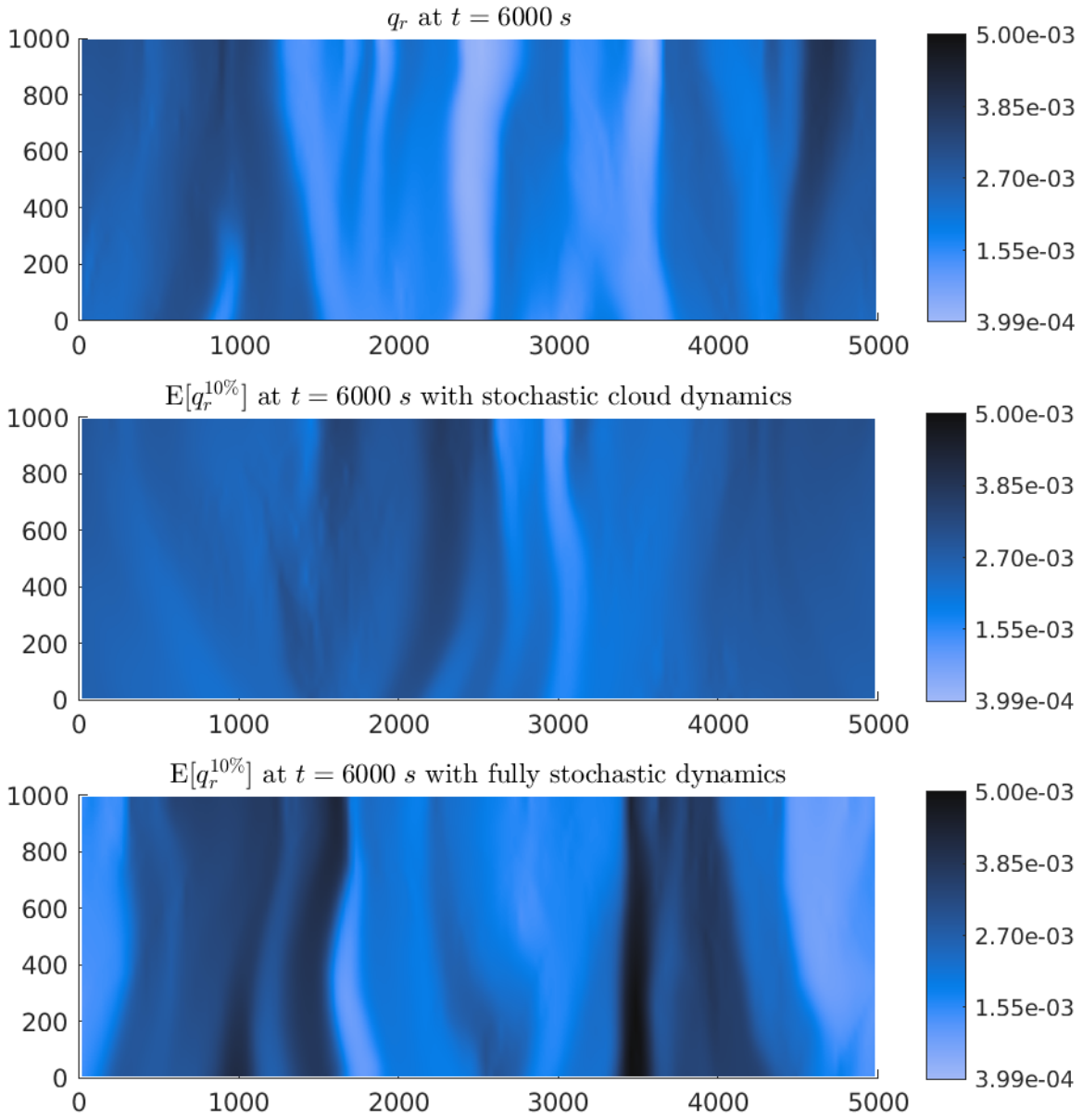

Figure 7.41: Example 7.7: Rain concentration q_r at time $t = 6000s$ with 0% and 10% perturbation of the initial water vapor concentration, where the latter was simulated with stochastic cloud dynamics and the fully stochastic dynamics.

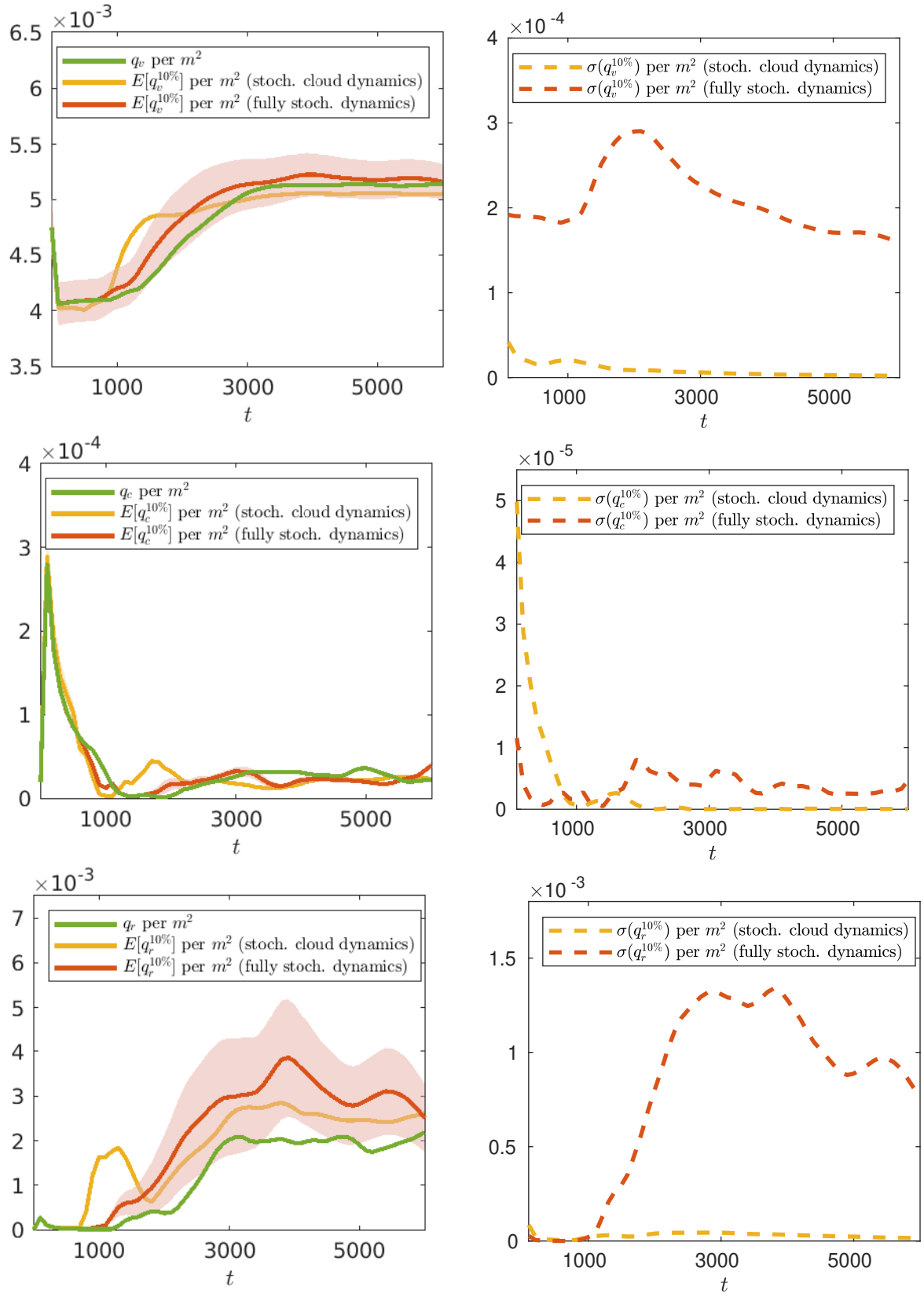

Figure 7.42: Example 7.7: Time evolution of the expected values with their standard deviations for the cloud variables per m^2 (shaded region, left column) and standard deviation (right column) using 0% and 10% perturbation of the initial data in q_v, where the latter was simulated with stochastic cloud dynamics and the fully stochastic dynamics.

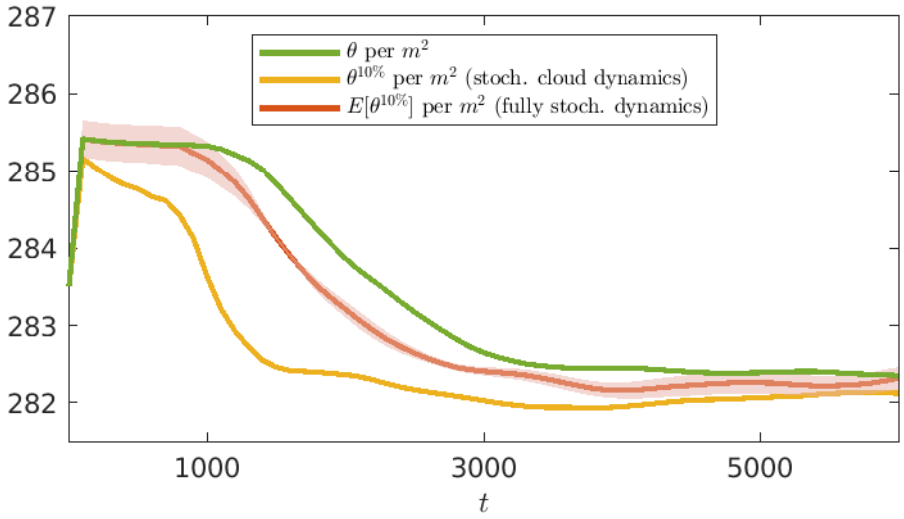

Figure 7.43: Example 7.7: Time evolution of the expected values with their standard deviations (shaded region) for the potential temperature θ per m^2 using 0% and 10% perturbation of the initial data in q_v, where the latter was simulated with stochastic cloud dynamics and the fully stochastic dynamics.

Example 7.8 (Stochastic cloud dynamics Rayleigh-Bénard convection in 3D)

In this example, we investigate the uncertainty quantification in 3D Rayleigh-Bénard convection in the case of stochastic cloud dynamics simulated with (M2). We consider a 0%, 10%, 20% and 50% perturbation of the initial water vapor concentration and realize the initial conditions of the two-dimensional experiment in Example 7.6 in 3D. Thus, we take (6.4) for the initial Navier-Stokes variables and the following initial values for the cloud variables

$$\begin{aligned} (\widehat{q_v})_0(\boldsymbol{x},0) &= 0.025\,(\theta'(\boldsymbol{x},0))_+,\ (\widehat{q_v})_1(\boldsymbol{x},0) = \nu\,(\widehat{q_v})_0(\boldsymbol{x},0), \\ &\qquad (\widehat{q_v})_k(\boldsymbol{x},0) = 0 \quad \text{for } 2 \le k \le M, \\ (\widehat{q_c})_0(\boldsymbol{x},0) &= 10^{-4}\,(\theta'(\boldsymbol{x},0))_+,\ (\widehat{q_c})_k(\boldsymbol{x},0) = 0 \quad \text{for } 1 \le k \le M, \\ (\widehat{q_r})_0(\boldsymbol{x},0) &= 10^{-6}\,(\theta'(\boldsymbol{x},0))_+,\ (\widehat{q_r})_k(\boldsymbol{x},0) = 0 \quad \text{for } 1 \le k \le M, \end{aligned} \tag{7.6}$$

for $\nu = 0, 0.1, 0.2, 0.5$. The solution is computed on a domain $\Omega = [0, 5000] \times [0, 5000] \times [0, 1000]\, m^3$ which is discretized using $50 \times 50 \times 50$ mesh cells.

In Figure 7.44, we show the influence of 0%, 10%, 20% and 50% perturbation on the potential temperature θ and in Figures 7.46–7.48 the influence on the expected value of the cloud variables at times $t = 1000$ and $6000s$. The influence on the oversaturated and undersaturated regions is highlighted in Figure 7.45 and as 2D slice at $x_3 = 700$ and $x_1 = 3000$ in Figures 7.49 and 7.50, where we depict the difference of the expected water vapor concentration to the saturation mixing ratio. For a better comparison, we have used the same range of values for different perturbations in all of the plots. As in the 2D case, the potential temperature distribution changes considerably at lower levels of the 3D domain since evaporative cooling of precipitation is a dominant process. The results for 0%, 10% and 20% of perturbation are comparable, while the ones for 50% are rather

different from the others. This is because for positive perturbations, clouds can form even at low vertical upward motions. The latent heat release increases the vertical motions in the convective cells, which leads to additional feedback, such as stronger cloud formation at time $t = 1000s$, which in turn leads to the formation of a larger amount of rain water. For 50% of perturbation, this means formed clouds rain out until time $t = 6000s$ so that there are no clouds and consequently no rain anymore. Figures 7.45, 7.49 and 7.50 also show that for 50% of perturbation there are no oversaturated regions at time $t = 6000s$ anymore. Concerning cloud structures, we can observe that the convective cells have a more roll-like shape in the deterministic case, while they have a quasi hexagonal one in the cases with 10% and 20% of perturbation.

The above observations can be confirmed in Figure 7.51, where, in order to be able to investigate the influence of perturbations over time more properly, the time evolution of the mean expected value per m^3 as well as the mean standard deviation per m^3 for the cloud variables are presented for the cases with 0%, 10%, 20% and 50% perturbation of the initial water vapor concentration. It can be observed that the solutions with 10% and 20% of perturbation behave similarly in the expected values, but that the standard deviation increase with more perturbation. In contrast to that, the standard deviation for the cloud drops and rain concentration is around zero at later times, because there are no clouds and rain anymore.

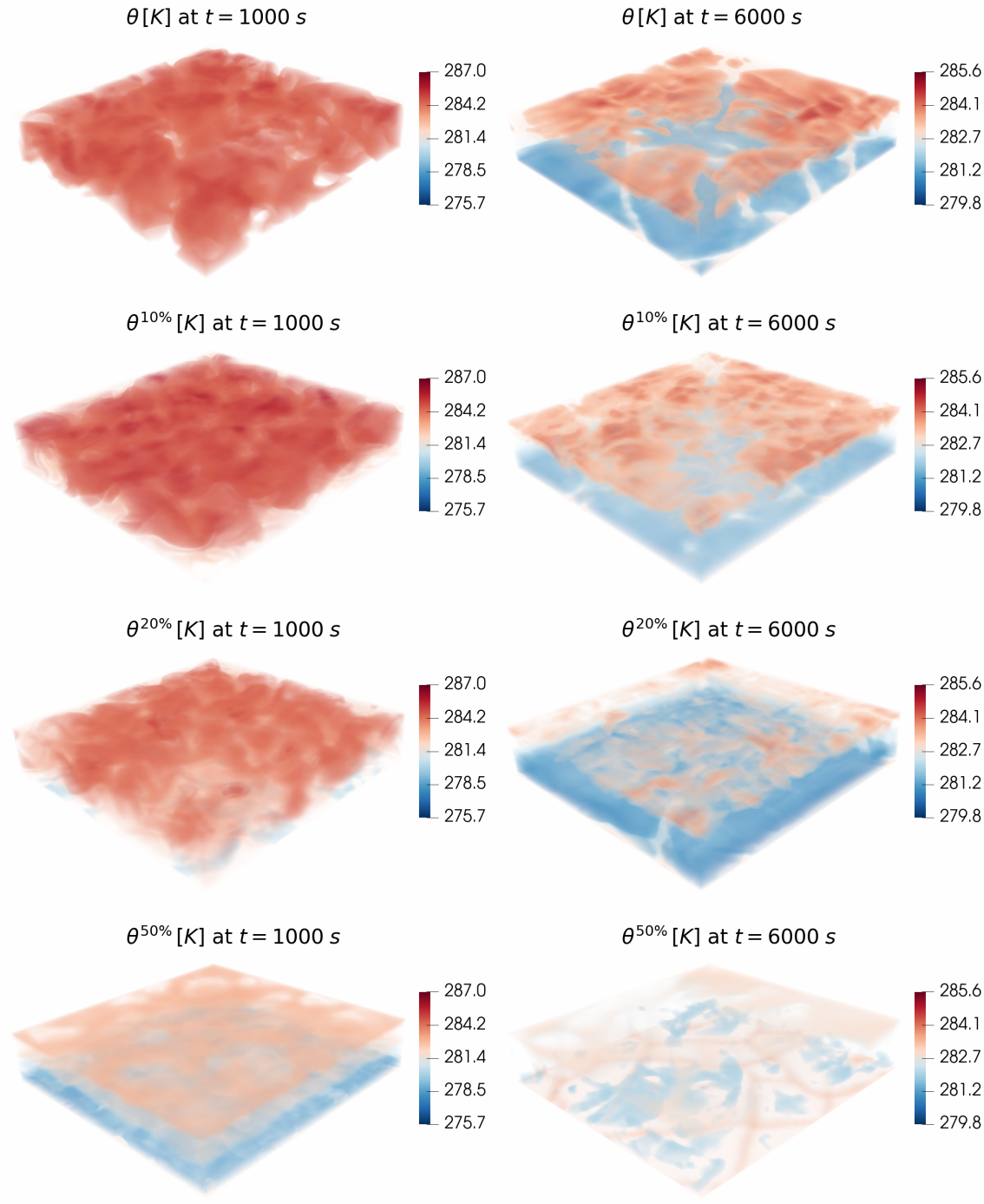

Figure 7.44: Example 7.8: Potential temperature θ at times $t = 1000$ and $6000s$ with 0%, 10%, 20% and 50% perturbation of the initial water vapor concentration simulated on a $50 \times 50 \times 50$ mesh.

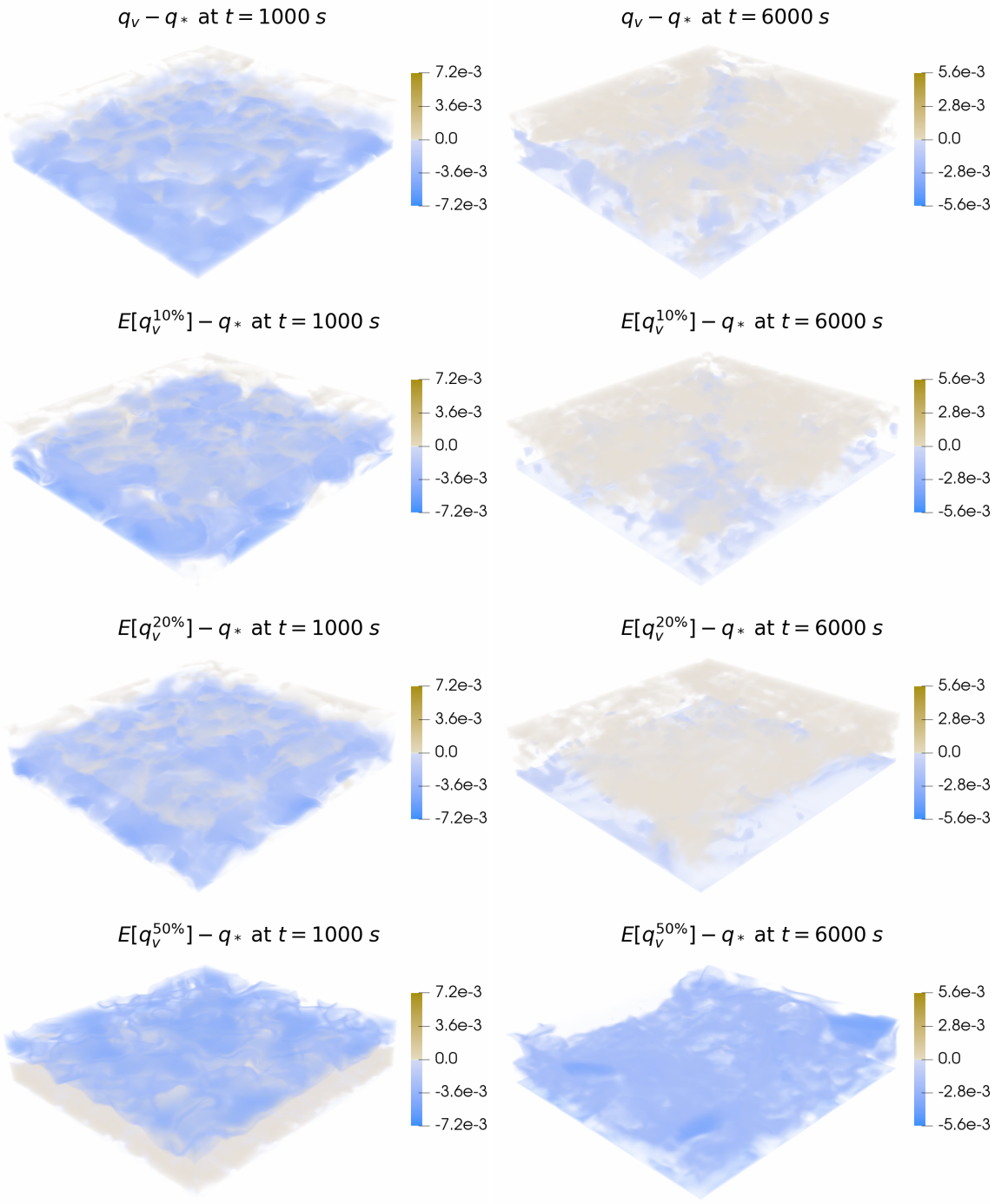

Figure 7.45: Example 7.8: Difference of the expected value of the water vapor concentration to the saturation mixing ratio $E[q_v] - q_*$ at times $t = 1000$ and $6000s$ with 0%, 10%, 20% and 50% perturbation of the initial water vapor concentration simulated on a $50 \times 50 \times 50$ mesh.

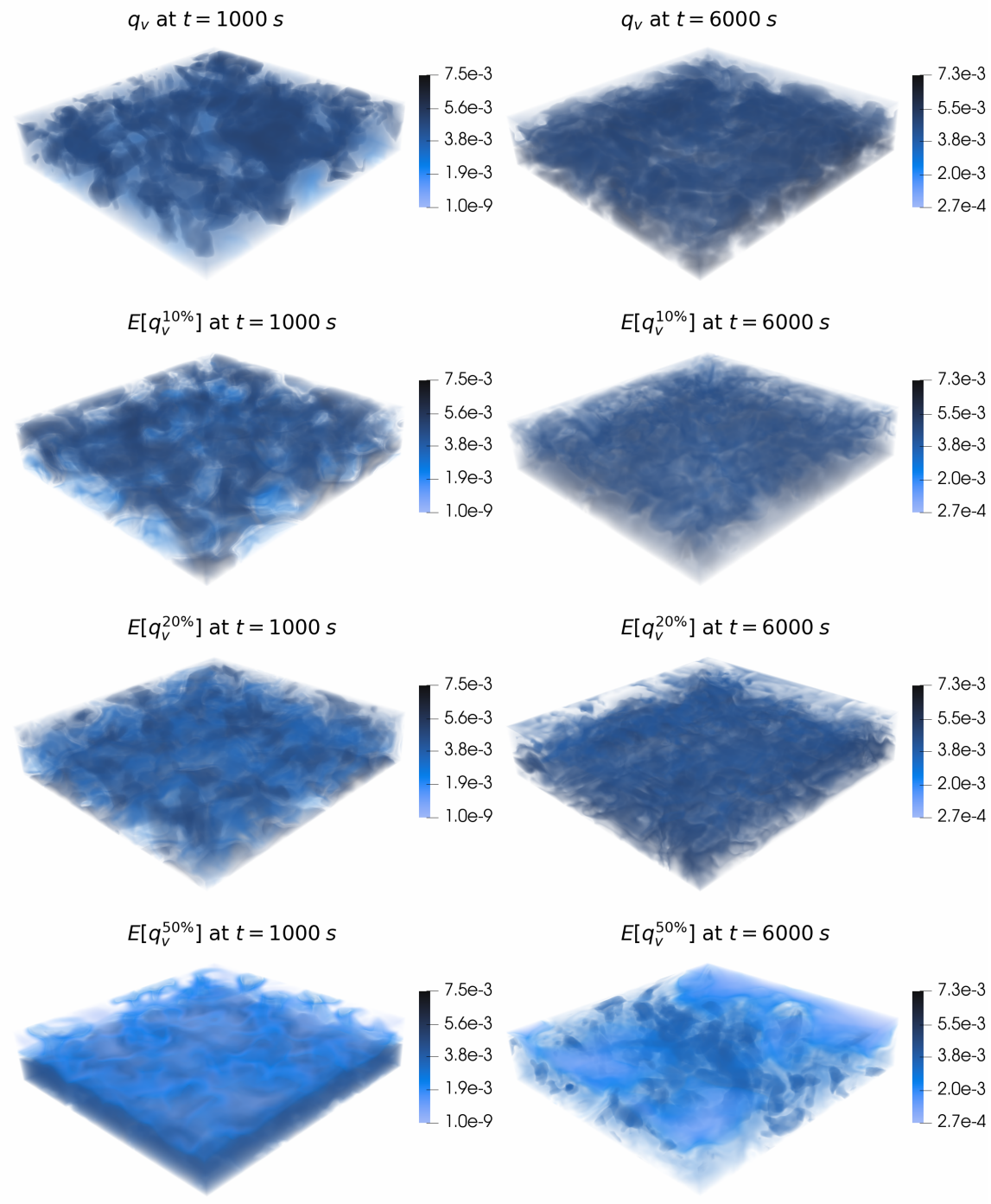

Figure 7.46: Example 7.8: Expected value of the water vapor concentration q_v at times $t = 1000$ and $6000s$ with 0%, 10%, 20% and 50% perturbation of the initial water vapor concentration simulated on a $50 \times 50 \times 50$ mesh.

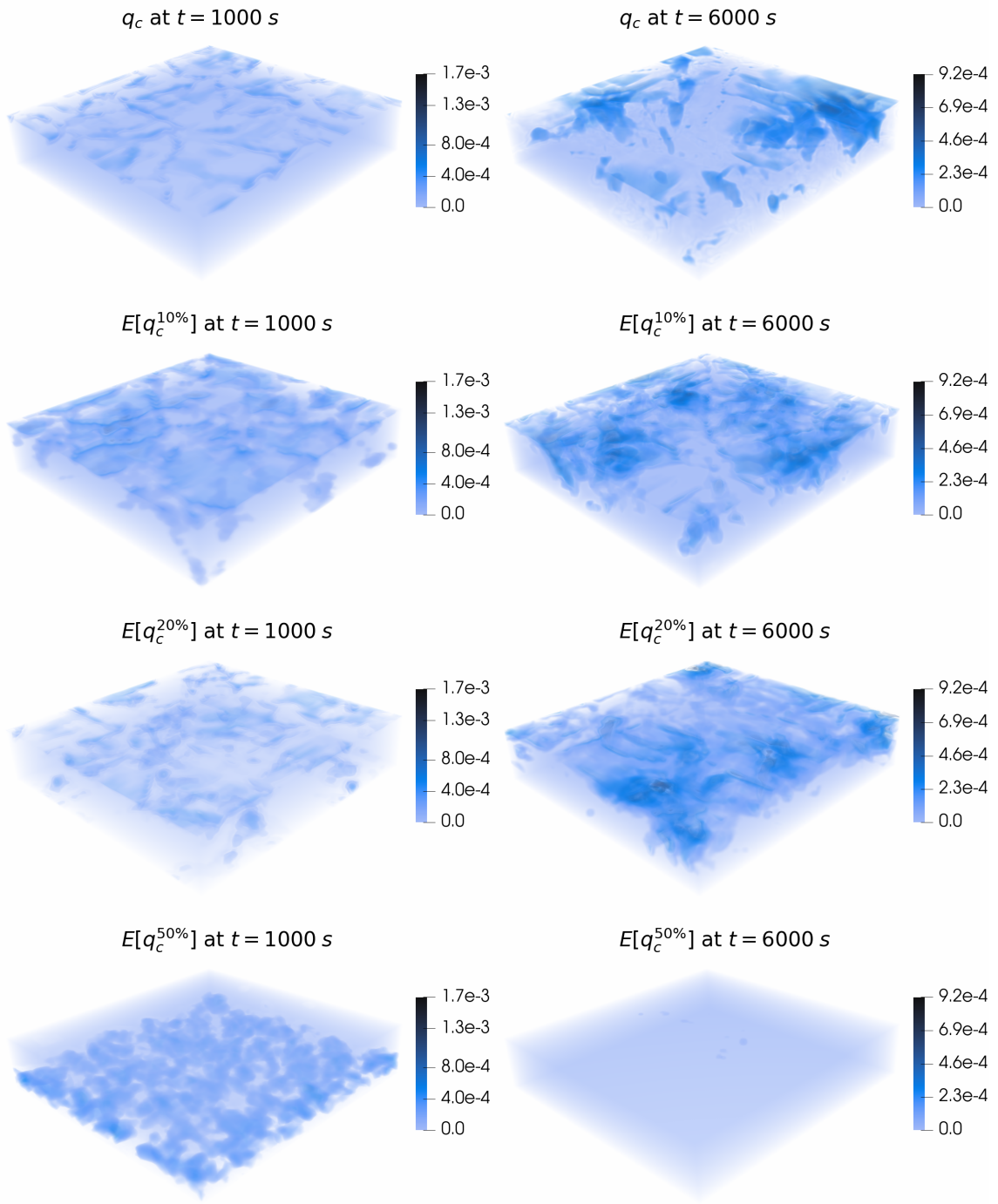

Figure 7.47: Example 7.8: Expected value of the cloud drops concentration q_c at times $t = 1000$ and $6000s$ with 0%, 10%, 20% and 50% perturbation of the initial water vapor concentration simulated on a $50 \times 50 \times 50$ mesh.

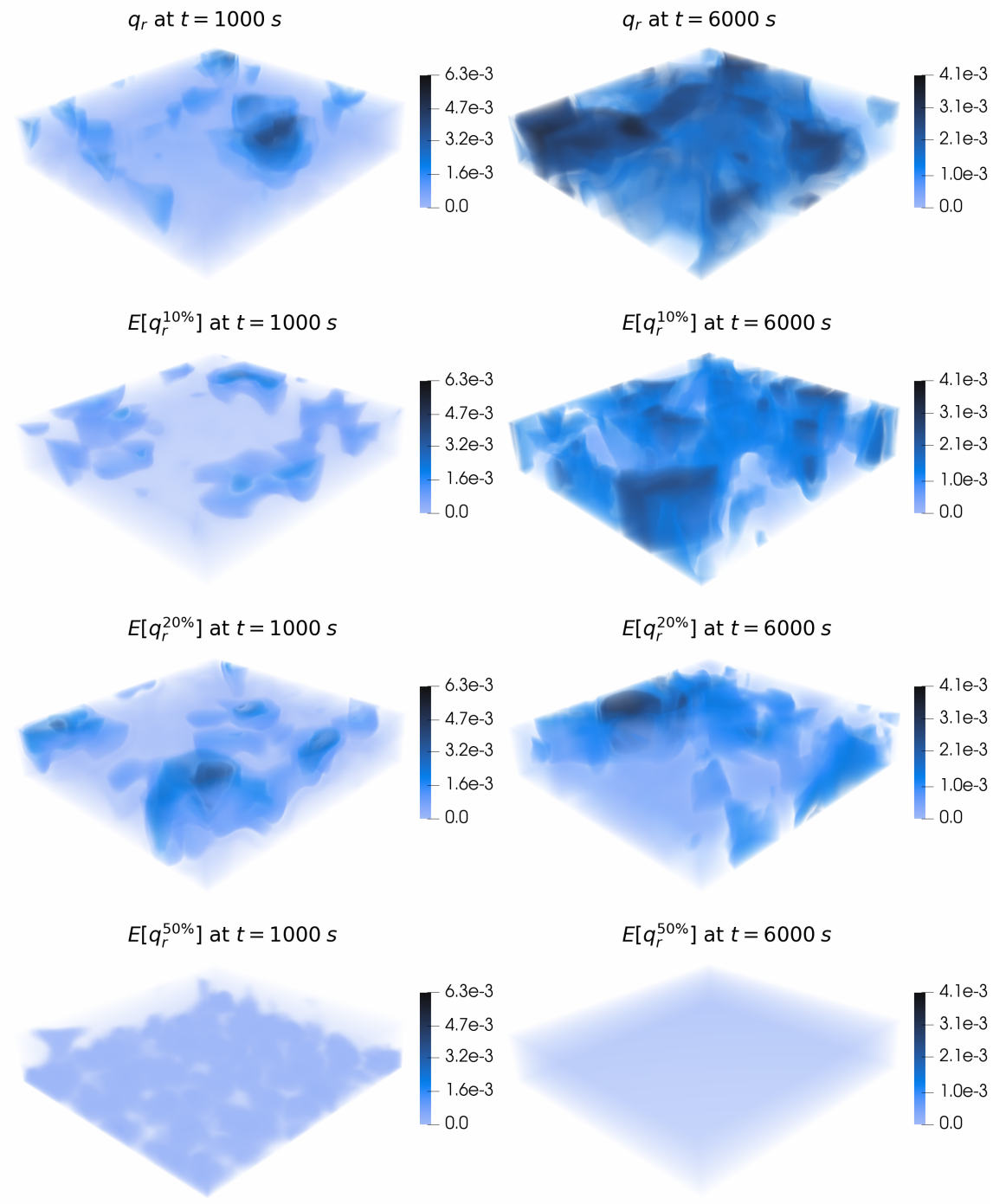

Figure 7.48: Example 7.8: Expected value of the rain concentration q_r at times $t = 1000$ and $6000s$ with 0%, 10%, 20% and 50% perturbation of the initial water vapor concentration simulated on a $50 \times 50 \times 50$ mesh.

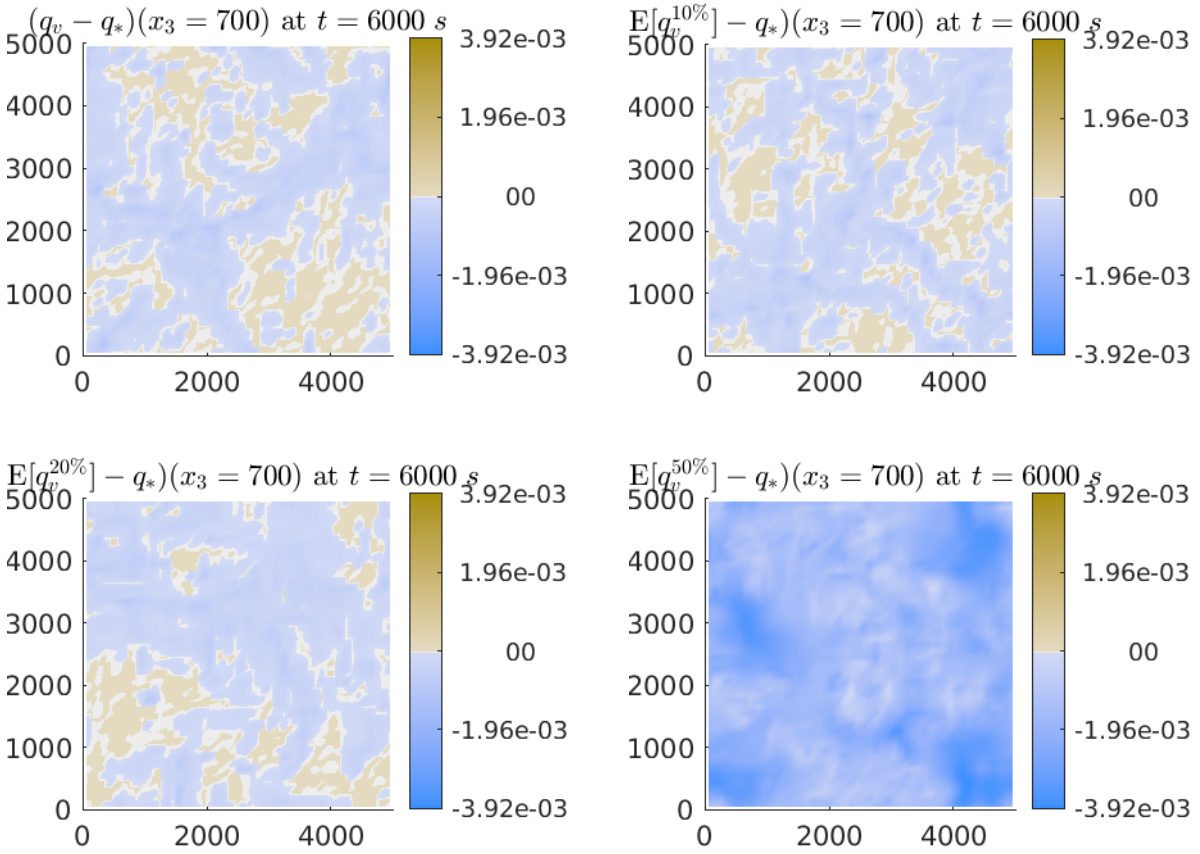

Figure 7.49: Example 7.8: Slices of the difference of water vapor to the saturation mixing ratio $q_v - q_*$ at $x_3 = 700$ at time $t = 6000s$ with 0%, 10%, 20% and 50% perturbation of the initial water vapor concentration simulated on a $50 \times 50 \times 50$ mesh.

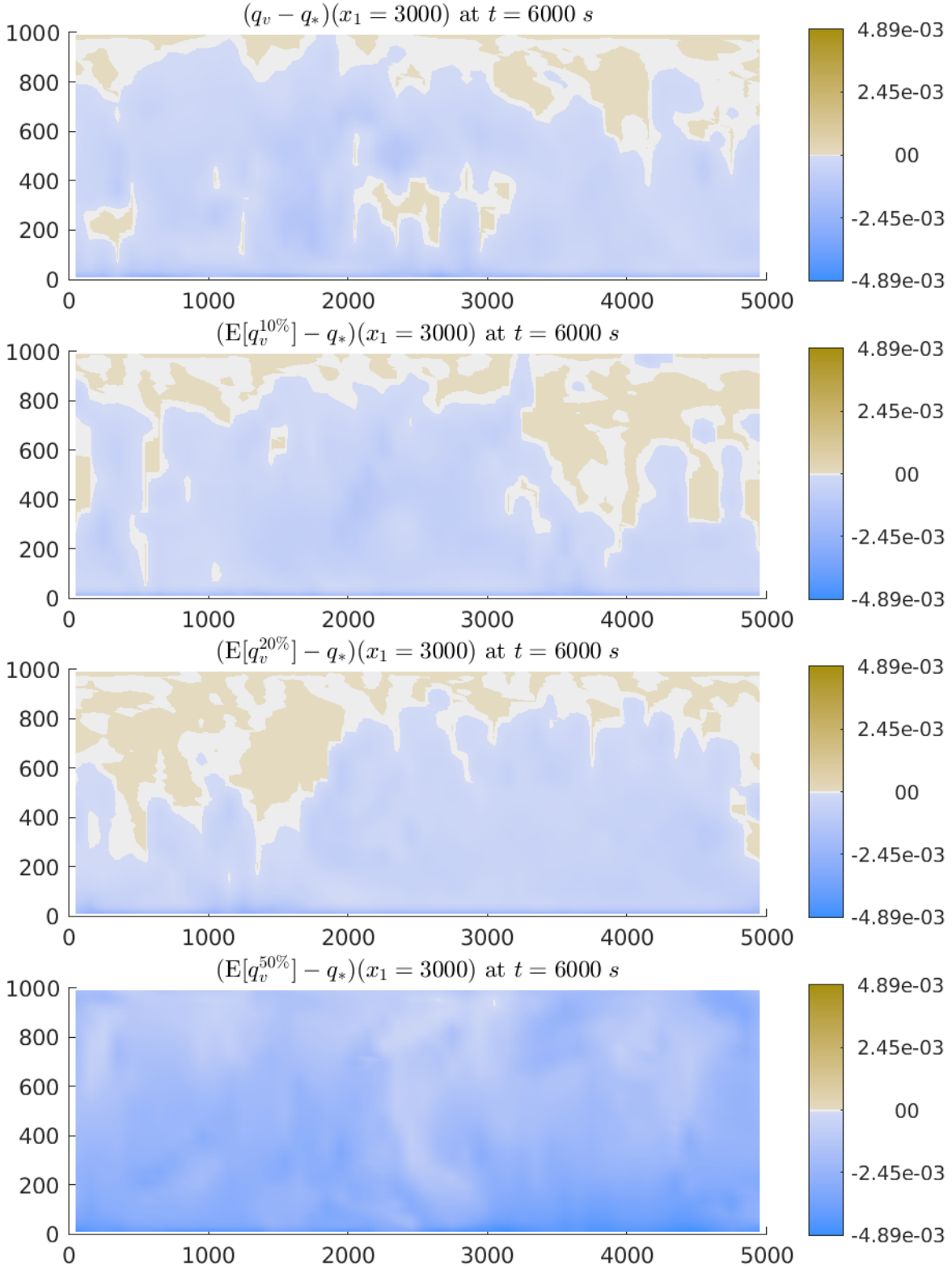

Figure 7.50: Example 7.8: Slices of the difference of water vapor to the saturation mixing ratio $q_v - q_*$ at $x_1 = 3000$ at time $t = 6000s$ with 0%, 10%, 20% and 50% perturbation of the initial water vapor concentration simulated on a $50 \times 50 \times 50$ mesh.

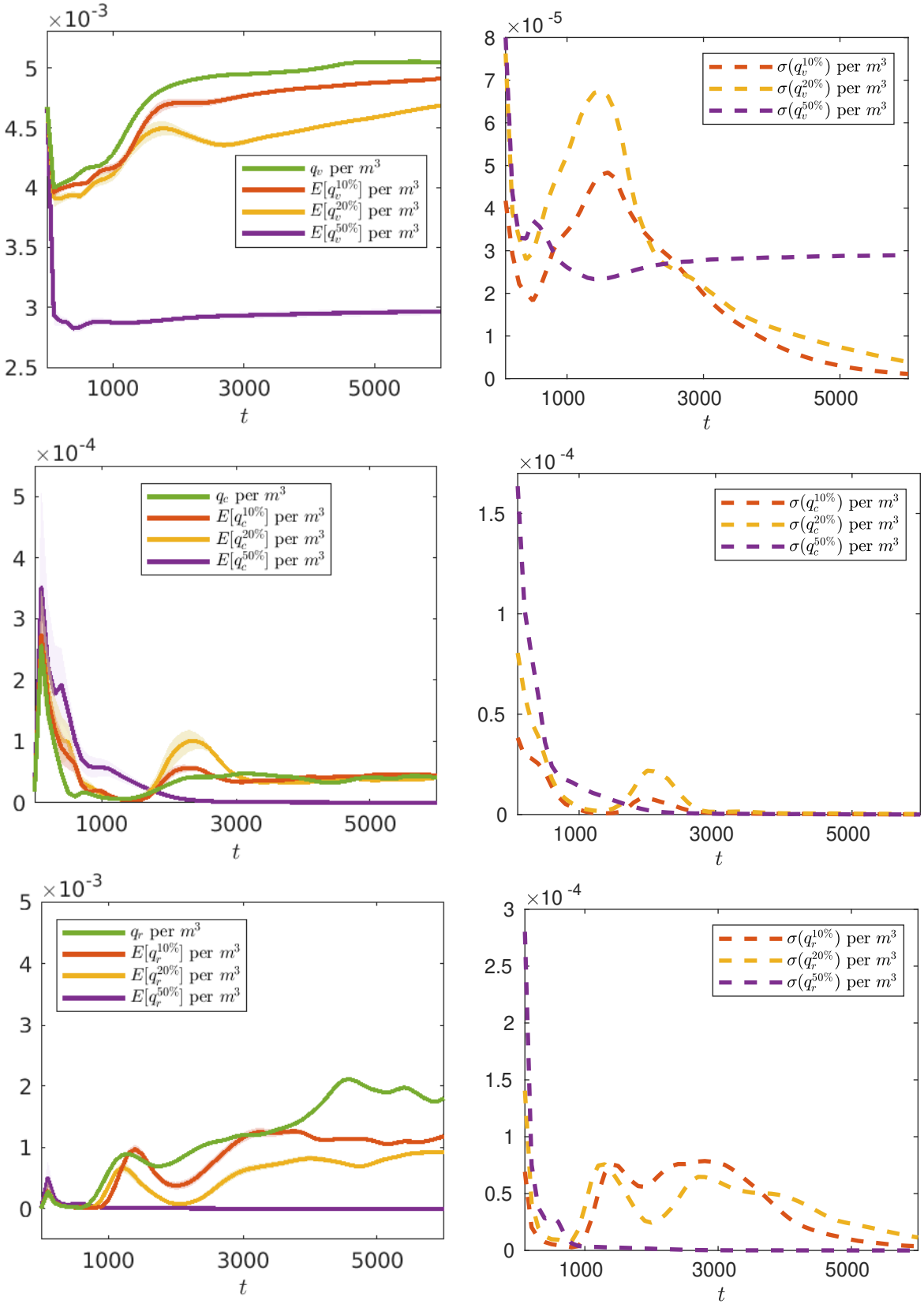

Figure 7.51: Example 7.8: Time evolution of the expected values with their standard deviations for the cloud variables per m^3 (shaded region, left column) and standard deviation (right column) using 0%, 10%, 20% and 50% perturbation of the initial data in q_v.

Example 7.9 (**Fully stochastic Rayleigh-Bénard convection in 3D**)

Here, we investigate the uncertainty quantification in 3D Rayleigh-Bénard convection in the case of the fully stochastic cloud model (M3). To compare it with the previous Exmaple 7.8, where just stochastic cloud dynamics were considered, we use the same initial conditions as in that case. Thus, we consider a 0%, 10%, 20% and 50% perturbation of the initial water vapor concentration and take (7.6) for the initial cloud variables and transfer the deterministic initial Navier-Stokes variables from Example 7.8 to their expansion coefficients

$$
\begin{aligned}
&(\widehat{\rho'})_0(\boldsymbol{x},0) = -\bar{\rho}(\boldsymbol{x})\frac{(\widehat{\theta'})_0(\boldsymbol{x},0)}{\bar{\theta}(\boldsymbol{x}) + (\widehat{\theta'})_0(\boldsymbol{x},0)},\ (\widehat{\rho'})_k(\boldsymbol{x},0) = 0 \quad \text{for } 1 \le k \le M,\\
&(\widehat{\rho u_1})_0(\boldsymbol{x},0) = 0.001\left((\widehat{\rho'})_0(\boldsymbol{x},0) + \bar{\rho}(\boldsymbol{x})\right),\ (\widehat{\rho u_1})_k(\boldsymbol{x},0) = 0 \quad \text{for } 1 \le k \le M,\\
&(\widehat{\rho u_2})_0(\boldsymbol{x},0) = 0.001\left((\widehat{\rho'})_0(\boldsymbol{x},0) + \bar{\rho}(\boldsymbol{x})\right),\ (\widehat{\rho u_2})_k(\boldsymbol{x},0) = 0 \quad \text{for } 1 \le k \le M,\\
&(\widehat{\rho u_3})_0(\boldsymbol{x},0) = \sin\left(2\pi\frac{x_3}{1000}\right)\left((\widehat{\rho'})_0(\boldsymbol{x},0) + \bar{\rho}(\boldsymbol{x})\right),\ (\widehat{\rho u_3})_k(\boldsymbol{x},0) = 0 \quad \text{for } 1 \le k \le M,\\
&(\widehat{(\rho\theta)'})_0(\boldsymbol{x},0) = \bar{\rho}(\boldsymbol{x})(\widehat{\theta'})_0(\boldsymbol{x},0) + \bar{\theta}(\widehat{\rho'})_0(\boldsymbol{x},0) + (\widehat{\theta'})_0(\boldsymbol{x},0)(\widehat{\rho'})_0(\boldsymbol{x},0),\\
&\qquad\qquad (\widehat{(\rho\theta)'})_k(\boldsymbol{x},0) = 0 \quad \text{for } 1 \le k \le M,
\end{aligned}
$$

where

$$
(\widehat{\theta'})_0(\boldsymbol{x},0) = 0.6\sin\left(2\pi\frac{x_3}{1000}\right),\ (\widehat{\theta'})_k(\boldsymbol{x},0) = 0 \quad \text{for } 1 \le k \le M
$$

and $\bar{\theta}(\boldsymbol{x})$ and $\bar{\rho}(\boldsymbol{x})$ are chosen as in (6.1). The solution is again computed on a domain $\Omega = [0, 5000] \times [0, 5000] \times [0, 1000]\, m^3$ which is discretized using $50 \times 50 \times 50$ mesh cells.

In Figures 7.52 and 7.54–7.56, we present the influence of the 0%, 10%, 20% and 50% initial water vapor perturbation on the expected value of potential temperature and the cloud variables at times $t = 1000$ and $6000s$. The influence on the oversaturated and undersaturated regions is highlighted in Figure 7.53 and as 2D slice at $x_3 = 700$ and $x_1 = 3000$ in Figures 7.57 and 7.58, where we depict the difference of the expected water vapor concentration to the saturation mixing ratio. For a better comparison, we have used the same range of values for different perturbations in all of the plots. Here, we can clearly observe a different behavior than that in the case of stochastic cloud dynamics in Example 7.8. The vertical gradient of the potential temperature increases for perturbations, see Figure 7.52, and the pattern of the developed convection cells is similar for different perturbations. This can also be observed for the water vapor content in Figure 7.54. Again, the latent heat release increases the vertical motions in the convective cells, which leads to additional feedback, such as stronger and more cloud formation, see Figure 7.55, which in turn leads to the formation of a much larger amount of rain water, especially at a later time $t = 6000s$, see Figure 7.56. At the time $t = 1000s$ we can see that the roll-like structure of the clouds in the deterministic case (i.e., 0% perturbation) again end up in a more cell-like structure in the cases of perturbed initial water vapor concentration.

In Figures 7.59 and 7.60, we show the time evolution of the mean expected value per m^3 as well as the mean standard deviation per m^3 for the cloud variables and the potential

temperature for the cases with 0%, 10%, 20% and 50% perturbation of the initial water vapor concentration. For increasing perturbations, the spread is increased, mostly for the water vapor concentration q_v and the rain concentration q_r. The averaged quantities are dominated by the positive perturbations, leading to (i) earlier cloud formation, (ii) thicker clouds due to more available water vapor, and (iii) enhanced rain formation. These three features can be seen very nicely in the pictures resulting from the largest initial perturbation ($\nu = 0.5$), where a large spread in water vapor concentration is accompanied by a strong increase in cloud water and an earlier onset of strong precipitation. Due to the strong rain formation the cloud concentration decreases with larger perturbations and also the amount of oversaturated regions is much less as can be observed in Figures 7.53, 7.57 and 7.58 which leads to less new formation of clouds. We would also like to note that the spread is only given by the standard deviation, whereas the actual minima (for instance, almost no cloud formation) cannot be seen directly, although these scenarios are possible.

In Figures 7.61 and 7.62, we additionally compare the time evolution of the mean expected value and the mean standard deviation of the potential temperature and the cloud variables obtained with the three different models (M1)–(M3). Thereby, we used 10% of perturbation for the initial water vapor concentration in the cases of the stochastic cloud dynamics model (M2) and the fully stochastic model (M3). As in the 2D case, one can notice a clear difference between the two stochastic models already with 10% of initial perturbation. The spread is much higher for all the variables in the fully stochastic case compared to the case with stochastic cloud dynamics and also the mean cloud and rain concentration exhibit a different behavior over time. Additionally, the potential temperature decreases much more for the stochastic cloud dynamics case which was also observed in the 2D case. Thus, we can conclude that these differences are caused by the missing feedback of the stochastic cloud variables to the potential temperature in the stochastic cloud dynamics model (M2).

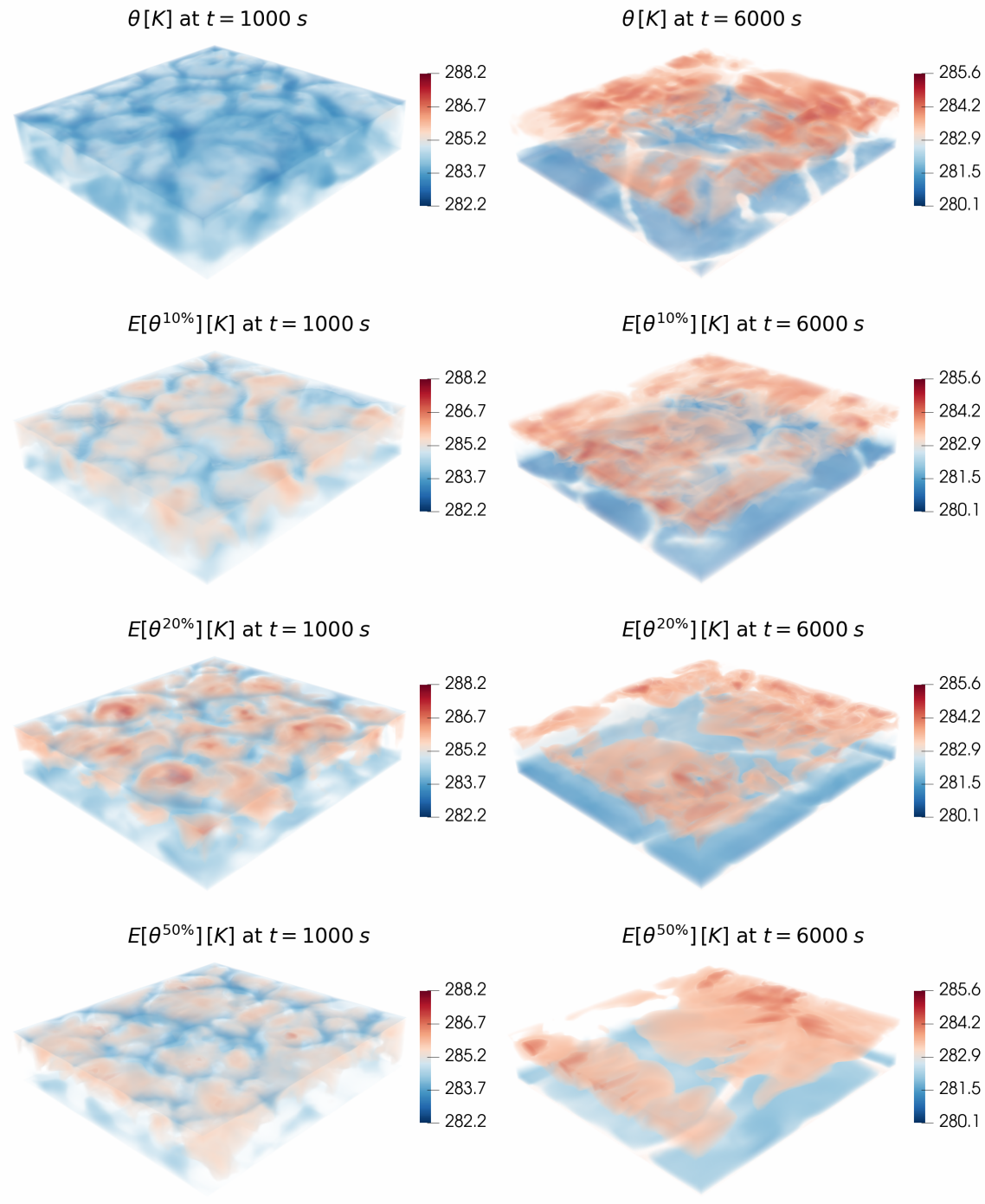

Figure 7.52: Example 7.9: Expected value of the potential temperature θ at times $t = 1000$ and $6000s$ with 0%, 10%, 20% and 50% perturbation of the initial water vapor concentration simulated on a $50 \times 50 \times 50$ mesh.

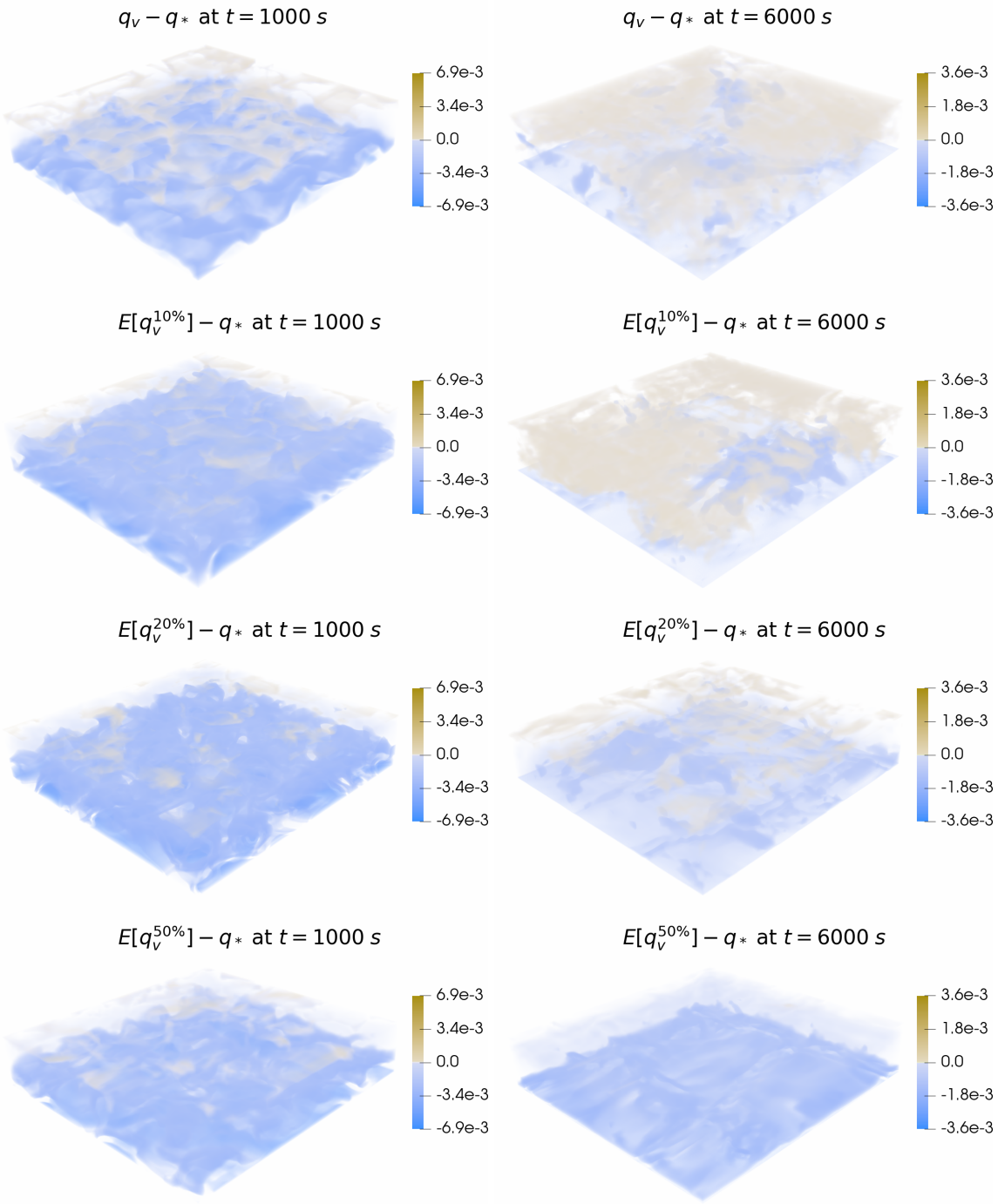

Figure 7.53: Example 7.9: Difference of the expected value of the water vapor concentration to the saturation mixing ratio $E[q_v] - q_*$ at times $t = 1000$ and $6000s$ with 0%, 10%, 20% and 50% perturbation of the initial water vapor concentration simulated on a $50 \times 50 \times 50$ mesh.

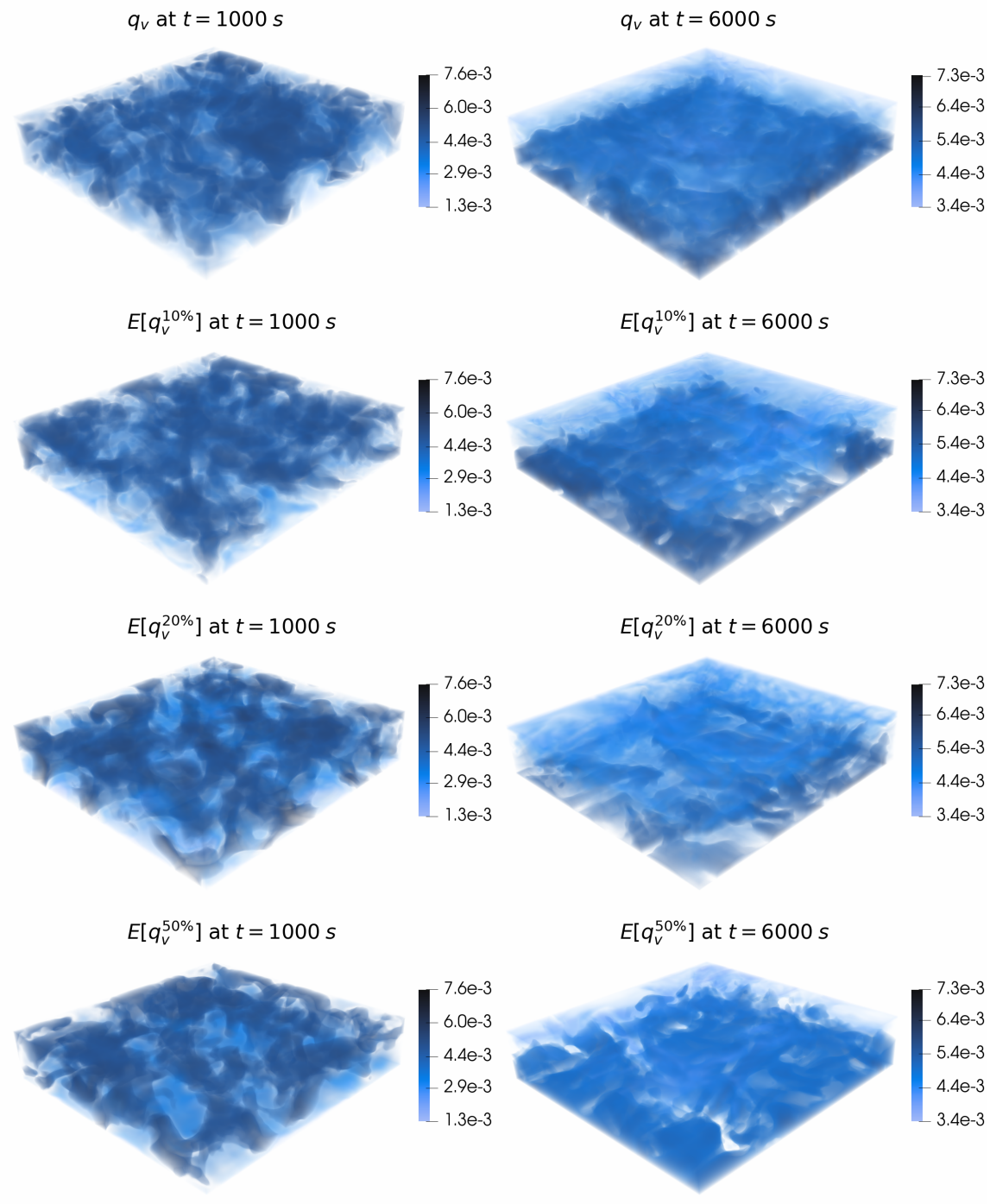

Figure 7.54: Example 7.9: Expected value of the water vapor concentration q_v at times $t = 1000$ and $6000s$ with 0%, 10%, 20% and 50% perturbation of the initial water vapor concentration simulated on a $50 \times 50 \times 50$ mesh.

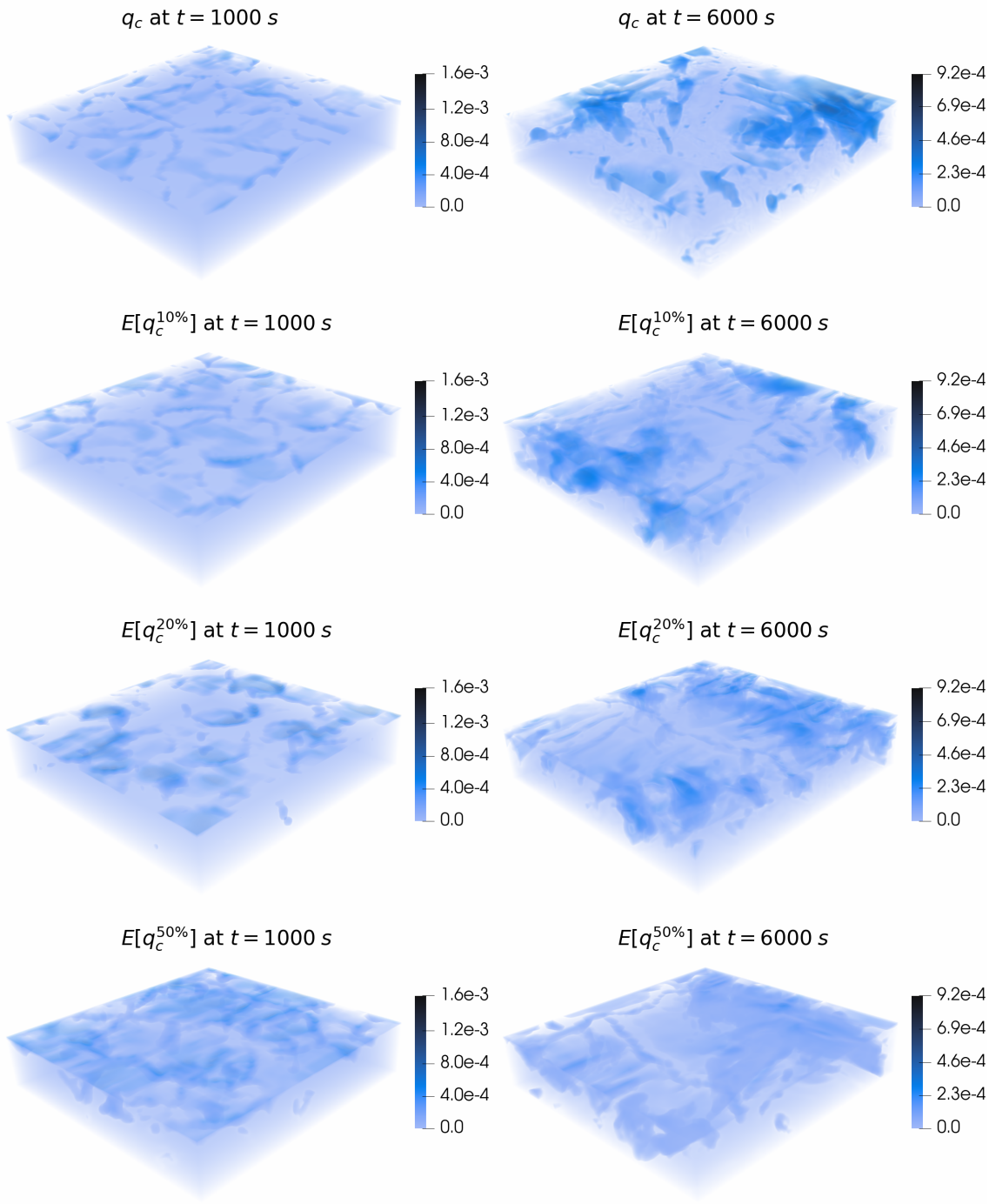

Figure 7.55: Example 7.9: Expected value of the cloud drops concentration q_c at times $t = 1000$ and $6000s$ with 0%, 10%, 20% and 50% perturbation of the initial water vapor concentration simulated on a $50 \times 50 \times 50$ mesh.

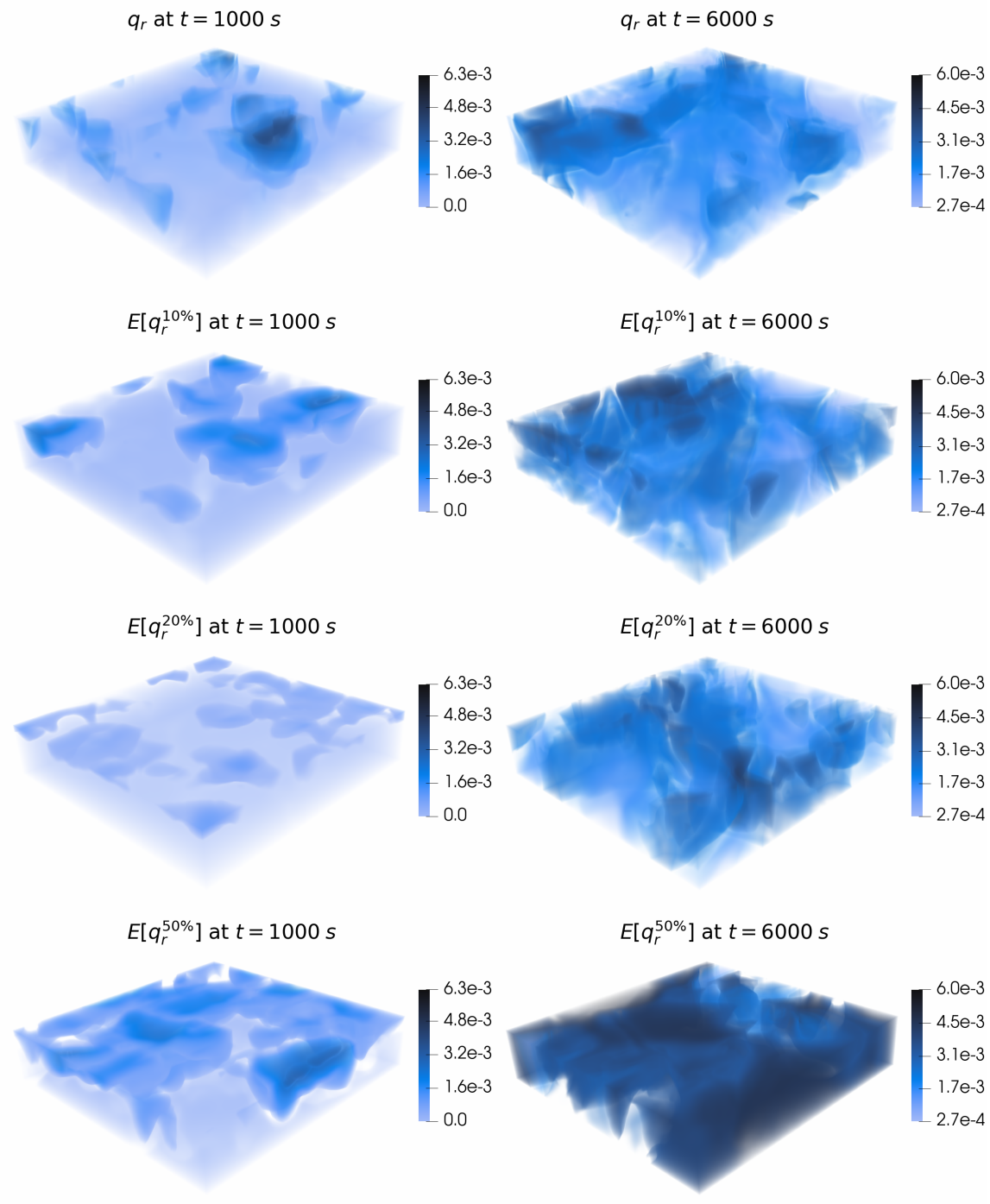

Figure 7.56: Example 7.9: Expected value of the rain concentration q_r at times $t = 1000$ and $6000s$ with 0%, 10%, 20% and 50% perturbation of the initial water vapor concentration simulated on a $50 \times 50 \times 50$ mesh.

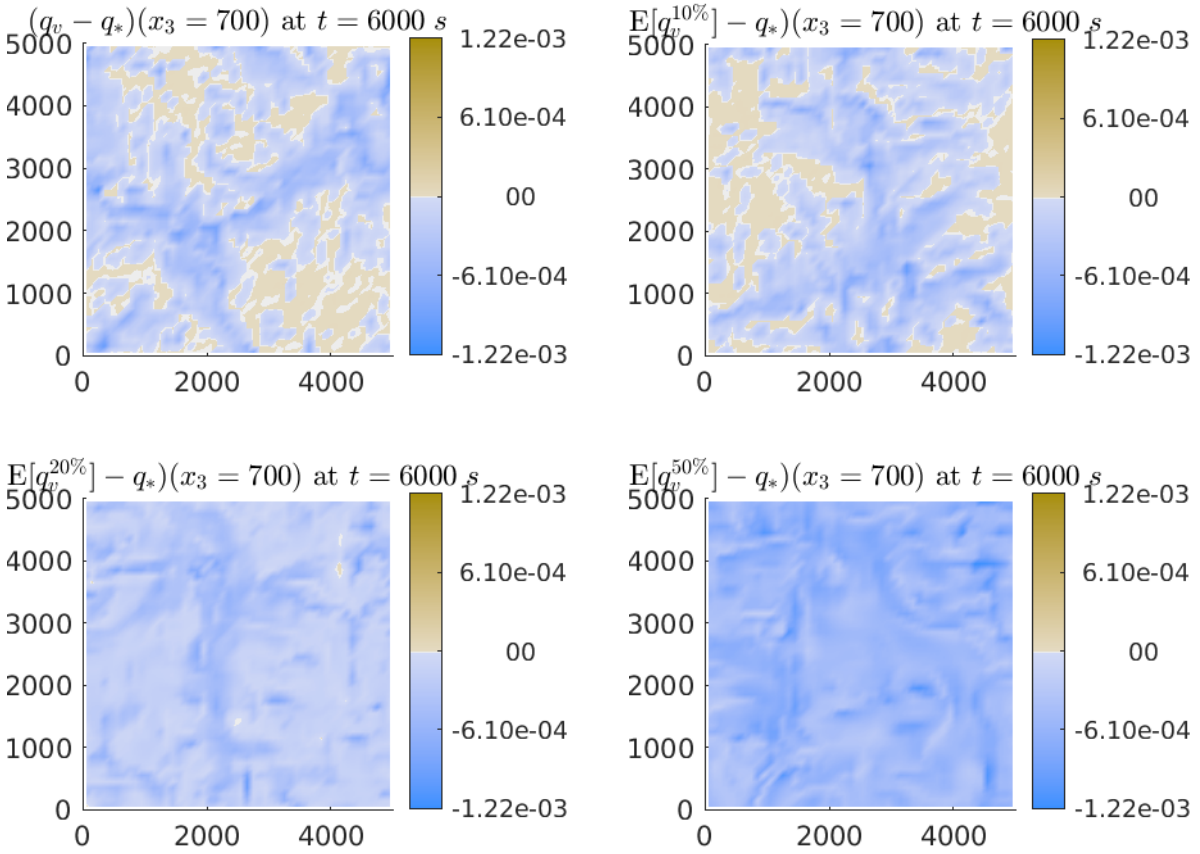

Figure 7.57: Example 7.9: Slices of the difference of water vapor to the saturation mixing ratio $q_v - q_*$ at $x_3 = 700$ at time $t = 6000s$ with 0%, 10%, 20% and 50% perturbation of the initial water vapor concentration simulated on a $50 \times 50 \times 50$ mesh.

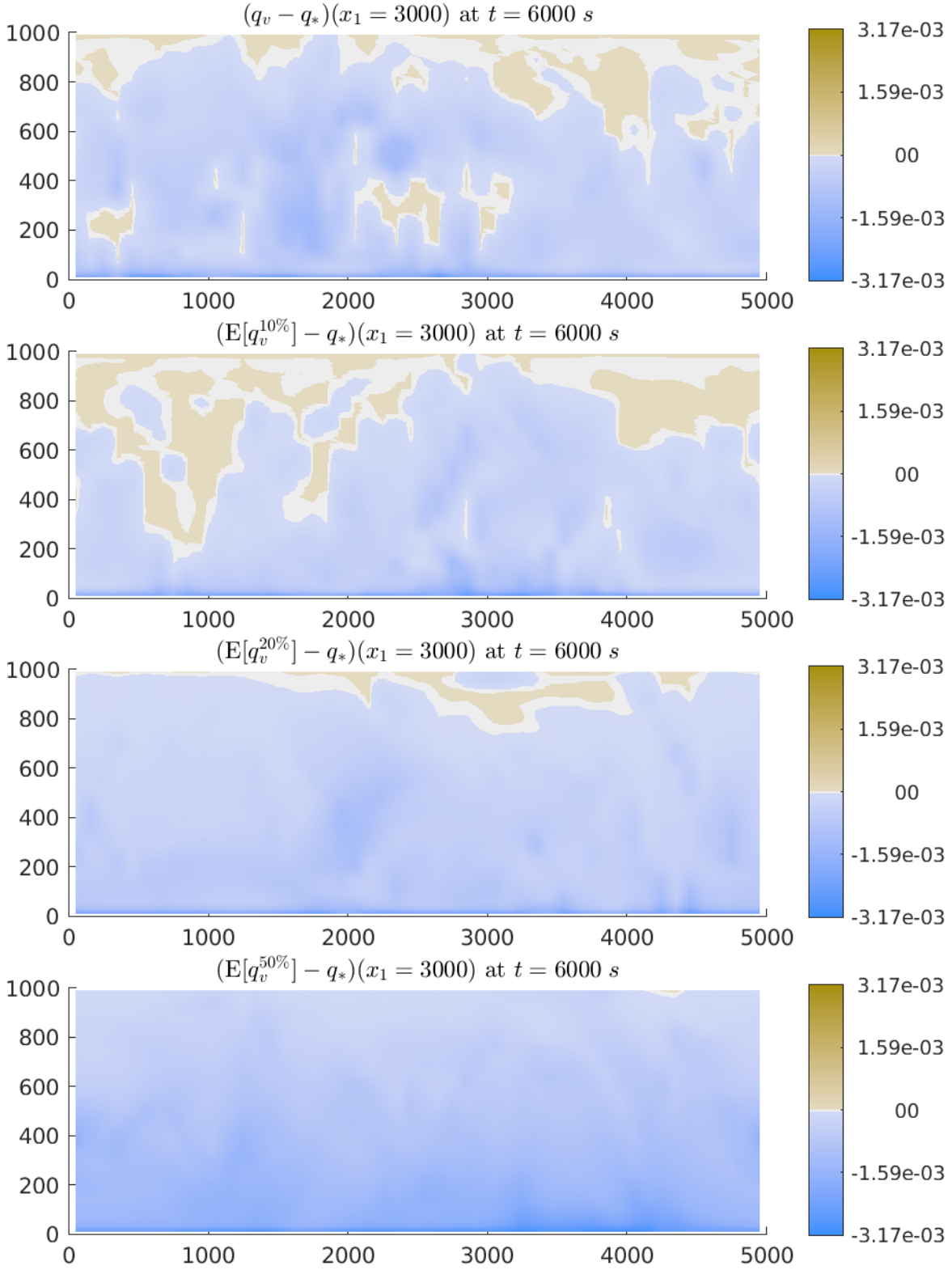

Figure 7.58: Example 7.9: Slices of the difference of water vapor to the saturation mixing ratio $q_v - q_*$ at $x_1 = 3000$ at time $t = 6000s$ with 0%, 10%, 20% and 50% perturbation of the initial water vapor concentration simulated on a $50 \times 50 \times 50$ mesh.

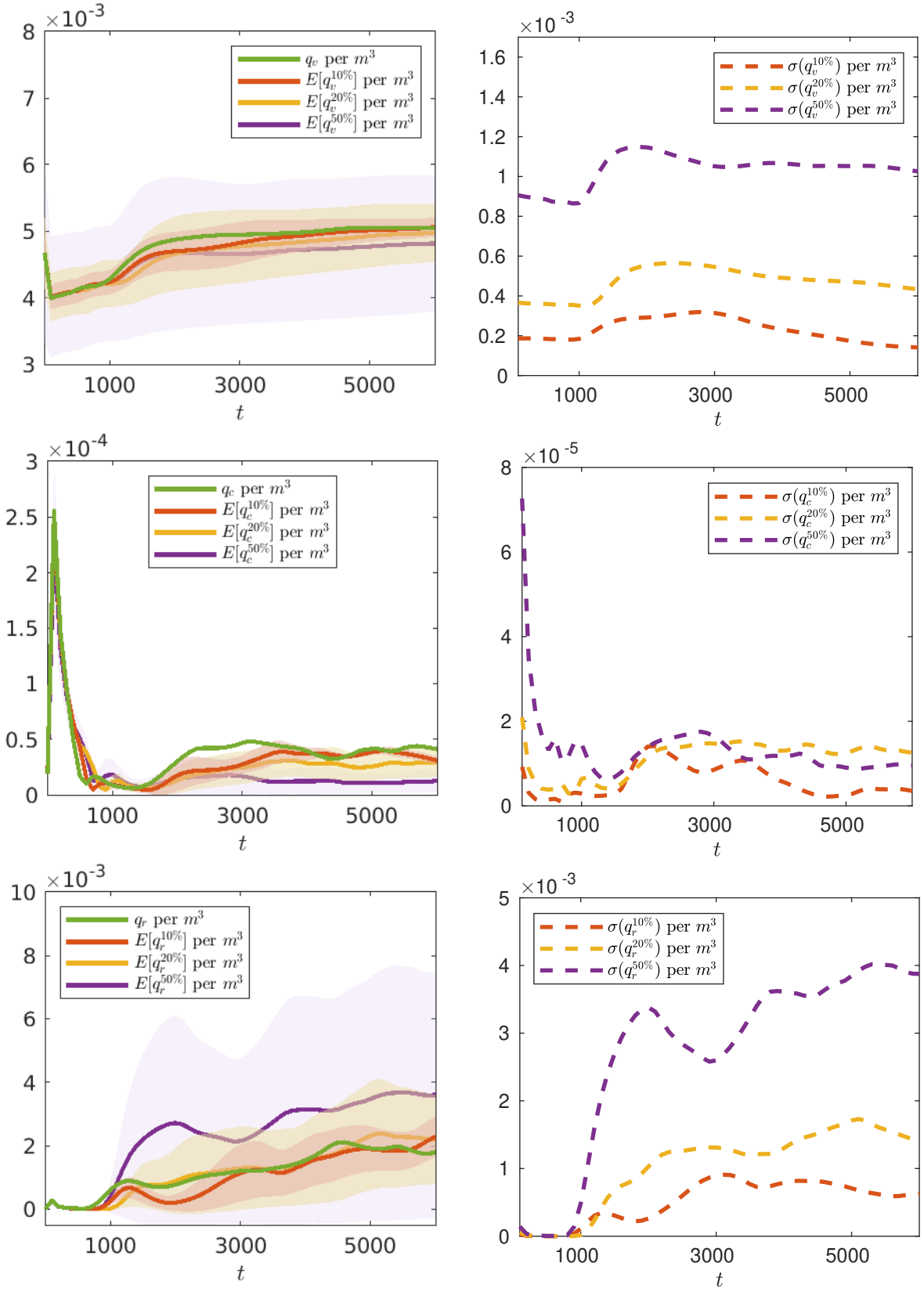

Figure 7.59: Example 7.9: Time evolution of the expected values with their standard deviations for the cloud variables per m^3 (shaded region, left column) and standard deviation (right column) using 0%, 10%, 20% and 50% perturbation of the initial data in q_v.

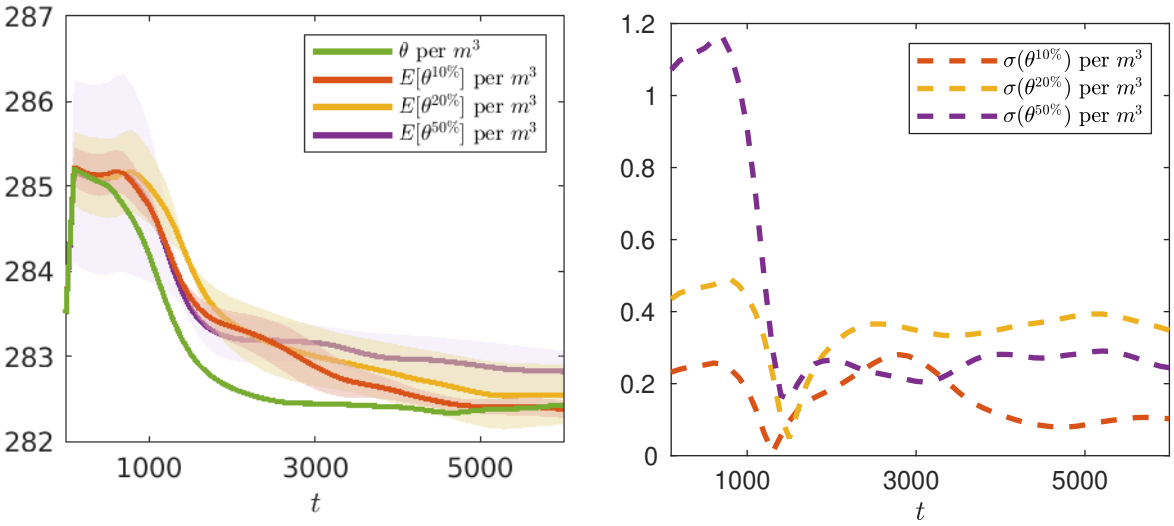

Figure 7.60: Example 7.9: Time evolution of the expected values with their standard deviations for the potential temperature θ per m^3 (shaded region, left column) and standard deviation (right column) using 0%, 10%, 20% and 50% perturbation of the initial data in q_v.

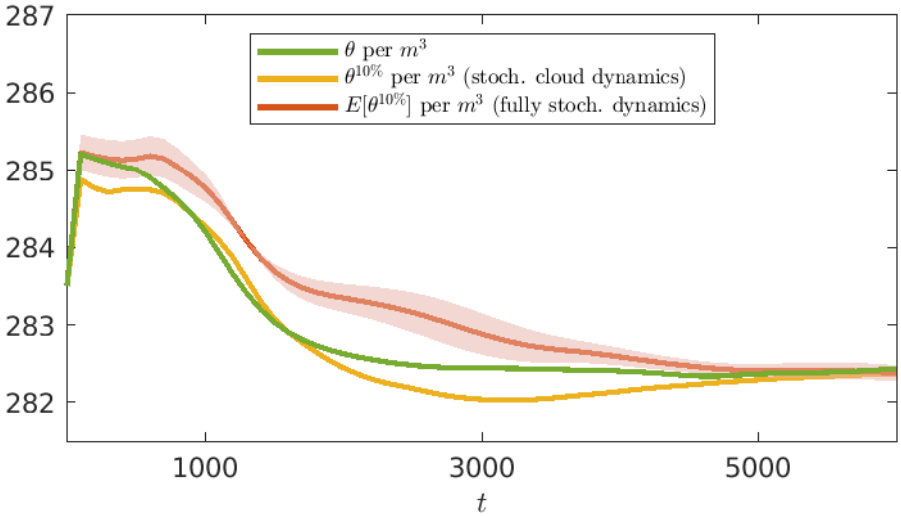

Figure 7.61: Example 7.9: Time evolution of the expected values with their standard deviations (shaded region) for the potential temperature θ per m^3 using 0% and 10% perturbation of the initial data in q_v, where the latter was simulated with stochastic cloud dynamics and the fully stochastic dynamics.

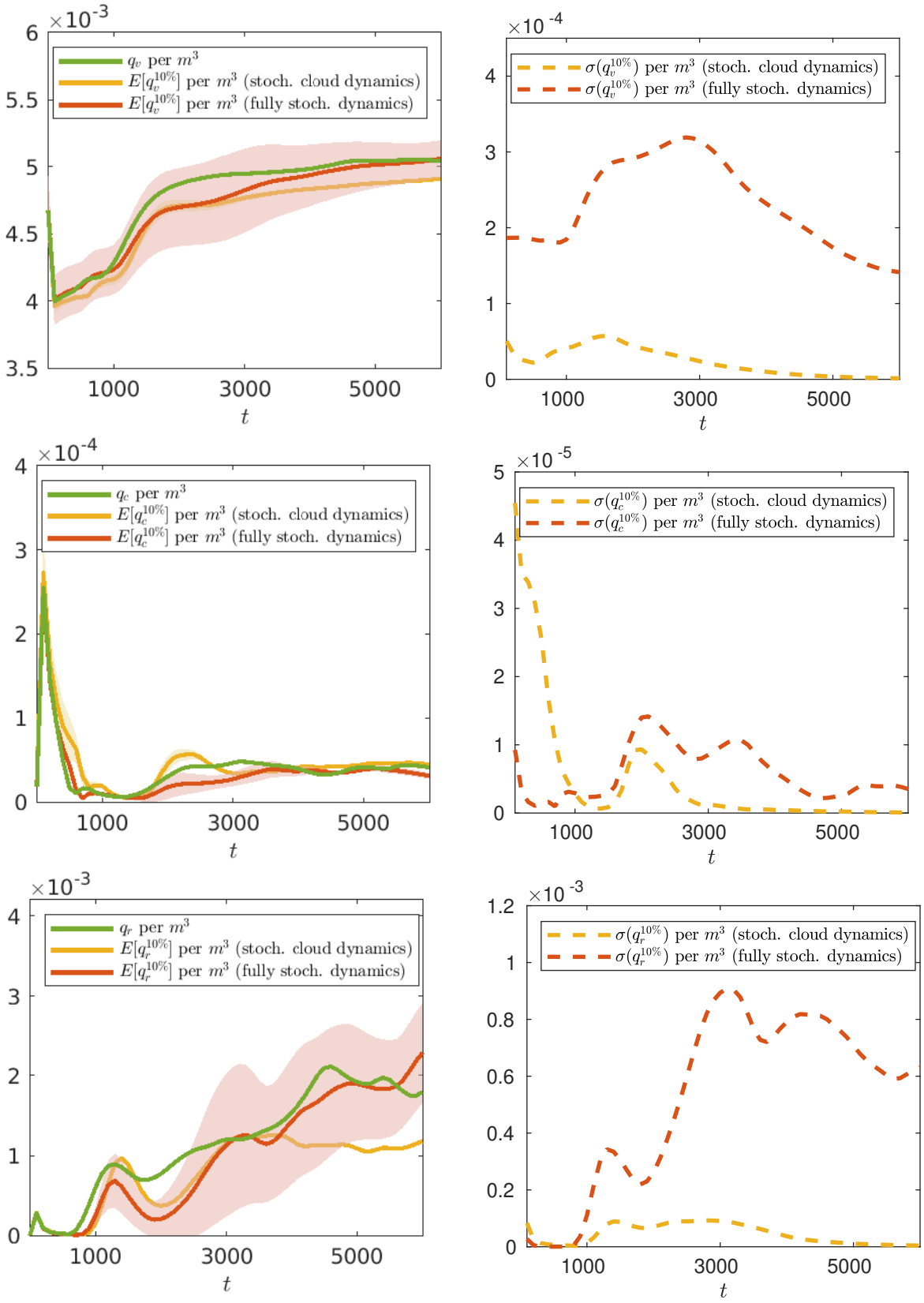

Figure 7.62: Example 7.9: Time evolution of the expected values with their standard deviations for the cloud variables per m^3 (shaded region, left column) and standard deviation (right column) using 0% and 10% perturbation of the initial data in q_v, where the latter was simulated with stochastic cloud dynamics and the fully stochastic dynamics.

7.3 Comparison of the stochastic Galerkin, stochastic collocation and Monte Carlo method

In this section, we compare the results of the stochastic Galerkin method, see Section 5.2.1, on which our numerical schemes for the stochastic models are based, with the Monte Carlo and the stochastic collocation method, see Section 5.2.2, in 2D. To do so, we simulate the stochastic warm air bubble test with the fully stochastic model (M3) and uniform initial perturbation, see Example 7.4, with all of the three methods. In Figures 7.63–7.66 the errors are computed to a reference solution obtained with the stochastic Galerkin method with 20 modes and in Figures 7.67 and 7.68 a self convergence study is presented.

In Figures 7.63 and 7.64, the errors of the stochastic Galerkin and the stochastic collocation method are presented for the cloud and Navier-Stokes variables with a semi-logarithmic scale in the plots. One can observe that for this test case and for a time $t = 10s$ the stochastic Galerkin method outperforms the stochastic collocation method. Experimentally, the errors of the stochastic Galerkin method exhibit an exponential decay, whereas the errors of the stochastic collocation method, which is just a pseudo-spectral method, behave as those for an interpolation method. In Figures 7.65 and 7.66, the errors of all the three methods, the stochastic Galerkin, the Monte Carlo and the stochastic collocation method, at time $t = 10s$ are depicted. Here, we computed the errors of the expected values and used a semi-logarithmic scale for the stochastic Galerkin and the stochastic collocation method and a double-logarithmic scale for the Monte Carlo method. Also in this case, the errors of the stochastic Galerkin method are much smaller than the ones of the other two methods and one can observe again the exponential decay, whereas the other two methods exhibit a polynomial decay rate. In Figures 7.67 and 7.68, we show the self convergence study of the methods. One can observe that the stochastic Galerkin solution with 20 modes as reference solution achieves comparable and in most cases smaller errors than the Monte Carlo solution with 10000 samples and much smaller ones than the stochastic collocation method with 20 points. We did not fully investigate the computational times, but we noticed that the runtimes of the stochastic Galerkin method scale faster than just linearly as in the case of the stochastic collocation and the Monte Carlo method. In [21], we investigated the runtimes of the stochastic Galerkin and stochastic collocation method in the case of stochastic cloud dynamics, i.e. model (M2), which already indicated that the stochastic Galerkin method is computationally more expensive. An appropriate test would be to compare the runtimes of the methods for the same achieved error. This is left for future work.

Remark 7.2*:* Figures 7.65–7.68 emerged from a joint project with Tijana Janjic Pfander and Yvonne Ruckstuhl from LMU in Munich.

Remark 7.3*:* The here presented results give a first insight into how the different methods behave but do not represent a thorough comparison. For that, one should consider the behavior of the errors at later times. Moreover, further experiments, for example, the stochastic Rayleigh-Bénard convection should be considered and, in particular, an appropriate test to compare the computational costs of the methods has to be found.

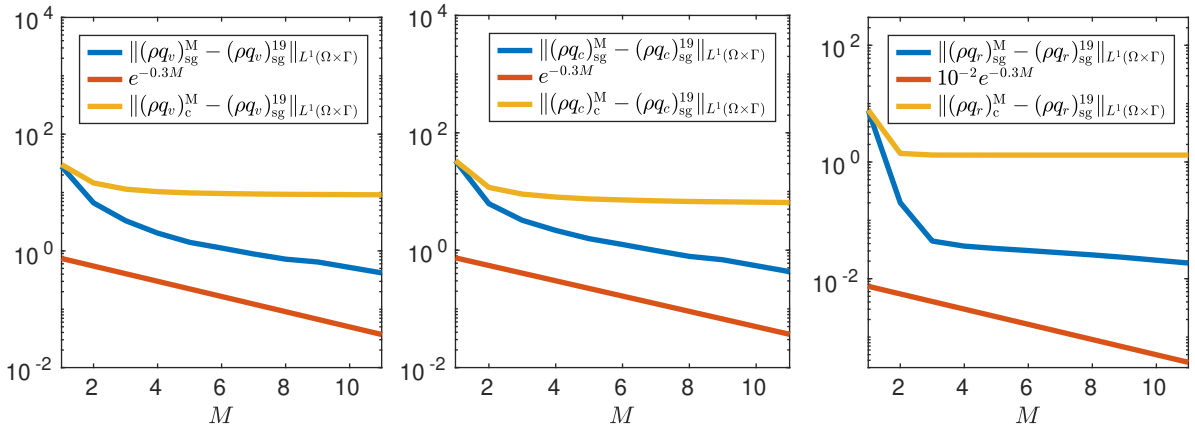

Figure 7.63: Comparison of the errors of the stochastic Galerkin and the stochastic collocation method for the cloud variables $(\rho q_\ell), \ell \in \{v, c, r\}$, at time $t = 10s$ using $\Delta t = 0.01$ and $M = L$.

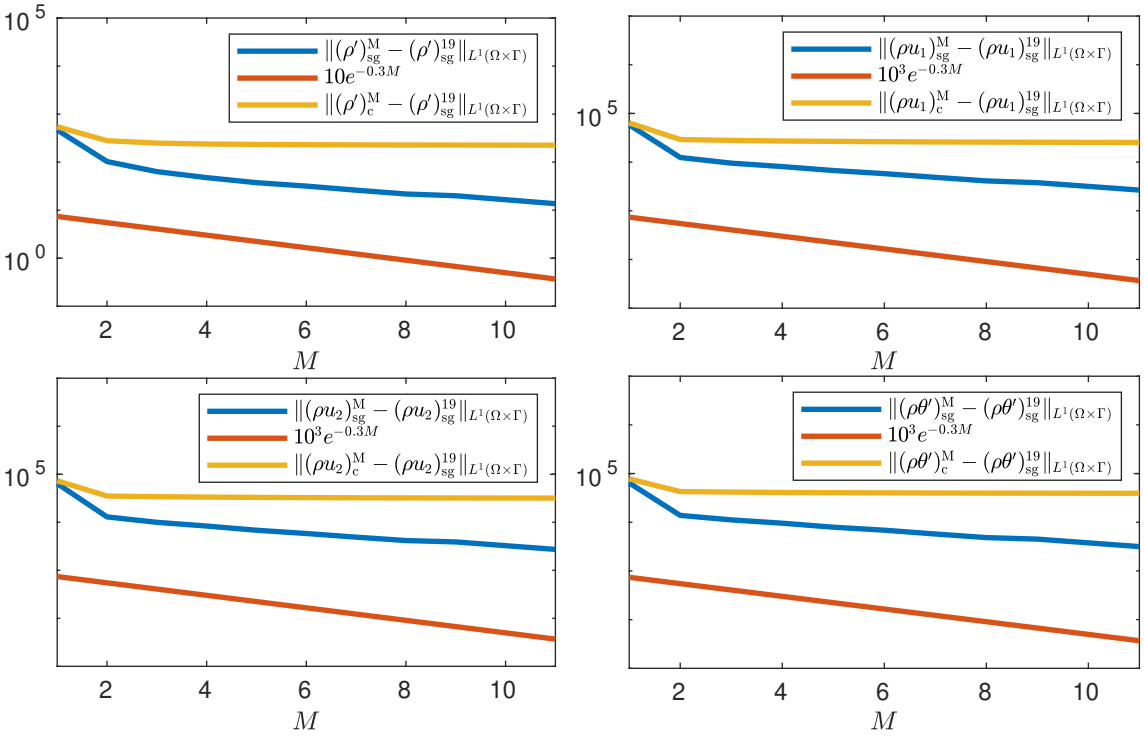

Figure 7.64: Comparison of the errors of the stochastic Galerkin and the stochastic collocation method for the Navier-Stokes variables ρ', ρu_1, ρu_2 and $(\rho\theta)'$ at time $t = 10s$ using $\Delta t = 0.01$ and $M = L$.

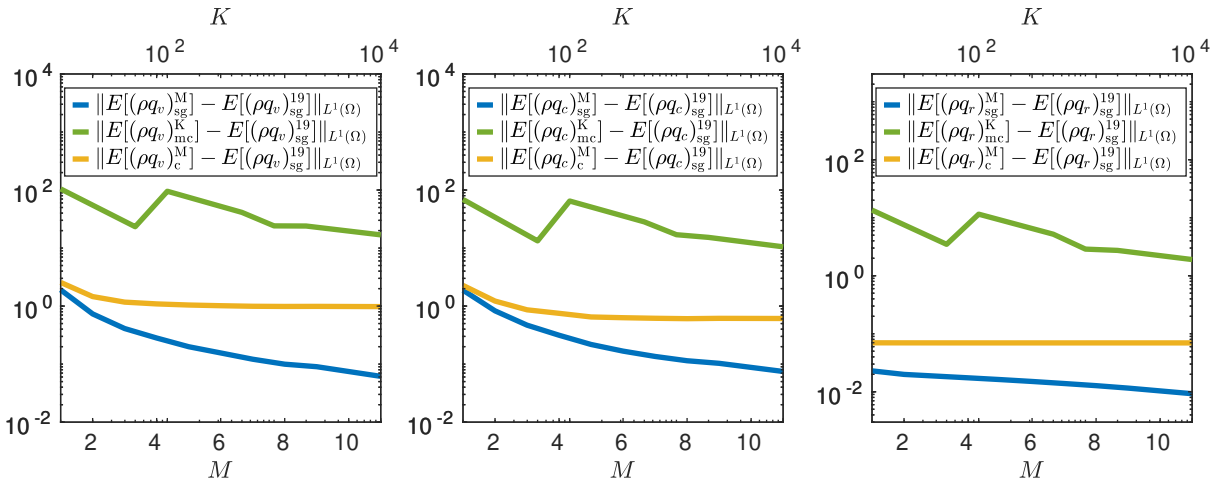

Figure 7.65: Comparison of the errors of the stochastic Galerkin, stochastic collocation and the Monte Carlo method for the expected values of the cloud variables $(\rho q_\ell), \ell \in \{v, c, r\}$, at time $t = 10s$ using $\Delta t = 0.01$ and $M = L$.

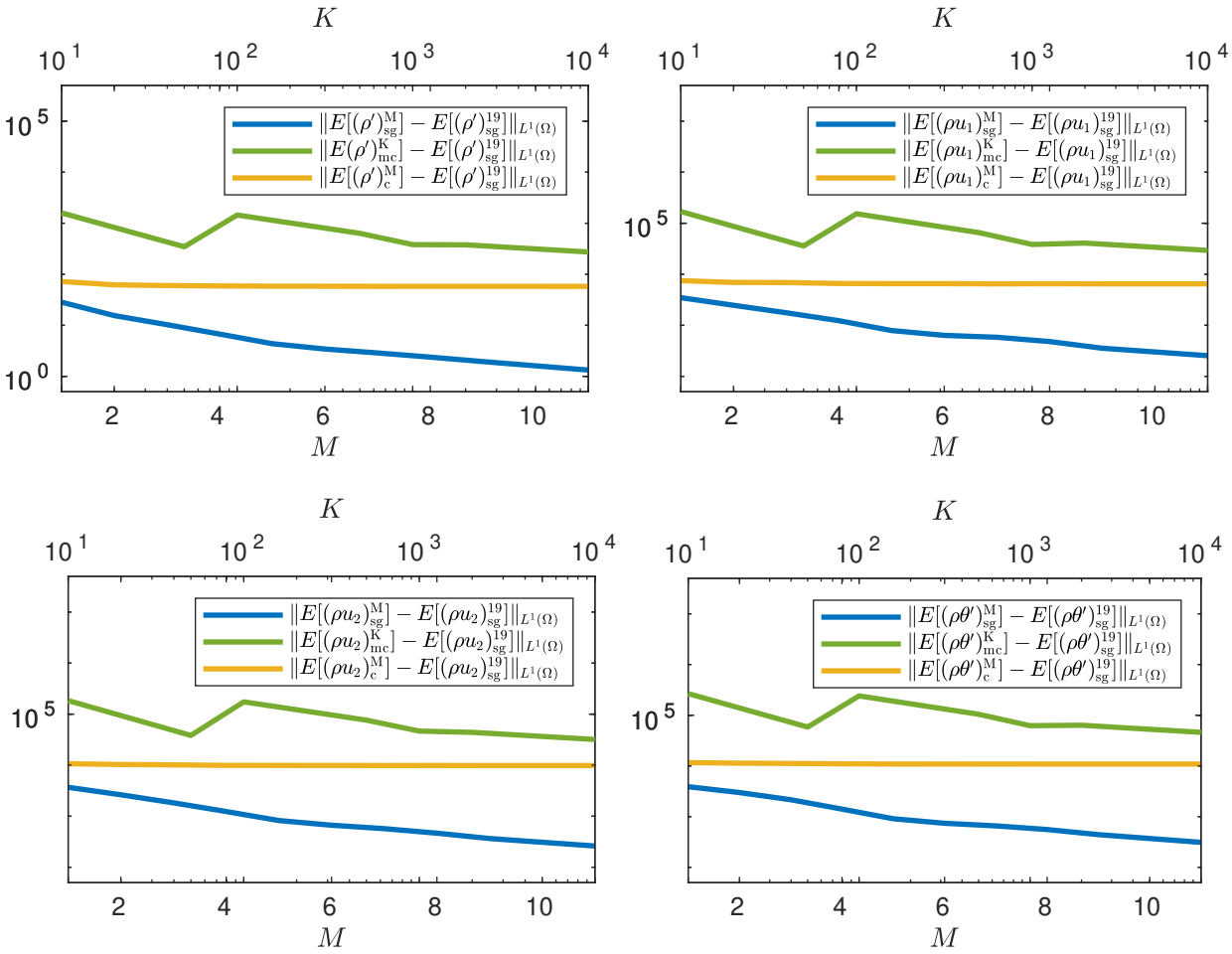

Figure 7.66: Comparison of the errors of the stochastic Galerkin, stochastic collocation and the Monte Carlo method for the expected values of the Navier-Stokes variables ρ', ρu_1, ρu_2 and $(\rho\theta)'$ at time $t = 10s$ using $\Delta t = 0.01$ and $M = L$.

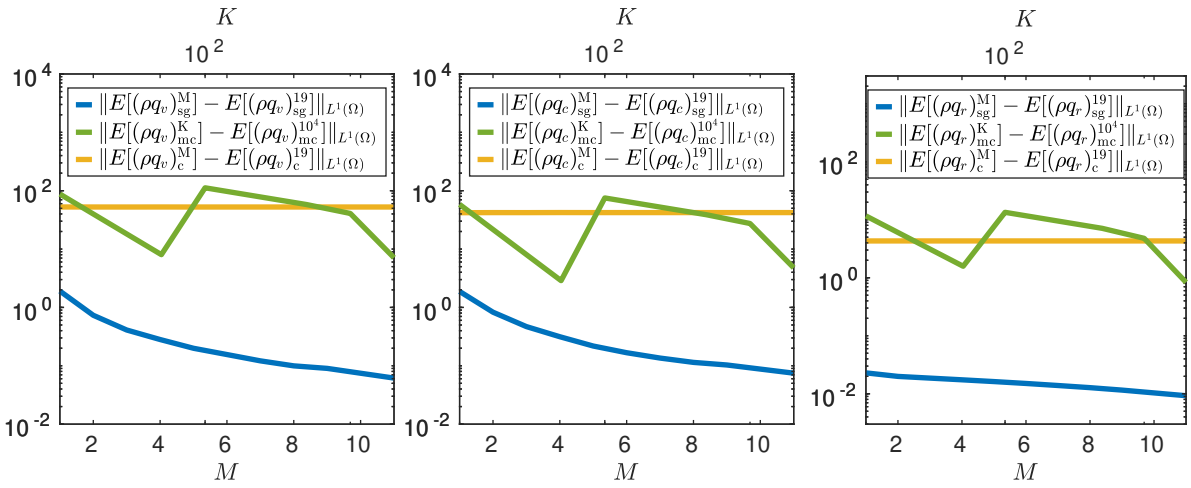

Figure 7.67: Comparison of the self convergences of the stochastic Galerkin, stochastic collocation and the Monte Carlo method for the expected values of the cloud variables $(\rho q_\ell), \ell \in \{v, c, r\}$, at time $t = 10s$ using $\Delta t = 0.01$ and $M = L$.

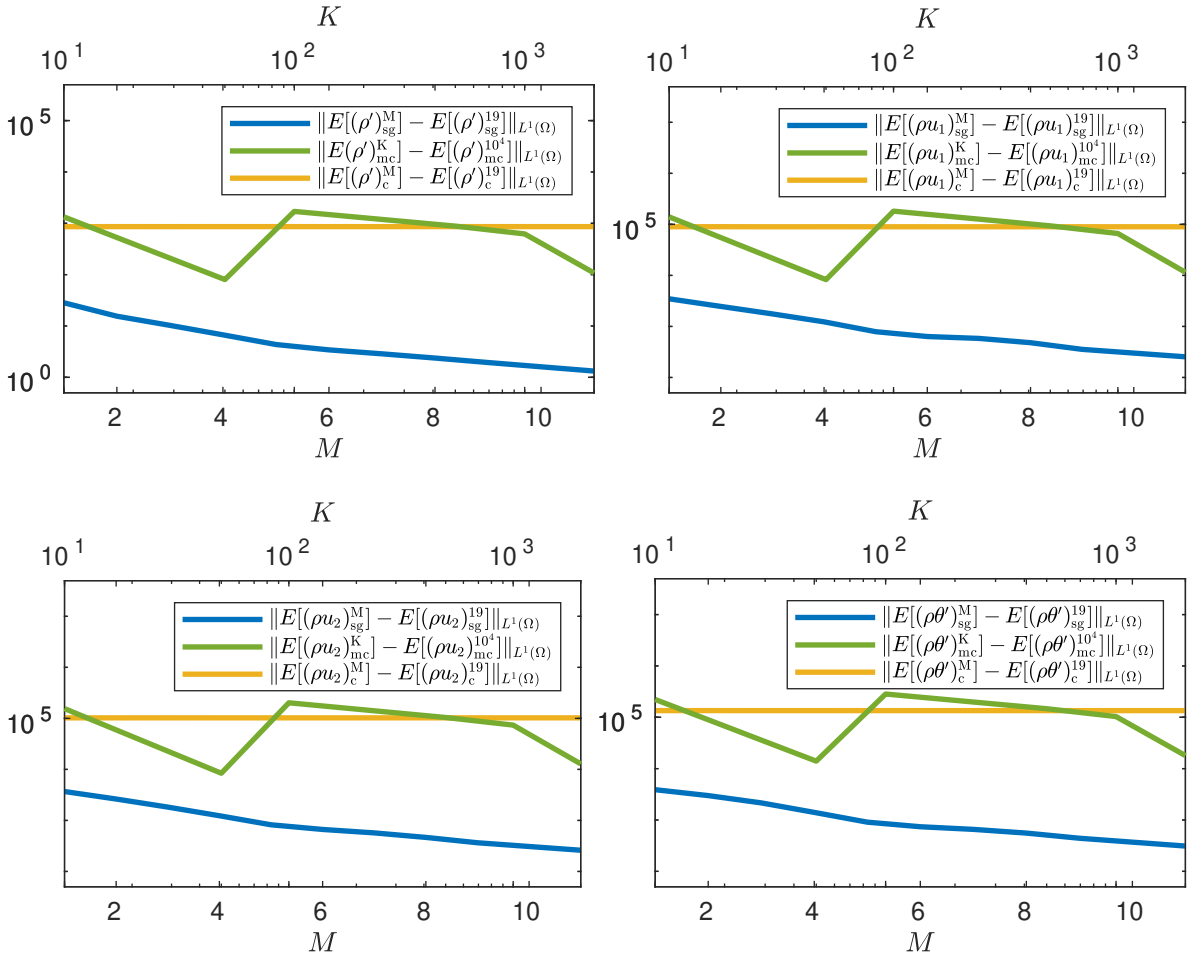

Figure 7.68: Comparison of the self convergences of the stochastic Galerkin, stochastic collocation and the Monte Carlo method for the expected values of the Navier-Stokes variables at time $t = 10s$ using $\Delta t = 0.01$ and $M = L$.

8 Conclusion

In this thesis, we have studied uncertainty propagation in an atmospheric model for warm clouds governed by the Navier-Stokes equations for weakly compressible fluids which are combined with the equations for cloud dynamics. The latter has been proposed as an ODE system in [103] and is based on the single moment approach considering evolution equations for the mass concentrations of the liquid water phases, which are water vapor, cloud drops and rain drops. To investigate the effect of the uncertainty we considered the model without any uncertainty (M1), the model with uncertainty just in the cloud representations (M2) and the fully stochastic model (M3). For these models, we have developed and tested numerical schemes which resolve the rich dynamics and multi-scale effects of the systems properly and quantify efficiently and accurately uncertainties in solutions of the stochastic models.

Concerning the numerical methods, we have started with the discretization of the deterministic model (M1) and then adapted this scheme also for the stochastic models by combining it with the approximation in the stochastic space. We point out that atmospheric flows are weakly compressible which leads to the low Mach number problem. One, therefore, needs to use a finite volume method, which is accurate and efficient in the low Mach number regime, see [13, 14]. Thus, as discretization for model (M1), we have chosen a suitable linear-nonlinear splitting between the fast and slow flow variables and a second-order IMEX discretization in time (the ARS (2,2,2) scheme). The coupling between the cloud equations (M1.b) and the Navier-Stokes system (M1.a) is realized numerically by the second-order Strang splitting. The cloud equations are approximated in space by a finite volume method and in time using an explicit third-order Runge-Kutta method with an enlarged stability region. Due to the multi-scale behavior of the cloud system, the microscopic cloud dynamics requires a smaller time step than the flow dynamics and thus several microscopic cloud subiterations are realized within one macroscopic splitting time step, whose size is dictated by the flow dynamics. For the stochastic models (M2) and (M3), we combine this discretization with a spectral method in the stochastic space, the stochastic Galerkin method, which leads to a deterministic system of PDEs for the expansion coefficients. To the best of our knowledge, this is the first contribution that combines an accurate and efficient method for the weakly compressible Navier-Stokes equations with the stochastic Galerkin method for the uncertainty quantification in atmospheric models.

Having developed these new cloud models and suitable numerical methods, we have conducted different numerical experiments. We performed extensive numerical benchmarking for the deterministic and stochastic models. For the deterministic model (M1), we clearly exhibited a spatial experimental order of convergence of two in 2D and 3D when the time increments were chosen according to the time step restriction. We also demonstrated that this spatial experimental order of convergence is preserved in the stochastic schemes. For the stochastic models (M2) and (M3) we additionally exhibited an experimentally determined exponential convergence rate of the errors in the stochastic space. This experimental convergence rate was observed for both stochastic models in various perturbation scenarios: uniform and normal distribution of the initial uncertainty, perturbation of initial conditions and perturbation of cloud model parameter. We also compared the errors obtained by the stochastic Galerkin method to the ones of another spectral method, the stochastic collocation method, as well as to a standard sampling method, the Monte Carlo method, and in our test case, the stochastic Galerkin method exhibited lower errors and a faster experimental convergence rate. Additionally, we studied the numerical solutions of the three cloud models in 2D and 3D Rayleigh-Bénard convection and obtained interesting results. First, we have observed a clear effect of the moisture to structure formation of cloud in the deterministic case of model (M1). By illustrating the behavior of clouds in different perturbed scenarios with the two stochastic models (M2) and (M3), we then demonstrated that perturbations in the cloud initial conditions can crucially change the time evolution in the moist Rayleigh-Bénard convection. The results also exhibited a clear difference of the solutions of the two stochastic models in 3D Rayleigh-Bénard convection, which indicates that initial perturbations in the cloud equations propagate to the Navier-Stokes equations and have a non-negligible effect on the solution. Our numerical study clearly demonstrates the applicability of the stochastic Galerkin method for the uncertainty quantification in complex atmospheric models and paves the path for more extensive numerical studies.

With the derived method, it is also possible to perform parameter studies. A first choice would be to determine the diffusivities for the liquid water phases and the thermal conductivity μ_h. In this thesis, we assumed for simplicity that all the liquid water phases have the same diffusivity μ_q and that it is equal to μ_h. Now, one could apply the stochastic Galerkin method successively for the different diffusivities and conduct sensitivity and uncertainty studies to determine them.

A future investigation directly rising from the obtained results is to compare the performance of the stochastic Galerkin method more extensively with the stochastic collocation and the Monte Carlo method. Considerable aspects are the computational cost, the accuracy for long-time simulations, as well as the results obtained in some realistic meteorological scenarios. We already made the first step in this direction by implementing the stochastic Galerkin method in the cloud physics scheme of the numerical weather model ICON, which is currently used by the German Weather Service. The next step is to compare the performance of the stochastic Galerkin method with the ensemble approach (a sampling method) of ICON.

Other possible future investigations might involve considering different mutually independent random effects, such as initial data, boundary data and model parameters simul-

taneously. This will allow one to quantify more precisely the propagation of small-scale stochastic errors initiated at cloud scales to macroscopic scales of flow dynamics. The investigation requires an extension to a multivariate stochastic Galerkin method, where the multivariate orthogonal basis polynomials can be obtained as tensor products of univariate orthogonal polynomials. We note that in such a complex atmospheric system this leads to a big increase in the computational cost due to the high dimensionality of the system. To handle this problem one can, for example, use sparse tensor product representations, see [8, 10, 111], as well as low-rank tensor decompositions, see [9].

Another important extension of the numerical method would be to preserve the non-negativity of the solution. Especially for the cloud representation, this is a crucial point, because the solutions do not only get nonphysical but also unstable. In our method as well as in other atmospheric models and numerical weather prediction models this is usually achieved by truncation at zero.

Apart from that, one can analyze in a future work a simplified model, for example, linearized Navier-Stokes equations, from a theoretical point of view, deriving a rigorous error analysis concerning the space and times discretization as well as the spectral approximation in the stochastic space. The corresponding error analysis has already been applied to a simplified incompressible flow model in [42]. Concerning the error analysis of the fully nonlinear Navier-Stokes equations combined with the cloud equations, a promising technique is to apply the relative energy, see, e.g., [18, 28, 80].

A Closure for single moment schemes

Here, we state a closure for single moment schemes which was presented in [21].

The number concentration of rain drops can be approximated by a function of the respective mass concentration $n_r = f(q_r, c_r)$. Since we implicitly assume that rain drops are distributed according to a size distribution, this approach should be used for mimicking the shape of the distribution properly. If we use a constant mean mass of rain drops, the function will be a simple linear relation $n_r = \frac{1}{\overline{m_r}} q_r$. We extend this approach and propose the following nonlinear relation:

$$n_r = c_r \cdot q_r^{\gamma}, \quad 0 < \gamma \leq 1.$$

Using this approach, one can replace the quantity n_r in the processes related to rain drop number concentration. For the simple case of a constant mean mass $\overline{m_r}$, we can determine the constants as $c_r = \overline{m_r}^{-1}$ and $\gamma = 1$. This approach would be meaningful for the case of a symmetric size distribution of rain droplets centered around the mean mass. However, it is well-known that size distributions of rain are usually skew to larger sizes and thus a linear relation is inappropriate. For sizes of rain drops, an exponential distribution is often assumed (see [86]), namely:

$$f(r) = B_r e^{-\lambda r}$$

with a constant parameter $B_r = 2 \cdot 10^7\,\mathrm{m}^{-4}$ and the drop radius r. Using the general moments of the distribution,

$$\mu_k[r] = \frac{\Gamma(k+1)}{\lambda^{k+1}} B_r$$

with the gamma function $\Gamma(x) := \int_0^\infty t^{x-1} \exp(-t)\, dt$, we obtain

$$\rho n_r = \mu_0[r] = \frac{B_r}{\lambda} \quad \text{and} \quad \rho q_r = \frac{4}{3}\pi\rho_\ell \frac{\Gamma(4)}{\lambda^4} B_r.$$

Using these relations, one can derive the following function for the number concentration n_r, i.e.

$$n_r = \underbrace{B_r^{\frac{3}{4}} \rho^{-\frac{3}{4}} (8\pi\rho_\ell)^{-\frac{1}{4}}}_{=c_r} q_r^{\frac{1}{4}} = c_r q_r^{\gamma} \quad \text{with} \quad \gamma = \frac{1}{4}.$$

We stress that c_r is, in fact, a function of the air density ρ, that is, $c_r = c_{r0} \cdot \rho^{-\frac{3}{4}}$.

B Explicit formulation of the cloud equations

We present the equations of microphysical processes explicitly as they are used in our numerical experiments. In Tables B.1 and B.2, we present physical constants and model parameters with their values used in our numerical simulations. The content is taken from [21].

$$
\begin{aligned}
n_c &= q_c \frac{8 \cdot 10^8}{q_c + 4.1888 \cdot 10^{-7}} \coth\left(\frac{q_c}{5.236 \cdot 10^{-13}}\right), \\
C_{\text{act}} &= 6.2832 \cdot 10^{-3} D_v G \rho \left(q_v - q_*\right)_+, \\
C_1 &= 0.7796 D_v G \left(q_v - q_*\right) \left(\frac{8 \cdot 10^8}{q_c + 4.1888 \cdot 10^{-7}} \coth\left(\frac{q_c}{5.236 \cdot 10^{-13}}\right)\right)^{\frac{2}{3}} \rho q_c, \\
p_s(T) &= \exp\Big\{54.842763 - {}^{6763.22}/_T - 4.21 \ln T + 0.000367T + \tanh(0.0415(T - 218.8)) \\
&\quad \cdot (53.878 - {}^{1331.22}/_T - 9.44523 \ln T + 0.014025T)\Big\}, \\
n_r &= 23752.6753 \rho^{-\frac{3}{4}} q_r^{\frac{1}{4}}, \\
r &= \left(\frac{1.21 \cdot 10^{-5}}{q_r + 0.2874 \rho^{-\frac{3}{4}} q_r^{\frac{1}{4}}}\right)^{\frac{4}{15}}, \\
E &= -0.7796 D_v G \left(q_* - q_v\right)_+ \left(644.5198 \sqrt{\rho q_r} + 17.5904 \mu^{-\frac{1}{6}} D_v^{-\frac{1}{3}} \sqrt{\alpha r} \rho^{\frac{13}{24}} q_r^{\frac{91}{120}}\right), \\
A_1 &= 10^{-3} k_1 \rho q_c^2, \\
A_2 &= 0.3846 \alpha k_2 \rho^{\frac{1}{4}} q_c r q_r^{\frac{61}{60}}, \\
v_q &= 1.1068 \alpha q_r^{\frac{4}{15}} r \rho^{-\frac{1}{2}}.
\end{aligned}
$$

Constant	Description
$p_* = 101\,325\,\mathrm{Pa}$	reference pressure
$T_* = 288\,\mathrm{K}$	reference temperature
$T_0 = 273.15\,\mathrm{K}$	melting temperature
$\rho_* = 1.225\,\mathrm{kg\,m^{-3}}$	reference air density
$\rho_\ell = 1000\,\mathrm{kg\,m^{-3}}$	density of liquid water
$R_v = 461.52\,\mathrm{J\,kg^{-1}\,K^{-1}}$	specific gas constant, water vapor
$c_p = 1005\,\mathrm{J\,kg^{-1}\,K^{-1}}$	specific heat capacity, dry air
$g = 9.81\,\mathrm{m\,s^{-2}}$	acceleration due to gravity
$L = 2.53 \times 10^6\,\mathrm{J\,kg^{-1}}$	latent heat of vaporization
$\varepsilon = \frac{M_{\mathrm{mol},v}}{M_{\mathrm{mol},a}} = 0.622$	ratio of molar masses of water and dry air
$D_0 = 2.11 \times 10^{-5}\,\mathrm{m^2\,s^{-1}}$	diffusivity constant

Table B.1: Physical constants and reference quantities, [103].

Parameter	Description
$\alpha = 190.3 \pm 0.5 \cdot 190.3\,\mathrm{m\,s^{-1}\,kg^{-\beta}}$	parameter for terminal velocity
$k_1 = 4083 \pm 0.5 \cdot 4083\,\mathrm{kg\,s^{-1}}$	parameter for autoconversion
$k_2 = 0.8 \pm 0.5 \cdot 0.8\,\mathrm{kg}$	parameter for accretion
$\beta = \frac{4}{15}$	parameter for terminal velocity
$m_t = 1.21 \times 10^{-5}\,\mathrm{kg}$	parameter for terminal velocity
$N_0 = 1000\,\mathrm{m^{-3}}$	parameter for activation
$N_\infty = 8 \times 10^8\,\mathrm{kg^{-1}}$	parameter for activation
$m_0 = 5.236 \times 10^{-16}\,\mathrm{kg}$	parameter for activation
$a_E = 0.78$	parameter for evaporation
$a_v = 0.78$	parameter for ventilation
$b_v = 0.308$	parameter for ventilation

Table B.2: Model parameters, [103].

Bibliography

[1] *Personal discussion with F. Otto about the initial conditions for moist Rayleigh-Bénard convection simulations.*

[2] *Personal discussion with R. Klein about the effect of the grid resolution of the numerical spatial discretization on the cell pattern in Rayleigh-Bénard convection.*

[3] A. Abdulle, *Fourth order Chebyshev methods with recurrence relation*, SIAM J. Sci. Comput., 23 (2002), pp. 2041–2054.

[4] A. Abdulle and A. A. Medovikov, *Second order Chebyshev methods based on orthogonal polynomials*, Numer. Math., 90 (2001), pp. 1–18.

[5] T. Alboussière and Y. Ricard, *Rayleigh-Bénard stability and the validity of quasi-Boussinesq or quasi-anelastic liquid approximations*, J. Fluid Mech., 817 (2017), pp. 264–305.

[6] U. M. Ascher, S. J. Ruuth, and R. J. Spiteri, *Implicit-explicit Runge-Kutta methods for time-dependent partial differential equations*, Appl. Numer. Math., 25 (1997), pp. 151–167. Special issue on time integration (Amsterdam, 1996).

[7] I. Babuška, R. Tempone, and G. E. Zouraris, *Galerkin finite element approximations of stochastic elliptic partial differential equations*, SIAM J. Numer. Anal., 42 (2004), pp. 800–825.

[8] M. Bachmayr, A. Cohen, D. Dũng, and C. Schwab, *Fully discrete approximation of parametric and stochastic elliptic PDEs*, SIAM J. Numer. Anal., 55 (2017), pp. 2151–2186.

[9] M. Bachmayr, A. Cohen, and W. Dahmen, *Parametric PDEs: sparse or low-rank approximations?*, IMA J. Numer. Anal., 38 (2018), pp. 1661–1708.

[10] M. Bachmayr, A. Cohen, R. DeVore, and G. Migliorati, *Sparse polynomial approximation of parametric elliptic PDEs. Part II: Lognormal coefficients*, ESAIM Math. Model. Numer. Anal., 51 (2017), pp. 341–363.

[11] M. Baldauf, J. Förstner, S. Klink, T. Reinhardt, C. Schraff, A. Seifert, and K. Stephan, *Kurze Modell- und Datenbankbeschreibung COSMO-DE (LMK)*, (2014).

[12] K. D. Beheng, *The Evolution of Raindrop Spectra: A Review of Microphysical Essentials*, in Rainfall: State of the Science, F. Y. Testik and M. Gebremichael, eds., Geophysical Monograph Series, 2010, pp. 29–48.

[13] G. Bispen, *IMEX finite volume methods for the shallow water equations*, dissertation, Johannes Gutenberg-Universität Mainz, 2015.

[14] G. Bispen, M. Lukáčová-Medviďová, and L. Yelash, *Asymptotic preserving IMEX finite volume schemes for low Mach number Euler equations with gravitation*, J. Comput. Phys., (2017).

[15] E. Bodenschatz, W. Pesch, and G. Ahlers, *Recent developments in Rayleigh-Bénard convection*, Annual Review of Fluid Mechanics, 32 (2000), pp. 709–778.

[16] F. Bouchut, *Nonlinear stability of finite volume methods for hyperbolic conservation laws and well-balanced schemes for sources*, Frontiers in Mathematics, Birkhäuser Verlag, Basel, 2004.

[17] S. C. Brenner and L. R. Scott, *The mathematical theory of finite element methods*, vol. 15 of Texts in Applied Mathematics, Springer, New York, third ed., 2008.

[18] A. Brunk, H. Egger, O. Habrich, and M. Lukáčová-Medviďová, *Relative energy estimates for the Cahn-Hilliard equation with concentration dependent mobility*, submitted.

[19] G. H. Bryan and J. M. Fritsch, *A benchmark simulation for moist nonhydrostatic numerical models*, Mont. Weather Rev., 130 (2002), pp. 2917–2928.

[20] A. Chertock, *Lecture notes on finite-volume methods for hyperbolic conservation laws*, 2019.

[21] A. Chertock, A. Kurganov, M. Lukáčová-Medviďová, P. Spichtinger, and B. Wiebe, *Stochastic Galerkin method for cloud simulation*, Math. Clim. Weather Forecast., 5 (2019), pp. 65–106.

[22] A. Cohen, R. DeVore, and C. Schwab, *Convergence rates of best N-term Galerkin approximations for a class of elliptic sPDEs*, Found. Comput. Math., 10 (2010), pp. 615–646.

[23] R. Courant, K. Friedrichs, and H. Lewy, *Über die partiellen Differenzengleichungen der mathematischen Physik*, Math. Ann., 100 (1928), pp. 32–74.

[24] R. M. Davies and F. J. Taylor, *The mechanism of large bubbles rising through extended liquids and through liquids in tubes*, Proc. Royal Soc. Lond. A, 200 (1950), pp. 375–390.

[25] B. Després, G. Poëtte, and D. Lucor, *Robust uncertainty propagation in systems of conservation laws with the entropy closure method*, in Uncertainty quantification in computational fluid dynamics, vol. 92 of Lect. Notes Comput. Sci. Eng., Springer, Heidelberg, 2013, pp. 105–149.

[26] J. Dixon, *The Shock Absorber Handbook*, Wiley, 2007.

[27] H. C. Elman, C. W. Miller, E. T. Phipps, and R. S. Tuminaro, *Assessment of collocation and Galerkin approaches to linear diffusion equations with random data*, Int. J. Uncertain. Quantif., 1 (2011), pp. 19–33.

[28] E. Feireisel, M. Lukáčová-Medviďová, H. Mizerová, and B. She, *Numerical Analysis of Compressible Fluid Flows*, MS&A, Springer International Publishing, first ed., 2021.

[29] E. Feireisl, *On weak-strong uniqueness for the compressible Navier-Stokes system with non-monotone pressure law*, Comm. Partial Differential Equations, 44 (2019), pp. 271–278.

[30] E. Feireisl, P. Gwiazda, A. Świerczewska Gwiazda, and E. Wiedemann, *Dissipative measure-valued solutions to the compressible Navier-Stokes system*, Calc. Var. Partial Differential Equations, 55 (2016), pp. Art. 141, 20.

[31] E. Feireisl, B. J. Jin, and A. Novotný, *Relative entropies, suitable weak solutions, and weak-strong uniqueness for the compressible Navier-Stokes system*, J. Math. Fluid Mech., 14 (2012), pp. 717–730.

[32] E. Feireisl, T. G. Karper, and M. Pokorný, *Mathematical theory of compressible viscous fluids*, Advances in Mathematical Fluid Mechanics, Birkhäuser/Springer, Cham, 2016. Analysis and numerics, Lecture Notes in Mathematical Fluid Mechanics.

[33] E. Feireisl and M. Lukáčová-Medviďová, *Convergence of a mixed finite element–finite volume scheme for the isentropic Navier-Stokes system via dissipative measure-valued solutions*, Found. Comput. Math., 18 (2018), pp. 703–730.

[34] E. Feireisl, M. Lukáčová-Medviďová, and H. Mizerová, *Convergence of finite volume schemes for the Euler equations via dissipative measure-valued solutions*, Found. Comput. Math., 20 (2020), pp. 923–966.

[35] ——, *A finite volume scheme for the Euler system inspired by the two velocities approach*, Numer. Math., 144 (2020), pp. 89–132.

[36] E. Feireisl, M. Lukáčová-Medviďová, H. Mizerová, and B. She, *Convergence of a finite volume scheme for the compressible Navier-Stokes system*, ESAIM Math. Model. Numer. Anal., 53 (2019), pp. 1957–1979.

[37] ——, *On the convergence of a finite volume method for the Navier–Stokes–Fourier system*, IMA J. Numer. Anal, (2020).

[38] E. Feireisl and A. Novotný, *Singular limits in thermodynamics of viscous fluids*, Advances in Mathematical Fluid Mechanics, Birkhäuser/Springer, Cham, second ed., 2017.

[39] E. Feireisl, A. Novotný, and H. Petzeltová, *On the existence of globally defined weak solutions to the Navier-Stokes equations*, J. Math. Fluid Mech., 3 (2001), pp. 358–392.

[40] M. Feistauer, *Mathematical methods in fluid dynamics*, vol. 67 of Pitman Monographs and Surveys in Pure and Applied Mathematics, Longman Scientific & Technical, Harlow; copublished in the United States with John Wiley & Sons, Inc., New York, 1993.

[41] M. Frank, J. Kusch, and J. Wolters, *Entropy–based methods for uncertainty quantification of hyperbolic conservation laws*, in SEMA SIMAI Springer Series, Springer International Publishing, 2021, pp. 29–56.

[42] J. Frech, *Error analysis of the stochastic Galerkin method for incompressible Navier-Stokes equations*, master thesis, Johannes Gutenberg-Universität Mainz, 2018.

[43] A. V. Getling, *Rayleigh-Bénard convection, Structure and Dynamics*, World Sci. Publ., Singpore, 2001.

[44] S. K. Godunov, *A difference method for numerical calculation of discontinuous solutions of the equations of hydrodynamics*, Mat. Sb. (N.S.), 47 (89) (1959), pp. 271–306. (Russian).

[45] W. W. Grabowski, *Untangling microphysical impacts on deep convection applying a novel modeling methodology*, J. Atmos. Sci., 72 (2015), pp. 2446–2464.

[46] A. Guillou and B. Lago, *Domaine de stabilité associé aux formules d'intégration numérique d'équations différentielles, à pas séparés et à pas liés*, 1er Congr. Assoc. Fran. Calcul, AFCAL, Grenoble, (1961), pp. 43–56.

[47] M. E. Gurtin, *An introduction to continuum mechanics*, vol. 158 of Mathematics in Science and Engineering, Academic Press, Inc. [Harcourt Brace Jovanovich, Publishers], New York-London, 1981.

[48] E. Hairer and G. Wanner, *Solving ordinary differential equations. II*, vol. 14 of Springer Series in Computational Mathematics, Springer-Verlag, Berlin, second ed., 1996. Stiff and differential-algebraic problems.

[49] M. Hanke-Bourgeois, *Grundlagen der numerischen Mathematik und des wissenschaftlichen Rechnens*, Mathematische Leitfäden. [Mathematical Textbooks], B. G. Teubner, Wiesbaden, second ed., 2006.

[50] S. Hittmeir and R. Klein, *Asymptotics for moist deep convection I: refined scalings and self-sustaining updrafts*, Theor. Comput. Fluid Dyn., 32 (2018), pp. 137–164.

[51] S. Hittmeir, R. Klein, J. Li, and E. S. Titi, *Global well-posedness for the primitive equations coupled to nonlinear moisture dynamics with phase changes*, Nonlinearity, 33 (2020), pp. 3206–3236.

[52] W. Hundsdorfer and J. Verwer, *Numerical solution of time-dependent advection-diffusion-reaction equations*, vol. 33 of Springer Series in Computational Mathematics, Springer-Verlag, Berlin, 2003.

[53] A. L. Igel and S. C. van den Heever, *The role of latent heating in warm frontogenesis*, Quart. J. Roy. Met. Soc., 140 (2014), pp. 139–150.

[54] E. Isaacson and H. B. Keller, *Analysis of numerical methods*, John Wiley & Sons, Inc., New York-London-Sydney, 1966.

[55] S. Jin, *Efficient asymptotic-preserving (AP) schemes for some multiscale kinetic equations*, SIAM J. Sci. Comput., 21 (1999), pp. 441–454.

[56] K. H. Karlsen and T. K. Karper, *A convergent nonconforming finite element method for compressible Stokes flow*, SIAM J. Numer. Anal., 48 (2010), pp. 1846–1876.

[57] ——, *Convergence of a mixed method for a semi-stationary compressible Stokes system*, Math. Comp., 80 (2011), pp. 1459–1498.

[58] ——, *A convergent mixed method for the Stokes approximation of viscous compressible flow*, IMA J. Numer. Anal., 32 (2012), pp. 725–764.

[59] T. K. Karper, *A convergent FEM-DG method for the compressible Navier-Stokes equations*, Numer. Math., 125 (2013), pp. 441–510.

[60] E. Kessler, *On the distribution and continuity of water substance in atmospheric circulations.*, vol. 32 of Meteorol. Monographs, American Meteorological Society, Boston, 1969.

[61] A. P. Khain, M. Ovtchinnikov, M. Pinsky, A. Pokrovsky, and H. Krugliak, *Notes on the state-of-the-art numerical modeling of cloud microphysics*, Atmos. Res., 55 (2000), pp. 159 – 224.

[62] V. I. Khvorostyanov, *Mesoscale processes of cloud formation, cloud-radiation interaction, and their modeling with explicit cloud microphysics*, Atmos. Res., 39 (1995), pp. 1–67.

[63] R. Klein and A. J. Majda, *Systematic multiscale models for deep convection on mesoscales*, vol. 20, 2006, pp. 525–551.

[64] H. Köhler, *The nucleus in and the growth of hygroscopic droplets.*, T. Faraday Soc., 32 (1936), pp. 1152–1161.

[65] N. Kolbe, *A tumor invasion model for heterogeneous cancer cell populations: mathematical analysis and numerical methods*, dissertation, Johannes Gutenberg-Universität Mainz, 2017.

[66] A. Kurganov, *Finite-volume schemes for shallow-water equations*, Acta Numer., 27 (2018), pp. 289–351.

[67] D. Lamb and J. Verlinde, *Physics and chemistry of clouds*, Cambridge University Press, 2011.

[68] O. P. Le Maître and O. M. Knio, *Spectral methods for uncertainty quantification*, Scientific Computation, Springer, New York, 2010. With applications to computational fluid dynamics.

[69] V. I. Lebedev, *How to solve stiff systems of differential equations by explicit methods*, in Numerical methods and applications, CRC, Boca Raton, FL, 1994, pp. 45–80.

[70] ——, *Zolotarev polynomials and extremum problems*, Russian J. Numer. Anal. Math. Modelling, 9 (1994), pp. 231–263.

[71] ——, *Explicit difference schemes for solving stiff problems with a complex or separable spectrum*, Zh. Vychisl. Mat. Mat. Fiz., 40 (2000), pp. 1801–1812.

[72] V. I. Lebedev and S. A. Finogenov, *The use of ordered Čebyšev parameters in iteration methods*, Ž. Vyčisl. Mat i Mat. Fiz., 16 (1976), pp. 895–907, 1084.

[73] V. I. Lebedev and A. A. Medovikov, *An explicit method of the second order of accuracy for solving stiff systems of ordinary differential equations*, Izv. Vyssh. Uchebn. Zaved. Mat., (1998), pp. 55–63.

[74] R. J. LeVeque, *Numerical methods for conservation laws*, Lectures in Mathematics ETH Zürich, Birkhäuser Verlag, Basel, second ed., 1992.

[75] ——, *Finite volume methods for hyperbolic problems*, Cambridge Texts in Applied Mathematics, Cambridge University Press, Cambridge, 2002.

[76] P.-L. Lions, *Mathematical topics in fluid mechanics. Vol. 2*, vol. 10 of Oxford Lecture Series in Mathematics and its Applications, The Clarendon Press, Oxford University Press, New York, 1998. Compressible models, Oxford Science Publications.

[77] W.-L. Loh, *On Latin hypercube sampling*, Ann. Statist., 24 (1996), pp. 2058–2080.

[78] M. Lukáčová-Medviďová, *Lecture notes on numerical modelling in computational fluid dynamics*, 2003.

[79] M. Lukáčová-Medviďová, J. Rosemeier, P. Spichtinger, and B. Wiebe, *IMEX finite volume methods for cloud simulation*, in Finite volumes for complex applications VIII—hyperbolic, elliptic and parabolic problems, vol. 200 of Springer Proc. Math. Stat., Springer, Cham, 2017, pp. 179–187.

[80] M. Lukáčová-Medviďová and A. Schömer, *DMV-strong uniqueness principle for the compressible Navier-Stokes system with potential temperature transport*, in preparation.

[81] ——, *Existence of dissipative solutions to the compressible Navier-Stokes system with potential temperature transport*, submitted.

[82] X. Ma and N. Zabaras, *An adaptive hierarchical sparse grid collocation algorithm for the solution of stochastic differential equations*, J. Comput. Phys., 228 (2009), pp. 3084–3113.

[83] D. Maltese, M. Michálek, P. B. Mucha, A. Novotný, M. Pokorný, and E. Zatorska, *Existence of weak solutions for compressible Navier-Stokes equations with entropy transport*, J. Differential Equations, 261 (2016), pp. 4448–4485.

[84] P. Manneville, *Rayleigh-Bénard convection: thirty years of experimental, theoretical, and modeling work*, in Dynamics of Spatio-temporal Cellular Structures, I. Mutabazi, J. E. Wesfreid, and E. Guyon, eds., Springer, 2006, pp. 41–64.

[85] P. J. Marinescu, S. C. van den Heever, S. M. Saleeby, S. M. Kreidenweis, and P. J. DeMott, *The microphysical roles of lower-tropospheric versus midtropospheric aerosol particles in mature-stage MCS precipitation*, J. Atmos. Sci., 74 (2017), pp. 3657–3678.

[86] J. S. Marshall and W. M. Palmer, *The distributions of raindrops with size*, J. Meteorol., 5 (1948), pp. 165–166.

[87] M. Massot, *Lecture notes: Map 551 - systèmes dynamiques pour la modélisation et la simulation des milieux réactifs multi-échelles (2018-2019).*

[88] A. Matsumura and T. Nishida, *The initial value problem for the equations of motion of compressible viscous and heat-conductive fluids*, Proc. Japan Acad. Ser. A Math. Sci., 55 (1979), pp. 337–342.

[89] ——, *The initial value problem for the equations of motion of viscous and heat-conductive gases*, J. Math. Kyoto Univ., 20 (1980), pp. 67–104.

[90] A. A. Medovikov, *Dumka 3 code, available at http://dumkaland.org/.*

[91] ——, *High order explicit methods for parabolic equations*, BIT, 38 (1998), pp. 372–390.

[92] A. Meister, *Numerik linearer Gleichungssysteme*, SpringerLink : Bücher, Vieweg, Wiesbaden, third ed., 2008.

[93] S. Mishra, *Lecture notes on numerical methods for conservation laws and related equations*, 2003.

[94] S. Mishra and C. Schwab, *Sparse tensor multi-level Monte Carlo finite volume methods for hyperbolic conservation laws with random initial data*, Math. Comp., 81 (2012), pp. 1979–2018.

[95] S. Mishra, C. Schwab, and J. Šukys, *Multi-level Monte Carlo finite volume methods for uncertainty quantification in nonlinear systems of balance laws*, in Uncertainty quantification in computational fluid dynamics, vol. 92 of Lect. Notes Comput. Sci. Eng., Springer, Heidelberg, 2013, pp. 225–294.

[96] W. J. Morokoff and R. E. Caflisch, *Quasi-Monte Carlo integration*, J. Comput. Phys., 122 (1995), pp. 218–230.

[97] D. Murphy and T. Koop, *Review of the vapour pressure of ice and supercooled water for atmospheric applications*, Quarterly Journal of the Royal Meterorological Society, 131 (2005), pp. 1539–1565.

[98] H. Najm, *Uncertainty quantification and polynomial chaos techniques in computational fluid dynamics*, in Annual review of fluid mechanics. Vol. 41, vol. 41 of Annu. Rev. Fluid Mech., Annual Reviews, Palo Alto, CA, 2009, pp. 35–52.

[99] H. Niederreiter, *Random number generation and quasi-Monte Carlo methods*, vol. 63 of CBMS-NSF Regional Conference Series in Applied Mathematics, Society for Industrial and Applied Mathematics (SIAM), Philadelphia, PA, 1992.

[100] O. Pauluis and J. Schumacher, *Idealized moist Rayleigh-Bénard convection with piecewise linear equation of state*, Comm. Math. Sci., 8 (2010), pp. 295–319.

[101] M. D. Petters and S. M. Kreidenweis, *A single parameter representation of hygroscopic growth and cloud condensation nucleus activity*, Atmos. Chem. Phys., 7 (2007), pp. 1961–1971.

[102] G. Poëtte, B. Després, and D. Lucor, *Uncertainty quantification for systems of conservation laws*, J. Comput. Phys., 228 (2009), pp. 2443–2467.

[103] N. Porz, M. Hanke, M. Baumgartner, and P. Spichtinger, *A consistent model for liquid clouds*, Math. Clim. Weather Forecast., 4 (2018), pp. 50–78.

[104] H. R. Pruppacher and J. D. Klett, *Microphysics of Clouds and Precipitation*, Springer, 2010.

[105] O. Reynolds, *Papers on mechanical and physical subjects*, vol. 3 of The submechanics of the universe, Cambridge University Press, 1903.

[106] W. Riha, *Optimal stability polynomials*, Computing (Arch. Elektron. Rechnen), 9 (1972), pp. 37–43.

[107] Y. Saad and M. H. Schultz, *GMRES: a generalized minimal residual algorithm for solving nonsymmetric linear systems*, SIAM J. Sci. Statist. Comput., 7 (1986), pp. 856–869.

[108] V. K. Saul'ev, *Integration of equations of parabolic type by the method of nets*, Translated from the Russian by G. J. Tee. Translation edited and editorial introduction by K. L. Stewart. International Series of Monographs in Pure and Applied Mathematics, Vol. 54, Pergamon Press, London-Edinburgh-New York, 1960.

[109] A. Schömer, *Existence of dissipative measure-valued solutions to the compressible Navier-Stokes equations with entropy transport*, master thesis, Johannes Gutenberg-Universität Mainz, 2020.

[110] D. Schuster, S. Brdar, M. Baldauf, A. Dedner, R. Klöfkorn, and D. Kröner, *On discontinuous Galerkin approach for atmospheric flow in the mesoscale with and without moisture*, Meteorol. Z., 23 (2011), pp. 449–464.

[111] C. Schwab and C. J. Gittelson, *Sparse tensor discretizations of high-dimensional parametric and stochastic PDEs*, Acta Numer., 20 (2011), pp. 291–467.

[112] D. R. Smith, *An introduction to continuum mechanics—after Truesdell and Noll*, vol. 22 of Solid Mechanics and its Applications, Kluwer Academic Publishers Group, Dordrecht, 1993.

[113] R. C. Smith, *Uncertainty quantification*, vol. 12 of Computational Science & Engineering, Society for Industrial and Applied Mathematics (SIAM), Philadelphia, PA, 2014. Theory, implementation, and applications.

[114] M. Stein, *Large sample properties of simulations using Latin hypercube sampling*, Technometrics, 29 (1987), pp. 143–151.

[115] G. Strang, *On the construction and comparison of difference schemes*, SIAM J. Numer. Anal., 5 (1968), pp. 506–517.

[116] ——, *Variational crimes in the finite element method*, in The mathematical foundations of the finite element method with applications to partial differential equations (Proc. Sympos., Univ. Maryland, Baltimore, Md., 1972), 1972, pp. 689–710.

[117] J. Šukys, S. Mishra, and C. Schwab, *Multi-level Monte Carlo finite difference and finite volume methods for stochastic linear hyperbolic systems*, in Monte Carlo and quasi-Monte Carlo methods 2012, vol. 65 of Springer Proc. Math. Stat., Springer, Heidelberg, 2013, pp. 649–666.

[118] T. J. Sullivan, *Introduction to uncertainty quantification*, vol. 63 of Texts in Applied Mathematics, Springer, Cham, 2015.

[119] M. Szakall, K. Diehl, S. K. Mitra, and S. Borrmann, *A wind tunnel study on the shape, oscillation, and internal circulation of large raindrops with sizes between 2.5 and 7.5 mm*, Journalof the Atmospheric Sciences, 66 (2009), pp. 755–765.

[120] M. Szakall, S. K. Mitra, K. Diehl, and S. Borrmann, *Shapes and oscillations of falling raindrops - a review*, Atmospheric Research, 97 (2010), pp. 416–425.

[121] A. Tani, *On the first initial-boundary value problem of compressible viscous fluid motion*, Publ. Res. Inst. Math. Sci., 13 (1977), pp. 193–253.

[122] R. Temam and M. Ziane, *Some mathematical problems in geophysical fluid dynamics*, in Handbook of mathematical fluid dynamics. Vol. III, North-Holland, Amsterdam, 2004, pp. 535–657.

[123] R. A. Todor and C. Schwab, *Convergence rates for sparse chaos approximations of elliptic problems with stochastic coefficients*, IMA J. Numer. Anal., 27 (2007), pp. 232–261.

[124] E. F. Toro, *Riemann solvers and numerical methods for fluid dynamics*, Springer-Verlag, Berlin, third ed., 2009. A practical introduction.

[125] J. Tryoen, O. Le Maître, M. Ndjinga, and A. Ern, *Intrusive Galerkin methods with upwinding for uncertain nonlinear hyperbolic systems*, J. Comput. Phys., 229 (2010), pp. 6485–6511.

[126] A. M. Turing, *The chemical basis of morphogenesis*, Philos. Trans. Roy. Soc. London Ser. B, 237 (1952), pp. 37–72.

[127] A. Valli, *A correction to the paper: "An existence theorem for compressible viscous fluids" [Ann. Mat. Pura Appl. (4)* **130** *(1982), 197–213; MR 83h:35112]*, Ann. Mat. Pura Appl. (4), 132 (1982), pp. 399–400 (1983).

[128] ——, *An existence theorem for compressible viscous fluids*, Ann. Mat. Pura Appl. (4), 130 (1982), pp. 197–213.

[129] P. J. van der Houwen, *Construction of integration formulas for initial value problems*, North-Holland Publishing Co., Amsterdam-New York-Oxford, 1977. North-Holland Series in Applied Mathematics and Mechanics, Vol. 19.

[130] P. J. van der Houwen and B. P. Sommeijer, *On the internal stability of explicit, m-stage Runge-Kutta methods for large m-values*, Z. Angew. Math. Mech., 60 (1980), pp. 479–485.

[131] B. van Leer, *Towards the ultimate conservative difference scheme. V. A second-order sequel to Godunov's method [J. Comput. Phys.* **32** *(1979), no. 1, 101–136]*, vol. 135, 1997, pp. 227–248. With an introduction by Ch. Hirsch, Commemoration of the 30th anniversary of J. Comput. Phys.

[132] J. G. Verwer, *Explicit Runge-Kutta methods for parabolic partial differential equations*, vol. 22, 1996, pp. 359–379. Special issue celebrating the centenary of Runge-Kutta methods.

[133] J.-P. Vila, *Convergence and error estimates in finite volume schemes for general multidimensional scalar conservation laws. I. Explicit monotone schemes*, RAIRO Modél. Math. Anal. Numér., 28 (1994), pp. 267–295.

[134] W. Walter, *Gewöhnliche Differentialgleichungen*, Springer-Lehrbuch. [Springer Textbook], Springer-Verlag, Berlin, fifth ed., 1993. Eine Einführung. [An introduction].

[135] X. Wan and G. E. Karniadakis, *Long-term behavior of polynomial chaos in stochastic flow simulations*, Comput. Methods Appl. Mech. Engrg., 195 (2006), pp. 5582–5596.

[136] G. Warnecke, *Analytische Methoden in der Theorie der Erhaltungsgleichungen*, vol. 138 of Teubner-Texte zur Mathematik [Teubner Texts in Mathematics], B. G. Teubner Verlagsgesellschaft mbH, Stuttgart, 1999.

[137] J. Warner, *The microstructure of cumulus cloud. Part I. general features of the droplet spectrum*, J. Atmos. Sci., 26 (1969), pp. 1049–1059.

[138] T. Watanabe, *Flow pattern and heat transfer rate in Rayleigh-Bénard convection*, Phys. Fluids, 16 (2004), pp. 972–978.

[139] T. Weidauer, O. Pauluis, and J. Schumacher, *Cloud patterns and mixing properties in shallow moist Rayleigh-Bénard convection*, New Journal of Physics, 12 (2010).

[140] T. Weidauer and J. Schumacher, *Toward a mode reduction strategy in shallow moist convection*, New Journal of Physics, 15 (2013), pp. 125025–125249.

[141] P. Wesseling, *Principles of computational fluid dynamics*, vol. 29 of Springer Series in Computational Mathematics, Springer-Verlag, Berlin, 2001.

[142] N. Wiener, *The Homogeneous Chaos*, Amer. J. Math., 60 (1938), pp. 897–936.

[143] J. A. S. Witteveen, A. Loeven, and H. Bijl, *An adaptive stochastic finite elements approach based on Newton-Cotes quadrature in simplex elements*, Comput. & Fluids, 38 (2009), pp. 1270–1288.

[144] D. Xiu, *Numerical methods for stochastic computations*, Princeton University Press, Princeton, NJ, 2010. A spectral method approach.

[145] D. Xiu and J. S. Hesthaven, *High-order collocation methods for differential equations with random inputs*, SIAM J. Sci. Comput., 27 (2005), pp. 1118–1139 (electronic).

[146] D. Xiu and G. E. Karniadakis, *The Wiener-Askey polynomial chaos for stochastic differential equations*, SIAM J. Sci. Comput., 24 (2002), pp. 619–644 (electronic).

[147] ——, *Modeling uncertainty in flow simulations via generalized polynomial chaos*, J. Comput. Phys., 187 (2003), pp. 137–167.

[148] S. Zhang, K. Morita, K. Fukuda, and N. Shirakaw, *Simulation of three-dimensional convection patterns in a Rayleigh-Bénard system using the MPS method*, Memoirs Fac. Eng. Kyushu Univ., 66 (2006), pp. 29–37.

Declaration

I hereby declare that I wrote the dissertation submitted without any unauthorized external assistance and used only sources acknowledged in this work. All textual passages which are appropriated verbatim or paraphrased from published and unpublished texts as well as all information obtained from oral sources are duly indicated and listed in accordance with bibliographical rules. In carrying out this research, I complied with the rules of standard scientific practice as formulated in the statutes of Johannes Gutenberg-University Mainz to ensure standard scientific practice.

Mainz, September 2021 Bettina Wiebe